DEUTSCHES ELEKTRONEN-SYNCHROTRON DESY

DESY 80/13
February 1980

SELECTED TOPICS ON e^+e^- PHYSICS

by

Günter Wolf

NOTKESTRASSE 85 · 2 HAMBURG 52

Erratum
DESY 80/13 : Selected Topics on e^+e^- Physics
February 1980
Günter Wolf

The following corrections should be made:

Page 50	second paragraph. The last sentence should read: .... but one has to wait for the final analysis. third paragraph. The third sentence should read: Radiation in the initial state has the tendency to reduce the height of the two peaks and will fill in the valley in between them.
page 61,62	the two pages should be interchanged.
page 74	The reference to DELCO is 8.4
page 75	last paragraph. The reference to 8.7 was omitted.
page 118	first paragraph, second sentence: The main focus points were tests of QED (see Section 3), an exploration of the ....
page 137	sketch: The labelling of the two axes $\hat{n}_2$ and $\hat{n}_3$ should be interchanged.

SELECTED TOPICS ON e^+e^- PHYSICS*

Günter Wolf

DESY, Hamburg

Content

1. Introduction
2. Electron Positron Storage Rings
    - 2.1 Event rate
    - 2.2 Luminosity
    - 2.3 Energy spread
    - 2.4 Beam polarization
3. Purely Electromagnetic ee Interactions
    - 3.1 General remarks
    - 3.2 Tests of quantum electrodynamics
4. Phenomenology of Hadron Production
    - 4.1 General remarks
    - 4.2 Properties of the one-photon channel
    - 4.3 σ^{tot} in the quark-parton model
5. e^+e^- Annihilation at Low Energies and the Q^2 Behaviour of Formfactors
    - 5.1 The total cross section
    - 5.2 Formfactors
6. The Heavy Lepton τ
    - 6.1 Expected properties of a heavy lepton
    - 6.2 Experimental results on the τ
    - 6.3 Summary of the τ properties
7. Charmonium States
    - 7.1 The J/ψ and ψ' particles
    - 7.2 The quark model interpretation of J/ψ and ψ'
    - 7.3 $c\bar{c}$ spectroscopy
    - 7.4 The vector states
    - 7.5 The p-wave states
    - 7.6 The pseudoscalar mesons
8. Charmed Particles
    - 8.1 The D mesons
    - 8.2 The F mesons
    - 8.3 Charmed baryons
9. The Υ Family

---

* Lectures given at the 1979 JINR-CERN School of Physics, Dobogókö, Hungary, 2-15 Sept. 1979.

1. Introduction

The exploration of electron-positron interactions at high energies has become a powerful and fascinating tool of particle physics. There is a simple reason for this: the annihilation diagram, which yields an intermediate state with the quantum numbers of a photon, dominates the cross section at low energies and can be separated from higher order diagrams at high energies. Furthermore the current is timelike and couples directly to the fundamental fermions, leptons and quarks, in a well defined way. These facts have lead to a series of stunning discoveries which have established the existence of two new quarks and a new lepton.

The following lectures will not attempt to cover the whole field of e^+e^- physics, rather, a few topics will be discussed which are at present of particular interest. These are: the behaviour of formfactors, the characteristics of the τ lepton, the charmonium spectroscopy, charmed mesons and baryons, the Υ, Υ' family and data obtained at the new DESY storage ring PETRA on jet formation and gluon bremsstrahlung. For more information on e^+e^- physics the reader is referred to previous lectures given at this school[1.1], to review articles[1.2] and to rapporteur talks given at recent conferences[1.3].
We begin with a brief introduction to the field of e^+e^- physics.

2. Electron Positron Storage Rings

Electron-positron annihilation in the GeV region has to be studied with storage rings where the full beam energy is available for particle production. For an accelerator with a stationary target only a fraction of the beam energy contributes to the c.m. energy, $W/s \equiv \sqrt{s}$, the remainder being lost in the motion of the center of mass system.

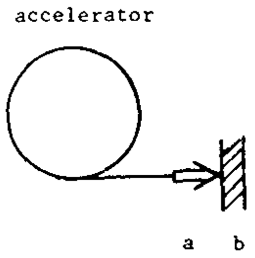

$\vec{p}_b = 0$

$s = m_a^2 + m_b^2 + 2m_b E_a$

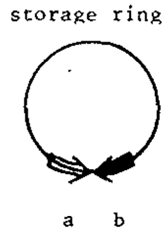

$\vec{p}_a = -\vec{p}_b$

$s = (E_a + E_b)^2$

The c.m. energy grows with the square root of the beam energy; the growth rate is determined by the target mass and is minute for an electron target. It is instructive to compare storage ring and accelerator for e^+e^- and pp collisions.

	c.m.energy (GeV)	beam energy (GeV) accelerator	required storage ring energy
pp	10	52	5
	100	5400	50
	1000	$5.4 \cdot 10^5$	500
e^+e^-	1	10^3	0.5
	10	10^5	5
	100	10^7	50

The price one pays for the favorable kinematics of a storage ring is a low target density and therefore small counting rates.

2.1 Event Rate

(a) accelerator

For a fixed target of length L with nucleon density ρ, the rate N of events for a cross section σ is given by

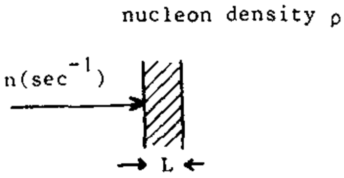

$$N(\text{sec}^{-1}) = n \cdot \rho \cdot L \cdot \sigma \qquad (2.1)$$

Typically, $n = 10^{12}(\text{sec}^{-1})$ and $\rho \cdot L = 10^{23}\,\text{cm}^{-2}$ yielding $N = 10^{35}(\text{cm}^{-2}\text{s}^{-1}) \cdot \sigma$ or 10^5 events/sec for $\sigma = 1\ \mu b$. Hence, accelerator experiments have typically a luminosity $\mathcal{L} \equiv N/\sigma$ of the order of $10^{35}\,\text{cm}^{-2}\text{sec}^{-1}$.

(b) storage ring

We consider head on collisions between bunches of particles:

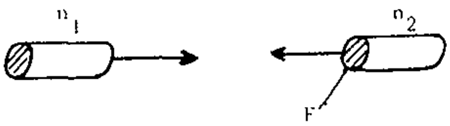

Defining

n_1, n_2	number of particles per bunch
F	beam cross section
B	number of bunches per beam
f	rotation frequency

the event rate for a cross section σ is given by

$$N = \frac{n_1 \cdot n_2 \cdot f}{F} \cdot B \cdot \sigma \equiv \mathcal{L} \cdot \sigma \qquad (2.2)$$

where $\mathcal{L}$ is the luminosity. A gaussian particle density distribution with rms radii σ_x, σ_y has a cross section of

$$F = 4\pi\sigma_x\sigma_y$$

Expressing $\mathcal{L}$ in terms of the beam currents, $i = n \cdot e \cdot f \cdot B$ (e electron charge) one has

$$\mathcal{L} = \frac{1}{4\pi e^2} \frac{i_1 \cdot i_2}{\sigma_x\sigma_y \cdot f \cdot B} \tag{2.3}$$

For a typical set of e^+e^- storage ring parameters,

$B = 1$
$f = 10^6\ s^{-1}$
$i_i = 50\ mA \triangleq 3.3 \cdot 10^{17}$ e/sec
$\sigma_x = 0.1$ cm
$\sigma_y = 0.01$ cm

the luminosity is $\mathcal{L} = 10^{31}\ cm^{-2} sec^{-1}$ leading to N = 10 events/sec for $\sigma = 1\ \mu b$. Hence, the luminosity of a storage ring is several orders of magnitude smaller than that of a typical accelerator experiment.

2.2 Luminosity

The maximum luminosity depends strongly on energy (2.1). The main limiting factors are beam-beam interactions at low energies and synchrotron radiation at high energies. A typical luminosity curve is shown in Fig. 2.1. At energies below some maximum E_o the luminosity for a fixed tune grows like E^4. At energies $E > E_o$ the rate of energy loss through synchrotron radiation has reached the available power limit and the luminosity drops like E^{-10}.

2.3 Energy Spread

The energy spread σ_E of the beams is determined by synchrotron radiation. It depends on E and the ring radius ρ:

$$\sigma_E \sim \frac{E^2}{\sqrt{\rho}} \tag{2.4}$$

For DORIS and SPEAR

$$\sigma_E (\mathrm{MeV}) \approx 0.9 \left(\frac{E}{2\ \mathrm{GeV}}\right)^2 \tag{2.5}$$

2.4 Beam Polarization

The magnetic guide field together with the synchrotron radiation lead to a polarization of the beams with the positron (electron) spin parallel (antiparallel) to the magnetic field$^{2.2)}$. The polarization arises because e.g. in the case of an e^+ the transition from the $\vec{S},\vec{B} = \downarrow\uparrow$ to the $\vec{S},\vec{B} = \uparrow\uparrow$ state is energetically favored over the inverse transition. Since the synchrotron radiation is strongly energy dependent the build-up time

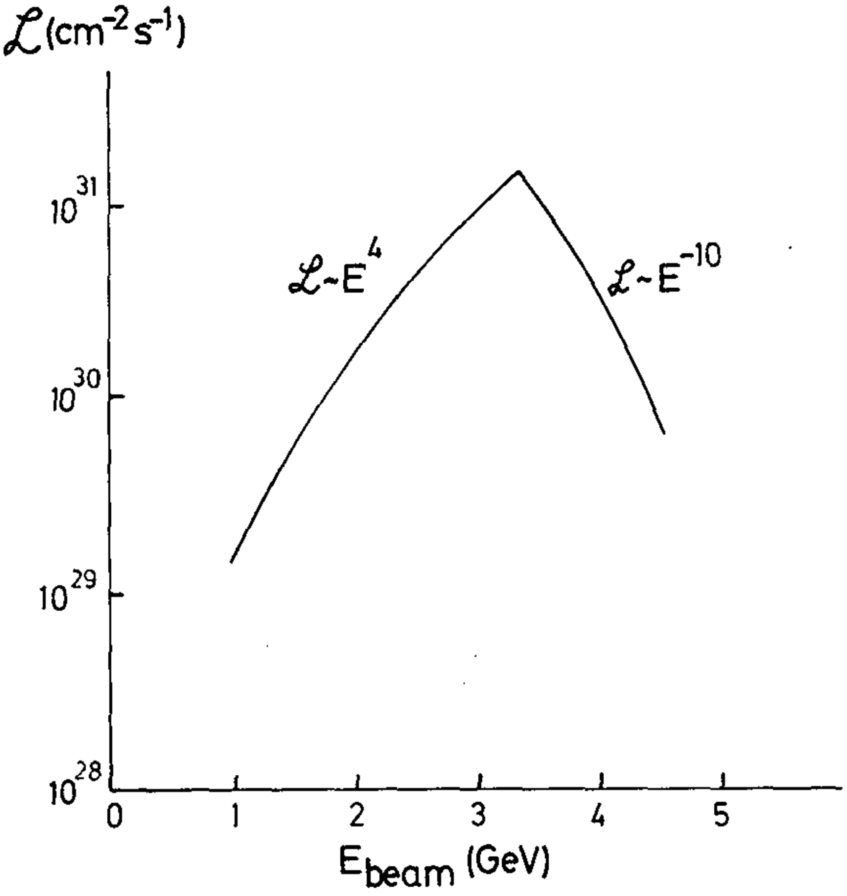

Fig. 2.1 A typical luminosity curve as a function of the beam energy.

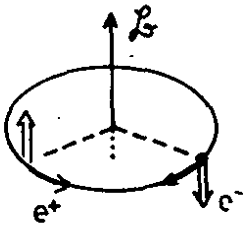

for the polarization will depend strongly on E, as well. Defining ρ to be the bending radius in the magnets, and R the average radius of the ring, the degree of polarization as a function of time is given by

$$P(t) = P_o\,(1 - e^{-t/\tau}), \tag{2.6}$$

with
$$P_o = \frac{8\sqrt{3}}{15} = 0.92$$

and
$$\tau^{-1} = \frac{5\sqrt{3}}{8}\, c\, \frac{r_o^2}{\alpha}\, \frac{\gamma^5}{\rho^2 R} \tag{2.7}$$

where $\gamma = E/m_e$ and $\alpha = 1/137$. For DORIS and SPEAR one has

$$\tau \approx \frac{165\ h}{E^5}\ , \qquad E \text{ in GeV} \tag{2.8}$$

τ = 5h for E = 2 GeV and τ = 15 min for E = 4 GeV.
Since the average beam life time (defined here as the time over which the luminosity drops by a factor of e) is of the order of 3 - 5 hrs, studies with polarized beams at DORIS and SPEAR become practical for $E \gtrsim 3$ GeV.

For PETRA $\tau = 2.5\cdot 10^5/E^5$(h); polarization measurements become feasible for $E \gtrsim 13$ GeV.

The polarization is destroyed when the ring operates near a machine resonance. For this reason polarized beams will be obtained only for certain sets of machine parameters.

Table 2.1 and Fig. 2.2 summarize the existing and planned ee storage rings.

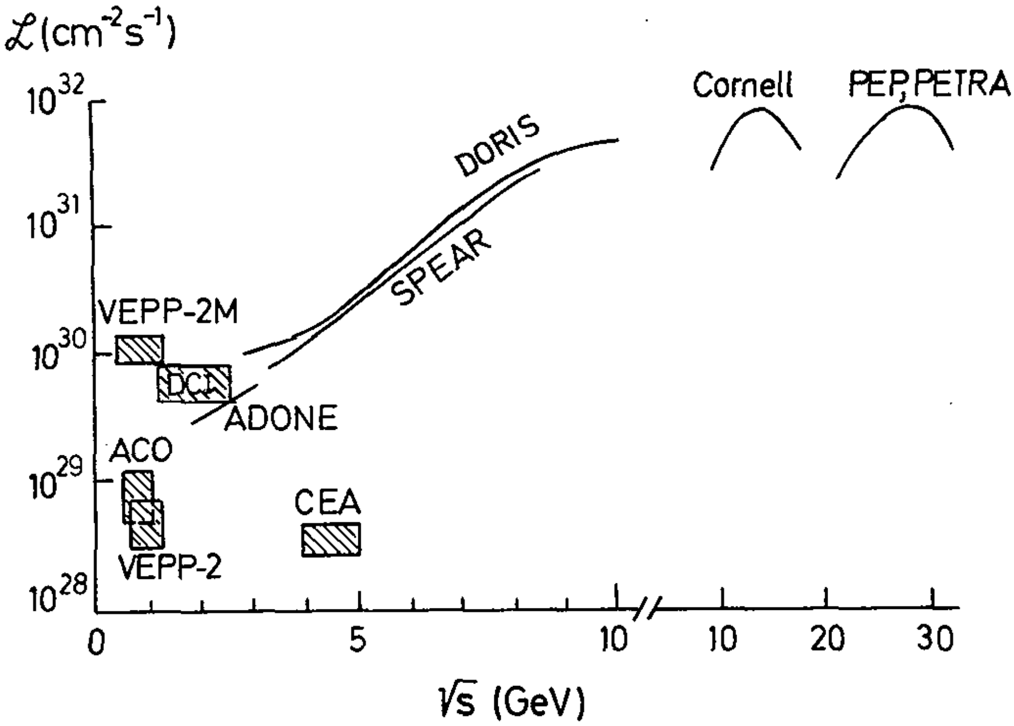

Fig. 2.2 Luminosity versus total c.m. energy for existing or planned e^+e^- storage rings.

Table 2.1 Existing and planned ee storage rings

Ring		Start of operation		Beam energy (GeV)
Ada	Frascati	1960	e^+e^-	0.25
Princeton-Stanford	Stanford	1962	e^-e^-	0.55
ACO	Orsay	1966	e^+e^-	0.2 - 0.55
VEPP-2	Novosobirsk	1966	e^+e^-	0.2 - 0.55
ADONE	Frascati	1969	e^+e^-	0.7 - 1.55
BYPASS	Cambridge (USA)	1971	e^+e^-	~1.5 - 3.5
SPEAR	Stanford	1972	e^+e^-	1.2 - 4.2
DORIS	Hamburg	1974	e^+e^-	~1 - 5.1
VEPP-2M	Novosibirsk	1975	e^+e^-	0.2 - 0.67
DCI	Orsay	1976	e^+e^-	0.5 - 1.7
VEPP-4	Novosibirsk	1978	e^+e^-	
PETRA	Hamburg	1978	e^+e^-	5 - 19
CESR	Cornell	1979	e^+e^-	3 - 8
PEP	Stanford	1980	e^+e^-	5 - 18
LEP	Europe		e^+e^-	22 - 130

3. Purely Electromagnetic ee Interactions

3.1 General remarks

We start with a brief discussion of the phenomenology of electromagnetic e^+e^- interactions. The electron will be assumed to have only electromagnetic interactions.

The lowest order processes are of order α^2, such as Bhabha scattering or μ pair production.

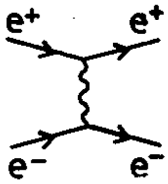

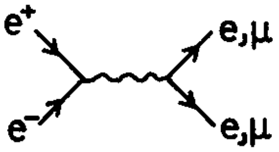

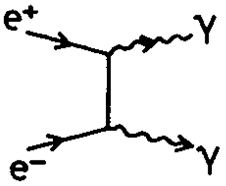

The next higher order processes constitute radiative corrections to the first ones:

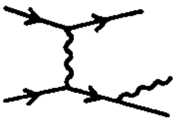

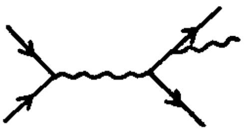

Although of order α^3, their contributions can be important. Since they depend strongly on the properties of the experimental setup (such as energy and angular resolution) the experimental results are usually presented with the contributions from radiative corrections removed.

A new class of processes is encountered in fourth order: the virtual photon clouds of the two incident beams interact with each other. After integration over the photon spectra the cross section is proportional to $\alpha^4 \ln^2 (\frac{E}{m_e})$. Since $\ln \frac{E}{m_e} \sim 10$ for energies in the GeV region one power

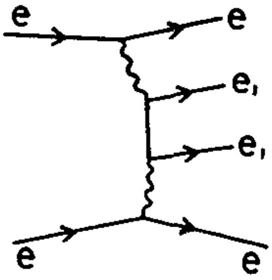

of α is essentially cancelled by the integration. Events of this type have been observed at Novosibirsk[3.1] and at Frascati[3.2].

3.2 Tests of quantum electrodynamics

Purely electromagnetic processes can be calculated directly from QED[3.3]. A comparison between experiment and theory provides therefore a stringent test of the validity of QED. Such tests have been done for four different processes:

(a) $e^- e^- \to e^- e^-$ (Møller scattering)

Two diagrams with space like photons contribute:

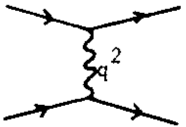

(A)

+

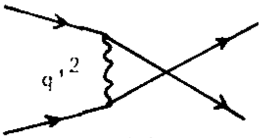

(B)

The differential cross section for producing an e^- at an angle Θ is given by

$$\frac{d\sigma}{d\Omega} = \frac{\alpha^2}{2s}\left\{\underset{|A|^2}{\frac{q'^4 + s^2}{q^4}} + \underset{2AB^*}{\frac{s^2}{q^2 q'^2}} + \underset{|B|^2}{\frac{q^4 + s^2}{q'^4}}\right\}$$

$$\text{with } q^2 = -s\cos^2\Theta/2\,,\; q'^2 = -s\sin^2\Theta/2 \qquad (3.1)$$

The angular distribution is strongly peaked forward and backward.

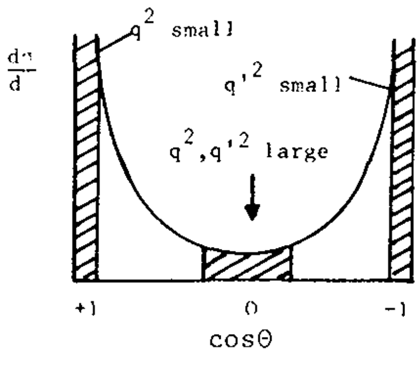

Deviations from the QED prediction could occur e.g. due to strong interaction contributions at the vertices or in the photon propagator.

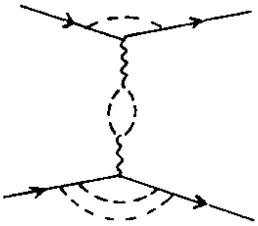

These contributions, which can only depend on the mass of the virtual photon, lead to the following modification of eqn (3.1):

$$\frac{d\sigma}{d\Omega} = \frac{\alpha^2}{2s}\left\{\frac{q'^4 + s^2}{q^4}\left|F(q^2)\right|^2 + \frac{s^2}{q^2 q'^2}\,\mathrm{Re}(F(q^2)F^*(q'^2)) + \frac{q^2 + s^2}{q'^4}\left|F(q'^2)\right|^2\right\} \tag{3.1'}$$

It is customary to parametrize $F(q^2)$ by[3.4)]

$$F(q^2) = 1 \mp \frac{q^2}{q^2 - \Lambda_\pm^2} \tag{3.2}$$

where $\Lambda_\pm$ is a cut-off parameter which characterises the mass of the exchanged system, viz:

$$\frac{1}{q^2} \to \frac{1}{q^2} \mp \frac{1}{q^2 - \Lambda_\pm^2}$$

Experimentally, the test on the validity of QED consists in a study of the shape of the angular distribution: the forward and backward peaks are determined at small four-momentum transfers for which QED is known to be correct. Deviations from QED will be most prominent in the central region ($\cos\Theta \approx 0$) corresponding to large values of q^2 and q'^2.

(b) $e^+e^- \to e^+e^-$ (Bhabha scattering)

Space-like and time-like photon exchange contribute to Bhabha scattering.

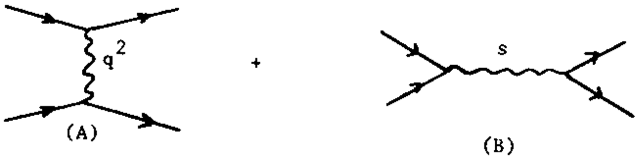

The differential cross section for finding an e^+ scattered under an angle Θ with respect to the e^+ beam is:

$$\frac{d\sigma}{d\Omega} = \frac{\alpha^2}{2s}\left\{\frac{q'^4 + s^2}{q^4} + \frac{2q'^4}{q^2 s} + \frac{q'^4 + q^4}{s^2}\right\} \tag{3.3}$$

The angular distribution possesses a sharp forward peak due to the first diagram.

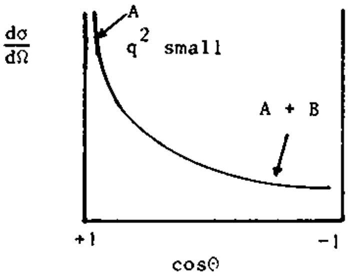

The modifications to the QED cross section are similar to those for Møller scattering. As before, the QED test consists in a measurement of the shape of the angular distribution. Bhabha scattering tests the photon propagator in the space-like and time-like region.

(c) $e^+e^- \rightarrow \mu^+\mu^-$ (μ pair production)

This is the simplest of all QED reactions. It proceeds via time-like photon exchange.

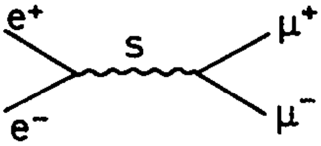

The differential cross section reads

$$\frac{d\sigma}{d\Omega} = \frac{\alpha^2}{4s}\,\beta_\mu \left\{(1 + \cos^2\Theta) + (1 - \beta_\mu^2)\sin^2\Theta\right\} \qquad (3.4)$$

where $\beta_\mu = p_\mu / E_\mu$. For $p_\mu \approx E_\mu$

$$\frac{d\sigma}{d\Omega} = \frac{\alpha^2}{4s}\,(1 + \cos^2\Theta) \qquad (3.5)$$

The integrated cross section is given by

$$\sigma_{\mu\mu} \approx \frac{4\pi}{3}\,\frac{\alpha^2}{s} = \frac{\pi}{3}\,\frac{\alpha^2}{E^2} = \frac{21.9\ \text{nb}}{E^2} \qquad (\text{E in GeV}) \qquad (3.6)$$

Possible deviations from QED will depend on s and can only be detected by measuring the absolute magnitude of the cross section. This can be done e.g. by comparing μ-pair production to small angle Bhabha scattering.

(d) $e^+e^- \rightarrow \gamma\gamma$ (Two-photon annihilation)

Two-photon annihilation proceeds via electron exchange.

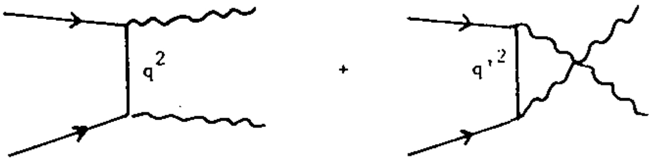

The differential cross section is given by

$$\frac{d\sigma}{d\Omega} = \frac{\alpha^2}{2s} \left\{ \frac{q'^2}{q^2} + \frac{q^2}{q'^2} \right\} \tag{3.7}$$

where $q^2 = -\, s \cos^2\Theta/2$, $q'^2 = -\, s \sin^2\Theta/2$

The angular distribution is strongly peaked towards forward and backward angles.

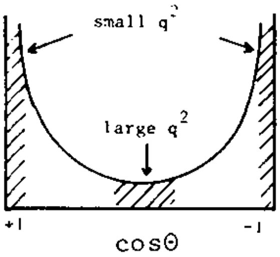

Deviations from the QED prediction will show up as a change in the shape of the angular distribution. A measurement of two-photon annihilation will not test the electron propagator as one might think at first. As was shown by Kroll[3.5] the effect of corrections to the electron propagator cancel each other due to charge conservation. The electron propagator can be tested, however, in processes with closed electron loop diagrams. The measurement of two-photon annihilation provides instead a test on the contribution from the "sea-gull" term[3.5, 3.6]

The four QED processes discussed above have the same s-dependence, $\sigma \sim s^{-1}$. In Fig. 3.1 the differential cross sections are compared for a beam energy of 1 GeV. The largest cross section by far is for Bhabha scattering at small angles. For this reason and since QED is known to work at small momentum transfers, Bhabha scattering at small angles is generally used to measure the luminosity.

The sensitivity on deviations from QED increases with the energy. The most stringent limits at present come from PETRA experiments. A comparison between QED predictions and the measured cross sections for Bhabha scattering, two-photon annihilation, μ and τ-pair production is shown in Figs. 3.2 - 3.4 (Ref. 3.7 - 3.9). The experimental results agree with theory.

The cut-off parameters deduced from these experiments are listed in Table 3.1. Bearing in mind that they have been determined under the assumption that whatever modifies the photon propagator or the $\ell\ell\gamma$ vertex has the coupling strength e, the results of Table 3.1 can be rephrased by saying that QED has been tested down to distances of $\approx 2 \cdot 10^{-16}$ cm. Perhaps the most significant result is the proof that the τ is point like (3.9, 3.8).

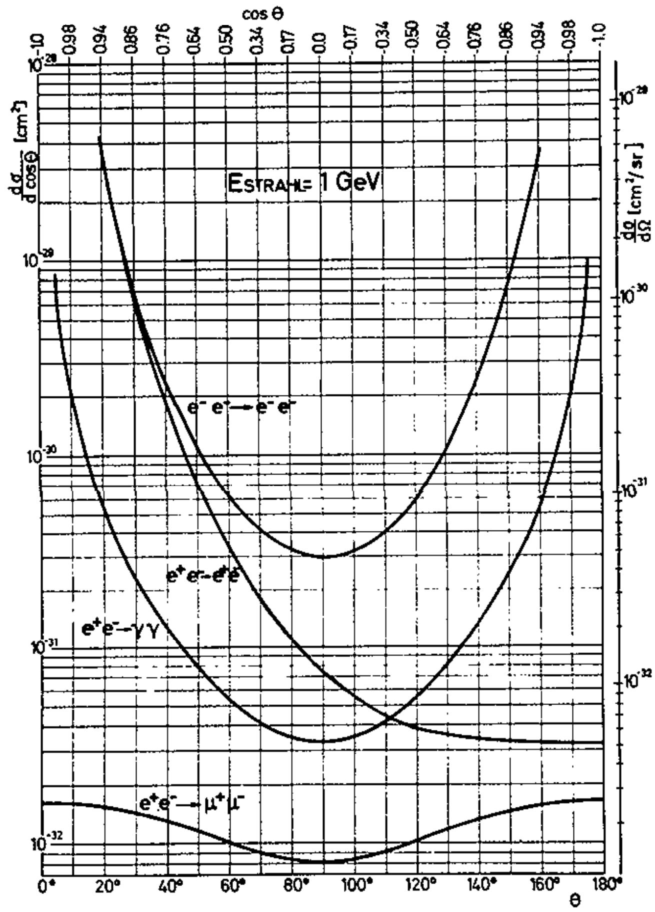

Fig. 3.1 Differential cross sections for $e^-e^- \to e^-e^-$. $e^+e^- \to e^+e^-$, $e^+e^- \to \gamma\gamma$ and $e^+e^- \to \mu^+\mu^-$ for a beam energy of 1 GeV.

Table 3.1 QED cutoff parameters: 95 % confidence lower limits in GeV.

experiment	electron Λ_-	electron Λ_+	muon Λ_-	muon Λ_+	tau Λ_-	tau Λ_+
JADE (3.7)	89	74				
MARK J (3.8)	95	74	97	71	53	47
PLUTO (3.9)	60	40	31	16		

4. Phenomenology of Hadron Production

4.1 General remarks

The lowest order e^+e^- scattering processes leading to hadron production are:

one-photon annihilation

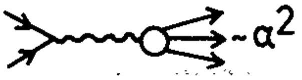

radiative corrections to
one-photon annihilation

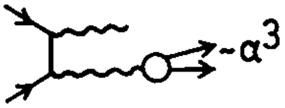

two-photon scattering

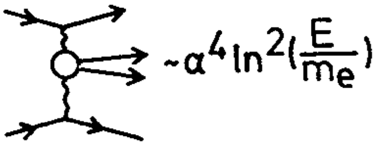

As in the purely electromagnetic case the two-photon scattering contribution is effectively of order α^3 after integration over the photon spectra. Furthermore, while the cross section for one-photon annihilation decreases as s^{-1} with energy (see below) the two-photon contribution increases ~ln s and eventually will win over the one-photon contribution. The importance of the two-photon process was first recognized by Low[4.1] and by Kessler and coworkers[4.2]. Evidence for this mechanism was first found at Frascati[4.3]. Systematic studies of γγ interactions are beginning now and undoubtedly will open an interesting field of physics. In the following, however, only the one-photon channel will be considered.

4.2 Properties of the one-photon channel

The hadron system produced by one-photon annihilation has the quantum numbers of the photon, $J^{PC} = 1^{--}$. For this reason the angular momentum L of the incident e^+ and e^- is limited to 0 and 2. Since L = R·E, the radius of interaction will be of order $\frac{1}{E}$ leading to a total cross section for hadron production of

$$\sigma^{tot} \approx \alpha^2 \pi R^2 = \frac{\alpha^2 \pi}{E^2} \simeq \frac{60\ \text{nb}}{E^2} \qquad \text{E in GeV} \tag{4.1}$$

From this simple minded exercise we expect σ^{tot} to decrease with energy as s^{-1}. Because $J^P = 1^-$ the most general angular distribution with respect to the beam direction for a particle h produced via $e^+e^- \to hX$ is of the form

$$\frac{d\sigma}{d\Omega} = a + b\cos^2\Theta \tag{4.2}$$

which is radically different from typical angular distributions in hadron hadron collisions.

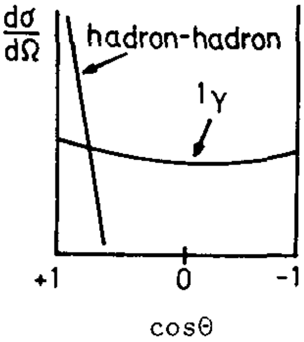

4.3 σ^{tot} in the quark-parton model

The observation of scaling in deep inelastic electron-nucleon scattering led to the hypothesis that the photon-hadron interaction is basically a photon-quark interaction[4.4).

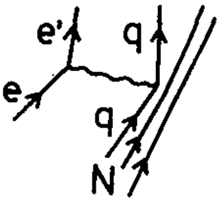

As a consequence we expect $e^+e^- \to$ hadrons to proceed via the formation of a quark-antiquark pair.

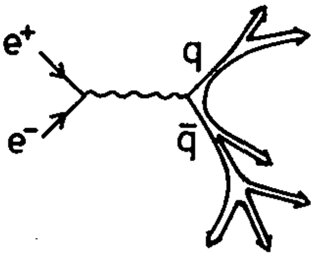

We assume the quarks have spin 1/2 and are pointlike. Then the cross section for producing a free $q\bar{q}$ pair is the same as for producing a $\mu^+\mu^-$ pair (see eq. 3.6) except that the quark charge Q_i replaces the muon charge 1:

$$\sigma(e^+e^- \to q\bar{q}) = Q_i^2\,\sigma_{\mu\mu} = Q_i^2\,\frac{4\pi\alpha^2}{3s} \qquad (\beta_q = 1 \text{ is assumed}) \tag{4.3}$$

Assuming further that the produced $q\bar{q}$ pair turns into hadrons with probability one, the total hadron cross section is found by summing over all possible $q\bar{q}$ pairs:

$$\sigma^{tot} = \sum_i Q_i^2 \, \sigma_{\mu\mu} \qquad (4.4)$$

As we see from eqn (4.4) the quark model predicts the total hadron cross section to decrease with energy as $\sigma^{tot} \sim s^{-1}$ and its magnitude to be of the order of the μ pair production. The value of Q_i^2 depends on the specific quark scheme:

quark model	Q_i^2
u, d, s	$\frac{4}{9} + \frac{1}{9} + \frac{1}{9} = \frac{2}{3}$
(u, d, s) • color	$3 \cdot \frac{2}{3} = 2$
(u, d, s, c) • color	$3 \cdot \frac{10}{9} = \frac{10}{3}$
Han-Nambu (u, d, s)	4
" (u, d, s, c)	6

Because of the expected behaviour (eq. 4.4) it is customary to study the ratio $R \equiv \sigma^{tot}(e^+e^- \to \text{hadrons})/\sigma_{\mu\mu}$.

The discussion above concerned the high energy behaviour of σ^{tot}. At low energies we expect to produce nonstrange vector mesons which have the same quantum numbers as the photon.

The cross section for V production and decay into the final state f near the resonance, $W \approx m_V$ is given by

$$\sigma(e^-e^- \to V \to f) = \frac{3\pi}{W^2} \; \frac{\Gamma_{ee}\,\Gamma_f}{(W - m_V)^2 + \Gamma^2/4} \qquad (4.5)$$

5. e^+e^- Annihilation at Low Energies and the Q^2 Behaviour of Formfactors

5.1 The total cross section

The total cross section for e^+e^- annihilation into hadrons, σ_{tot}, is computed from the number of events N observed, the integrated luminosity L and the acceptance A for hadronic events. Furthermore a correction factor f has to be applied to account for radiative effects in the initial state. The result is

$$\sigma_{tot} = \frac{N}{L} \cdot \frac{f}{A} \qquad (5.1)$$

In general the accuracy of the measured σ_{tot} values is limited by systematical errors and not by statistics. The largest uncertainties are caused by the incomplete coverage of the solid angle. Extrapolation to the full solid angle can be done by means of a Monte Carlo program that includes assumptions on the multiplicities of charged and neutral particles, the dynamics of the production process etc. The assumptions can be checked by comparing the Monte Carlo data with the measured results. The systematic uncertainty of A determined in this way is typically 5 - 15 %. The luminosity is determined from small angle (few degrees) and/or large angle Bhabha scattering, $e^+e^- \to e^+e^-$. The systematic errors mainly due to acceptance and radiative corrections are on the order of a few percent.

The radiative correction factor f primarily accounts for processes where the incoming electron (positron) has emitted a photon: as a result the total c.m. energy available for hadron production is reduced and the c.m. system is moving in the laboratory frame leading to a change in acceptance. In order to apply radiative corrections a good knowledge of the total cross section and the behaviour of the final states at lower energies is required. The uncertainty of this correction, in a region where σ_{tot} is smooth, is typically a few percent but may be considerably larger if σ_{tot} is structured.

Fig. 5.1 shows the ratio $R = \sigma_{tot}/\sigma_{\mu\mu}$ at low energies up to 2.4 GeV.$^{5.1-5.4*)}$ The error bars include only statistical uncertainties. To these an overall systematic uncertainty of 10 - 15 % has to be added.

The energy region up to 1.1 GeV is dominated by the excitation of the vector mesons ρ, ω and Φ. Between 1.1 and 1.4 GeV R seems to be constant with a value near one. Between 1.4 and 1.5 GeV R rises from one to two and stays then almost constant up to 2.4 GeV. The step near 1.4 GeV seems to be correlated with the onset of "inelastic" kaon production, $e^+e^- \to KK\pi...$ (5.5).

5.2 Formfactors

At low energies a few exclusive final states build up the total cross section such as pair production of pions and kaons. The pair production channels measure the time-like form factors of the corresponding particle, e.g. two pion production, $e^+e^- \to \pi^+\pi^-$, measures the pion form factor, F_π. The differential cross section is given by

$$\frac{d\sigma}{d\Omega} = \frac{\alpha^2}{8s} \beta_\pi^3 \sin^2\Theta \, |F_\pi(s)|^2 \tag{5.1}$$

with $\beta_\pi = P_\pi/E_\pi$. Near the rho, F_π has a Breit-Wigner behaviour,

$$F_\pi(s) = \frac{m_\rho^2}{m_\rho^2 - s - i m_\rho \Gamma} \cdot F_o \tag{5.2}$$

From the normalization condition,

$$F\,(0) = 1$$

it follows that $F_o = 1$ if we assume the Breit-Wigner eqn.(5.2) to be valid down to $s = 0$. Finite width corrections and the contribution from the ω via its two-pion decay mode modify this simple expression (see e.g. Gounaris and Sakurai (5.6)).

---

*) The three data points between 1.1 and 1.4 GeV were obtained by adding the cross section data for the final states $\pi^+\pi^-$ (Novosibirsk), $\pi^+\pi^-\pi^o$ (Orsay), $\pi^+\pi^+\pi^-\pi^-$ and $\pi^+\pi^-\pi^o\pi^o$ (Frascati, Novosibirsk, Orsay).

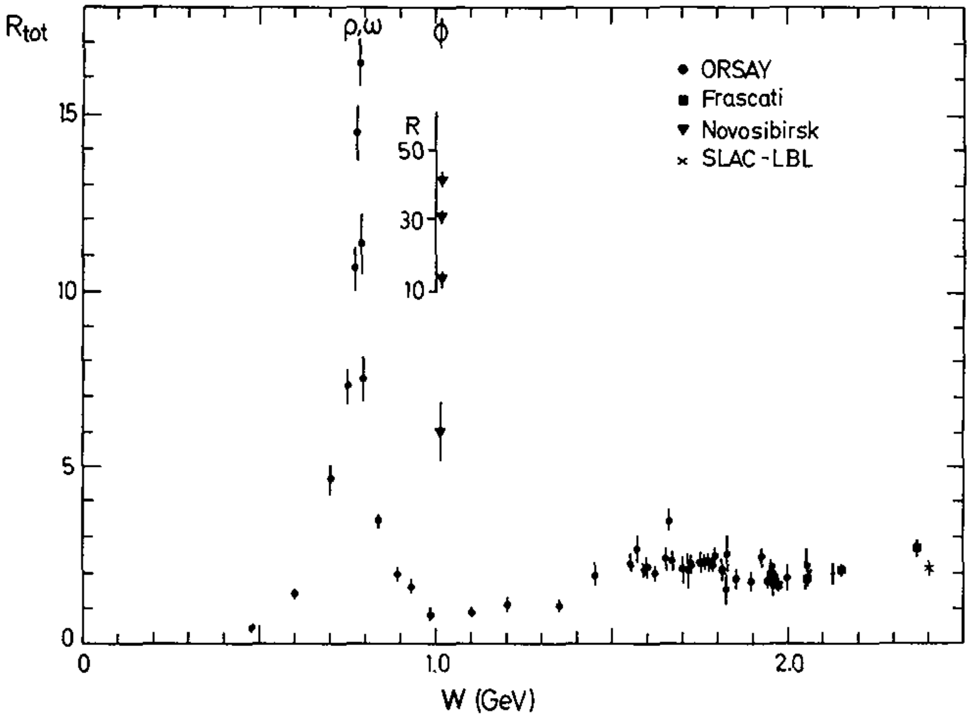

Fig. 5.1 Measurements of R from Refs. 5.1 - 5.4

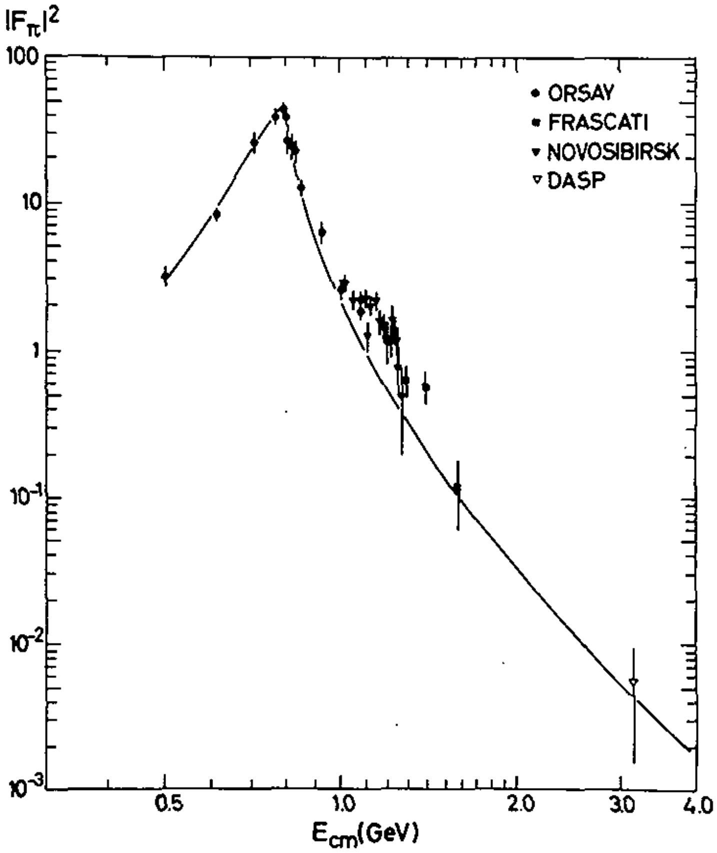

Fig. 5.2 The square of the pion form factor as a function of the total cms energy

In Fig. 5.2 $|F_\pi|^2$ is shown as a function of energy. The dominant feature is the excitation of the rho. The rho pole accounts for the energy dependence up to the highest energies measured (see curve in Fig. 5.2) except for a bump centered around 1.2 GeV. This bump which has been explored in particular by the Novosibirsk group might indicate the excitation of the hypothetical vectorstate $\rho'(1250)$.
In Fig. 5.3 the measurements on $|F_\pi|^2$ in the time-like and space-like regions are combined. The space-like values were determined from $\pi^\pm$ electroproduction, $eN \rightarrow eN\pi$ (5.7, 5.8). There is a smooth transition from the region $s > 0$ to $s > 0$. The data can be represented by adding the $\omega\pi$ channel and a $\rho'(1250)$ contribution to the ρ pole (5.1).

The kaon formfactor as deduced from data on $e^+e^- \rightarrow K^+K^-$ is shown in Fig. 5.4. As expected there is a sharp peak due to the excitation of the $\phi(1020)$. The fall-off towards high energies qualitatively is reproduced by the ω and ϕ contributions as calculated by Renard5.9). Quantitatively, however, there are discrepancies and the most recent studies made by the DM1 group made at DCI5.10) indicate that the physics behind F_K is more complex.

The data on the proton formfactor in the time-like region are scanty. The differential cross section depends on the electric and magnetic formfactors, G_E and G_M:

$$\frac{d\sigma}{d\Omega} = \frac{\beta\alpha^2}{4s}\left\{|G_E|^2 \frac{4m_p^2}{s}\sin^2\Theta + |G_M|^2 (1 + \cos^2\Theta)\right\} \qquad (5.3)$$

where m_p is the proton mass and β its velocity. The normalization conditions for G_E and G_M are

$$G_E(0) = 1$$
$$G_M(0) = \mu \quad = \text{proton magnetic moment in units of } e/2m_p.$$

The contributions from G_E and G_M can be separated by analysing the angular distribution. So far the small number of detected events did not permit such an analysis. Instead the two formfactors were assumed to be the same, $G_E(s) = G_M(s)$, which is exact for $s = 4m_p^2$ if only s-wave constributions are present. The result is shown in Fig. 5.5 which besides e^+e^- data includes a measurement of the line reversed process $p\bar{p} \rightarrow e^+e^-$. A fast decrease of $|G_E|^2 = |G_M|^2$ is observed with rising energy. The dipole prediction,

$$G_E = (1 - s/0.71)^{-2}$$

which works well in the space-like region is more than an order of magnitude below the data near threshold, $\sqrt{s} = 2m_p$. The vector dominance calculation by Körner and Kuroda5.14) who took the contributions from ρ, ω, ϕ, J/ψ and their recurrences into account describes the data well.

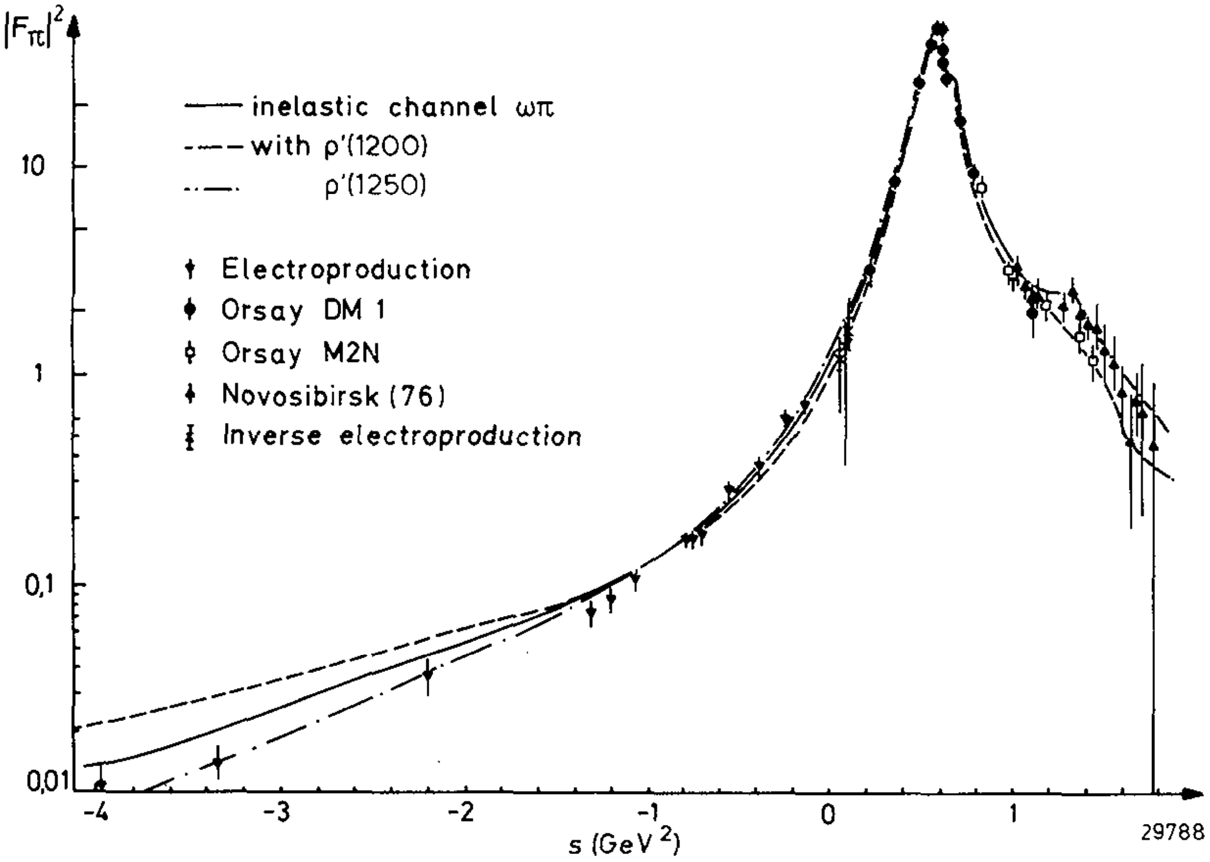

Fig. 5.3 The square of the pion formfactor, $|F_\pi|^2$ in the spacelike and timelike region.

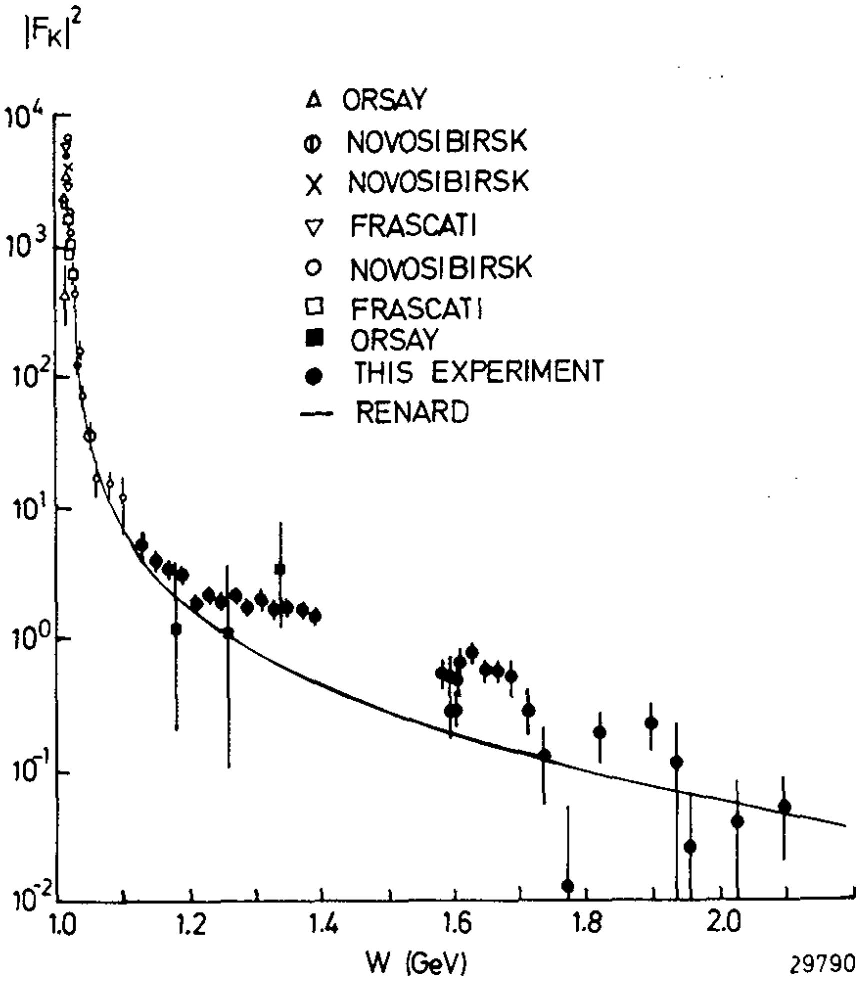

Fig. 5.4 The square of the charged kaon formfactor, $|F_K|^2$. (Ref. 5.12)

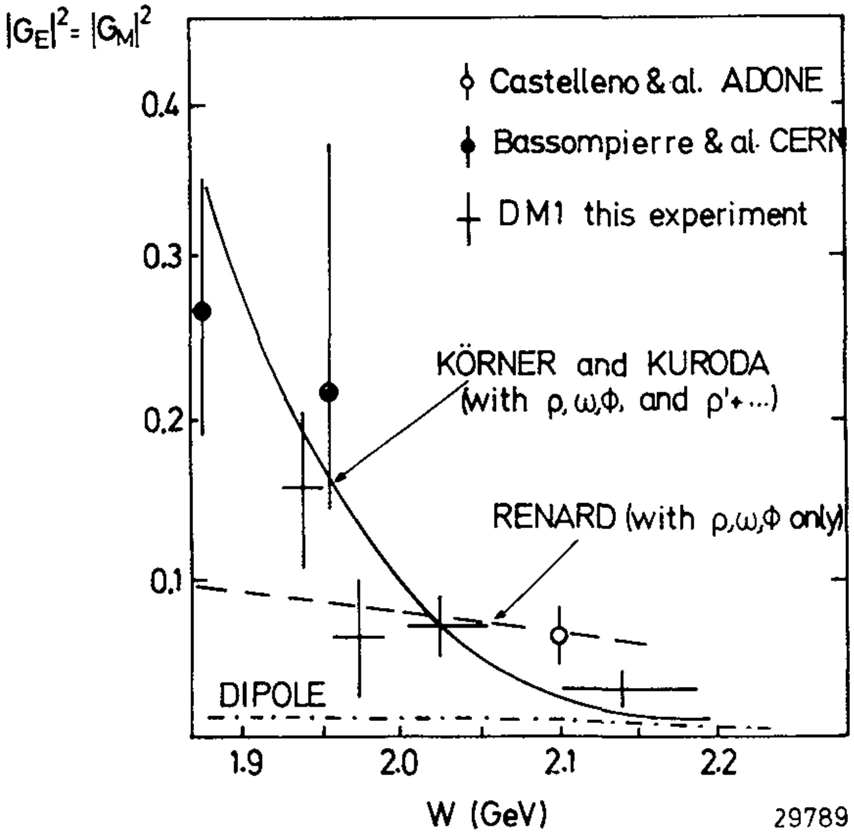

Fig. 5.5 The square of the nucleon formfactor determined under the assumption $|G_E|^2 = |G_M|^2$ (Ref.5.12).

6. The Heavy Lepton τ

We begin with a discussion of the properties expected for a heavy lepton τ (6.1).

6.1 Expected properties of a heavy lepton

Assuming the lepton τ to be pointlike the e^+e^- production cross section is given by

$$\sigma_{\tau\bar{\tau}} = \frac{4\pi\alpha^2}{3s}\, \beta_\tau \left(1 + \frac{1-\beta_\tau^2}{2}\right) \tag{6.1}$$

where $\beta_\tau = p/E$ is the τ velocity.
If the lepton decays weakly and the decay is mediated by the standard V-A weak current the partial decay widths can be calculated or estimated (see Fig. 6.1).

The leptonic decay modes can be computed unambiguously:

$$\Gamma_e \equiv \Gamma(\tau \to \nu_\tau\, e\bar{\nu}_e) = \frac{G_F^2 \cdot m_\tau^5}{192\pi^3}$$

$$\Gamma_\mu \equiv \Gamma(\tau \to \nu_\tau\, \mu\bar{\nu}_\mu) = \Gamma_e \cdot F(y)$$

$$G_F = \frac{1.02}{m_p^2} \times 10^{-5} (\mathrm{GeV}^{-2}) \quad \text{and}$$

$$F(y) = (1 - 8y + 8y^3 - y^4 - 12y^2 \cdot \ln y). \tag{6.2}$$

$F(y = m_\mu^2/m_\tau^2)$ is a small phase space correction.

A lepton decays semihadronically as shown in Fig. 6.1b. Conventional theory predicts that the τ decays into final states of low multiplicity and a small ratio of kaons to pions. This is indeed reproduced in actual calculations[6.1),6.2)] and an estimate of various branching ratios is listed in Table 6.1.

Some of the decay widths are rather well known:

$\tau \to \nu_\tau \pi$: The pion mode is directly related to the $\pi \to \mu\nu$ decay as shown in Figs, 6.1c,d. Note that the mass squared of the weak current is the same in both cases ($Q^2 = m_\pi^2$). As a consequence the value of the formfactor is the same for both decays. The partial width is given by

$$\frac{\Gamma(\tau^- \to \nu_\tau \pi^-)}{\Gamma_e} = \frac{12\pi^2 f_\pi^2 \cos^2\Theta_c}{m_\tau^2} = \frac{2.1\, m_p^2}{m_\tau^2} \tag{6.3}$$

with $f_\pi = 0.137\, m_p$ (m_p = proton mass), and $\Theta_c = 0.23$ the Cabibbo angle.

$\tau \to \nu_\tau K$: This decay is directly related to $K \to \bar{\nu}_\mu \mu$

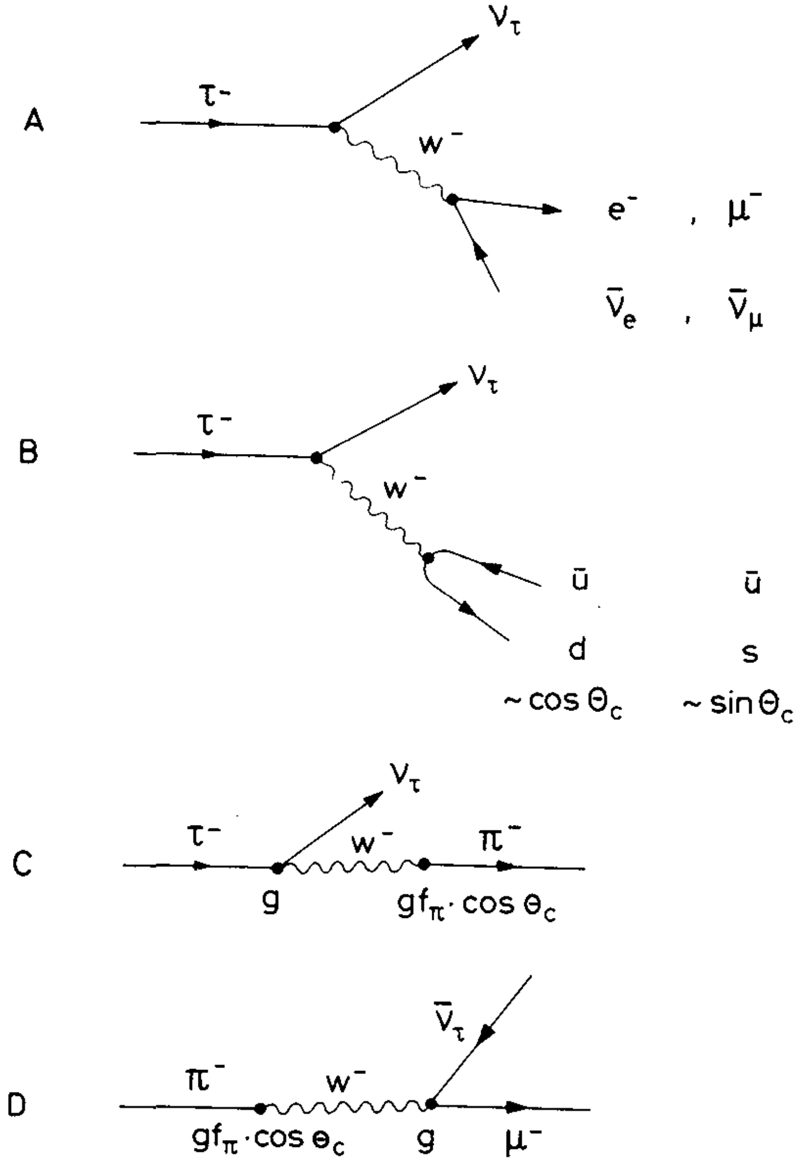

Fig. 6.1a,b) The graphs for leptonic and semihadronic decays of a heavy sequential lepton

c,d) The relationship between $\pi^- \to \bar{\nu}_\mu \mu$ and $\tau^- \to \nu_\tau \pi^-$

$\tau \rightarrow \nu_\tau \rho$: This decay is related via CVC to $e^+e^- \rightarrow \rho$. The width for $\tau \rightarrow \nu_\tau \rho$ can be evaluated with an accuracy of 20 % using the measured values of the ρ-coupling constant.

$\tau \rightarrow \nu_\tau \cdot (n\pi)$: These decay modes are related via CVC to $e^+e^- \rightarrow (n\pi)$. (n even)

Table 6.1 Branching ratios for a sequential lepton of mass 1.8 GeV. (Kawamoto and Sanda, ref. 6.2).

Decay mode	Branching ratio	$\Gamma(\tau \rightarrow \nu_\tau X)/\Gamma(\tau \rightarrow \nu_\tau e\, \nu_e)$
$\nu_\tau e \bar{\nu}_e$	0.18	1
$\nu_\tau \mu \nu_\mu$	0.18	0.97
$\nu_\tau \pi$	0.10	0.60
$\nu_\tau \rho$	0.22	1.24
$\nu_\tau A_1$	∿ 0.1	0.41
$\nu_\tau\ 4\pi$	0.2	∿ 0.44 ± 0.10
$\nu_\tau\ 5\pi$		∿ 0.44
$\nu_\tau\ 6\pi$		∿ 0.11
$\nu_\tau\ 7\pi$		∿ 0.11
ν_τ K	< 0.01	0.03
$\nu_\tau\ K^*(892)$	0.01	0.05
ν_τ Q	< 0.01	0.02
ν_τ (K·nπ) n > 3	0.01	0.07

Pairproduction of new leptons will lead to mixed electron muon events via:

$$e^+e^- \rightarrow \tau\bar{\tau} \rightarrow (\nu_\tau e \bar{\nu}_e)(\bar{\nu}_\tau\ \mu\nu_\mu).$$

The number of eμ-events can be written as

$$N_{e\mu} = 2\sigma_{\tau\bar{\tau}} \cdot L \cdot A_e \cdot A_\mu \cdot B_e \cdot B_\mu$$

The $\tau\bar{\tau}$ cross section (eq. 6.1) varies rapidly near threshold and a measurement in this energy region can be used to determine the τ mass. Well above threshold the cross section is not very sensitive to the precise value of the τ mass and is given by the point cross section. L is the luminosity, A_e and A_μ the acceptances for electrons and muons. The acceptances depend on the shape of the decay lepton spectrum, i.e. on the form of the weak coupling. The difference in acceptance introduced by a V-A or a V+A coupling is small as long as the leptons are measured down to low momenta.

A measurement of the eμ-yield at high energies can therefore be used to determine $B_e \cdot B_\mu$ without knowledge of the exact mass of the lepton and the form of the weak coupling, If eμ universality is valid as expected both for sequential and ortholeptons[6.3] (lepton number of the τ^- = lepton number of the e^- or μ^-) then $B_e \equiv B_\mu$ and the B_e value can be directly determined. However if the τ is a paraelectron or a paramuon (lepton number of τ^+ = lepton number of e^- or μ^-) then $B_\mu/B_e = 1/2$ or 2.

The lepton assignment can in principle be determined from a measurement of the final states:

$$
\begin{aligned}
e^+e^- &\to \tau\bar{\tau} \to e^+e^- + \text{missing energy}\\
&\to \tau\bar{\tau} \to \mu^+\mu^- + \text{missing energy.}
\end{aligned}
$$

However, unlike the eμ channel which is rather clean, e^+e^- and $\mu^+\mu^-$ final state events are contaminated with electromagnetic events.

Information on semihadronic decays of the heavy lepton can be obtained from a measurement of inclusive electron (muon) events resulting from:

$$e^+e^- \to \tau\bar{\tau} \to (\nu_\tau \; \ell \; \bar{\nu}_e) \; (\bar{\nu}_\tau \cdot \text{hadrons}).$$

The rate for the inclusive events is given by

$$N_{\ell,h} = 2\sigma_{\tau\bar{\tau}} \cdot L \cdot A_\ell \cdot A_h \cdot B_\ell \cdot B_h$$

with the nomenclature defined above.

τ production can be strongly enhanced relative to charm production either by selecting events with low multiplicity or by demanding the decay lepton to have momenta above 1.0 GeV/c. Only a small fraction of the semileptonic charm decays satisfy these conditions. Most experiments reported have therefore measured the lepton two prong cross section:

$$N_{\ell,1p} = 2\sigma_{\tau\bar{\tau}} \cdot L \cdot A_\ell \cdot A_{1p} \cdot B_\ell \cdot B_{1p}$$

with $B_{1p} = B(\tau \to \nu_\tau + 1 \text{ charged} + \geq 0 \text{ photons})$.
Electrons were sometimes excluded from the one prong modes.

6.2 Experimental results on the τ

The first e^+e^- experiments searching for a new lepton heavier than the muon were conducted at Frascati[6.4, 6.5] at energies up to 3 GeV. No signal was found and a lower limit of 1.15 GeV was put on the mass of a possible heavy lepton.

In 1975 Perl et al. reported evidence for events of the type

$$e^+e^- \to e^\pm\mu^\mp + \text{nothing} \tag{6.4}$$

where "nothing" meant that no other particles were registered in the detector[6.6]. The analysis was hampered by background from purely hadronic processes: hadrons had an 18 % (20 %) probability to fake an electron (a muon). Of the 24 eμ events found 6-8 events were estimated to come from hadronic background. There was also the question whether or not other strongly or electromagnetically interacting particles had been produced together with e and μ. Since the detector covered only two thirds of 4π additionally produced particles had a fair chance to escape detection. Measurements by the PLUTO group[6.7, 6.8] with a superior e and μ identification and with a larger solid angle coverage confirmed the results of Ref. (6.6).

Besides the experimental uncertainties there was the question of interpretation. Electron-muon events can arise, e.g. from the pair production of charmed particles or of a new lepton. The two mechanisms can be distinguished by their different production and decay patterns. Measurements on

1) $e^+e^- \to e\mu$ + nothing
2) $e^+e^- \to e(\mu)$ + minimum ionizing track
+ any number of photons

provided convincing evidence that above 4 GeV besides charmed particles a new type of weakly decaying particle, τ, is being produced[6.9]. The final proof that this particle indeed exists was given by the DASP collaboration which first observed τ-pairproduction below charm threshold at the ψ' [6.10].

Basically all studies on the τ were done in the 3.5 to 5 GeV region. At higher energies - above 10 GeV - the detection of the τ would have been much easier. This is illustrated in Fig. 6.2 which shows a τ pair event of the kind

$$e^+e^- \to \tau^- \tau^+ \quad \tau^- \to \nu + 3\ \text{charged} \quad \tau^+ \to \mu^+ \nu\nu$$

observed at PETRA at 13 GeV [6.11]. The probability for hadronic events of this topology with which τ events could be confused is very small.

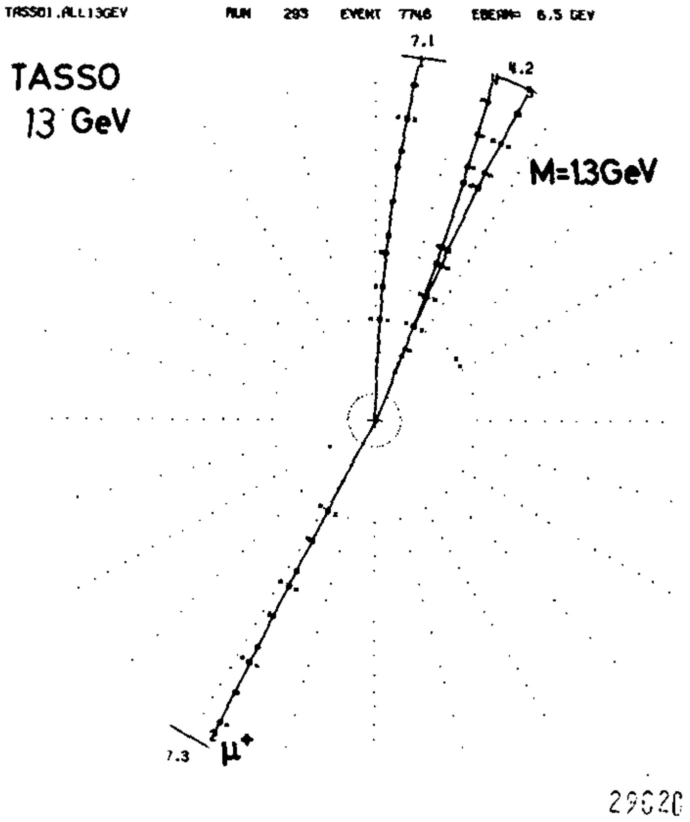

Fig. 6.2 Candidate for τ pair production,

$$e^+e^- \rightarrow \underset{\lfloor \rightarrow \mu^+ \nu\nu}{\tau^+} \quad \underset{\lfloor \rightarrow \nu + 3\ \text{charged}}{\tau^-}$$

as observed by TASSO at 13 GeV. (6.11)

Table 6.2: Summary of e^+e^- experiments searching for a heavy lepton

Experiment	c.m. energy (GeV)	Final State	p_μ^{min} (GeV/c)	p_e^{min} (GeV/c)	events		Lepton identification
					observed	background	
Bernardini et al.[6.4)]	1.2-3.0	eμ	–	–	no signal above background M_L > 1.0 GeV		e,μ: shower and range chambers
Orito et al.[6.5)]	2.6-3.0	eμ	–	∿ 0.30	no event found M_L > 1.15 GeV		e: shower chambers μ: range > 290 g/cm of Fe
SLAC-LBL[6.6, 6.12)]	3.8-7.8	eμ ee μμ μX	0.65 0.65 0.65 0.91	0.65 0.65 0.65 –	190 230	46 94	μ: by range e: lead-scintillation counters
Maryland, Princeton Pavia[6.13, 6.14)]	7	μX	1.0	– –	13	4	μ: by range
PLUTO[6.7, 6.8)]	3.6-5.0	eμ μX	1.0 1.0	0.30 –	23 273	1.9 62	μ: by range e: lead proportional chambers
LBL-SLAC[6.15)]	3.7-7.4	eμ eX	0.65 0.65	0.40 0.40	21 31	0.4 12.1	e: lead-glass counters
DASP[6.10, 6.16)]	4.0-5.2	eμ eX μX	0.70 – 1.0	0.20 0.20 –	13 89 25	1.2 16 4.0	μ: by range e: Cerenkov counters and lead scintillation counters
Ironball[6.17)]	7	μμX	1.3	–	16	5	μ: by range
DESY-Heidelberg[6.18)]	3.6-4.4	eX+ee μX+μμ μe	– 0.6 0.6	0.5 – 0.5	182 94 23	∿ 11 ∿ 2 –	e: NaI and lead glass counters μ: by range
DELCO[6.19)]	3.77-7.84	eX	–	0.20	692	< 42	e: Cerenkov and shower counters

* X contains in general one nonshowering track only

Table 6.2 summarizes the experiments that searched for heavy leptons in e^+e^- annihilation.

6.2.1 τ mass and spin

The cross section for pair production of a τ with spin 0, 1/2, 1 reads as follows:

spin 0:

$$\sigma_{\tau\bar{\tau}} = 1/4\ \sigma_{\mu\mu}\ \beta_\tau^3\ |F|^2\ B_e \cdot B_{ns} \qquad (6.5)$$

where $\sigma_{\mu\mu} = \frac{4\pi\ \alpha^2}{3\ s}$ and F is the τ formfactor.

spin 1/2:

$$\sigma_{\tau\bar{\tau}} = \sigma_{\mu\mu}\ \beta_\tau \left\{ 1 + 1/2(1 - \beta_\tau^2) \right\} B_e \cdot B_{ns} \qquad (6.6)$$

The τ is ssumed to be pointlike.

spin 1:

$$\sigma_{\tau\bar{\tau}} = \sigma_{\mu\mu}\ \beta_\tau^3 \left\{ \left(\frac{s}{4M_\tau^2}\right)^2 + 5\,\frac{s}{4M_\tau^2} + 3/4 \right\} \cdot B_e \cdot B_{ns} \qquad (6.7)$$

The τ is assumed to have the same electromagnetic properties as the W boson[6.20].

Fig. 6.3 shows the ratio

$$R^{2p}_{wx} = \sigma(e^+e^- \to e^\pm + X^\mp + \geq 0 \text{ photons})/\sigma_{\mu\mu}$$

for events with one electron and one nonshowering charged particle as measured by the DELCO group[6.19]. The curves show for the spin assignments 1/2, 1 and 3/2 best fits to the data treating the τ mass and the products of the branching ratios $B(\tau \to e\nu\nu) \cdot B(\tau \to X + \geq 0 \text{ photons})$ as free parameters. Spin 3/2 is clearly ruled out; Spin 1 is ruled out if the data from SLAC-LBL[6.12] taken at higher energies are included; for spin 0 the observed cross section is far too large. The only spin assignment consistent with the data is J = 1/2. The result for the τ mass is

$$m_\tau = 1.782\ {}^{+\ 0.002}_{-\ 0.009}\ \text{GeV}$$

which is in agreement with the earlier results from DASP[6.10] $m_\tau = 1.807 \pm 0.020$ GeV and with a measurement of the DESY-Heidelberg group[6.18] $m_\tau = 1.787\ {}^{+\ 0.010}_{-\ 0.018}$ GeV.

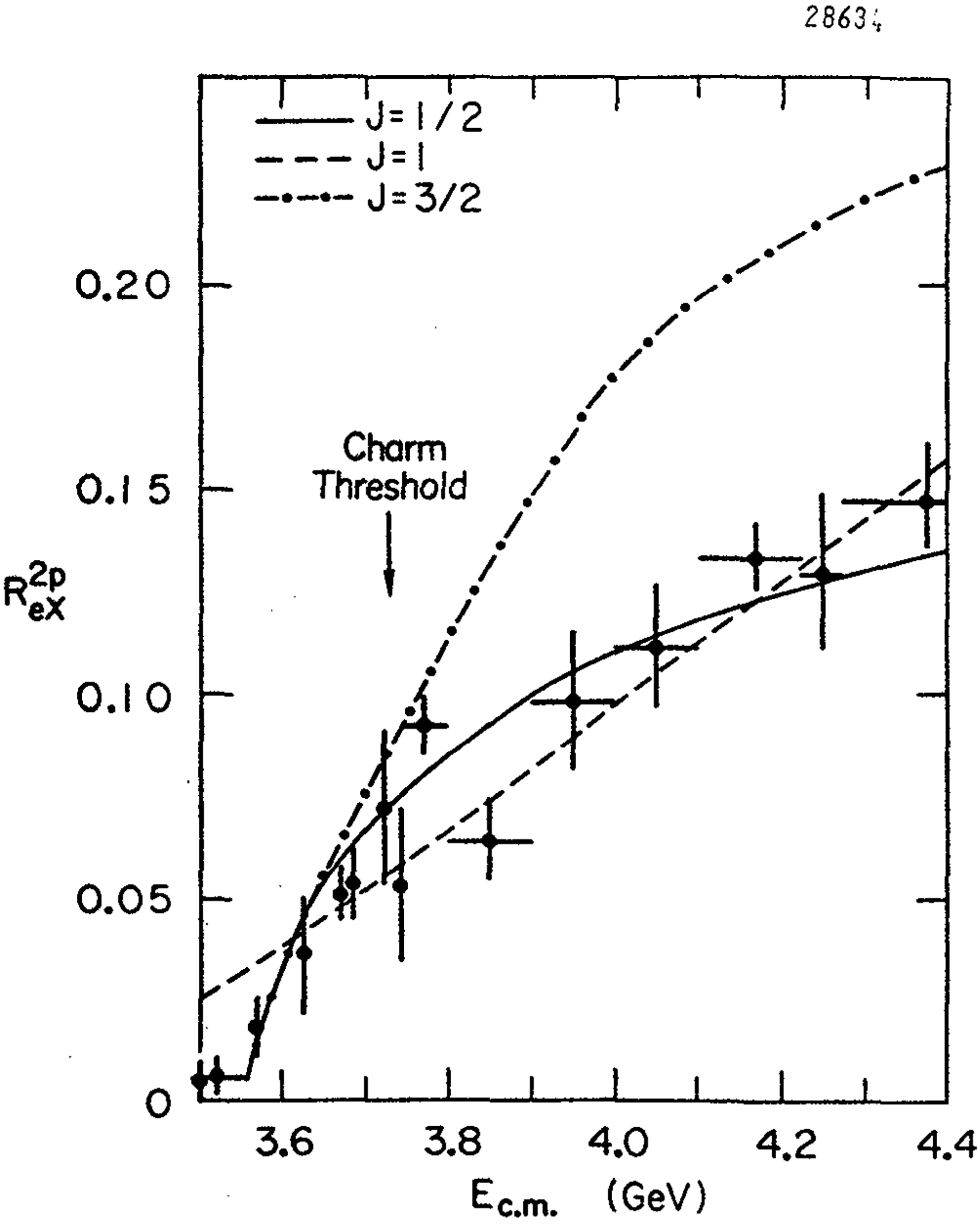

Fig. 6.3 The ratio $\sigma(e^+e^- \rightarrow e^\pm X^\mp, X \neq e^-)/\sigma_{\mu\mu}$ as measured by DELCO (Ref. 6.19).

6.2.2 Decay branching ratios

We sketch briefly the procedure followed to determine the decay branching ratios of the τ. The measured results are summarized in Table 6.3 below. By comparing e and μ final states the ratio of the e and μ decay rates B_e, B_μ ($B_e \equiv B(\tau \to e\nu\nu)$) was deduced:

$$\frac{B_e}{B_\mu} = \frac{\sigma(e^+e^- \to \tau\bar{\tau} \to e + f)}{\sigma(e^+e^- \to \tau\bar{\tau} \to \mu + f)}$$

The data were found to be consistent with e–μ universality, $B_e = B_\mu$: The world average[6.22)] is $B_\mu/B_e = 1.13 \pm 0.16$. Due to the mass differences of e and μ theory predicts $B_\mu/B_e = 0.973$. Assuming $B_e = B_\mu$ the anomalous eμ events could be used to determine B_e:

$$\sigma(e^+e^- \to \tau\bar{\tau} \to e\mu) = \sigma_{\tau\bar{\tau}}\, B_e B_\mu = \sigma_{\tau\bar{\tau}}\, B_e^2$$

The world average is $B_e = 17.5 \pm 1.2$ % which agrees well with the theoretical value of 18.5 %.

The first clear evidence for the $\tau \to \nu\pi$ decay was presented by the SLAC-LBL group[6.23)] from an analysis of events of the type

$$e^+e^- \to \pi^\pm X^\mp \; 0\gamma$$

for c.m. energies between 4.8 and 7.4 GeV. Fig. 6.4 shows the pion energy spectrum measured in a recent experiment at SPEAR[6.24)]. As expected for a two body decay of a moving object the spectrum is constant over a wide energy range. The fall-off at the high-energy end is caused by the fact that the data were not taken at a single beam energy.
The world average of $B_\pi = 9.1 \pm 1.1$ % is in good agreement with theory which predicted $B_\pi = 10$ %.

The DASP group has also searched for events of the type

$$e^+e^- \to \tau\bar{\tau} \to \{(K\nu)\;(e\nu\nu) + (\mu\nu\nu) + (\pi\nu)\}$$

$$= K^\pm + \text{charged track} + \text{missing energy.}$$

Only one event with $p_K > 1.0$ GeV/c was found[6.16)]. This yielded a 90 % confidence upper limit of $B_K < 0.016$ in agreement with theory.

The decay $\tau \to \nu\rho$ was first observed by DASP[6.16)] studying events of the type

$$e^+e^- \to e^\pm X^\mp + 2\gamma$$

The MARK II group at SPEAR recently reported results of the final state

$$e^+e^- \to e^\pm\pi^\mp\pi^0$$

The $\pi^\pm\pi^0$ mass distribution is shown in Fig. 6.5. The average branching ratio from the two experiments is $B_\rho = 20.9 \pm 3.7$ % to be compared with the theoretical value of 22 %.

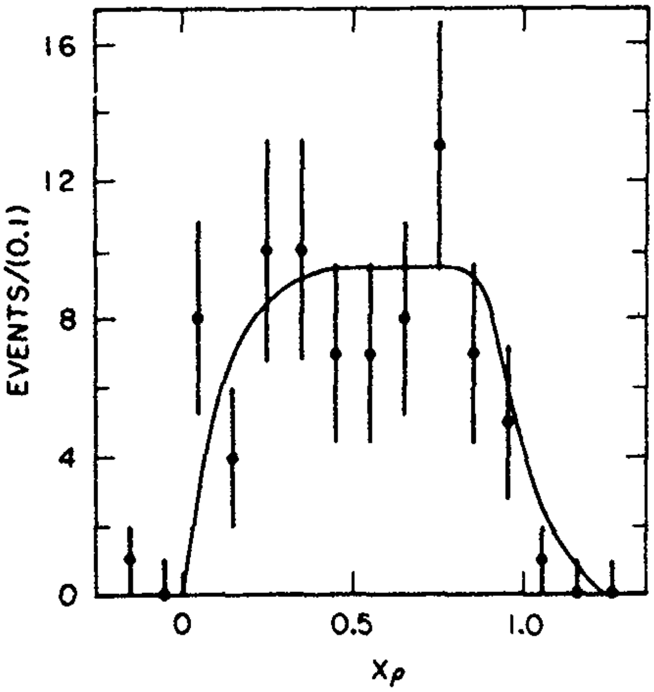

Fig. 6.4 The π energy spectrum for the decay $\tau^{\pm} \rightarrow \pi^{\pm}\nu$ in the energy range $4.5 < W < 6.0$ GeV (SLAC-LBL, Ref. 6.24).

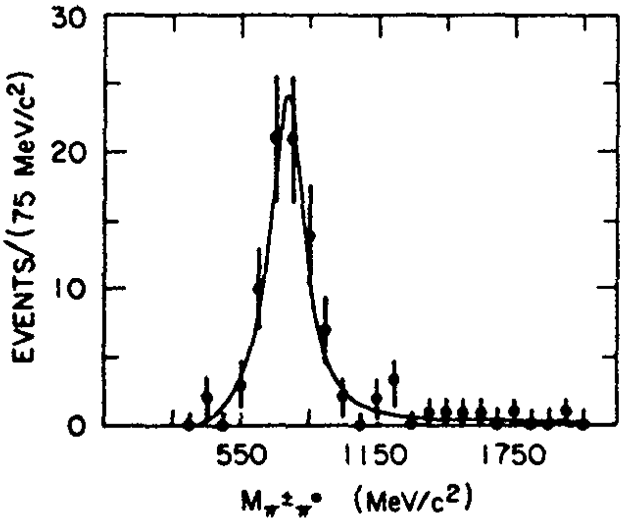

Fig. 6.5 The $\pi^{\pm}\pi^{0}$ effective mass distribution from the decay $\tau^{\pm} \rightarrow \pi^{\pm}\pi^{0}\nu$ (SLAC-LBL, Ref. 6.24)

The PLUTO group analyzed the three charged pion decay of the τ via

$$e^+e^- \to \tau\bar{\tau} \to (e\ \nu\nu)\ (\pi^\pm\pi^\pm\pi^\mp\nu)$$

The $\pi^+\pi^-$ mass distribution indicates the presence of a ρ^0 signal (Fig.6.6a). If only the higher of the two $\pi^+\pi^-$ mass distributions is selected the dashed histogram is obtained which is compatible with the assumption that the decay proceeds a hundred percent via $\tau \to \nu\rho^0\pi$. The shape of the 3π mass spectrum is consistent with the S wave decay of a 1^+ object (Fig.6.6b). If this is interpretated to be the A_1 a Breit-Wigner fit yields M=1.1 GeV and Γ = 0.5 GeV. The branching ratio of $\tau \to \nu$"A_1" is found to be 10.8 ± 3.4 %.

The search for exotic decays of the τ such as τ → 3 charged leptons, $\tau \to e\gamma$, $\tau \to \mu\gamma$ has been unsuccessful (see Table 6.3).

The PLUTO[6.26] and DELCO[6.27] groups attempted to determine the τ lifetime T_τ by measuring the flight length of the τ. The present upper limit of $T_\tau < 2.3\cdot 10^{-12}$sec is still an order of magnitude above the theoretical prediction, $T_\tau = B_e \left(\frac{M_\mu}{M_\tau}\right)^5 .T_\mu = 2.8\cdot 10^{-13}$sec.

6.2.3 Space-time structure of the weak current in τ decay

The lepton spectrum permits a study of the space-time structure of the weak current mediating the decay of the τ.

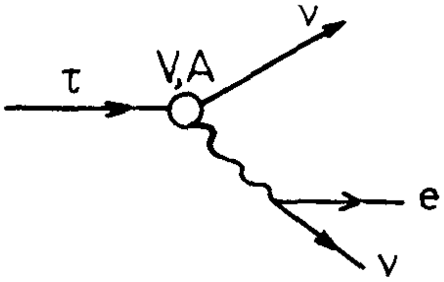

If only V and A type couplings are considered the Hamiltonian for $\tau \to \nu_\tau\ \ell\bar{\nu}_e$ is of the form[6.28].

$$H_{int} = \frac{G_F}{2}\left[\bar{\psi}_{\nu_e}\ \gamma_\mu\ (1-\gamma_5)\psi_e\right]\left[\bar{\psi}_\tau\left\{g_+\ \gamma_\mu(1+\gamma_5) + g_-\ \gamma_\mu(1-\gamma_5)\right\}\ \bar{\psi}_{\nu_\tau}\right] \qquad (6.9)$$

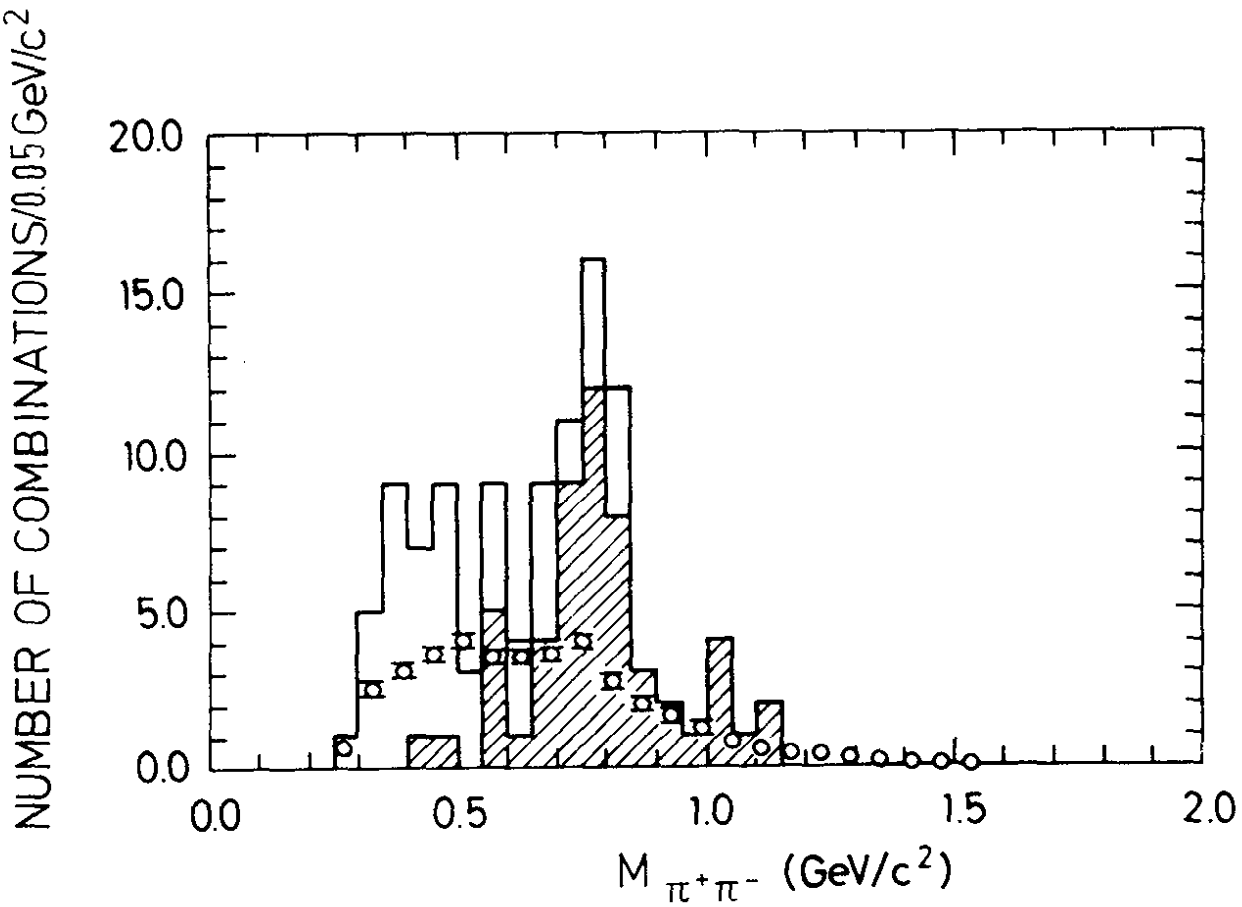

Fig. 6.6a The $\pi^+\pi^-$ mass spectrum observed by PLUTO$^{6.25)}$ in events containing only four prongs, $\tau^-\pi^-\pi^+$ lepton$^+$. The higher mass combination in each event is indicated by the dashed histogram. The background of hadronic events with a misidentified lepton is shown by the solid curve.

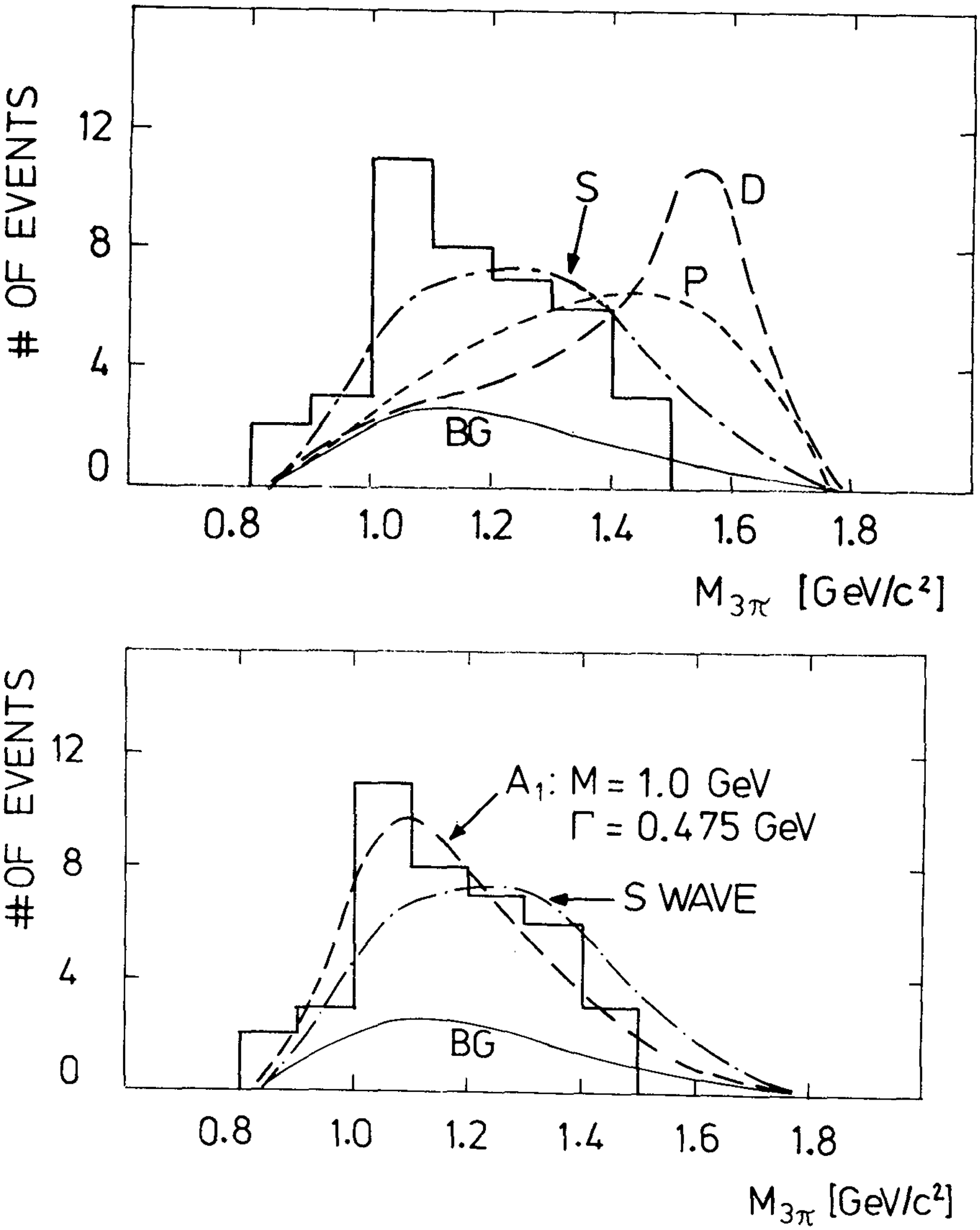

Fig. 6.6b,c The $\rho^0\pi$ mass spectrum measured by PLUTO$^{6.25)}$. The fitted curves, which are superimposed over the background (solid curve), correspond to τ decays into a) a non-resonant $\rho\pi$ system for several values of the relative angular momentum and b) a 1^+ resonant $\rho\pi$ system of mass 1.0 GeV/c^2 and width 0.48 GeV/c^2.

where $g_\pm$ are the coupling strengths for V ± A couplings. In the τ rest system the shape of the lepton spectrum can be expressed in terms of the lepton momentum p, energy E, maximum energy

$$E_{max} = \frac{m_\tau^2 + m_e^2 - m_\nu^2}{2m_\tau} \quad \text{and} \quad x = E/E_{max}:$$

$$\frac{dN(x)}{dx} = \text{const}\ x^2 \left\{3(1 - x) + 2\rho\left(\frac{4}{3}x - 1\right)\right\}$$

where terms of order m_e/m_τ have been neglected. The shape of the spectrum is then determined by the Michel parameter ρ[6.28) where ρ is defined as:

$$\rho = \frac{3}{4}\,\frac{g_-^2}{g_+^2 + g_-^2} \tag{6.10}$$

Special cases are:

pure V-A : $g_+ = 0$ $\rho = 3/4$
V+A : $g_- = 0$ $\rho = 0$
V : $g_+ = g_-$ $\rho = 3/8$
A : $g_+ = -g_-$ $\rho = 3/8$

Fig. 6.7 shows the electron momentum spectrum determined by the DELCO group (6.27) which finds for the Michel parameter

$\rho = 0.72 \pm 0.15.$

This result agrees well with V-A and excludes V+A. A pure V or pure A coupling appears to be unlikely. The analysis assumed a massless τ neutrino. If the ν_τ is massive the theoretical spectrum will be pushed towards smaller x values and hence V+A currents are ruled out for all values of x. An upper limit on the mass of the τ-neutrino of $m_{\tau_\nu} < 250$ MeV was obtained assuming a V-A current.

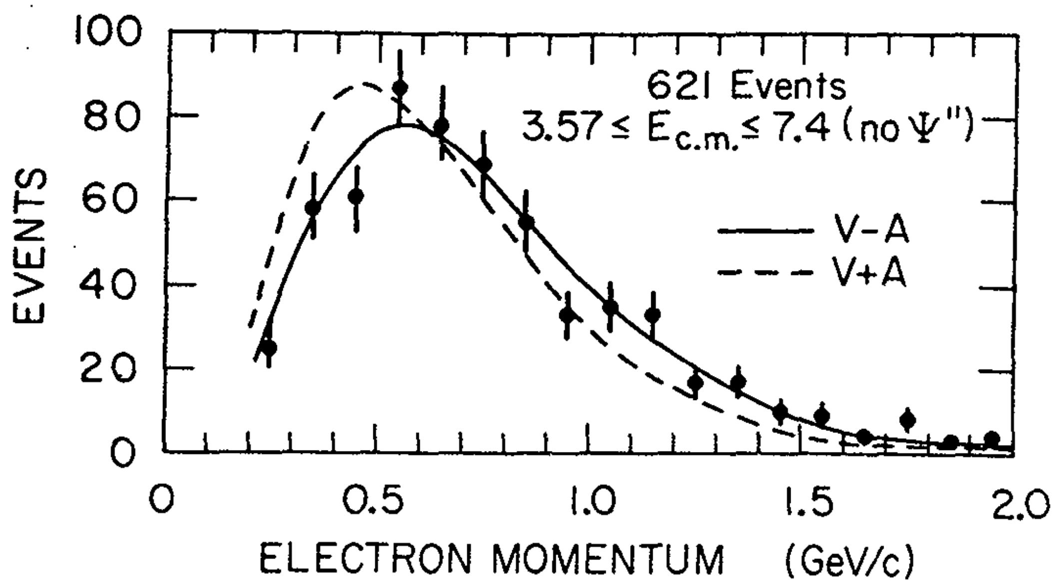

Fig.6.7: Electron momentum spectrum for events with electron + one charged track as measured by DELCO (Ref.6.27). The solid and dashed curves represent the spectra expected for V-A and V+A coupling at the $\tau\nu_\tau$ vertex, respectively.

6.2.4 Is the τ point like?

This question has already been answered in Section 3. Down to distances of 4.10^{-16} cm no evidence for an extended τ has been found.

6.3 Summary of the τ properties

Table 12.5 summarizes the experimental information on mass, leptonic and semihadronic decay modes of the τ.

The observation of the τ at the ψ' below charm threshold conclusively demonstrates that the τ signal has nothing to do with charm. The shape and magnitude of the $\tau\bar{\tau}$ production cross section exclude spin 0, 1 and 3/2 for the τ: they strongly favor the assignment as a pointlike, spin 1/2 fermion. The best value for the τ mass at present is $1.782 {}^{+0.002}_{-0.007}$ GeV. The analysis of the decay spectra puts a limit of 0.25 GeV on the mass of the τ neutrino. The lifetime of the τ is less than $2.3 \cdot 10^{-12}$ sec. The lepton momentum spectrum strongly favors a V-A type coupling of the weak current to the $\tau\bar{\nu}_\tau$ system. The measured leptonic decay rates are consistent with e/μ universality. The leptonic and semihadronic branching ratios agree with those expected from theory for a heavy lepton of mass 1.8 GeV.

The consistency with e/μ universality classifies the τ as either an ortholepton or a sequential lepton. In the first case the τ has the same lepton number as e or μ. In the second case the τ carries a new lepton number. Recent neutrino experiments rule out that the τ is μ-like.[6.29)]

Table 6.3 - Summary of the experimental results

Quantity	Experimental result	Predicted by theory (sequential lepton)	Experiment	Comments
Mass (GeV)	1.807 ± 0.020	-	DASP[6.10]	earlier experiments did not have data close to threshold
- " -	$1.782^{+0.002}_{-0.007}$	-	DELCO[6.19]	
- " -	$1.787^{+0.010}_{-0.018}$	-	D-HD[6.18]	
Spin	1/2	1/2	-	Spin 0, 1 and 3/2 are excluded
Lifetime(sec)	$< 9 \cdot 10^{-12}$	$2.8 \cdot 10^{-13}$	PLUTO[6.26]	
	$< 2.3 \cdot 10^{-12}$		DELCO[6.27]	
m_{ν_τ} (GeV)	< 0.25 GeV	0	DELCO[6.27]	
Structure	V-A $(\rho = 0.72 \pm 0.15)$	V-A $(\rho = 0.75)$	DELCO[6.27]	SLAC-LBL finds[6.12] $\chi^2 = 50\%$ for V-A compared to $\chi^2 = 0.1\%$ for V+A
B_μ/B_e	0.92 ± 0.32	0.98	DASP[6.10]	
$N_{ee}/N_{\mu e}$	$0.56 \pm 0.14^{+0.16}_{-0.19}$	0.5	SLAC-LBL[6.12]	ortholepton=0.5 paraelectron $N_{ee}/N_{\mu e}=0.86$ $N_{\mu\mu}/N_{\mu e}=0.29$
$N_{\mu\mu}/N_{\mu e}$	$0.70 \pm 0.15 \pm 0.19$	0.5	SLAC-LBL[6.12]	ortholepton=0.5 paramuon $N_{ee}/N_{\mu e}=0.29$ $N_{\mu\mu}/N_{\mu e}=0.86$
B_e	$0.186 \pm 0.010 \pm 0.028$	0.18	SLAC-LBL[6.12]	from eμ; assume $B_e=B_\mu$ and V-A
	0.16 ± 0.06		PLUTO[6.8]	from eμ, μX; assume V-A
	$0.224 \pm 0.032 \pm 0.044$		LBL-SLAC[6.15]	from eμ; assume $B_e=B_\mu$
	$0.182 \pm 0.028 \pm 0.014$		DASP[6.10]	from eμ; assume $B_e = B_\mu$ and V-A
	0.16 ± 0.04		DELCO[6.19]	from eX, assume $B(0\gamma)^{\text{exp}}_{\text{1 pion}} = 2B_e$
	$0.175 \pm 0.072 \pm 0.030$	0.18	SLAC-LBL[6.30]	from μX, assume $B(\text{all}\gamma)_{\text{1 prong}}=0.85$ and V-A
	0.14 ± 0.034		PLUTO[6.8]	from μX; assume V-A
	$0.22^{+0.07}_{-0.08}$		Iron ball[6.17]	from μμ
	0.20 ± 0.10		Maryland-Princeton-Pavia[6.13,6.14]	from μX

Table 6.3 continued:

	Experimental results	Predicted by theory	Experiment	Comments
B($\tau \to e\gamma$)	< 0.026		LBL-SLAC[6.31]	
B($\tau \to \mu\gamma$)	< 0.013	0	LBL-SLAC[6.31]	
B($\tau \to$ 3charged leptons)	< 0.006		SLAC-LBL[6.31]	
	< 0.01		PLUTO[6.9]	3 charged particles
B($\tau \to$ 1 charged + any photons)	0.70 ± 0.10		PLUTO[6.8]	
	0.90 ± 0.10		LBL-SLAC[6.15]	
	0.65 ± 0.12		DASP[6.10]	
	0.685 ± 0.03		DELCO[6.19]	
B($\tau \to$ 1 charged hadron + any photons)	0.40 ± 0.15		PLUTO[6.8]	
	0.45 ± 0.19		LBL-SLAC[6.15]	
	0.29 ± 0.11		DASP[6.10]	
B($\tau \to \geq$ 3 charged hadrons + any photons)	0.35 ± 0.11		DASP[6.10]	
	0.32 ± 0.05		DELCO[6.19]	
B($\tau \to \pi\nu$)	0.077 ± 0.013	0.10	SLAC-LBL[6.23], PLUTO[6.32] DELCO[6.19], and Ref. 6.33	
B($\tau \to K\nu$)	< 0.016	0.005	DASP[6.16]	
B($\tau \to \rho\nu$)	0.24 ± 0.09	0.22	DASP[6.16]	
B($\tau \to \rho^o\pi^\pm\nu$)	0.050 ± 0.015	~0.1	PLUTO[6.25]	spectrum consistent with A_1 decay. Including neutral decay modes would give B($\tau \to A_1\nu$) = 0.10 ± 0.03

* assuming a sequential lepton of mass 1.782.

7. Charmonium States

7.1 The J/ψ and ψ' Particles

The first member of the new family of particles was discovered at Brookhaven as the J-particle in the e^+e^- spectrum of p-Be collisions[7.1) (see Fig.7.1),

$$p\ Be \rightarrow e^+e^-X$$

and at SPEAR as the ψ particle in e^+e^- annihilation[7.2) (see Fig.7.2),

$$\begin{aligned} e^+e^- &\rightarrow \text{hadrons} \\ &\rightarrow e^+e^- \\ &\rightarrow \mu^+\mu^- \end{aligned}$$

The first evidence for the ψ' observed at SPEAR[7.3) is shown in Fig.7.3. The properties of J/ψ and ψ' were studied at SPEAR and DORIS and a plethora of decay modes was detected and analyzed[1.3). Both states were found to be nonstrange isoscalar vector mesons, $J^{PC} = 1^{--}$, $T^G = 0^-$. In terms of SU_3 J/ψ and ψ' are singlet states.

The mass and width parameters of J/ψ and ψ' are listed in Table 7.1 and compared to the corresponding values of the ρ meson. Γ_{direct} measures the partial width for the direct decay into hadrons, excluding the cascade decays in the case of the ψ'.

Table 7.1 Mass and widths parameters for ρ, J/ψ and ψ'

	ρ(770)	J/ψ	ψ'
m (MeV)	770	3096	3687
Γ (MeV)	150	0.07 ± 0.01	0.23 ± 0.06
Γ_{direct} (MeV)	150	0.05 ± 0.01	∼ 0.05
Γ_{ee} (KeV)	6.4 ± 0.8	4.8 ± 0.6	2.2 ± 0.3

The most exciting property of J/ψ and ψ' is their small decay widths. The direct decay is suppressed by roughly a factor of 10^4 compared to what one would expect for a conventional meson of 3 to 4 GeV mass. This is illustrated in Fig.7.4 which gives a plot of the width versus the mass of conventional nonstrange mesons. Despite its small decay width the J/ψ is a strongly interacting particle. This was established by photoproducing the J/ψ off nuclei; the t distribution exhibits a coherent part which leads to a total J/ψ nucleon cross section of ~ 1 mb near E_γ = 100 GeV. (Ref.7.4).

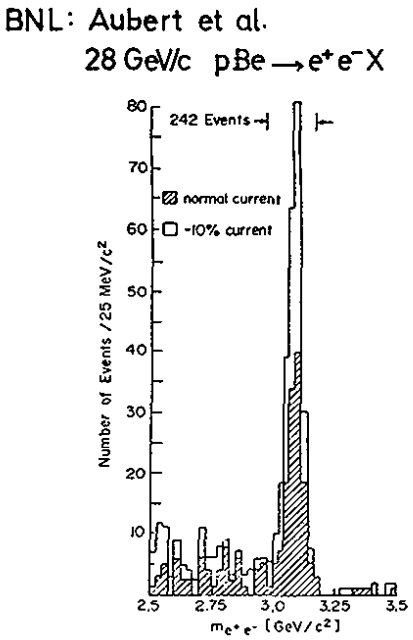

Fig.7.1 The e^+e^- effective mass spectrum from the reaction pBe → e^+e^-X (Ref. 7.1)

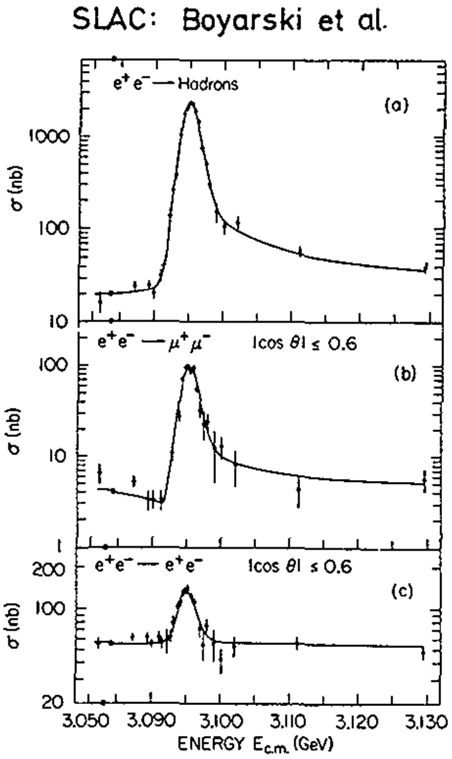

Fig.7.2 Energy dependence of the cross sections e^+e^- → hadrons, e^+e^- → $\mu^+\mu^-$ and e^+e^- → e^+e^- in the vicinity of the ψ (Ref. 7.2)

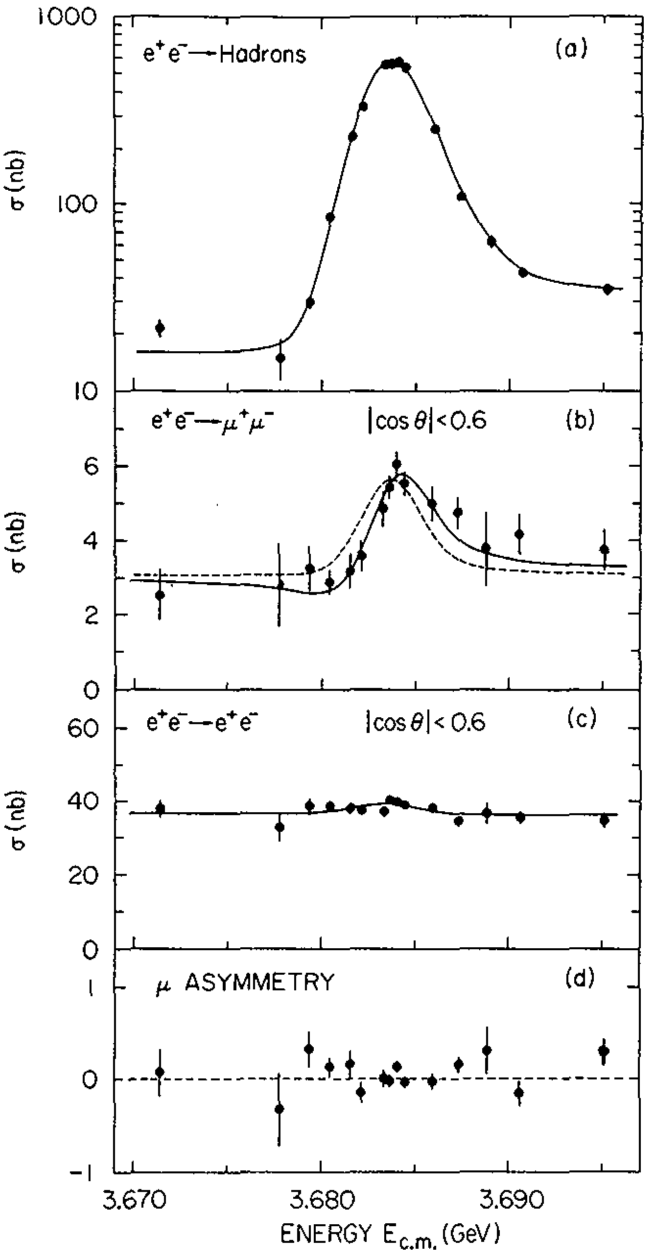

Fig. 7.3 Energy dependence of the cross sections $e^+e^- \to$ hadrons, $e^+e^- \to \mu^+\mu^-$, $e^+e^- \to e^+e^-$ and the forward-backward asymmetry in μ pair production in the vicinity of the ψ' (Ref. 7.3)

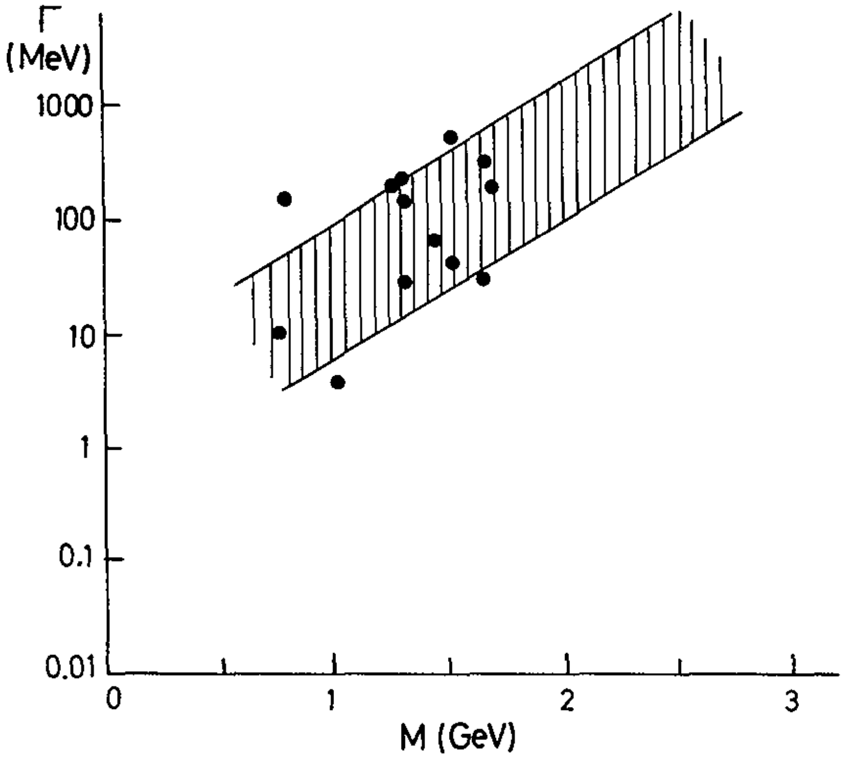

Fig. 7.4 A plot of width versus mass for nonstrange mesons

7.2 The Quark Model Interpretation of J/ψ and ψ'

An intuitively simple and by now accepted explanation for J/ψ and ψ' was offered by the quark model. It assumed that

a) besides the u, d and s quark a fourth quark Q exists which carries a new quantum number such that the decay $Q \rightarrow q$, $q = u$, d or s can proceed only weakly;

b) the J/ψ and ψ' are $Q\bar{Q}$ bound states.

Based on these assumption the model predicted the existence of further $Q\bar{Q}$ mesons and of mixed Q,q states of the type $(Q\bar{q})$ and $(\bar{Q},q)$. Since the widths of J/ψ and ψ' were small the masses of the $(Q\bar{q})$, $(\bar{Q}q)$ mesons were assumed to be $M_{Q\bar{q}} > M_{\psi'}/2$ which prevents decays of the type $\psi' \rightarrow (Q\bar{q})(\bar{Q}q)$.

In a next step the new quark Q was taken to be identical to the charm quark c which had been introduced before by Glashow, Iliopoulos and Maiani[7.5)] in order to understand certain weak interaction phenomena such as the smallness of the decay rate for $K_L^0 \rightarrow \mu^+\mu^-$ and the absence of strangeness changing neutral currents. The properties of the hypothesized charm quark c were

charge + 2/3

strangeness 0

charm 1 , where charm is a new quantum number

c decays only weakly into d or s quarks according to
$c \rightarrow -d \sin\Theta_c + s \cos\Theta_c$

where Θ_c is the Cabibbo angle, $\Theta_c = 0.23$ (GIM mechanism).

7.3 $c\bar{c}$ Spectroscopy

The variety of $c\bar{c}$ states in terms of J^{PC} follows directly from the spin 1/2 nature of the quark and is equivalent to that of positronium. For instance orbital angular momentum $L = 0$ leads to vector states (both quark spins parallel, also called orthocharmonium), and to pseudo scalars (spins antiparallel, paracharmonium). In order to compute level spacing, transition rates etc. more assumptions about the $c\bar{c}$ system are necessary. In most calculations the c quark is assumed to be sufficiently heavy such that the $c\bar{c}$ system can be described by a nonrelativistic Schrödinger equation.

The forces acting between $c\bar{c}$ quarks in nonrelativistic calculations are approximated by a steeply rising attractive potential[7.6)]. At short distances this force might be represented by gluon exchange. This will give rise to a term $-4/3\ \alpha_s/r$ in the potential where α_s is the strong interaction coupling constant. A linear term is added to the potential in order to ensure quark confinement:

$$V(r) = -\frac{4\alpha_s}{3r} + ar + V_0 \qquad (7.1)$$

A potential of this type(7.6-7.8) will lead to the level scheme shown in Fig.7.5. The levels are labeled by J^{PC} with $P = (-1)^{L+1}$ and $C = (-1)^{L+S}$. For each value of L there are two bands of radial excitations with opposite charge conjugation depending on whether $S = 0$ or 1. The spectro-

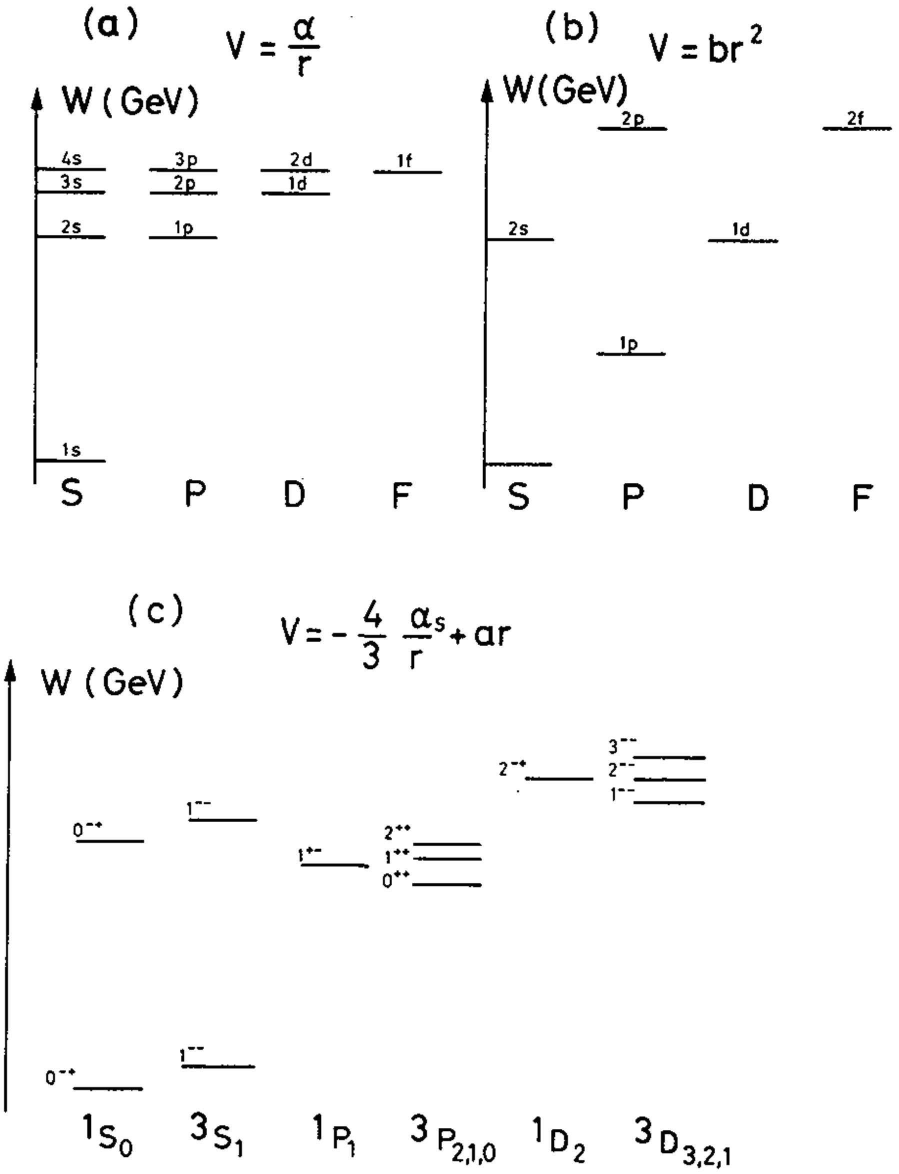

Fig. 7.5 Level scheme predicted for two fermions bound in a rising attractive potential

a) pure Coulomb potential $V = \alpha/r$

b) Harmonic oscillator potential $V = br^2$

c) $V = - \frac{4}{3}\, \alpha_s (m^2)/r + a\ r$

scopic notation $n^{2S+1}L_J$, where n - 1 is the number of radial nodes, is used to name the levels.

The triplet S states 1^3S_1 and 2^3S_1 are identified with the J/ψ and ψ', respectively. The potential (7.1) will lead to a small spin-spin force and hence to a small mass splitting between triplet ($^3S_1$) and singlet ($^1S_0$) states. The P levels will split into one state ($^1P_2$) with odd and three states ($^3P_{2,1,0}$) with even charge conjugation. In a pure Coulombic potential the first set of P levels would be degenerate in mass with the 2^3S_1 level. The addition of a confining potential pushes the mass of the 1P levels below the mass of the 2^3S_1 level.

The first L = 2 level splits into one state ($^2D_1$) with even and three states ($^3D_{3,2,1}$) with odd charge conjugation. The 1^3D_1 state has the quantum number of the photon. By mixing with the nearby 2^3S_1 state its wave function aquires a finite value at the origin . As a consequence the 1^3D_1 can show up e.g. in the total e^+e^- cross section. The observation of this state was one of the major triumphs of charmonium spectroscopy which had predicted (Eichten et al.[7.8]) the ψ'' two years before its discovery[7.10, 7.11].

The number and the quantum numbers of the predicted $c\bar{c}$ levels are mainly a consequence of the spin-1/2 nature of the c quark. The level spacing and the level widths on the other hand are strongly model dependent and cannot firmly be predicted.

7.4 The Vector States

The leptonic and hadronic widths of the J/ψ and the J/ψ - ψ' spacing can be used to fix the parameters of the potential (7.1). The $^3S_1$ state decays to lowest order into hadrons via a 3 gluon intermediate state. The hadronic width is given by

$$\Gamma(^3S_1 \rightarrow ggg \rightarrow \text{hadrons}) = \frac{160}{81}(\pi^2 - 9)\,\alpha_S^3\,\frac{|^3S_1(0)|^2}{M^2} \qquad (7.2)$$

where $^3S_1(0)$ describes the wave function at the origin. The width for the decay into a pair of leptons is given by

$$\Gamma(^3S_1 \rightarrow e^+e^-) = 64\pi\alpha^2/9\,\frac{|^3S_1(0)|^2}{M^2} \qquad (7.3)$$

where M is the mass of the vector state.
Applying these relations to the J/ψ yields $\alpha_s \simeq 0.19$. From the J/ψ - ψ' spacing the slope of the confining term is found to be a = 0.25 GeV^2. These parameter values should be considered as order of magnitude estimates only since higher gluonic corrections are sizeable[7.12]. The scale violations observed in neutrino interactions for instance prefer $\alpha_s \simeq 0.4$. The R dependence of the potential computed for α_s = 0.19, a = 0.25 GeV^2 is shown in Fig.7.6. It is evident that due to the large DeBroglie wavelength of the charm quark the charmonium spectrum as well as the decay rates will be controlled primarily by the linear part of the potential.

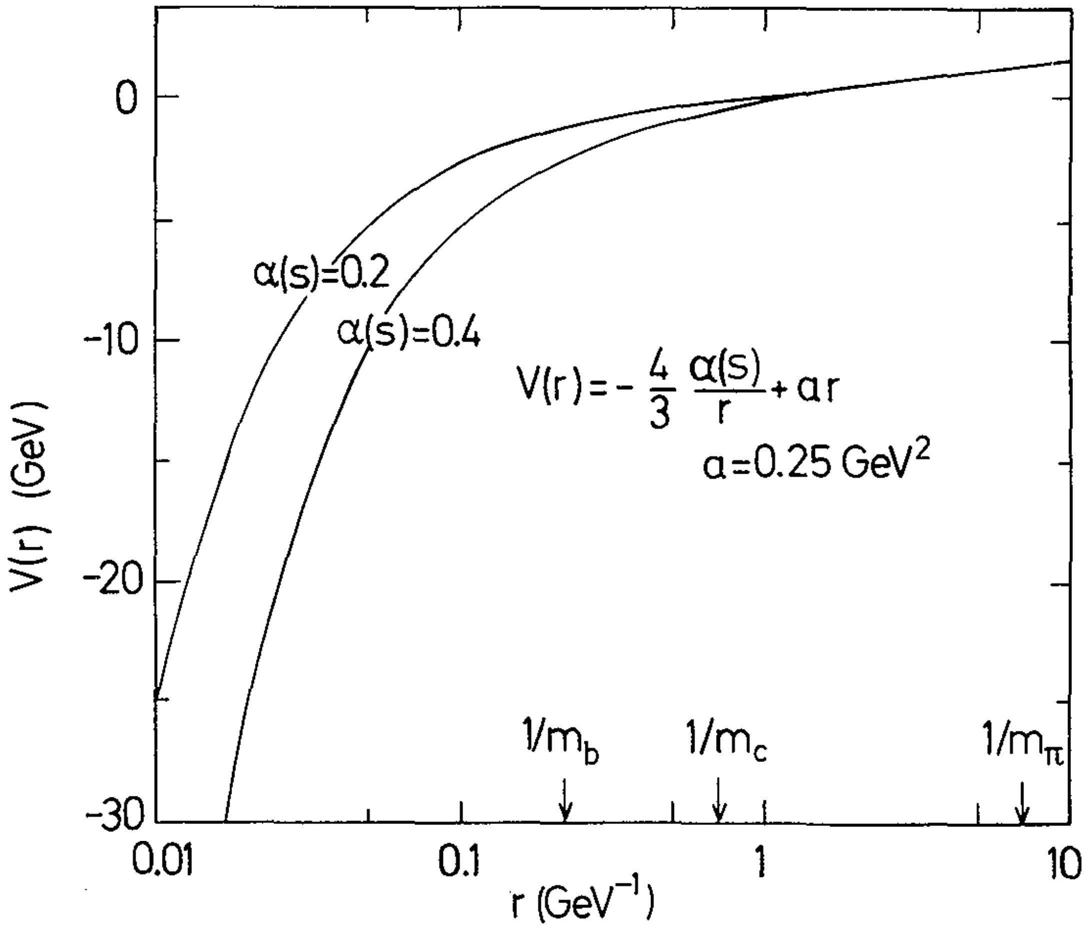

Fig. 7.6 The radius dependence of the charmonium potential.

With the α_s and a parameters determined from J/ψ and ψ' the third vector state ψ'' = 1^3D, was predicted to be at 3.755 GeV 7.8). Figs.7.7 and 7.8 show the excitation of the ψ'' in e^+e^- annihilation as measured by LBL-SLAC 7.10) and the DELCO group 7.11) at SPEAR.

The properties of the ψ'' are summarized in Table 7.2

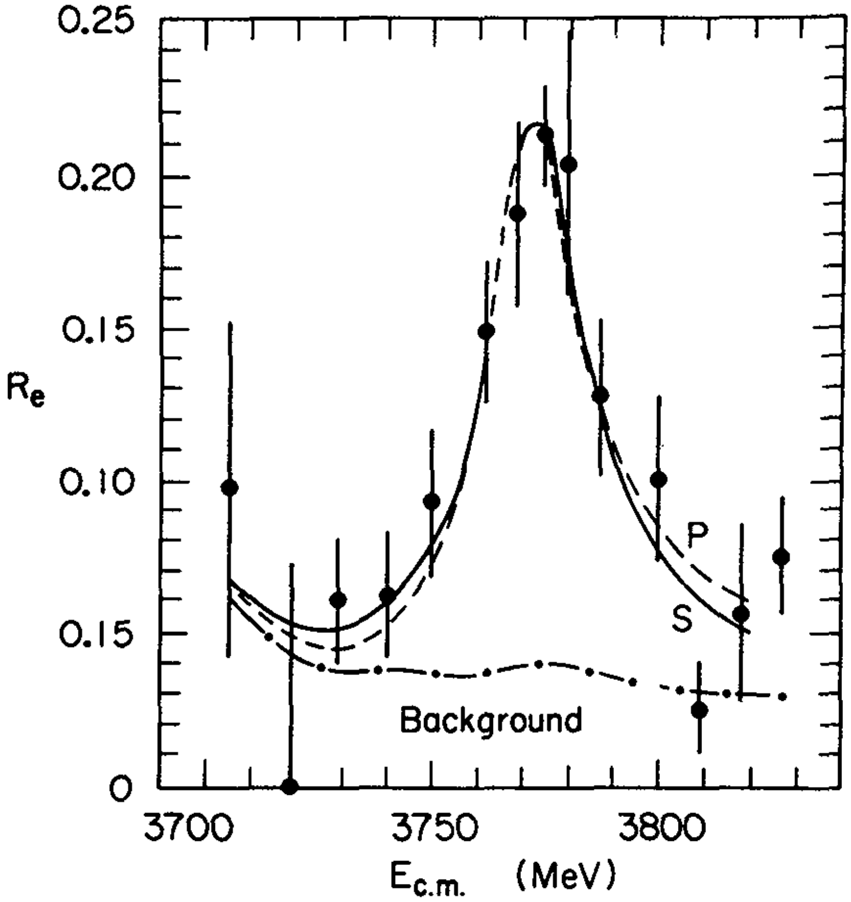

Fig. 7.7 R = $\sigma^{tot}/\sigma_{\mu\mu}$ near the ψ' after radiative correlations (Ref. 7.10)

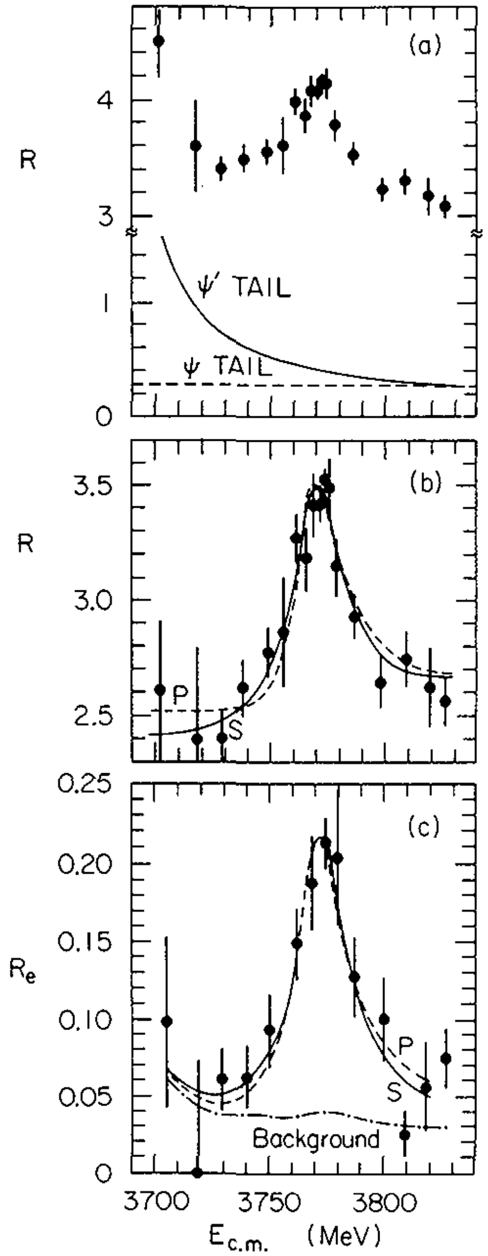

Fig. 7.8 $R = \sigma^{tot}/\sigma_{\mu\mu}$ near the " (Ref. 7.11)

a) measured R
b) after radiative corrections
c) $R_e = \sigma(e^+e^- \to eX)/\sigma_{\mu\mu}$

The ψ'' being ~ 45 MeV above the $D\bar{D}$ threshold is found to decay almost exclusively into a pair of D mesons and is therefore an ideal place to study the D properties (see Section 8.1).

Evidence for still heavier vector states has been found in studies of the total e^+e^- cross section above 4 GeV. Fig. 7.9 shows the measurements of SLAC-LBL[7.13], PLUTO[7.14], and DASP[7.15], and preliminary data from DELCO[7.11] and the Crystal Ball[7.19]. The error bars shown in Fig. 7.9 do not include systematic uncertainties which are primarily due to the limited solid angle and to radiative corrections. The systematic uncertainties are estimated to be ±10 to ±15 %. All but one experiment agree on the existence of narrow peaks centered at 4.028 GeV and 4.41 GeV. The DASP and PLUTO data exhibit also a narrow structure at 4.16 GeV. The DELCO and Crystal Ball data are not inconsistent with this observation, but has to wait for their final analysis.

The experimental difficulties in extracting these structures rest essentially with the radiative corrections. Consider the two narrow structures at 4.028 and 4.16 GeV. Radiation in the initial state have the tendency to reduce the height of the two peaks and will in the valley in between them. Since many charmed particle channels open up in this energy region (D^*D^*, $D^{**}D^*$, FF, ...) an interpretation of the structure observed is not straightforward. If they are assumed to be resonances one finds the mass and width values given in Table 7.3. They should be considered as preliminary since a precise determination will probably require a coupled channel analysis[7.17]. The result of the resonance fit to the DASP data is shown by the solid curve in Fig. 7.9.

Table 7.2 Properties of the $\psi''(3771)$

Mass (MeV)	Γ(MeV)	Γ_{ee} (eV)
3772 ± 6	28 ± 5	370 ± 90 LBL-SLAC[7.10]
3770 ± 6	24 ± 5	180 ± 60 DELCO[7.11]

branching ratios:

$\psi'' \to D^oD^o$	49 ± 25%
$\to D^+D^-$	50 ± 38%

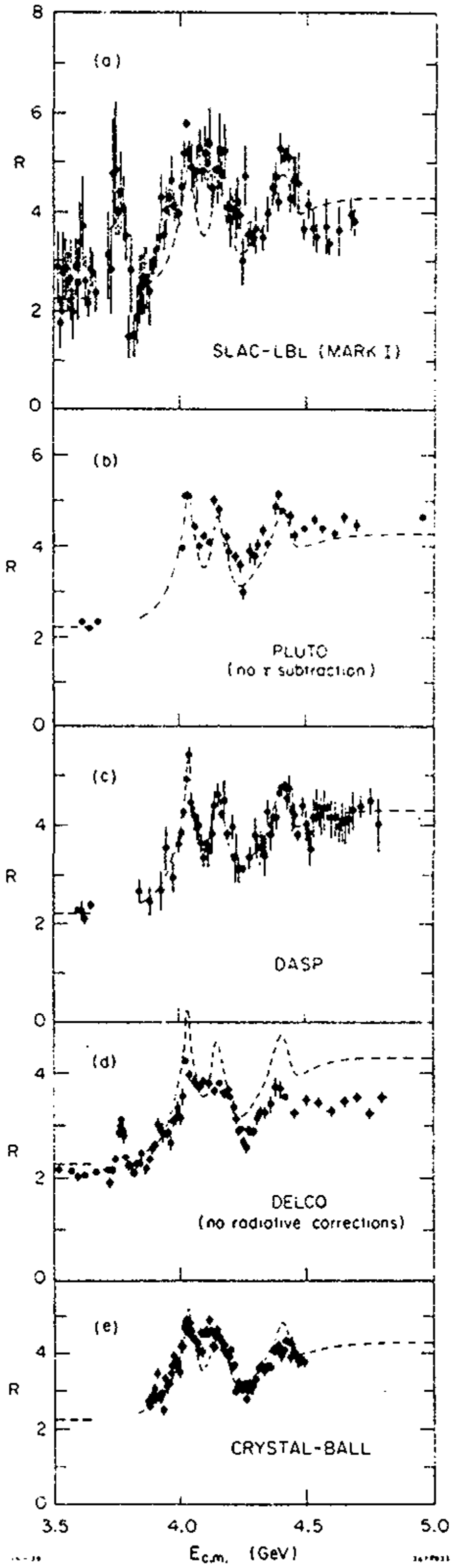

Fig. 7.9 The R values measured near charm threshold[7.11,7.13,7.14,7.15,7.19]). All data are corrected for radiative effects and contamination from the τ, unless indicated otherwise.

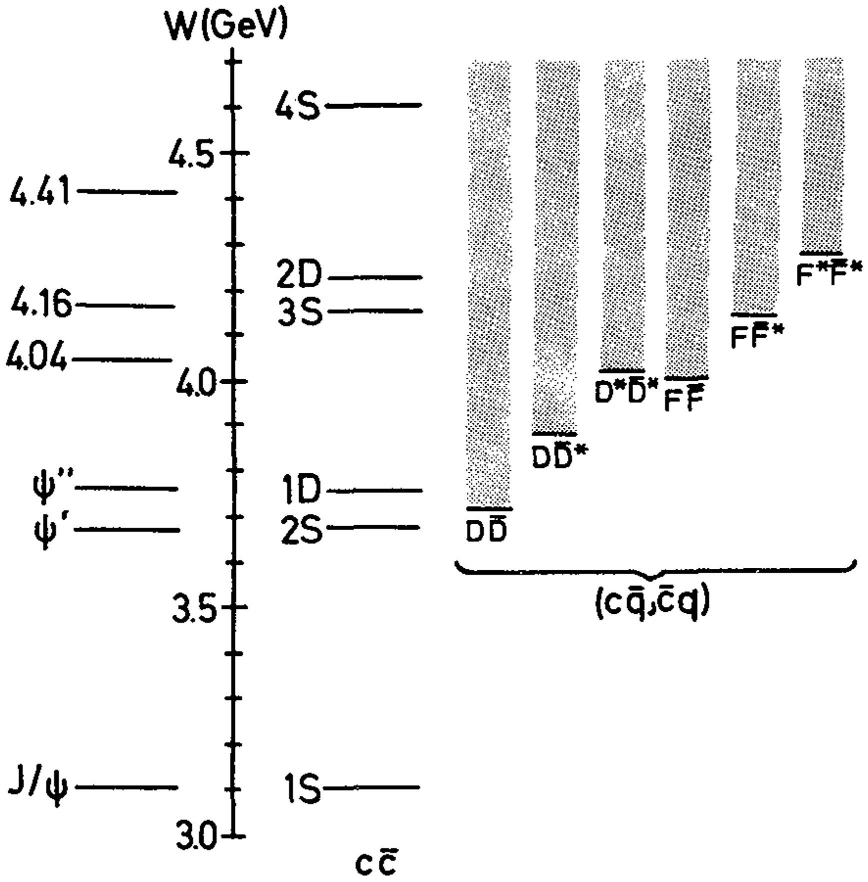

Fig. 7.10 The $c\bar{c}$ levels, the lowest lying charmed meson channels and the measured position of vector mesons (after Ref. 7.17)

Table 7.3 Resonance parameters of vector states between 3 and 4.5 GeV

	Mass (MeV)	Γ(MeV)	Γ_{ee}(keV)	$B_{ee} = \frac{\Gamma_{ee}}{\Gamma}$	
J/ψ	3095± 2	0.069±0.015	4.8 ±0.6	$6.9\pm0.9\cdot10^{-2}$	SLAC-LBL[7.16]
ψ'	3686± 2	0.228±0.056	2.1 ±0.3	$9.3\pm1.6\cdot10^{-3}$	SLAC-LBL[7.16]
ψ''(3771)		28±5	0.37±0.09	$(1.3\pm0.2)\cdot10^{-5}$	LBL-SLAC[7.10]
		24±5	0.18±0.06	$0.7\pm0.2\cdot10^{-5}$	DELCO[7.11]
4.04	4040±10	52±10	0.75±0.10	$1.4\pm0.4\cdot10^{-5}$	DASP[7.15]
4.16	4159±20	78±20	0.77±0.20	$0.9\pm0.3\cdot10^{-5}$	DASP[7.15]
4.41	4414± 7	33±10	0.44±0.14	$1.3\pm0.3\cdot10^{-5}$	SLAC-LBL[7.13]
		66±15	0.40±0.10	$0.7\pm0.2\cdot10^{-5}$	DASP[7.15]

In Fig.7.10 the observed vector mesons are compared to vector state levels predicted by a charmonium model. Between J/ψ and 4.6 GeV the number of vector states known at present agrees with the number of states expected by theory. Whether the interpretation of the observed states as suggested by Fig.7.10 is the correct one, namely $\psi(4.04) = 3^3S_1$, $\psi(4.16) = 2^3D_1$ etc. is an open question.

7.5 P-Wave States

As mentioned above, three P-waves states $^3P_{2,1,0}$ are predicted between J/ψ and ψ' with even parity and even charge conjugation (Fig.7.5). If the $\psi' - {}^3P_J$ mass difference is smaller than $2\cdot m_\pi$ these states can be reached from the ψ' by photon emission only,

$$\psi' \to \gamma\,{}^3P_J \quad .$$

The ^3P_J decay can either be purely hadronic via gluon annihilation (diagrams a,b) or by radiative decay into the J/ψ (diagram c).

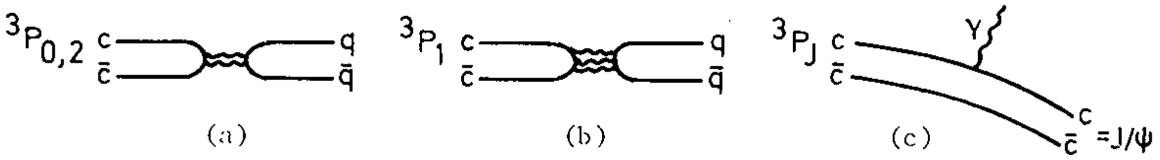

(a) (b) (c)

The decay widths for (a,b) are proportional to the wave functions squared at small distances. These widths have been estimated by Barbieri, Gatto and Kögerler[7.18)] as $\Gamma(2^{++})/\Gamma(0^{++}) = 4/15$ and $\Gamma(0^{++}) = 2.4$ MeV. The 1^{++} state is expected to be even narrower.

The decays $2^3S_1 \rightarrow \gamma^3P_J$ can proceed to lowest order by an electric dipole (E1) transition. The rate for an E1 transition is given by

$$\Gamma(2^3S_1 \rightarrow \gamma 1^3P_J) = \frac{16}{243}\ \alpha(2J+1)\ k^3\ |\langle 1P|r|2S\rangle|^2 \tag{7.4}$$

The rate depends on the overlap between the radial wave functions for the S and P levels. For an E1 transition the angular distribution of the photon with respect to the beam axis is of the form

$$\begin{aligned} 2^3S_1 &\rightarrow \gamma 1^2P_0 & & 1 + \cos^2\Theta \\ &\rightarrow \gamma 1^3P_1 & & 1 - 1/3\ \cos^2\Theta \\ &\rightarrow \gamma 1^3P_2 & & 1 + 1/13\ \cos^2\Theta \quad . \end{aligned} \tag{7.5}$$

For the latter two transitions also higher multipole amplitudes could contribute. For this reason only the prediction for $^3S_1 \rightarrow \gamma^3P_0$ is unique. The ^3P_J states were detected in three different ways: as discrete lines in the photon spectrum, through the cascade decay $\psi' \rightarrow \gamma^3P_J$, $^3P_J \rightarrow \gamma J/\psi$ and as peaks in $\pi\pi$, 4π ... mass distributions. The study of the cascade decay led to the first discovery of an intermediate state ($P_c(3510)$) by DASP [7.9)].

Fig.7.11 shows the inclusive photon spectrum from ψ' decay, $\psi' \rightarrow \gamma\ \chi$, as observed recently in the Crystal Ball detector [7.19)]. Four narrow peaks are seen centered at ~ 120 MeV, 170 MeV, 260 MeV and 380 MeV. The first three correspond to transitions to the intermediate states $\chi(3.56)$, $P_c(3.51)$ and $\chi(3.41)$. The fourth one results from the decay $P_c(3.51) \rightarrow \gamma\ J/\psi$. No evidence is seen for a state at 3.45 GeV (E_γ = 230 MeV) for which some evidence had been found previously by SLAC-LBL [7.20)]; nor is there any signal for a state near 3.60 GeV (E_γ = 86 MeV) as claimed by the DESY-Heidelberg group [7.21)]. Both states had been detected in the cascade channel, $\psi' \rightarrow \gamma\gamma\ J/\psi$.

Table 7.4 lists the branching ratios for the transitions $\psi' \rightarrow \gamma\ P_c\ \chi$ and Table 7.5 summarizes the measurements on the branching ratios for the cascade decays. For completeness Table 7.6 gives the branching ratios for the hadronic decay modes of the intermediate states.

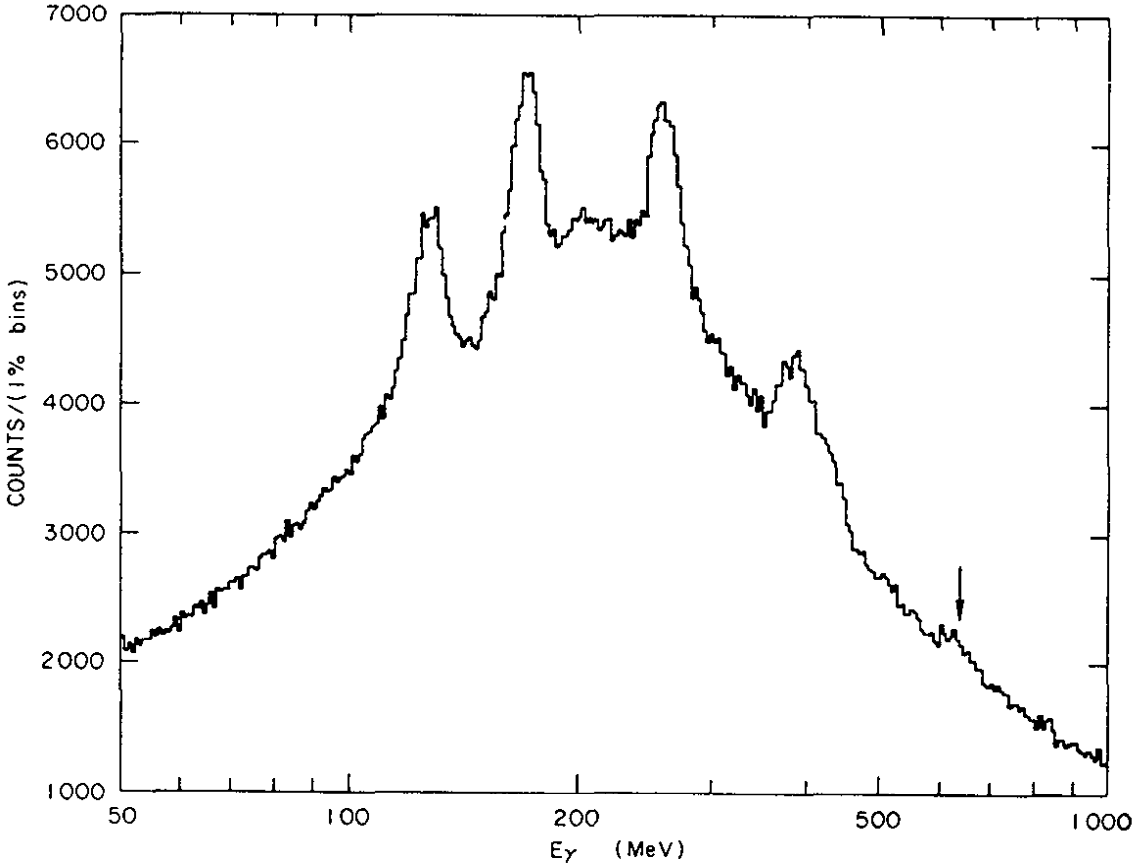

Fig. 7.11 The inclusive photon spectrum from ψ' decay, $\psi' \to \gamma X$, as measured by the Crystal Ball (Ref. 7.19).

Table 7.4 P_c/χ States

Decay	Branching ratio %	Γ (keV)	References	Theory (keV)
$\psi' \to \gamma\ \chi(3.41)$	7.2 ± 2.0	16 ± 5	7.22	44
	6.5 ± 2.2	15 ± 5	7.23	
$\psi' \to \gamma\ \chi(3.45)$	< 2.5%	< 5.7	7.22	18
$\psi' \to \gamma\ P_c(3.51)$	7.1 ± 2.0	16 ± 5	7.22	38
$\psi' \to \gamma\ \chi(3.55)$	7.0 ± 2.3	16 ± 5	7.22	27

Table 7.5 Cascade Decays $(\psi' \to \gamma\ P_c/\psi)(P_c/\chi \to \gamma\ J/\psi)$

Intermediate State	$BR(\psi' \to \gamma P_c/\chi) \cdot BR(P_c/\chi \to \gamma\ J/\psi)$ %	Reference
$\chi(3.41)$	3.3 ± 1.7	7.22
	0.3 ± 0.2	7.9
	0.14 ± 0.09	7.21
	0.2 ± 0.2	7.24
	< 0.05 90% CL	7.19
$\chi(3.45)$	< 0.61 90% CL	7.9
	< 0.25 90% CL	7.21
	0.8 ± 0.4	7.24
	< 0.045 90% CL	7.19
$P_c(3.51)$	5.0 ± 1.5	7.22
	2.1 ± 0.4	7.9
	2.5 ± 0.4	7.21
	2.4 ± 0.8	7.24
	2.10 ± 0.47	7.19
$\chi(3.56)$	2.2 ± 1.0	7.22
	1.6 ± 0.6	7.9
	1.0 ± 0.2	7.21
	1.0 ± 0.6	7.24
	1.13 ± 0.25	7.19
(3.59)	0.18 ± 0.06	7.21
	< 0.06 90% CL	7.19

Table 7.6 Properties of the Intermediate States

MASS (MeV)	Decay	$BR(\psi' \to \gamma P_c/\chi) \cdot BR(P_c/\psi \text{ decay})$ %	Reference	$BR(P_c/\psi \text{ decay})$ %
3413 ± 5	$\pi^+\pi^-$	0.07 ± 0.02	7.25	1.0 ± 0.3
		0.06 ± 0.02	7.9	
	K^+K^-	0.07 ± 0.02	7.25	1.0 ± 0.3
		0.055± 0.025	7.9	
	$p\bar{p}$	< 0.0095	7.9	
	$2\pi^+2\pi^-$	0.32 ± 0.06	7.25	4.7 ± 0.9
	$\pi^+\pi^-K^+K^-$	0.27 ± 0.07	7.25	3.9 ± 1.0
	$p\bar{p}\ \pi^+\pi^-$	0.04 ± 0.013	7.25	0.6 ± 0.2
	$3\pi^+3\pi^-$	0.14 ± 0.05	7.25	2.0 ± 0.7
	$\gamma J/\psi$	0.22 ± 0.08		3.2 ± 1.2
	$\gamma\ \gamma$	< 0.014	7.9	<0.2
	$\rho^0\pi^+\pi^-$	0.12 ± 0.04	7.25	1.8 ± 0.6
	$K^{0*}K^+\pi^-$	0.17 ± 0.06	7.25	2.5 ± 0.9
3.508 ± 4	$\pi^+\pi^- + K^+K^-$	< 0.015	7.25	< 0.21
	$2\pi^+2\pi^-$	0.11 ± 0.04	7.25	1.5 ± 0.6
	$\pi^+\pi^-K^+K^-$	0.06 ± 0.03	7.25	0.85± 0.42
	$p\bar{p}\pi^+\pi^-$	0.01 ± 0.008	7.25	0.14± 0.11
	$3\pi^+3\pi^-$	0.17 ± 0.06	7.25	2.4 ± 0.8
	$\gamma J/\psi$	2.4 ± 0.3		34 ± 4
	$\gamma\ \gamma$	< 0.013	7.9	< 0.18
	$\rho^0\pi^+\pi^-$	0.026± 0.022	7.25	0.37± 0.31
	$K^{0*}K^+$	0.31 ± 0.022	7.25	0.44± 0.31
3.552 ± 6	$\pi^+\pi^- + K^+K^-$	0.02 ± 0.01	7.25	0.29± 0.14
	$\pi^+\pi^-$	0.015± 0.008	7.9	
	K^+K^-	0.012± 0.009	7.9	
	$p\bar{p}$	< 0.0075	7.9	
	$2\pi^+2\pi^-$	0.16 ± 0.04	7.25	2.3 ± 0.6
	$\pi^+\pi^-K^+K^-$	0.14 ± 0.04	7.25	2.0 ± 0.6
	$p\bar{p}\ \pi^+\pi^-$	0.02 ± 0.01	7.25	0.29± 0.14
	$3\pi^+3\pi^-$	0.08 ± 0.05	7.25	1.1 ± 0.7
	$\gamma J/\psi$	1.9 ± 0.2		27 ± 3
	$\gamma\ \gamma$	< 0.004	7.9	< 0.06
	$\rho^0\pi^+\pi^-$	0.05 ± 0.03	7.25	0.71± 0.43
	$K^{0*}K^+\pi^-$	0.052± 0.031	7.25	0.74± 0.44

7.5.1 Quantum Numbers of the Intermediate States

The P_c/χ states have all charge conjugation C = + since they are populated via $\psi' \to \gamma\, P_c/\chi$. The spin parity assignment is made with the help of the hadronic decay modes, the angular distribution $W(\cos\Theta)$ of the primary photon with respect to the beam and the level scheme predicted by the charmonium mode. Fits of the form

$$W(\cos\Theta) = 1 + a \cos^2\Theta$$

yielded (7.25):

state:	$\chi(3.41)$	$P_c(3.51)$	$\chi(3.56)$
a	1.4 ± 0.4	0.1 ± 0.4	0.3 ± 0.4

For a spin 0 state a = 1. The $\chi(3.41)$ is therefore consistent with J = 0, whereas a J = 0 assignment for the $P_c(3.51)$ and the $\chi(3.56)$ is excluded on the 2σ level.

In the level scheme depicted in Fig. 7.5 there are four levels with even charge conjugation between the ψ' and the J/ψ, one pseudoscalar $^1S_0$ with $J^{PC} = 0^{-+}$ and three ^3P states with $J^{PC} = 2^{++}$, 1^{++} and 0^{++}. Are the levels found consistent with these quantum numbers?

$\chi(3.413)$ It follows from C = + and the observed decay into $\pi^+\pi^-$ and/or K^+K^- that the state is an isoscalar and has positive parity. The angular distribution is consistent with J = 0. We can therefore safely assign this state to $J^{PC} = 0^{++}$.

$P_c(3.508)$ The absence of $\pi^+\pi^-$ and K^+K^- decays are consistent with the state belonging to an unnatural spin-parity sequence 0^-, 1^+,.. . The angular distribution of the photon suggests $J \neq 0$ and isospin must be even since the resonance decays into an even number of pions.

$\chi(3.552)$ It follows from the observed decay into $\pi^+\pi^-$ and/or K^+K^- that the level is an isoscalar and belongs to a natural spin-parity sequence. The angular distribution of the photon excludes J = 0 with 2σ.

This is all that can be deduced from the data alone. However, comparing the available information with the levels expected in the charmonium model (Fig. 7.5) leads to a unique assignment using the following reasoning. The 3.41 GeV level must be the 0^{++} state. This leaves only one natural spin-parity level - the $^3P_2(2^{++})$ level - which then must be associated with the 3.56 GeV level. The 3.51 GeV level has $J \neq 0$ and must therefore be the $^3P_1(1^{++})$ level. This assignment is also consistent with the fact that $P_c(3.51) \to \pi^+\pi^-$, K^+K^- has not been observed.

The decays $\psi' \to \gamma\, ^3P_{2,1,0}$ are to lowest order electric dipole transitions. The measured widths are listed in Table 7.4 and compared to model calculations assuming E1. Note that the predicted rates are considerably larger than the measured values. If the matrix elements are independent of J then the relative rates for E1 transitions are given by $\Gamma \sim k^3\ (2J + 1)$. In this case we expect

$$\Gamma(2^3S_1 \to \gamma\ ^3P_0) : \Gamma(2^3S_1 \to \gamma\ ^3P_1) : \Gamma(2^3S_1 \to \gamma\ ^3P_2) =$$

$$1 \quad : \quad 0.9 \quad : \quad 0.6$$

compared to the observed ratios 1 : 1.04 : 1.02. Reversing the order of the levels i.e. $^3P_0 > {}^3P_1 > {}^3P_2$ leads to a gross disagreement between the predicted and the observed rates.

In QCD the 0^{++} and the 2^{++} states can decay to lowest order via 2 gluon emission into hadrons whereas the 1^{++} state must emit three gluons. The total hadronic width for 0^{++} and 2^{++} is therefore proportional to α_s^2 compared to α_s^3 for the 1^{++} state. Since α_s is less than one we naively expect the 1^{++} state to have a smaller hadronic width than the other two. This assertion is supported by detailed calculations[7.18,7.26] which find:

$$\Gamma(0^{++}) : \Gamma(2^{++}) : \Gamma(1^{++}) = 15 : 4 : 1$$

where the first ratio is the most reliable one. Experimentally we would therefore expect the 0^{++} level to have a smaller branching ratio for the radiative decay into the J/ψ than the other two and this is indeed supported by experiments.

The $^1P_1$ state.

Besides the three ^3P_J states the potential (7.1) predicts a singlet P state with $J^{PC} = 1^{+-}$ (Fig. 7.5). Because of odd C parity this level cannot be reached from the ψ' by a γ transition. The decay $\psi' \to \pi^0\ {}^1P_1$ is suppressed by isospin conservation. The strong decay $\psi' \to \pi\pi\ {}^1P_1$ is probably forbidden by kinematics. No evidence sofar was found for the existence of the $^1P_1$.

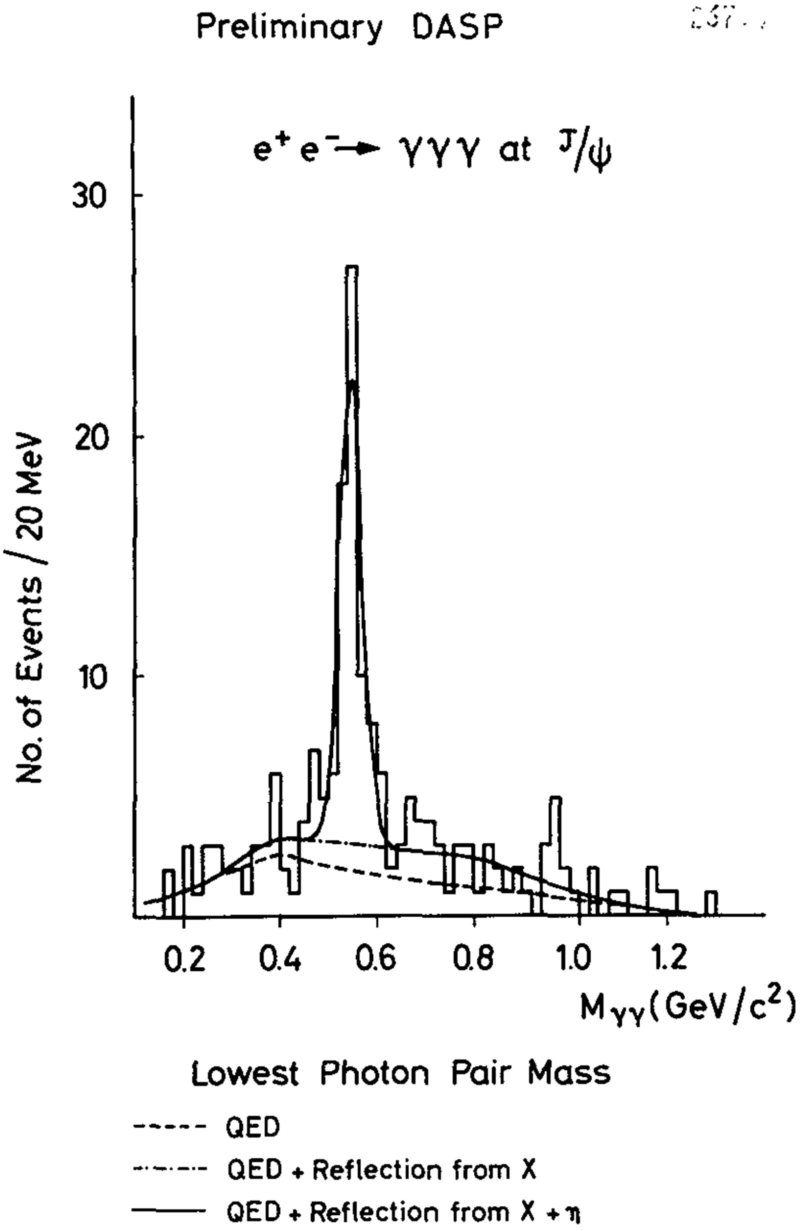

Fig. 7.12 Distribution of the lowest photon pair mass for three photon events at the J/ψ (Ref. 7.27).

The overlap integral $|<n_f|n_i>|^2$ is expected to be unity for $n_f = n_i$ and small for $n_f \neq n_i$. Table 7.7 shows the predicted width for $J/\psi \rightarrow \gamma\eta_c$ for the η_c mass.

Table 7.7 Predicted decay width Γ and branching ratio B for the decay $J/\psi \rightarrow \gamma\eta_c$ as a function of the η_c mass.

M_{η_c} (GeV)	photon energy (MeV)	Γ(keV)	B (%)
3.04	50	0.2	0.3
2.99	100	1.6	2
2.89	200	14	20
2.79	300	45	70

A search of the photon spectrum from J/ψ decay failed to produce evidence for the $J/\psi \rightarrow \gamma\eta_c$ transition (7.22). An upper limit of 1.7 % was put on the branching ratio $B(J/\psi \rightarrow \gamma\eta_c)$.

Evidence for a heavy and narrow resonance below the J/ψ was reported previously by the DASP group[7.27] in the decay $J/\psi \rightarrow \gamma X \rightarrow \gamma\gamma\gamma$.

Events with three photons were selected using the DASP inner detector. For each photon the production angles were measured taking the position of the interaction point from Bhabha events observed concurrently. A 1C fit was made to the hypothesis $J/\psi \rightarrow \gamma\gamma\gamma$ and events with a $\chi^2 < 2.7$ were retained. The photon energies for the accepted events were computed. Of the three possible $\gamma\gamma$ mass combinations only two are independent. The events were analyzed in terms of the lowest and the highest $\gamma\gamma$ masses in the event. The low mass plot shows a clear η signal and an indication for η' production (see Fig. 7.12). The position of the η(547.1 ± 4.2 MeV) agrees with its knows mass value; the observed η width ($\sigma = 24 \pm 4$ MeV) is consistent with the expected resolution of 20 MeV.

Fig. 7.13 shows the Dalitz plot distribution with lines indicating the position of the η and η'. The high mass data are shown in Fig. 7.14 together with the contributions from QED and $\eta + \eta'$. The QED curve was computed from the matrix elements evaluated by Berends and Gastmann[7.28]. The QED curve is an absolute prediction. The calculation was checked by measuring $e^+e^- \rightarrow \gamma\gamma\gamma$ at a c.m.energy of 3.6 GeV, i.e. away from resonances.

The high mass data show a peak near 2.82 GeV, called the X(2.8). In the mass interval 2.82 ± 0.04 GeV, 41 events are observed, compared to 19 events expected from QED and $\eta + \eta'$. This corresponds to a 5 standard deviation effect. The fitted mass is 2.82 ± 0.014 GeV; the value of the width is 0.04 ± 0.014 GeV. Considering the experimental resolution the measured width is consistent with that of a zero width resonance. The pro-

7.6 The Pseudoscalar States

The potential (7.1) predicts the pseudoscalar states ($\eta_c, \eta'_c \ldots$) $1\,^1S_0$, $2\,^1S_0$ ... to lie below the corresponding vector states (n^3S_1). The pseudoscalar states can decay into ordinary hadrons by two gluon exchange, i.e.

$$\Gamma(\eta_c \to \text{hadrons}) \sim \alpha_s^2$$

Hence one expects the $^1S_0$ states to have a larger width than the vector states for which $\Gamma \sim \alpha_s^3$. More precisely:

$$\Gamma(^1S_0 \to gg \to \text{hadrons}) = \frac{32\pi}{3} \alpha_s^2 \frac{|^1S_0(0)|^2}{M^2} \tag{7.6}$$

The $^1S_0$ states having C = + can also decay into two photons; the corresponding width is given by

$$\Gamma(^1S_0 \to \gamma\gamma) = \frac{256\pi}{27} \alpha^2 \frac{|^1S_0(0)|^2}{M^2} \tag{7.7}$$

A comparison of (7.6) and (7.7) leads to

$$\frac{\Gamma(^1S_0 \to \gamma\gamma)}{\Gamma(^1S_0 \to \text{hadrons})} = \frac{8}{9} \frac{\alpha^2}{\alpha_s^2} \simeq 1.3 \cdot 10^{-3} \tag{7.8}$$

for $\alpha_s = 0.2$. Under the assumption that $^3S_1$ and $^1S_0$ have the same radial wave functions equ (7.7) and (7.6) predict for the $^1S_0$ width

$$\Gamma(^1S_0 \to \text{hadrons}) = \frac{27}{5} \frac{\pi}{(\pi^2 - 9)\alpha_s} \Gamma(^3S_0 \to \text{hadrons}) \simeq 5 \text{ MeV} \tag{7.9}$$

If the triplet-singlet level splitting is small, the $^1S_0$ can be reached from the corresponding $^3S_1$ state by a radiative transition only, $^3S_1 \to \gamma\ ^1S_0$. This is a pure spinflip or M1 transition. The amplitude is proportional to the magnetic moment of the c quark. If this is assumed to be of the Dirac type,

$$\mu_c = \frac{2/3\ e}{2m_c} \tag{7.10}$$

m_c = mass of c quark

the transition rate is given by

$$\Gamma(n_i\ ^3S_1 \to n_f\ ^1S_0) = \frac{16}{27} \alpha \frac{k^3}{m_c^2} |\langle n_f | n_i \rangle|^2 \tag{7.11}$$

k is the photon energy.

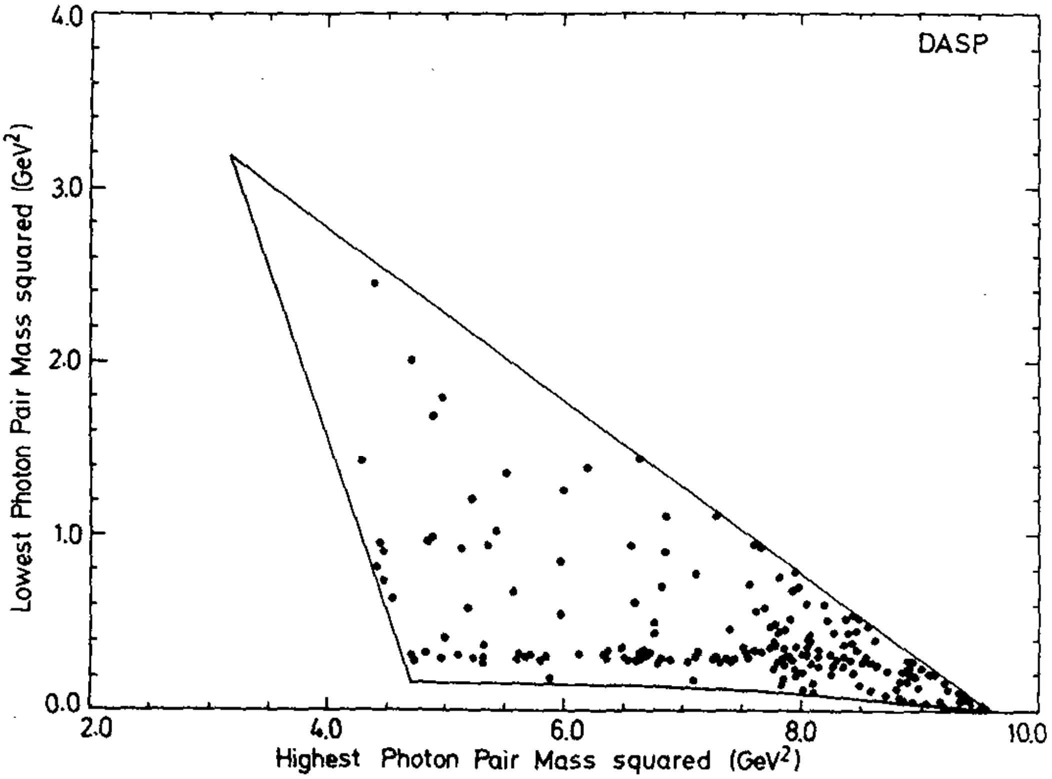

Fig. 7.13 Dalitz plot of coplanar three-photon events at the J/ψ (Ref. 7.27).

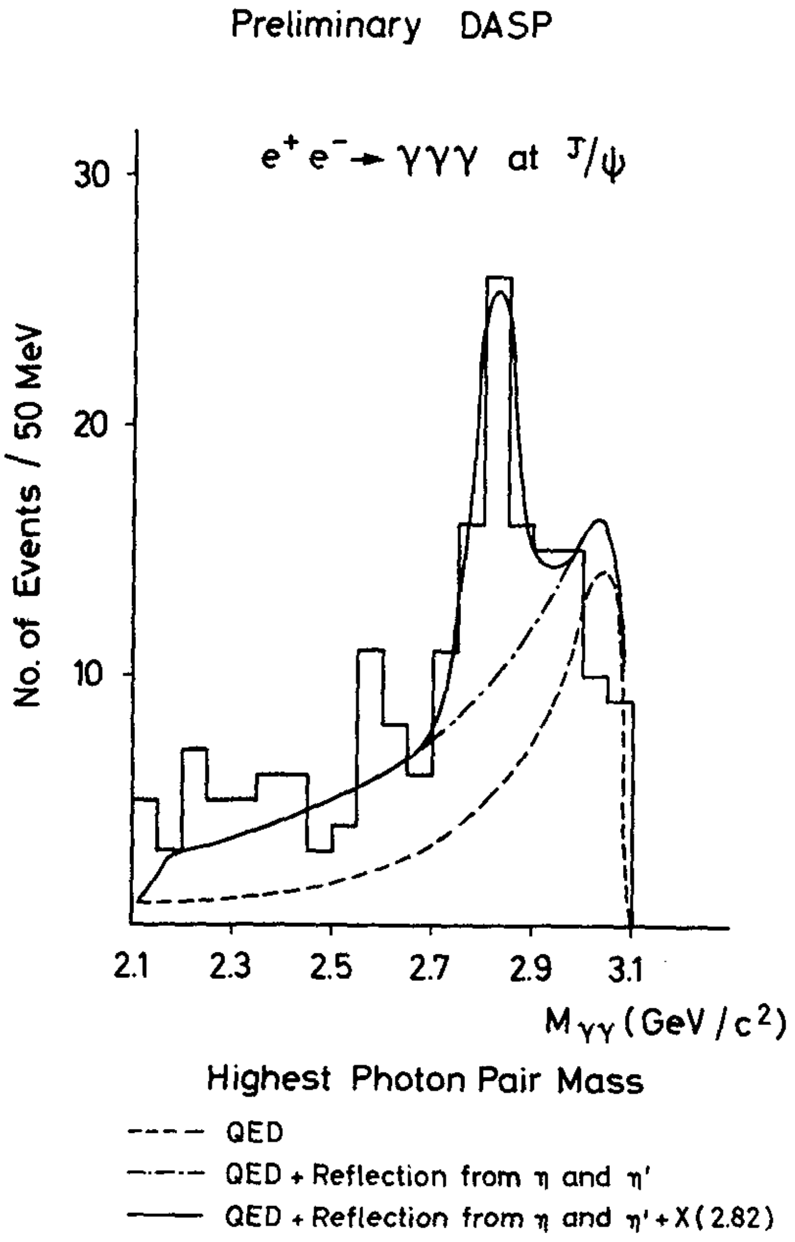

Fig. 7.14 J/ψ → γγγ measured by DASP[7.27]. Distribution of the highest photon pair mass.

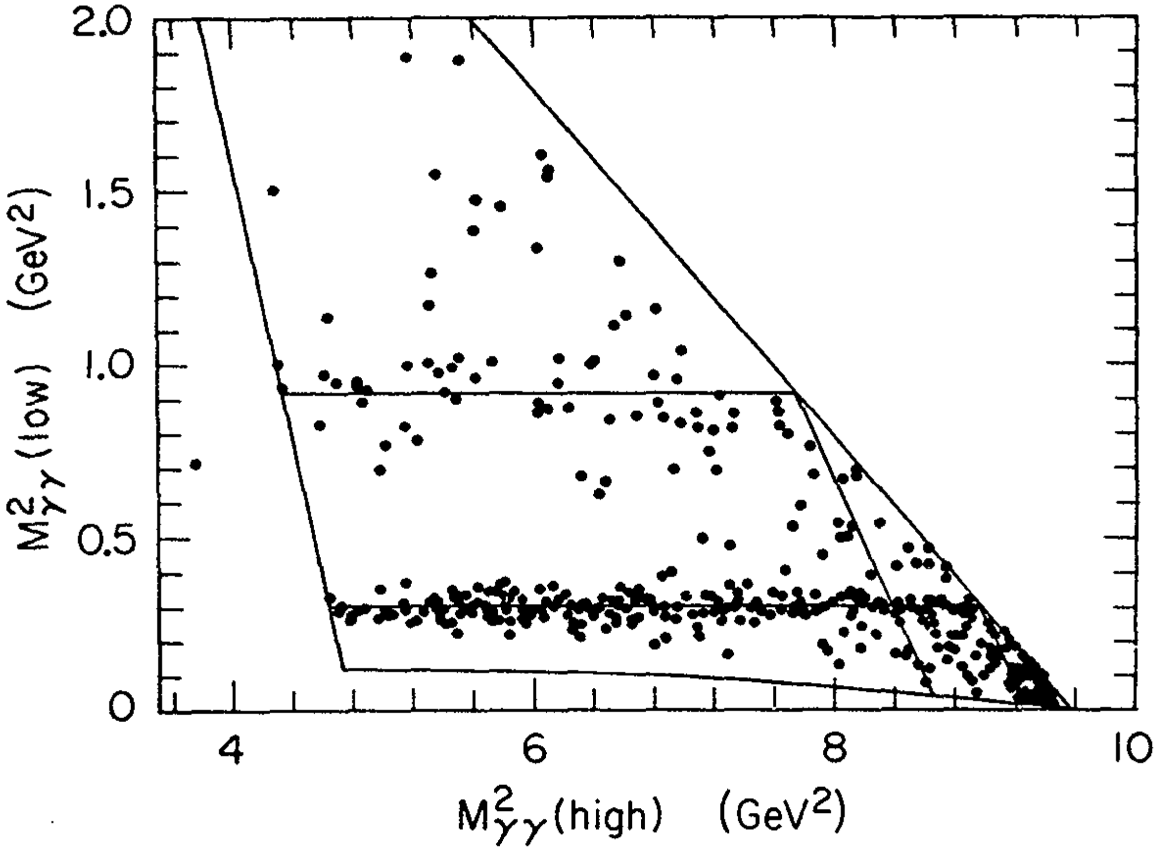

Fig. 7.15 Dalitzplot for the decay $J/\psi \to 3\gamma$ as observed by the Crystal Ball (Ref. 7.19).

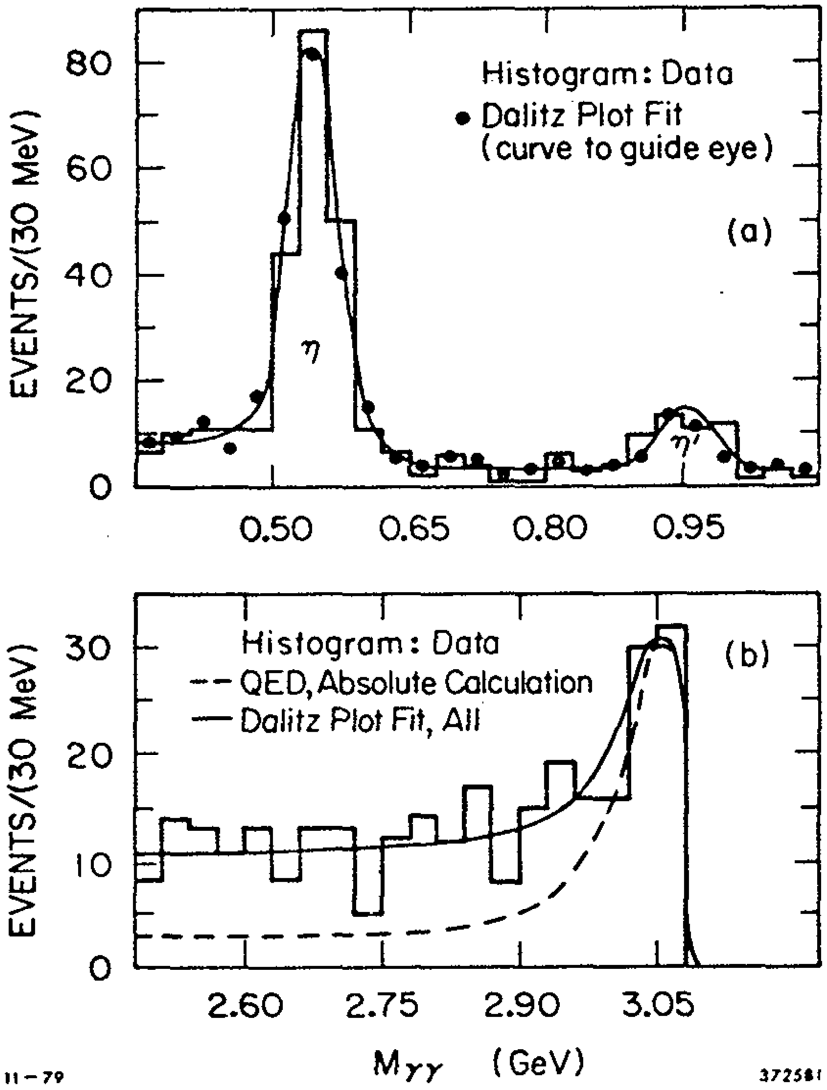

Fig. 7.16 The decay J/ψ → 3γ as observed by the Crystal Ball (Ref. 7.19).

(a) γγ mass distribution of the low mass solution;

(b) of the high mass solution.

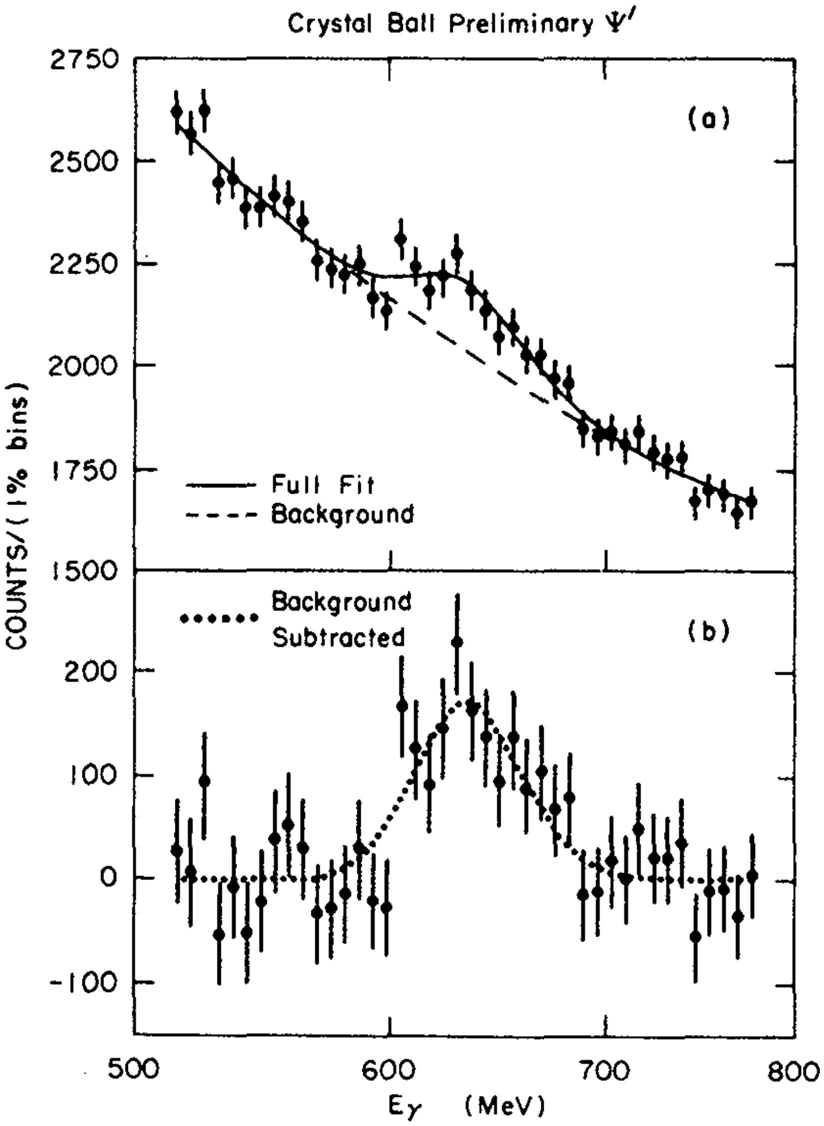

Fig. 7.17 The inclusive γ spectrum from ψ' decay, ψ' → γX in the region of the u(2.98) as measured by the Crystal Ball (Ref. 7.19)

(a) the observed spectrum

(b) after background subtraction

duct of the branching ratios was determined to

$$B(J/\psi \rightarrow \gamma X) \cdot B(X \rightarrow \gamma\gamma) = 1.4 \pm 0.4 \cdot 10^{-4}$$

We now discuss the data from the Crystal Ball experiment at SPEAR on the same reaction, $J/\psi \rightarrow 3\gamma$ (7.19). The angular resolution for photons is roughly a factor of two worse than in the DASP experiment but the energy resolution is considerably better, $\sigma/E = 2\,\%/E^{1/4}$. Fig.7.15 shows the Dalitz plot distribution. The η and η' lines stand out clearly. The high mass projection (Fig. 7.16) shows no evidence for the X(2.82). It should be noted that the mass resolution near the high energy end of the $\gamma\gamma$ spectrum is basically determined by the energy resolution of the third photon. This leads to $\sigma(M_{\gamma\gamma}) \approx 10$ MeV at 2.8 GeV. The upper limit on the branching ratio found in this experiment

$$B(J/\psi \rightarrow \gamma X(2.82)) \cdot B(X(2.82) \rightarrow \gamma\gamma) < 0.3 \cdot 10^{-4} \quad (90\ \%\ \mathrm{C.L.})$$

is a factor of 4 to 5 smaller than the value obtained by DASP which makes the existence of the X(2.82) rather unlikely.

So, where is the η_c? The Crystal Ball group in studying the radiative decays of the ψ' found preliminary evidence for a discrete photon line at 640 ± 20 MeV. The evidence is shown in Fig. 7.17 where the photon spectrum from Fig. 7.11 is replotted after subtracting a smooth background. The photon line in question is seen as a 5 s.d. signal. If taken for real the data imply a state with a mass of 2976 ± 20 MeV, called U(2976) by the authors. Obviously, more data are required to settle the question of the η_c. It is obvious, however, that the U would fit much better into the charmonium model (see Table 7.7 and the measured upper limit on $B(J/\psi \rightarrow \gamma\eta_c)$).

SUMMARY

The observed number of levels and their ordering is that expected for a pair of fermions bound in a steeply rising potential. The fine structure splitting of the P-levels i.e. $^3P_2 > {}^3P_1 > {}^3P_0$ is that expected for a vector force. A pure scalar potential would reverse the order and give a level assignment in contradiction to the experiments. The level splittings are larger than predicted but the radiative rates are smaller by a factor of two. Indirect evidence shows that the ratio of the hadronic widths of the P states are in agreement with predictions based on QCD.

8. Charmed Particles

The existence of a fourth quark besides the familiar u, d and s quarks implies that the SU(3) nonet of 8 + 1 mesons will be replaced8.1) by a hexadecimet of 15 + 1 states as shown in Fig. 8.1. Besides ordinary SU(3) resonances with $C = 0$ the hexadecimet contains six states with open charm, $C = \pm 1$ and one $c\bar{c}$ state with hidden charm. The quark content and the names given to the charmed pseudoscalar mesons are

$$\begin{array}{llllll} C = +1 : & D^+ = c\bar{d} & & D^o = c\bar{u} & & F^+ = c\bar{s} \\ \;\;\, = 0 : & \eta_c = 1^1S_o & = c\bar{c} & & & \\ \;\;\, = -1 : & D^- = \bar{c}d & & \overline{D^o} = \bar{c}u & & F^- = \bar{c}s \end{array}$$

In the baryon sector ten charmed baryon ground states can be formed:

$$\begin{array}{llll} & S = 0 & S = 1 & S = 2 \\ C = 3 : & (ccc)^{++} & & \\ \;\;\, = 2 : & (ccu)^{++}\ (ccd)^{+} & (ccs)^{+} & \\ \;\;\, = 1 : & (cuu)^{++}\ (cud)^{+}\ (cdd)^{o} & (csu)^{+}\ (csd)^{o} & (css)^{o} \end{array}$$

Higher mass charmed mesons or baryons will cascade by strong and/or electromagnetic decays into these states, which then decay weakly. For instance

$$\begin{aligned} D(F) &\rightarrow \ell\bar{\nu}_e \\ &\rightarrow \ell\bar{\nu}_e + \text{hadrons} \\ &\rightarrow \text{hadrons} \end{aligned}$$

The leptonic decay mode is suppressed by kinematics ($J_3^D = 0 \neq J_3^\ell + J_3^{\bar{\nu}} = 1$). Semileptonic decays are predicted with a branching ratio on the order of 20 % and most decays (80 %) will therefore yield only hadrons in the final state8.1,8.2). Any new flavour will produce mixed lepton-hadron final states and show up as narrow resonances above threshold. However, the flavour can be identified by the properties of the final states. The GIM mechanism7.5) (Fig. 8.2) leads for charmed mesons to the following Cabibbo favoured decay modes:

$$\begin{aligned} D^o &\rightarrow (e^+\nu_e)\ (K^-\ldots) \\ &\rightarrow (\bar{K}n\pi)^o \\ D^+ &\rightarrow (\ell^+\nu_e)\ (\overline{K^o}\ldots) \\ &\rightarrow (\bar{K}n\pi)^+ \\ F^+ &\rightarrow (\ell^+\nu_e)\ (\eta,\ \eta',\ K\bar{K},\ \ldots) \\ &\rightarrow (\eta n\pi)^+,\ (\eta' n\pi)^+,\ (K\bar{K}n\pi)^+ \end{aligned}$$

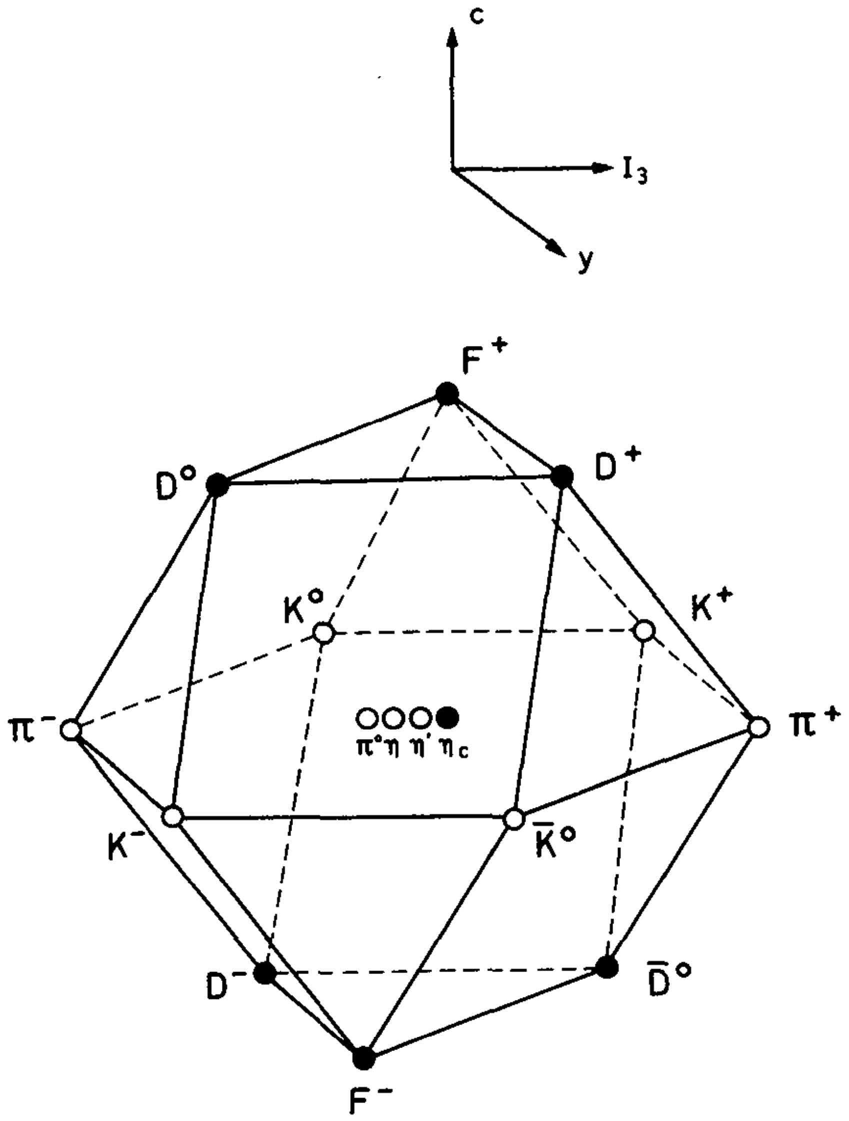

Fig. 8.1 The hexadecimet of the pseudoscalar mesons. Charm is plotted along the z-axis, Y and I_3 along respectively the y-axis and the x-axis. The π^o, η and η' mesons are denoted by the open circles at the origin, η_c by the black circle

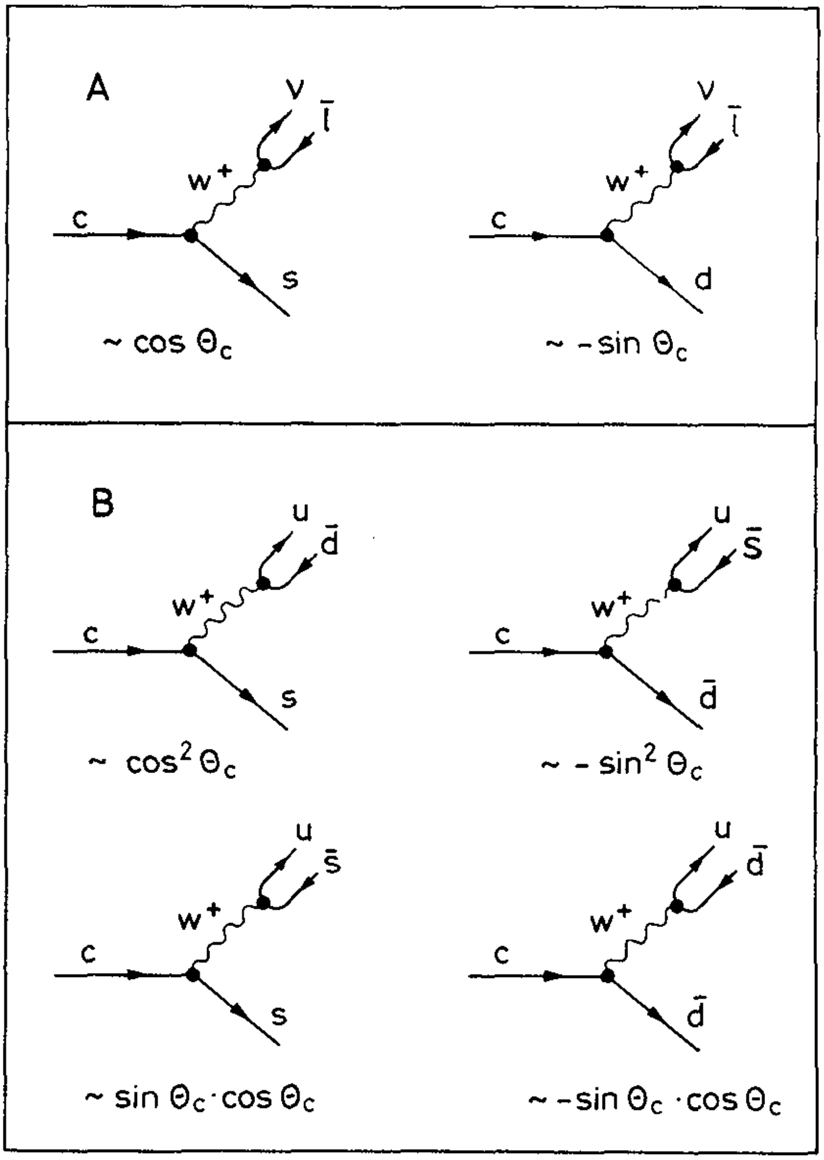

Fig. 8.2 a) Schematic diagrams for the semileptonic decay of the charmed quark

b) Schematic diagrams for the decay of the charmed quark into noncharmed quarks

The discussion of the experimental data on charmed particles as seen in e^+e^- annihilation will be very brief. It will be restricted to the new data presented at the 1979 Fermilab Conference8.3,8.4). More information may be found in the review articles listed under (1.3).

According to the GIM mechanism associated production of D mesons will show up as an increase in the yield of kaons, a strong correlation between leptons and kaons in multiprong final states and appearant exotic decays like $D^+ \to K^-\pi^+\pi^+$. The production of F mesons will produce an increase in the yield of particles with a large $s\bar{s}$ component like η, η' or ∅. The onset of charmed baryon production will be marked by a step in the yield of p, $\bar{p}$ and/or Λ's. Basically all these features have been observed experimentally. The D mesons and the first excited states D^* are well established.

Observation of the F mesons so far has been reported in print by only one experiment8.5). The first evidence for charmed baryon states produced in e^+e^- annihilation has been found only recently.

8.1 The D Mesons

Tables 8.1 and 8.2 list some properties of D and D^* mesons as determined by the SLAC-LBL group7.10).

Table 8.1 D and D^* mass values7.10)

	M (MeV)
D^0	1863.3 ±0.9
D^+	1868.4 ±0.9
D^{*0}	2006.0 ±1.5
D^{*+}	2008.6 ±1.0
$M_{D^+} - M_{D^0}$	5.1 ±0.8
$M_{D^*} - M_{D^{*0}}$	2.6 ±1.8

The decay modes listed in table 8.2 for D^0 and D^* are all Cabibbo allowed transitions ($\sim\cos^2\theta_C$). The MARKII group working at SPEAR recently observed also Cabibbo suppressed decays of the D^0, $D^0 \to \pi^+\pi^-$ and $D^0 \to K^+K^-$8.3). The evidence is shown in Fig. 8.3 giving the two particle mass combinations of particles with opposite charge. In Fig. 8.3b the two particles are assumed to be K^+,π^- or K^-,π^+. A strong signal at 1863 MeV is observed corresponding to the D^0. Taking both particles to be pions a weak D^0 signal of 9.3 ±3.9 events is seen; taking both particles to be kaons a D^0 consisting of 22 ±5 events is obtained.

The following ratios were obtained:

$$B(D^0 \to \pi^-\pi^+)/B(D^0 \to K^+\pi^-) = 0.033 \pm 0.015$$

$$B(D^0 \to K^+K^-)/B(D^0 \to K^+\pi^-) = 0.113 \pm 0.030$$

The GIM mechanism predicts both ratios to equal $\tan^2\theta_C \approx 0.05$. The data agree with this prediction to within 2 s. d..

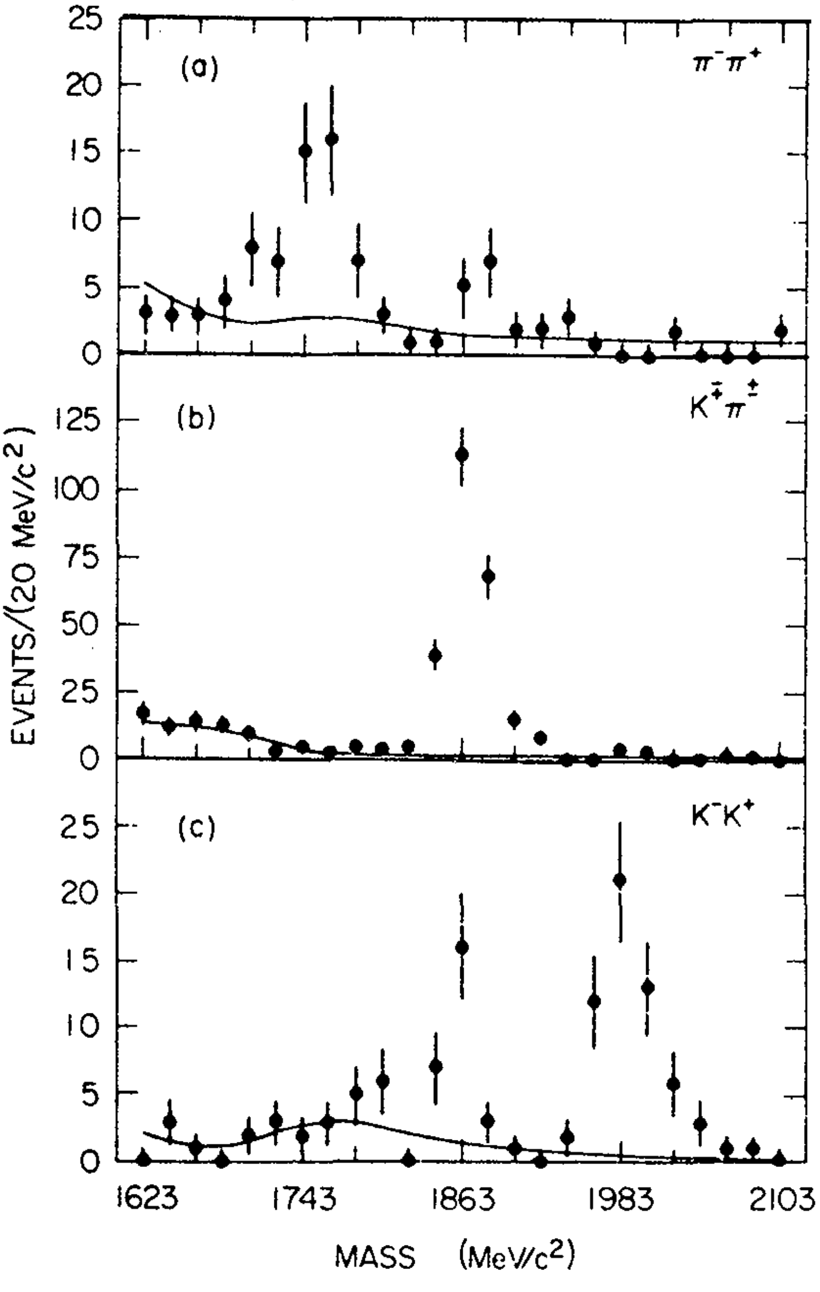

Fig. 8.3 Invariant mass of two particle combinations with momenta within 30 MeV/c of the expected D^0 momentum. (SLAC-LBL, Ref. 8.3)

Table 8.2 D and D^* branching ratios[7.10]

		B(D → f) (%)	Q (MeV)
D^0 →	$K^-\pi^+$	2.2 ± 0.6	
	$K^0\pi^+\pi^-$	3.5 ± 1.1	
	$K^-\pi^+\pi^+\pi^-$	2.7 ± 0.9	
D^+ →	$K^0\pi^+$	1.5 ± 0.6	
	$K^-\pi^+\pi^+$	3.5 ± 0.9	
D^{*0} →	$D^0\pi^0$	55 ± 15	7.7 ±1.7
	$D^0\gamma$	45 ± 15	142.7 ±1.7
D^{*+} →	$D^0\pi^+$	65 ± 9	5.7 ±0.5
	$D^+\pi^0$	29 ± 8	5.2 ±0.9
	$D^+\gamma$	2 - 10	140.2 ±0.9

$\Gamma(D^{*0})/\Gamma(D^{*+}) = 0.95 \pm 0.4$

Table 8.3 lists some measurements of the semileptonic branching ratio of D mesons. They were determined either near 4.03 GeV (DASP[8.6]) or via the decay $\psi''(3.77) \rightarrow D\bar{D}$ (DELCO[8.7], LBL-SLAC[8.8]).

Table 8.3 Semileptonic branching ratio of D mesons

Experiment		B(D → eX)
DASP	(8.6)	0.08 ±0.02
DELCO	(8.7)	0.11 ±0.03
LBL-SLAC	(8.8)	0.072 ±0.028

The semileptonic branching ratio is smaller than the value of 0.20 expected from simple counting arguments: the W decay can

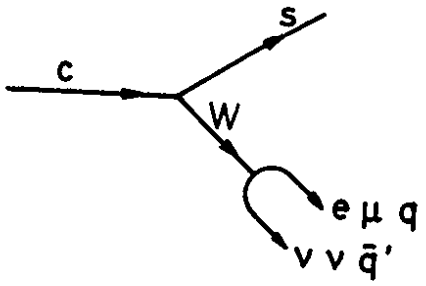

proceed in five different ways, W → eν, μν and $q\bar{q}'$ times three because of three different colours. Assuming the same coupling strength, each channel has the probability 1 : 5 = 0.2. The fact that the observed semileptonic branching ratio is smaller is attributed to an enhancement of the hadronic decay modes and is connected with the octet enhancement found in K decays. The origin of this effect is still being debated[8.9)].

The semileptonic branching ratios listed in Table 8.3 are averages over D^+ and D^o decays. The DELCO group[8.4)] has made an attempt to determine them separately by analysing the 1 electron and 2 electron yields from ψ'' decay, $\psi'' \to 1eX$ and $\psi'' \to 2eX$. Since for the Cabibbo allowed semileptonic decay $c \to se\bar{\nu}$, $\Delta I = 0$, the decay rates $\Gamma(D^+ \to e\nu X)$ and $\Gamma(D^o \to e\nu X)$ are equal. The ratio of the D^+ to D^o lifetimes is therefore given by $\tau(D^+)/\tau(D^o) = B(D^+ \to e\nu X)/B(D^o \to e\nu X)$. The preliminary result from DELCO is $B(D^o \to e\nu X) < 5\ \%$ (95 % C.L.) and $B(D^+ \to e\nu X) = 24 \pm 4\ \%$ which leads to $\tau(D^+)/\tau(D^o) > 4$ (95 % C.L.). Preliminary data from Mark II[8.3] are in agreement with these values: $\tau(D^+)/\tau(D^o) = 3.08\ ^{+4.1}_{-1.33}$.

Assuming, in accord with the electron momentum spectrum, that 45% of the D semileptonic decays proceed via D → keν, by analogy with K → πeν theory predicts $\tau(D \to Ke\nu) = (1.4 \pm 0.3)\cdot 10^{11}\ \mathrm{sec}^{-1}$. The DELCO values then lead to $\tau(D^o) < 3.5\cdot 10^{-13}$sec (95 % C.L.) and $\tau(D^+) = (8 \pm 5)\cdot 10^{-13}$sec.

The fact that D^+ and D^o have different lifetimes indicates that the role of the spectator quark cannot be neglected.

8.2 The F Mesons

The charm model predicts mesons carrying both charm and strangeness. The ground state is the $F^{\pm}$. The GIM favored decay of the F is into an $s\bar{s}$ system leading to final states containing $K\bar{K}$, Φ, η or η'.

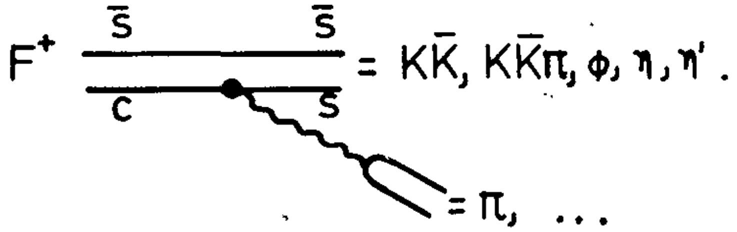

Sizeable η production is therefore an indication of F production. DASP[8.5)] searched for F production by studying events of the type

$$e^+e^- \to \eta + \geq 2 \text{ charged tracks} + X.$$

The η was identified by its decay into two photons.

Figure 8.4 shows the two-photon effective mass distribution for various center of mass energies between 4 and 5 GeV; while a clear π^0 peak is observed at all energies, an η signal is clearly seen only at 4.42 GeV, and possibly at 4.17 and 4.60 GeV. The lack of an η signal at the 4.03 GeV resonance, which is dominated by DD^* and $D^*\bar{D}^*$ production, indicates that the branching ratio for the decay $D \to \eta$ + anything is small.

In Fig. 8.5 the total inclusive η cross section is shown as a function of energy. While no η signal is seen at 4.03 GeV, a significant production is observed between 4.1 and 4.7. (Note that η production below 4.1 is less than 0.5 nb. This is surprisingly small: it is smaller than π^+ or π^- production by a factor of 50 to 80 and smaller than K^+ or K^- production by a factor of 10.)

In a second step an attempt was made to detect the F directly. Consider the first excited state F^*. Because of isospin the decay $F^* \to F\pi$ is forbidden. If, as expected, the F^*, F mass difference is smaller than $2\,m_\pi$ the F^* will decay via $F^* \to F_\gamma$, producing a low energy photon. Indeed, the DASP group found the η signal at 4.4 GeV to be associated mainly with a low energy photon. This observation suggested to look for the channel

$$\begin{array}{l} e^+ e^- \to F\,F^* \to F\;F\;\gamma_{\text{low}} \\ \qquad\qquad\qquad\quad\;\; \hookrightarrow \pi\;\eta \\ \qquad\qquad\qquad\qquad\quad\;\; \hookrightarrow \gamma\;\gamma \end{array} \tag{8.1}$$

in final states with a low energy γ ($E_\gamma < 0.2$ GeV), two photons in the η mass region and a charged pion. There were 43 events at 4.42 GeV and 79 events at all other energies that satisfied the selection criteria. These events were fitted to reaction (8.1). The fit is a 2C fit because of the mass constraint on $M_{(\gamma\gamma)}$ and the requirement that $\pi\eta$ and the missing vector must have the same mass m_F.

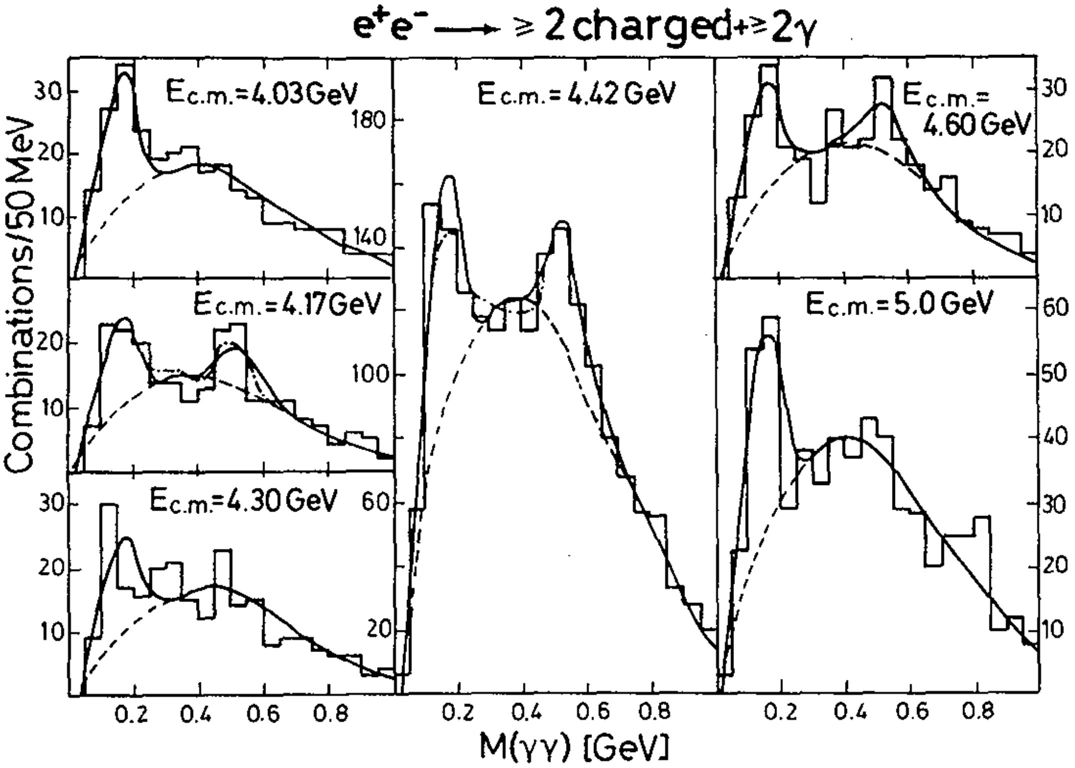

Fig. 8.4 M(γγ) mass distribution at the various c.m. energies. The solid lines are the results of a fit to a sum of background, π^o and η contributions. The dashed lines correspond to the amount of background required by the fit under the η and π^o peaks. The dashed dotted lines at 4.17 and 4.42 GeV are the results of a fit corresponding to the sum of F production and the background, described by the M(γγ) mass distribution at $E_{c.m.}$ = 4.03 GeV (ref. 8.5).

Figs. 8.6a and c show the fitted $\pi\eta$ mass versus the fitted recoil mass for the two regions. At 4.42 GeV a clustering is seen at $M(\gamma\gamma)$ = 2.04 GeV and M_{recoil} = 2.15 GeV while no such clustering is present for the other energies.

Because of the low energy of γ_{low} (average energy 0.11 ±0.046 GeV) the measurements did not permit to distinguish between reaction (8.1) and the following one:

$$\begin{array}{l} e^+ e^- \to F^* F^* \\ \qquad\quad \hookrightarrow \gamma_{low}\; F \\ \qquad\qquad\qquad \hookrightarrow \pi\;\eta \\ \qquad\qquad\qquad\quad\; \hookrightarrow \gamma\;\gamma \end{array} \tag{8.2}$$

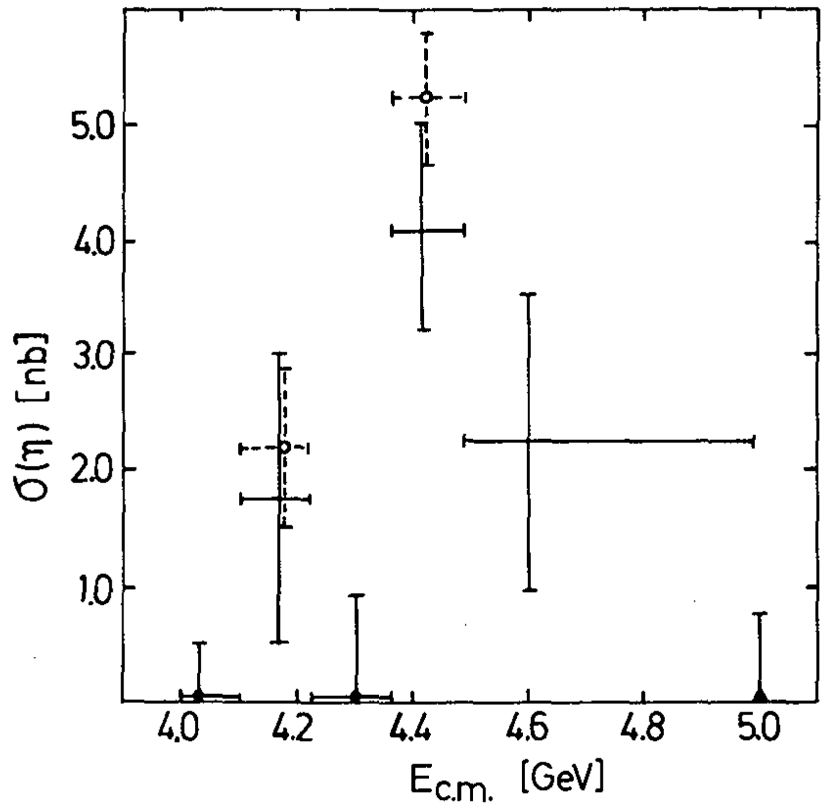

Fig. 8.5 The η inclusive cross section as a function of c.m. energy as measured by DASP (Ref. 8.5).

The events gave also an acceptable fit to reaction (8.2) yielding somewhat lower values for the F and F^* masses, 2.00 and 2.11 GeV, respectively.

Table 8.4 lists the best estimates for the F and F^* masses.

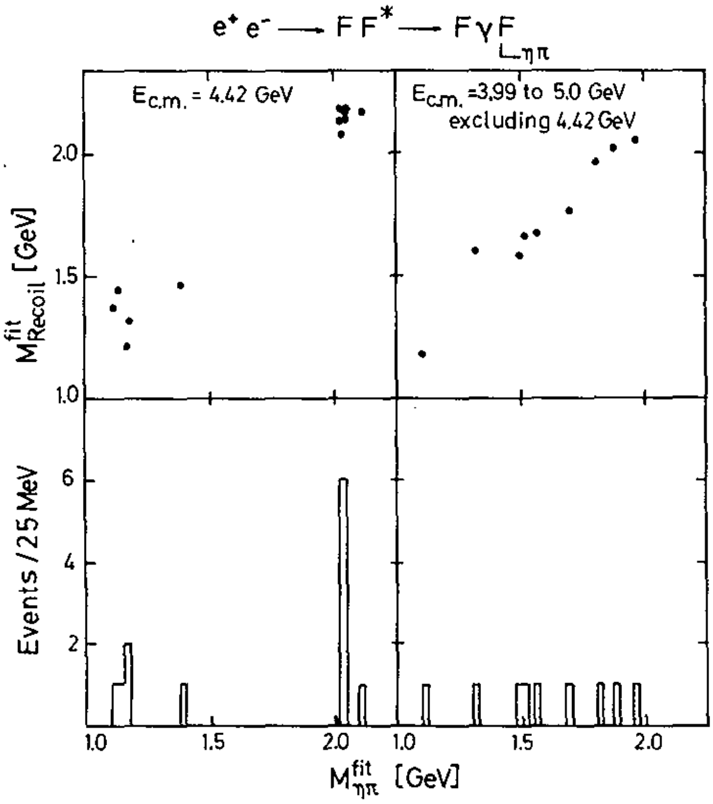

Fig. 8.6 Fitted $\eta\pi$ mass vs. fitted recoil mass, assuming $e^+e^- \to FF^*$, where $F^* \to F\gamma$ and $F \to \eta\pi$ at (a) E_{cm} = 4.42 GeV and (c) at all other energies excluding 4.42 GeV. Histograms (b) and (d) are the projections of Figs. (a) and (c), respectively, along the M($\eta\pi$) axis (Ref. 8.5).

Table 8.4 F and F^* mass values $^{8.5)}$

F^+	2.03 ±0.06 GeV
F^{*+}	2.14 ±0.06 GeV
$M_{F^*} - M_F$	0.11 ±0.046 GeV

For the branching ratio B(F→πη)/B(F→η+anything) a value of 0.09 ±0.05 (±30 % systematic error) was found$^{8.5)}$.

No other data have been published yet on F production. A preliminary analysis by the LBL-SLAC collaboration showed at an energy of 4.16 GeV a peak in the $K^+K^-\pi^+$ mass distribution at 2039 ±1 MeV$^{8.10)}$.

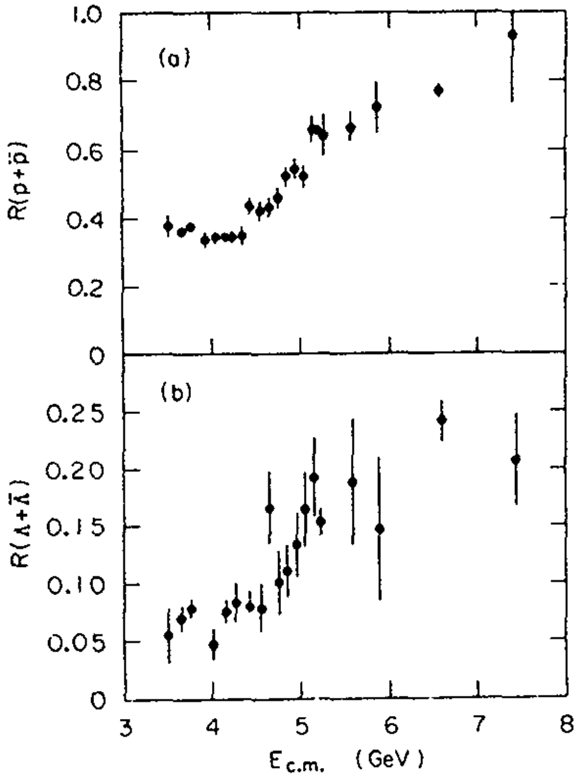

Fig. 8.7

(a) The ratio R of $p,\bar{p}$ production ($e^+e^- \to p$ or $\bar{p}X$) to μ pair production. (SLAC-LBL , Ref. 8.3).

(b) The same as (a) for $\Lambda,\bar{\Lambda}$ (SLAC-LBL, Ref. 8.3).

Fig. 8.8

$e^+e^- \to p(\bar{p})$ K X : Effective mass distributions as measured by SLAC-LBL (Ref. 8.3).

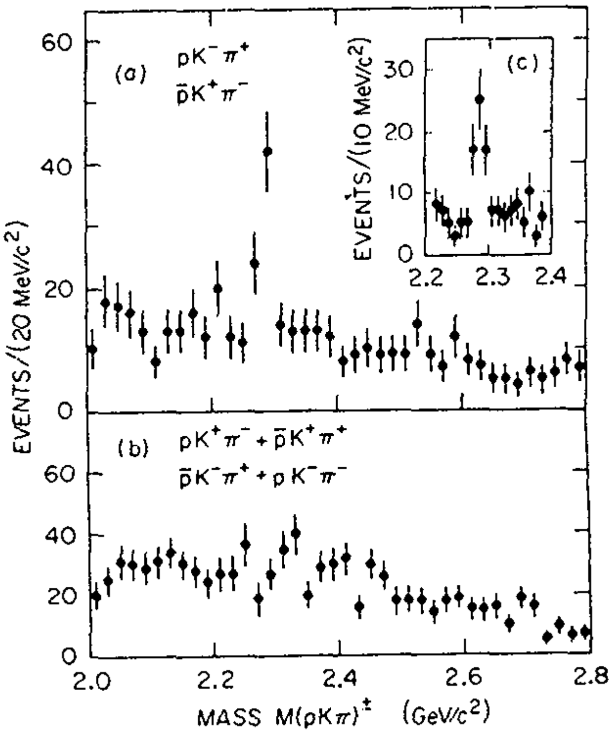

A photoproduction experiment at CERN using the Omega spectrometer presented preliminary evidence for the F in the $\eta 3\pi$ and $\eta' 3\pi$ mass distribution[8.11].

8.3 Charmed Baryons

In Fig. 8.7 cross section data on inclusive $p,\bar{p}$ and $\Lambda,\bar{\Lambda}$ production relative to $\sigma_{\mu\mu}$,

$$R_{p,\bar{p}} = \frac{\sigma(e^+e^- \to p(\bar{p})X)}{\sigma_{\mu\mu}}, \quad R_{\Lambda,\bar{\Lambda}} = \frac{\sigma(e^+e^- \to \Lambda(\bar{\Lambda})X)}{\sigma_{\mu\mu}}$$

are shown[8.3]. Both R parameters are consistent with constancy up to 4.5 GeV followed by a rise up to 5.5 GeV and by constancy at higher energies. The rise coincides with the threshold for the lowest charmed baryon seen first in νN and γN scattering[8.12,8.13], the Λ_c with a mass of 2.26 GeV. In e^+e^- the Λ_c was seen in the $pK^-\pi^+$ system and its charged conjugate state (see Fig. 8.8). The mass was found to be 2.285 ±0.002 GeV which is approximately 20 MeV higher than the mass value quoted by most of the other experiments[8.14]. Averaged over all data between 4.5 and 6.0 GeV a cross section of

$$\sigma(e^+e^- \to \Lambda_c^+ X) = 0.8 \pm 0.2 \text{ nb}$$

was obtained. The branching ratio $B(\Lambda_c^+ \to pK^-\pi^+)$ was estimated to be (2.0 ± 0.8) %.

9. The Υ Family

The observation of the Υ gave the impression of a déjà vu phenomenon in more than one respect. It was discovered by a Columbia-FNAL-Stony Brook Collaboration[9.1] studying the $\mu^+\mu^-$ mass spectrum produced via

$$400 \text{ GeV } p + N \to \mu^+ \mu^- + X$$

where Be, Cu and Pt were used as targets. Fig. 9.1 shows the latest data from this experiment[9.1]. Plotted is the $\mu^+\mu^-$ mass spectrum in terms of the differential cross section

$$B \left. \frac{d^2\sigma}{dm\,dy} \right|_{y=0}$$

per nucleon with $m = \mu^+\mu^-$ mass, y = c.m. rapidity of the $\mu^+\mu^-$ system, and B = branching ratio for the $\mu^+\mu^-$ channel. A broad enhancement is seen around 9.5 GeV riding on a falling background. No other structure is observed between 6 and 13 GeV. The background subtracted signal is plotted in Fig. 9.2. One observes a 500 MeV wide (FWHM) peak around 9.4 GeV followed by a second bump near 10 GeV. The r.m.s. mass resolution in this experiment was roughly 500 MeV.

The authors have fitted the mass spectra to a two peak and a three peak hypothesis. The latter was found to produce a lower chi square per degree of freedom. In both cases the resonances were assumed to be narrow which implies that the mass shapes are determined by the experimental resolution. The results from these fits are listed in Table 9.1.

Meanwhile further experiments have observed the Υ in hadron initiated reactions. (see Ref. 9.1).   1.

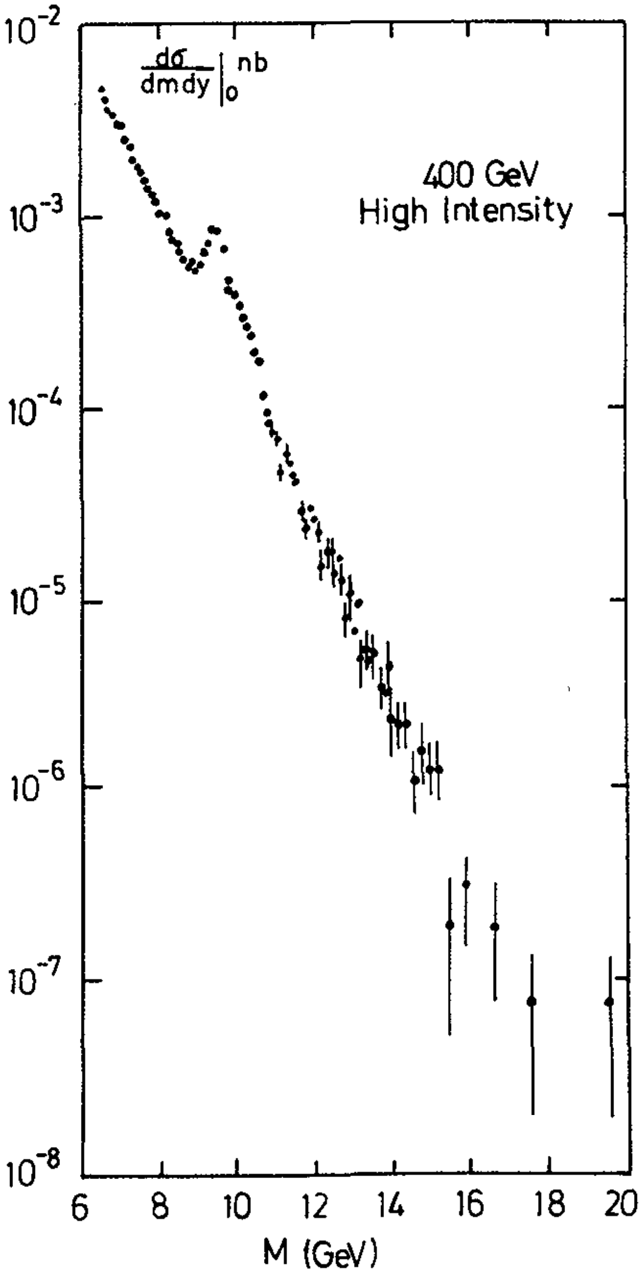

Fig. 9.1 Dimuon production at 400 GeV via $pN \to \mu^+\mu^- X$ as measured by the Columbia-FNAL-Stony Brook Collaboration (Ref. 9.1). Plotted is the cross section $d\sigma/(dm\,dy)$ at $y = 0$ as a function of the dimuon mass m.

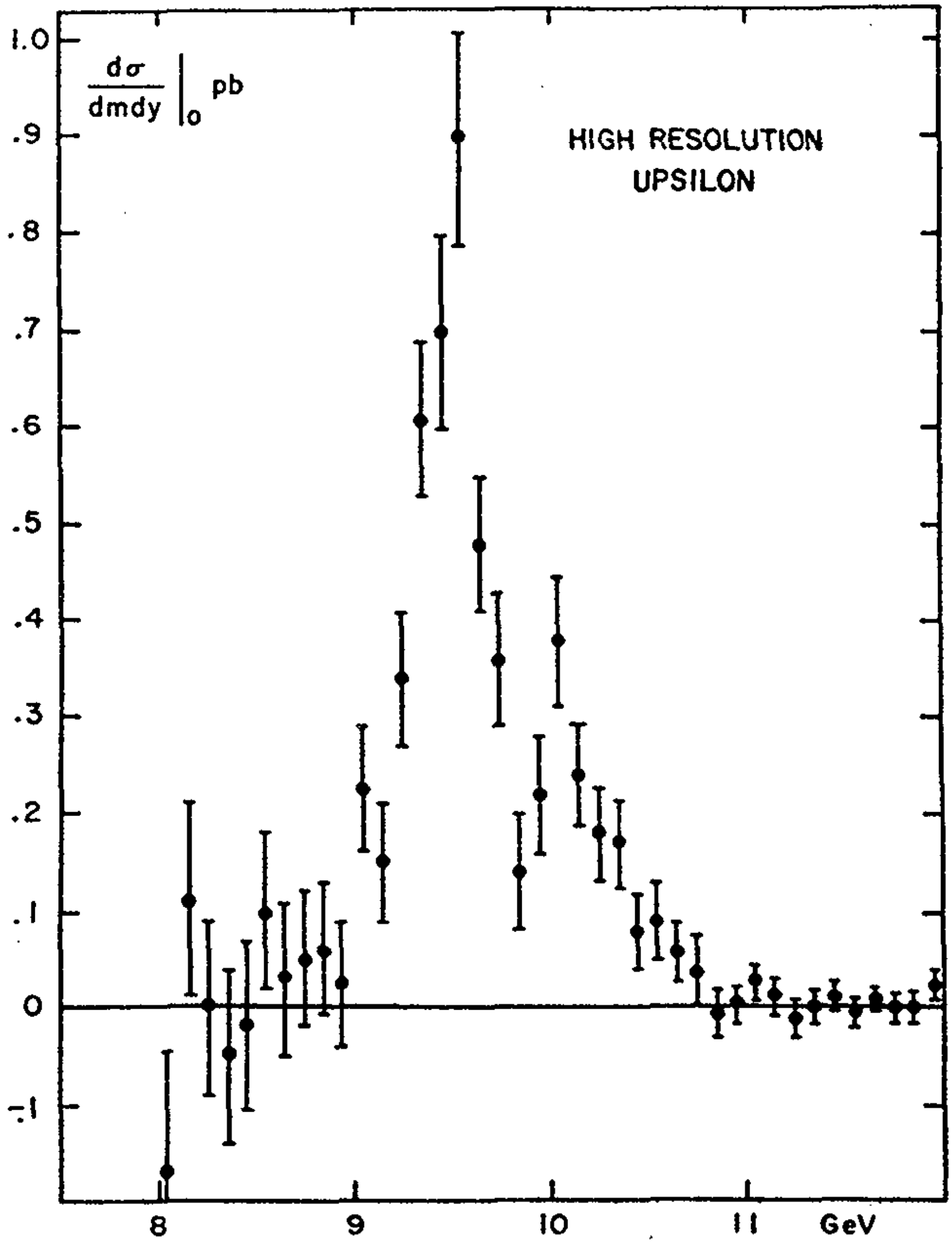

Fig. 9.2 Dimuon production via pN → $\mu^+\mu^-X$ as measured by the Columbia-FNAL-Stony Brook Collaboration (Ref. 9.1). Plotted is the dimuon mass spectrum obtained after subtracting a smooth background.

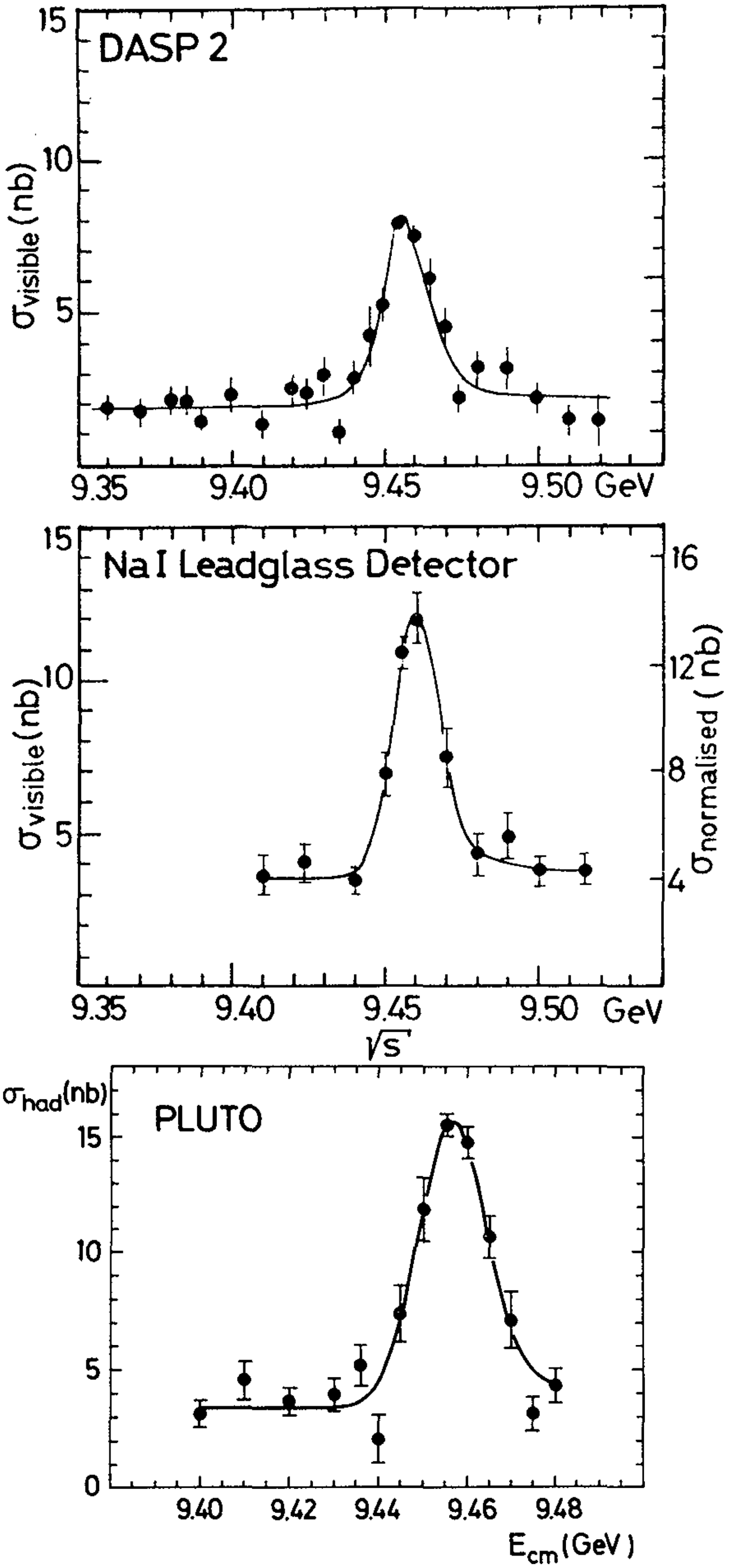

Fig. 9.3 The total cross section for hadron production in the T region. The top two measurements by DASP2 (Ref.9.3) and DESY-Hamburg-Heidelberg-Munich (Ref.9.4) give visible cross sections, the bottom measurement by the PLUTC group (Ref.9.2) shows the corrected cross section.

Table 9.1 Resonance fits to the background subtracted $\mu^+\mu^-$ mass spectrum (ref. 9.1)

		2 peaks	3 peaks	
Υ	M	9.41 ±0.013	9.40 ±0.013	GeV
	$B \left.\frac{d\sigma}{dy}\right\|_{y=0}$	0.18 ±0.01	0.18 ±0.01	pb
Υ'	M	10.06 ±0.03	10.01 ±0.04	GeV
	$B \left.\frac{d\sigma}{dy}\right\|_{y=0}$	0.069 ±0.006	0.065 ±0.007	pb
Υ''	M		10.40 ±0.12	GeV
	$B \left.\frac{d\sigma}{dy}\right\|_{y=0}$		0.011 ±0.007	pb

From the experience with the J/ψ it seemed natural to associate the Υ with a new heavy quark b. An important piece of information was missing, however, the widths of the Υ states. Are those states indeed narrow like the $J/\psi, \psi'$? This question can best be studied by producing the in an e^+e^- storage ring. DORIS, which at the time could reach a total c.m. energy of 2 x 4.3 = 8.6 GeV, was converted to a single ring machine in the fall of 1977 and subsequently upgraded to 2 x 5 = 10 GeV.

The efforts of the DORIS machine crew led to the observation of the Υ by the PLUTO$^{9.2)}$ and the DASP2 groups$^{9.3)}$ in June of 1978. In a subsequent running period at DORIS the Υ was also seen by a DESY-Hamburg-Heidelberg-Munich collaboration$^{9.4)}$. Fig. 9.3 shows the total cross section as measured by these experiments near the Υ mass region. Only the PLUTO data are corrected for acceptance. The Υ shows up as a narrow (<10 MeV wide) signal at 9.46 GeV. As in the case of the J/ψ and ψ' the observed width ($\sigma = 7.8 \pm 0.9$ MeV) is determined by the energy spread of the beams which for m = 9.5 GeV was calculated to give an r.m.s. resolution of σ_m = 8 MeV.

Integration of the resonance signal relates the hadronic cross section to the total, the hadronic and the leptonic widths Γ_{tot}, Γ_{had} and Γ_{ee}:

$$\frac{M^2}{6\,\pi^2} \int \sigma_{had}\, dm = \frac{\Gamma_{ee}\,\Gamma_{had}}{\Gamma_{tot}}$$

For Γ_{tot} we can write

$$\Gamma_{tot} = \Gamma_{had} + \Gamma_{ee} + \Gamma_{\mu\mu} + \Gamma_{\tau\tau} = \Gamma_{had} + 3\,\Gamma_{ee}$$

where e, μ, τ universality was assumed. In order to determine Γ_{had} and Γ_{ee} separately a measurement of a leptonic decay mode, say $\Upsilon \to \mu^+ \mu^-$, is required. This yields

$$\frac{M^2}{6\,\pi^2}\int \sigma_{\mu\mu}\,dm = \frac{\Gamma^2_{ee}}{\Gamma_{tot}} .$$

In addition to the observation of the Υ in the hadronic final states a first attempt was made to measure $B_{\mu\mu} \equiv \Gamma_{\mu\mu}/\Gamma_{tot}$ [9.5-9.7] and to deduce Γ_{ee} and Γ_{tot}. The mass and widths parameters as obtained by the three experiments are listed in table 9.2.

Table 9.2 Mass and widths parameters of the Υ as measured at DORIS

		PLUTO[9.5]	DASP2[9.6]	D-H-HD-M[9.7]
M_γ	(GeV)	9.46 ±0.01	9.46 ±0.01	9.46 ±0.01
Γ_{ee}	(keV)	1.33 ±0.14	1.5 ±0.4	1.1 ±0.3
$B_{\mu\mu}$	(%)	2.2 ±2.0	2.5 ±2.1	$1.0\ ^{+3.4}_{-1.0}$
Γ_{tot}	(keV)	>23 (2 s.d.)	>20 (2 s.d.)	>15 (2 s.d.)

The mean values are[9.8]:

M_Υ = 9.46 ±0.01 GeV
(The error reflects the 1 o/oo uncertainty in the energy calibration of DORIS)

Γ_{ee} = 1.3 ±0.2 keV

$B_{\mu\mu}$ = 2.6 ±1.4 %

Γ_{tot} > 25 keV (95 % C.L.); < 18 MeV; best value = 50 keV

The DASP2[9.6] and DESY-Hamburg-Heidelberg-Munich[9.4] collaboration also searched for the Υ'. The visible cross sections measured by these experiment around 10 GeV are displayed in Fig. 9.4. Both experiments

Table 9.3 Mass and width parameters of the Υ' as measured at DORIS

		DASP2[9.6]	D-H-HD-M[9.4]
$M_{\Upsilon'}$	(GeV)	10.012 ± 0.01	10.02 ± 0.02
$M_{\Upsilon'} - M_\Upsilon$	(MeV)	555 ±11	560 ±10
Γ_{ee}	(keV)	0.35 ± 0.14	0.32 ± 0.13
$\Gamma_{ee}(\Upsilon)/\Gamma_{ee}(\Upsilon')$		≈ 3	3.3 ± 0.9

Charge of the new quark:

In the nonrelativistic quark model the leptonic decay width for the vector states is directly proportional to the quark charge, Q:

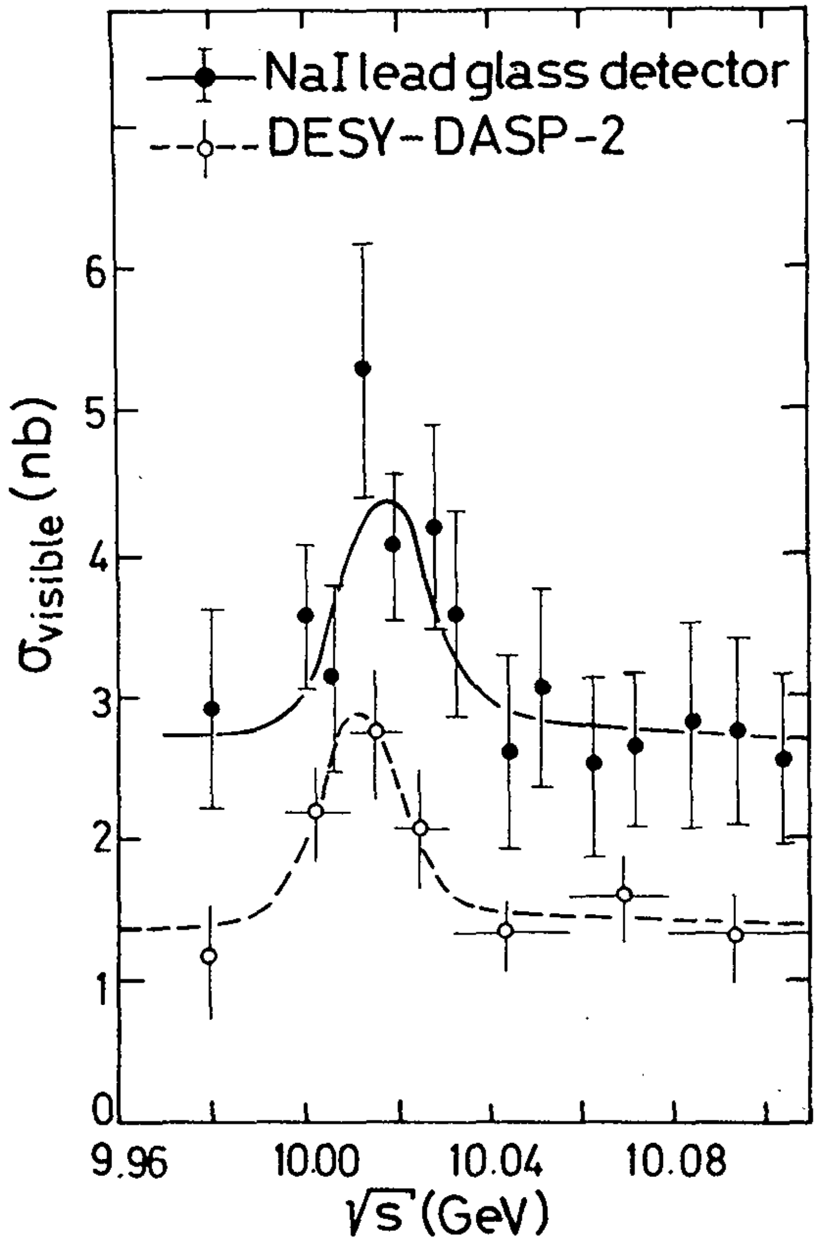

Fig. 9.4 Evidence for the Υ' as measured by the DASP2 (Ref. 9.6) and DESY-Hamburg-Heidelberg-Munich group (Ref. 9.4)

$$\Gamma_{vee} = \frac{16\ \pi\ \alpha^2\ Q^2}{M^2} \left| {}^3S_1(0) \right|^2 \qquad (9.1)$$

It is an empirical fact that the leptonic decay width divided by the average quark charge is approximately the same for all vector ground states, viz. ρ, ω, Φ and J/ψ: $\Gamma_{vee}/\sum|c_i\ Q_i|^2 \approx 11$. This is shown by Fig. 9.5. This rule applied to the Υ yields Q = 0.34 ±0.04 or Q = 1/3.

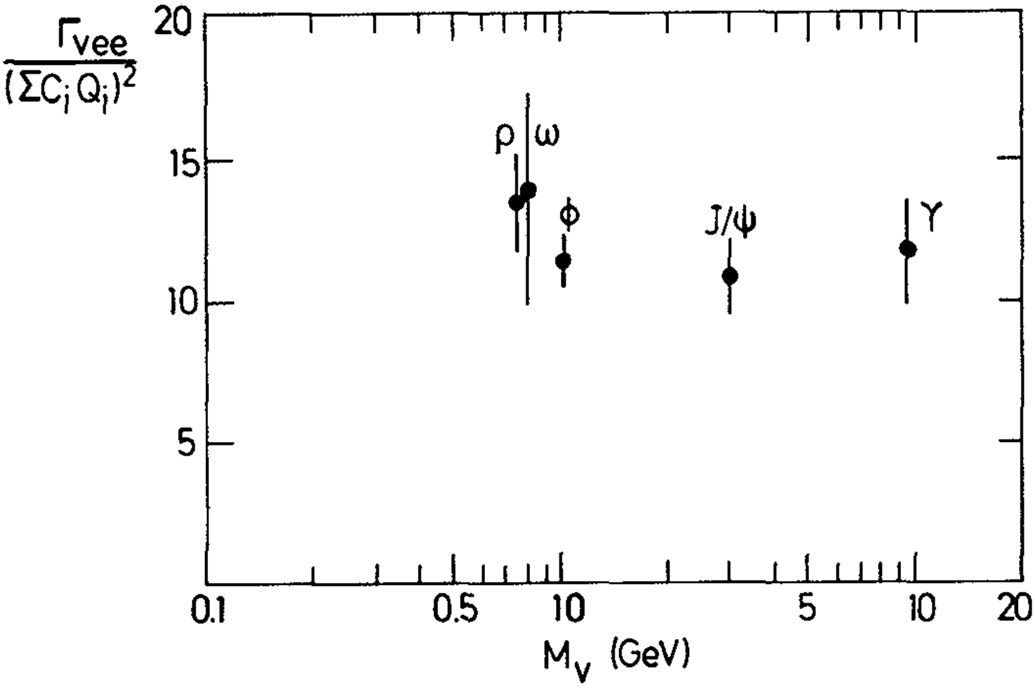

Fig. 9.5 The leptonic decay widths of vector mesons divided by the square of the average quark charge plotted as a function of the vector meson mass

The leptonic width depends on the wave function which is a function of the quark potential. In QCD the quark potential is flavour independent. Therefore the same potential which describes the J/ψ should also be applicable to the Υ provided that effects due to the difference in mass can be neglected. Their influence on the extraction of the quark charge can be reduced by comparing the leptonic widths of Υ and Υ' in relation to those of J/ψ and ψ'.

The theoretical prediction$^{9.9)}$ for Γ(Υ → ee) and Γ(Υ' → ee) is shown in Fig. 9.6. The solid lines indicate the lower limits for Q = 1/3, the dashed lines for Q = 2/3. The shaded region indicates the most propable values for the leptonic widths if Q = 1/3. They were determined from

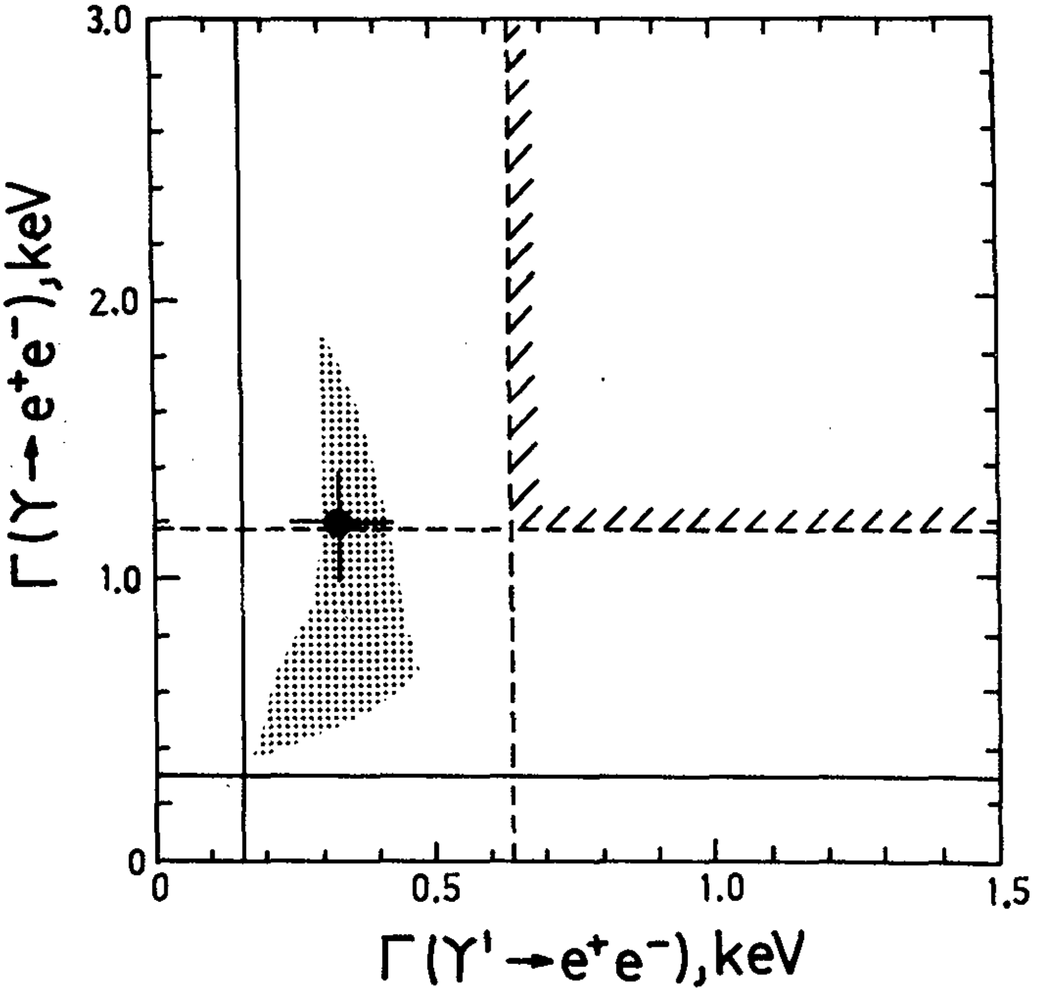

Fig. 9.6 Predictions of the quarkonium model for $\Gamma(\Upsilon \to ee)$ and $\Gamma(\Upsilon' \to ee)$ as computed by Quigg and Rosner (ref. 9.9). The solid lines show the lower limits for charge Q = 1/3 of the b quark, the dashed lines for charge Q = 2/3. The hatched area shows the most likely region for Q = 1/3. The data point indicates the average value of the DORIS experiments.

twenty different potentials which reproduce Γ_{ee} for J/ψ and ψ'. The cross shows the position of the average value measured by the DORIS experiments. The data disagree with the Q = 2/3 prediction but are consistent with Q = 1/3. The experiments do not fix the sign of the charge. The comparison with the d and s quarks suggests Q = −1/3, however. It has become customary to name the new quark b for bottom (or beauty).

The Υ-Υ' mass difference:

Despite the large difference in mass between J/Ψ and Υ the Υ-Υ' mass difference is almost the same as between J/Ψ and Ψ'. In a nonrelativistic quark model the mass difference depends on the type of the potential. If Υ and Υ' are assigned to the 1^3S_1 and 2^3S_1 states of the $b\bar{b}$ system, respectively, the model predicts the mass difference shown in table 9.4.

Table 9.4 The Υ-Υ' mass difference in the nonrelativistic quark model

m_Q = mass of quark

a) Experiment:

$m(\psi' - J/\psi) = 591 \pm 1$ MeV

$m(\Upsilon' - \Upsilon) = 558 \pm 10$ MeV

b) Theory:

type of potential	$\Delta m(2^3S_1 - 1^3S_1)$	$\Delta m(\Upsilon' - \Upsilon)^*$
coulomb	$\sim m_Q$	1800 MeV
linear	$\sim m_Q^{-1/3}$	400 MeV
logarithmic	const.	591 MeV

* computed from $\Delta m(\psi' - J/\psi)$

A pure logarithmic potential which predicts $\Delta m(\Upsilon' - \Upsilon)$ and $\Delta m(\psi' - J/\psi)$ to be the same is at variance with experiment while a superposition of a coulomb and a linear term could give the correct description.

Fig. 9.7 shows the potential

$$V = -\frac{4}{3}\frac{\alpha_s}{r} + a\,r$$

for $\alpha_s = 0.2$ and 0.4, and $a = 0.25$ GeV as a function of the radius. Indicated are also the compton wave lengths of the pion, the charm quark and the b quark. It seems reasonable to expect the $b\bar{b}$ spectroscopy to be slightly more Coulomb-like than the $c\bar{c}$ spectroscopy.

Υ final states:

Apart from the μ pair decay no other exclusive decay channel of the Υ has yet been identified. The analysis of the overall features of the hadronic final states, however, produced very interesting results. Maybe the most remarkable is the difference in jet formation on and off the Υ. These results will be discussed in section 10.

The average number of charged particles resulting from direct Υ decays is larger by roughly one unit than the charge multiplicity observed at nearby energies.

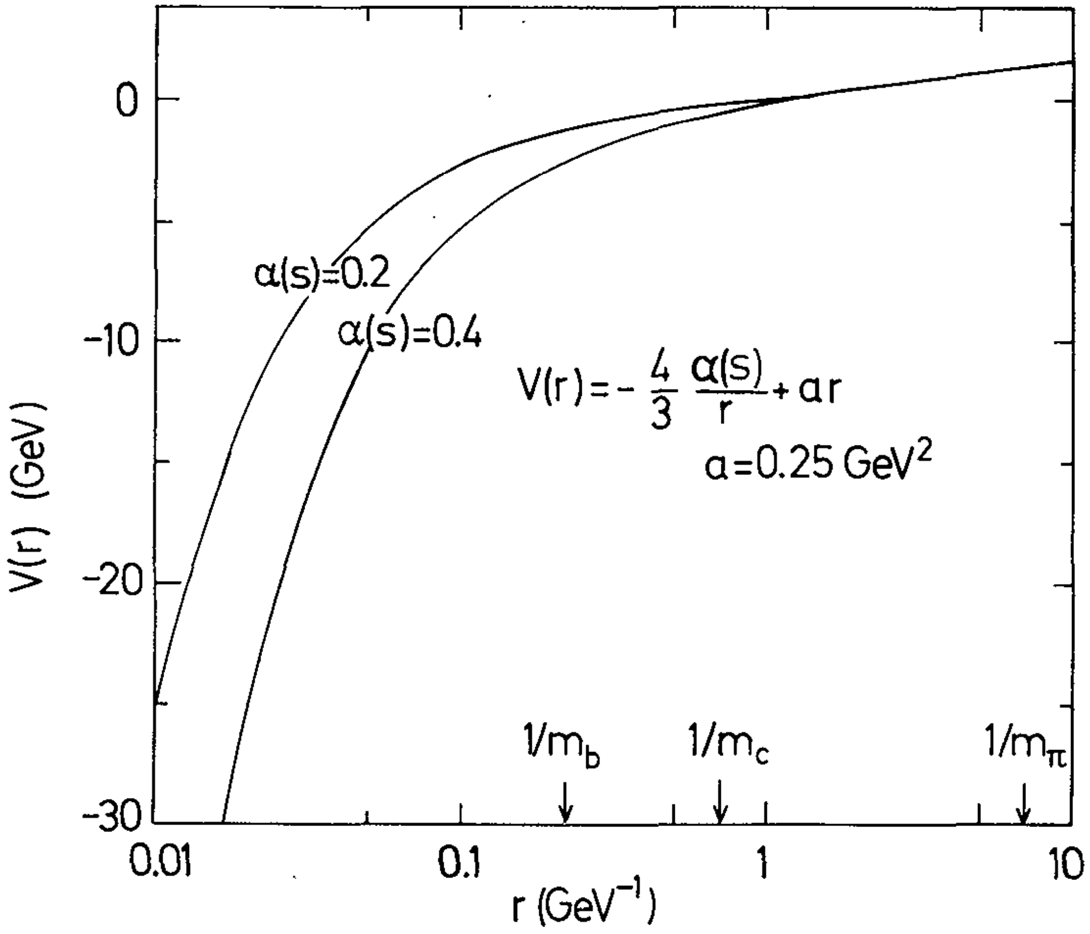

Fig. 9.7 The radius dependence of the quarkonium potential

Table 9.5 Average charged particle multiplicities at the Υ on and off resonance. The values quoted are raw numbers and have not been corrected for acceptance.

	DASP2[9.6)]	D-H-HD-M[9.4)]	PLUTO[9.8)]
$\langle n_{ch}\rangle$ off resonance	5.2 ±0.1	6.4 ±0.2	4.9 ±0.1
$\langle n_{ch}\rangle$ on resonance	5.7 ±0.1	6.9 ±0.2	5.4 ±0.1
$\langle n_{ch}\rangle$ direct decay	6.2 ±0.1	7.3 ±0.2	5.9 ±0.1

The PLUTO group has determined the cross section for inclusive K_S^o production. The ratio

$$\frac{\sigma_{on}\,(K_S^o)}{\sigma_{off}(K_S^o)} = 4.0 \pm 1.7$$

should be compared to the ratio of the total cross section

$$\frac{\sigma^{tot}_{on}}{\sigma^{tot}_{off}} \simeq 2.5.$$

In both cases an average was taken over the resonance region. No significant change is seen in K^o production on and off the resonance.

A similar conclusion was drawn by the DASP2 group from a measurement[9.6] of inclusive charged hadron production. The data are shown in terms of $\frac{s}{\beta}\frac{d\sigma}{dx}$ in Fig. 9.8. Within the large errors the same yield is found for $K^{\pm}$ and $\bar{p}$ relative to $\pi^{\pm}$ production.

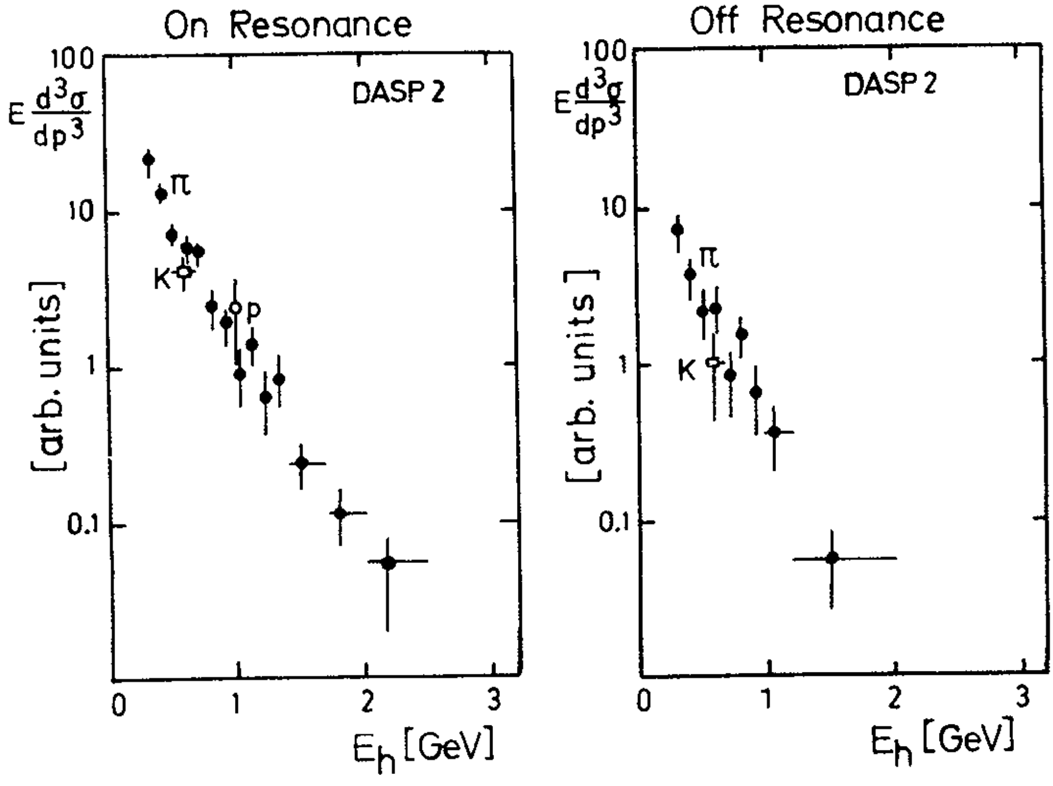

Fig. 9.8 The invariant cross section $E\frac{d^3\sigma}{dp^3}$ for the sum of $(\pi^+ + \pi^-)$, $(K^+ + K^-)$ and $2 \cdot \bar{p}$ production on and off the Υ resonance (ref. 9.6).

10. Jet Studies in the Υ Region

This section deals with the recent jet studies performed by three DORIS experiments for c.m. energies up to 10 GeV. Jet analyses off and on the Υ resonance are of great importance: they may provide a decisive test on QCD. In lowest order QCD the direct hadronic decays of the Υ proceed via a three gluon intermediate state. As a consequence we expect the hadrons to emerge in three rather than two jets (as in nonresonant $q\bar{q}$ formation). The expected properties of the three gluon jets have been widely discussed in recent papers[10.1-10.3]. We mention briefly some of the salient features[10.2].

Consider a $Q\bar{Q}$ system of mass $M_{Q\bar{Q}}$ which decays into three gluons of energies E_i. Define the scaled energies

$$\xi_i = 2\, E_i/M_{QQ} \tag{10.1}$$

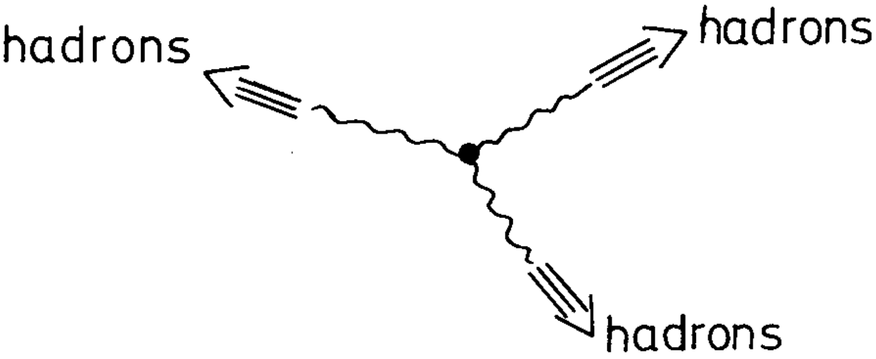

The energy distribution of the gluons is the same as for photons from orthopositronium decay:

$$\frac{1}{\sigma}\,\frac{d^2\sigma}{d\xi_1\, d\xi_2} = \frac{1}{\pi^2 - 9}\left\{\frac{1-\xi_3}{\xi_1\cdot\xi_2} + \frac{1-\xi_2}{\xi_1\cdot\xi_3} + \frac{1-\xi_1}{\xi_2\cdot\xi_3}\right\} \tag{10.2}$$

By integrating over e.g. ξ_2 one finds the energy distribution of one gluon (one jet):

$$\frac{1}{\sigma}\,\frac{d\sigma}{d\xi} = \frac{2}{\pi^2 - 9}\, F(\xi) \tag{10.3}$$

$$F(\xi) = \frac{\xi(1-\xi)}{(2-\xi)^2} + \frac{2-\xi}{\xi} + 2\left\{\frac{1-\xi}{\xi^2} - \frac{(1-\xi)^2}{(2-\xi)^3}\right\}\ln(1-\xi)$$

The function $F(\xi)$ is shown in Fig. 10.1. The most probable configuration is one where two of the three gluons share basically all of the available energy. Of course, such a configuration will produce two jet events.

Most probable configuration

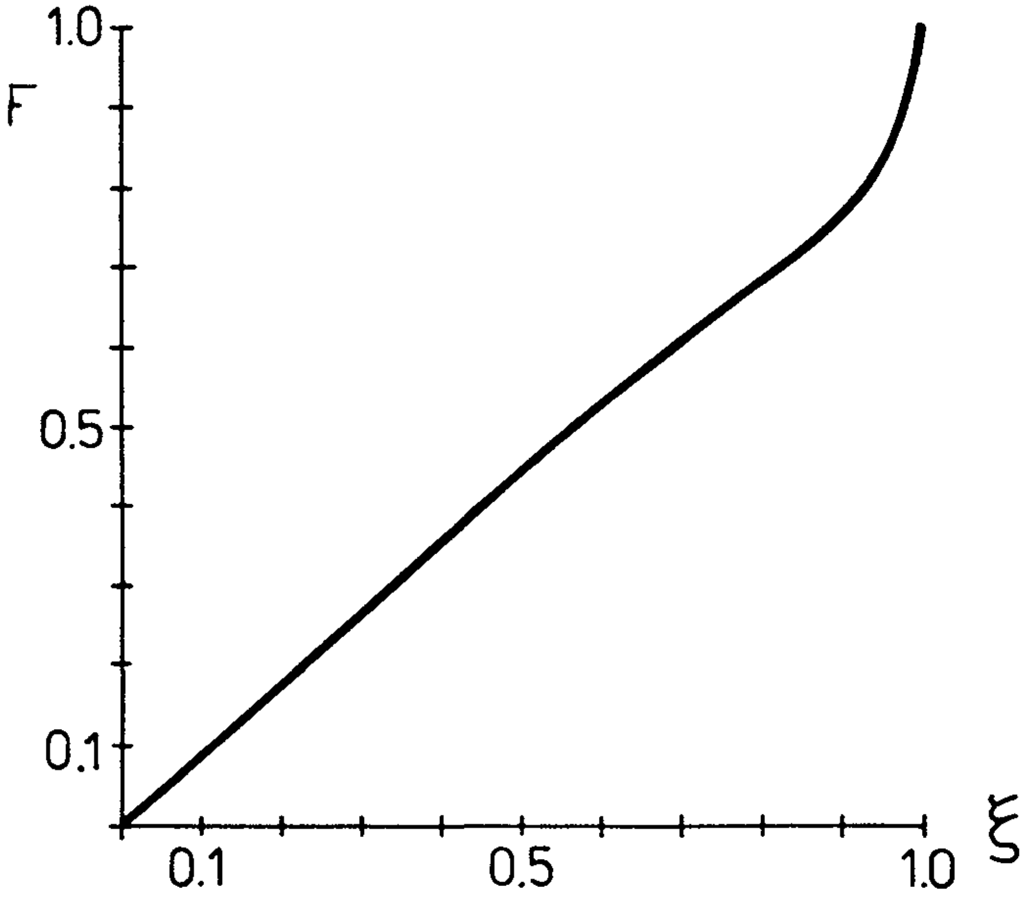

Fig. 10.1 Distribution of the gluon jet energy
(Fig. taken from ref. 10.2)

The geometrical structure of the three gluons can also be analized in terms of the angles θ and Φ between the gluons.

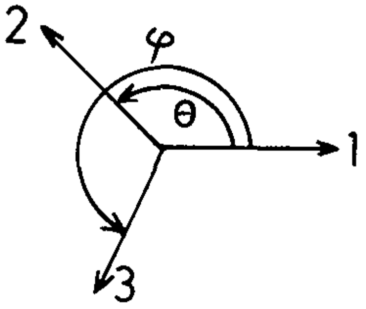

The scaled energies are related to θ and Φ in the following manner:

$$\xi_1 = \frac{2}{A}\sin(\theta - \phi)$$
$$\xi_2 = \frac{2}{A}\sin\phi \qquad (10.4)$$
$$\xi_3 = -\frac{2}{A}\sin\phi$$

where $A = \sin\phi - \sin\theta + \sin(\theta - \phi)$

We may ask for the probability of observing clean three-jet events. Theory predicts that in 38 % of the Υ gluonic decays the three gluons are emitted within ±20° of the symmetric three star directions.

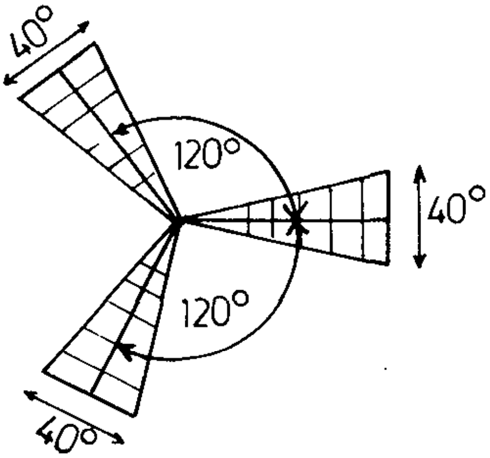

The orientation of the plane defined by the three gluons is a direct consequence of the vector nature of the gluons. If $\hat{n}$ denotes the normal to this plane and θ_n the angle between $\hat{n}$ and the incoming e^+ (or e^-) then

$$\frac{1}{\sigma}\,\frac{d\sigma}{d\cos\theta_n} = \frac{3}{16}\,(2 + \sin^2\theta_n) \tag{10.5}$$

Another test for the vector nature of gluons is provided by the angular distribution between one of the gluon and the incoming e^+. In the limit $\xi_i \to 1$

$$\frac{1}{\sigma}\,\frac{d\sigma}{d\cos\theta_i} \to \frac{3}{8}\,(1 + \cos^2\theta_i)\ . \tag{10.6}$$

According to present wisdom gluons do not become free but manifest themselves in hadron jets. For a detailed discussion of jet phenomena the reader is referred to the lectures by M. Jacob.

Various quantities have been devised to search for jets. Amongst them are sphericity and thrust[10.5]:

sphericity $$S = \frac{3\sum p_{\perp i}^2}{2\sum p_i^2} \qquad 0 \leq S \leq 1 \tag{10.7}$$

where the p_i are the particle momenta and $p_{\perp i}$ are the particle momenta transverse to the jet axis which is chosen such that $\sum p_{\perp i}^2$ is a minimum. Extreme jettiness yields S = 0.

thrust $$T = 2\,\frac{\tilde{\sum} p_{\parallel}^{i}}{\sum\limits_i |p_i|} \qquad \frac{1}{2} \leq T \leq 1 \tag{10.8}$$

$p_{\parallel}^{i}$ Longitudinal momentum of particle i.

where the summation $\tilde{\sum}$ is to be extended over all particles in one hemisphere; for practical applications the following definition of T was found to be better suited[10.6]:

$$T = \frac{\sum\limits_i |p_{\parallel}^{i}|}{\sum\limits_i |p_i|} \tag{10.8a}$$

For an event with no missing momentum the two definitions give the same result. In both cases the jet axis is chosen such that T is a maximum.

In contrast to sphericity for thrust the momenta are summed linearly. The advantage of T over S is that T is infrared insensitive and is therefore better suited for QCD calculations.

The PLUTO group[10.6] for their jet analysis selected events with four or more charged particles. The distributions presented below are the observed ones; no corrections were applied for acceptance, cuts or radiative effects. In comparing the observed distributions with theory a Monte-Carlo technique was used to impose the same acceptance criteria and cuts onto the theoretical events.

The mean sphericity <S> is plotted in Fig. 10.2 as a function of c.m. energy between 3 and 10 GeV. In agreement with the SLAC-LBL data[10.8)] <S> is seen to decrease with growing energy. The points measured at the J/ψ and ψ' are significantly higher than the value at 3.6 GeV. Perhaps most interesting is the rise in <S> seen directly above charm threshold at 4.03 GeV. The $c\bar{c}$ events do not show a jet structure.

At the ϒ the average sphericity is again larger than outside of the resonance at 9.4 GeV. The dashed band shows the expected <S> behaviour for phase space distributed events. At higher energies ($E_{cm} \gtrsim 6$ GeV) the observed sphericity values are well below the phase-space prediction. The point measured at 9.4 GeV is in reasonable agreement with the jet model calculated according to Field and Feynman[10.9)].

The analysis in terms of thrust leads to the same conclusions. Fig. 10.3 shows a plot of 1 - <T> versus E_{cm}.

We turn now to the PLUTO analysis of the ϒ events[10.7)]. Three processes can contribute to events in the ϒ region, the direct hadronic decay, the decay through the one-photon channel and the nonresonant continuum:

$$\sigma = \sigma_{dir} + \sigma_{1\gamma} + \sigma_{cont} \qquad (10.9)$$

For the continuum contribution the data at 9.4 GeV were used. Neglecting possible interference effects the one-photon part leads to the same final states as the continuum. The size of $\sigma_{1\gamma}$ relative to σ_{cont} can be computed from the rate of μ pairs observed on and off the ϒ:

$$\sigma_{1\gamma} = \frac{\sigma_{\mu\mu}^{on} - \sigma_{\mu\mu}^{off}}{\sigma_{\mu\mu}^{off}} \cdot \sigma_{cont} = (0.24 \pm 0.22)\ \sigma_{cont}$$

The total number of events available for the analysis were 1418 at the ϒ(9.45 - 9.47 GeV) and 420 in the continuum (9.30 - 9.44 GeV). The latter events were used to determine by proper subtraction the distributions for the direct decays of the ϒ.

Fig. 10.4a shows the average sphericity plotted versus E_{cm}. The <S> value of ϒ direct decays is markedly larger than for the continuum. The increase in <S> is not caused by the larger multiplicity. This is demonstrated by Fig. 10.4b where <S> is plotted for events with 4, 6 and 8 charged particles for 9.4 GeV and for the direct ϒ decays. The <S> values for the ϒ are significantly higher for every topology.

From the preceding discussion it is clear that the ϒ final states are less jet like than those of the continuum. They are incompatible with the two-jet model used to describe the continuum but also with pure phase space (see Fig. 10.4).

Analysing the event topologies the PLUTO group found that the data could best be described by the three-gluon model formulated by Koller and Walsh[10.1)]. In this model the gluon fragmentation into hadrons was assumed to be similar to that for quarks.

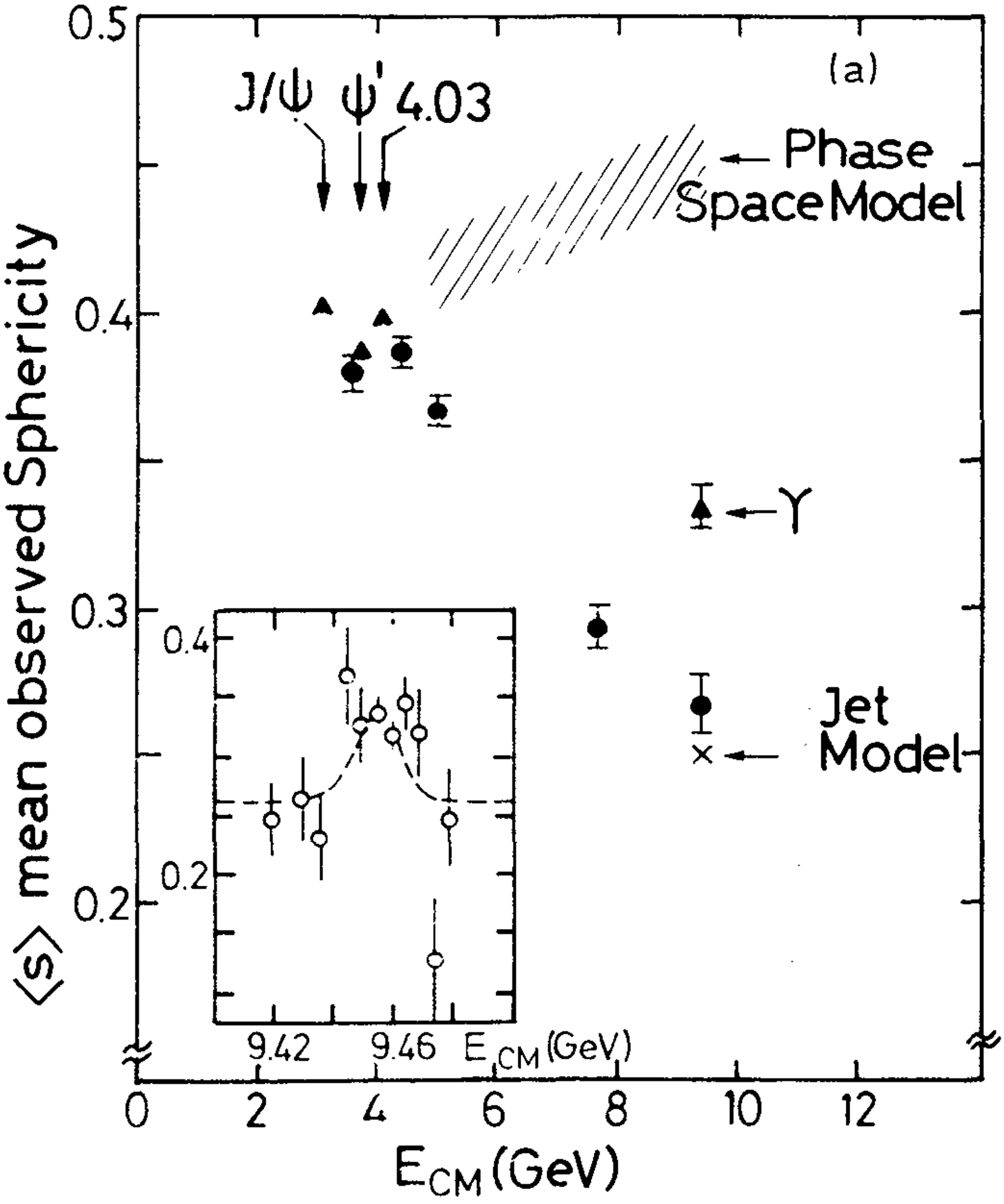

Fig. 10.2 Average observed sphericity as a function of energy (Ref. 10.6).

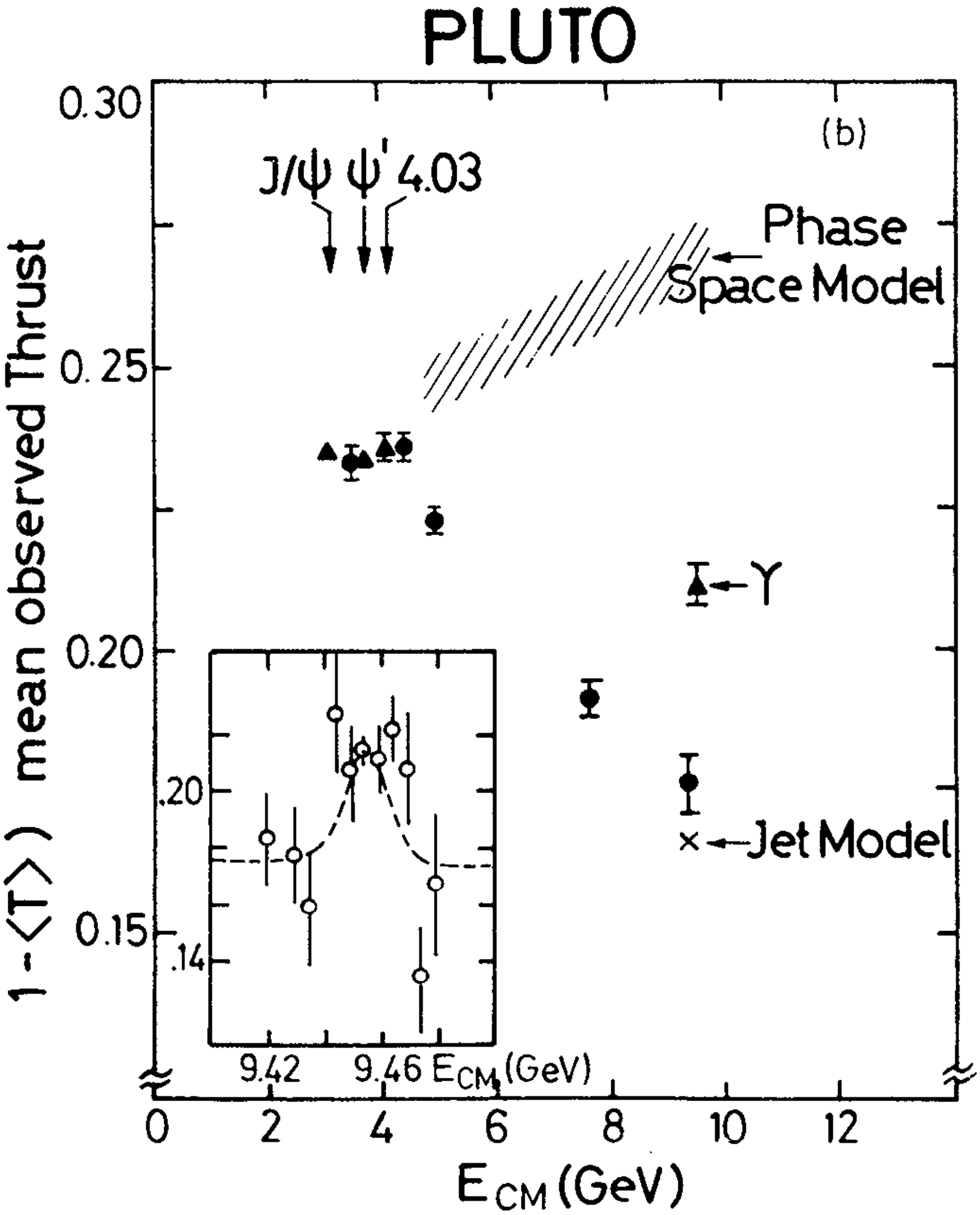

Fig. 10.3 The quantity 1 - <T> as a function of energy where <T> is the average observed thrust (ref. 10.6).

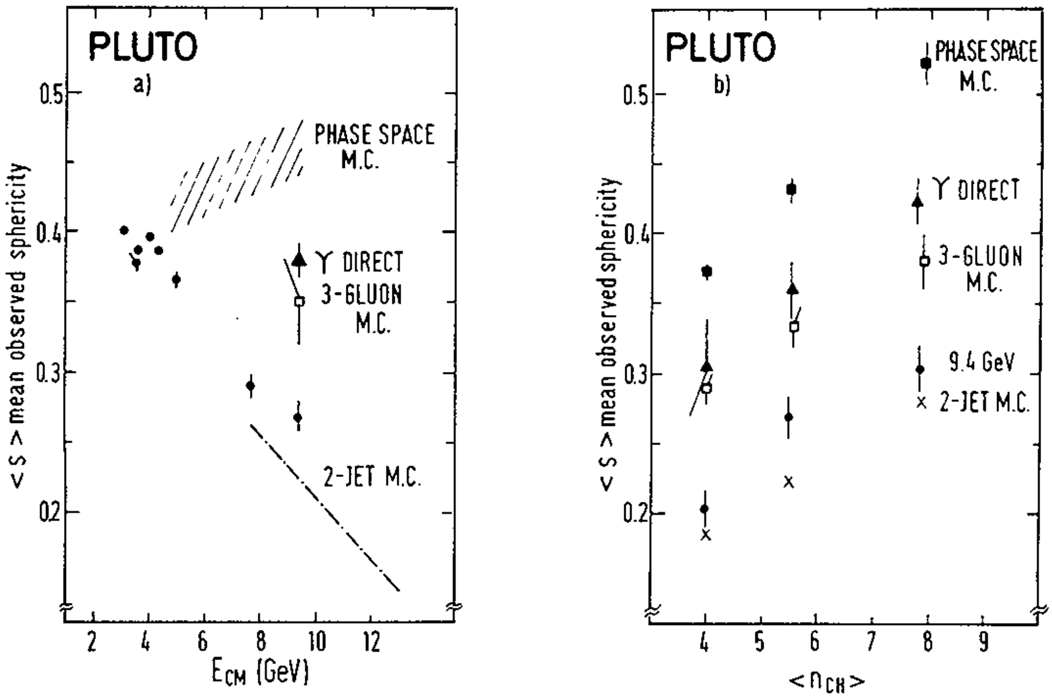

Fig. 10.4 (a) The average sphericity as a function of energy.

(b) The average sphericity for 9.4 GeV from Υ decay for events with different number of charged particles (ref. 10.7).

In order to search directly for the three jet structure the PLUTO group employed the triplicity analysis[10.10,10.11]. The triplicity is an extension of thrust and is defined as follows: Group the final state momentum vectors $\vec{p}_i$, $i = 1, \ldots, N$ into three nonempty classes C_1, C_2 and C_3 with the total momenta

$$\vec{p}(c_\ell) = \sum_{i \in C_\ell} \vec{p}_i ; \qquad \ell = 1, 2, 3 .$$

The triplicity, T_3, is then obtained by taking all possible permutations for the members of C_1, C_2 and C_3 and maximizing the sum of the moduli $|\vec{p}(C_\ell)|$ (see Fig. 10.5a).

$$T_3 = \underset{C_1, C_2, C_3}{\mathrm{Max}} \{ |\vec{p}(c_1)| + |\vec{p}(c_2)| + |\vec{p}(c_3)| \} / \sum_{i=1}^{N} |\vec{p}_i|$$

The limits for T_3 are $T_3 = 1$ for a perfect three-jet event and $T_3 = 3\sqrt{3}/8 = 0.65$ for a spherical event. Note, however, that a perfect two-jet event will also give $T_3 = 1$. The classes C_1, C_2, C_3 will be ordered such that $|\vec{p}(C_1)| \geq |\vec{p}(C_2)| \geq |\vec{p}(C_3)|$. The jet directions are given by the vectors $\hat{n}_\ell = \vec{p}(C_\ell)/|\vec{p}(C_\ell)|$ and the angles between the jets (see Fig. 10.5b) by:

$$\cos\theta_1^J = \hat{n}_2 \cdot \hat{n}_3 ; \quad \cos\theta_2^J = \hat{n}_3 \cdot \hat{n}_1 ; \quad \cos\theta_3^J = \hat{n}_1 \cdot \hat{n}_2$$

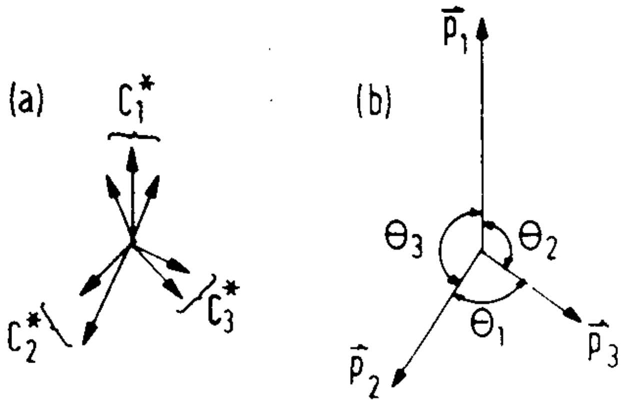

Fig. 10.5 Momentum configuration of hadrons (a) and jets (b) obtained by grouping hadrons into 3 classes.

Assuming the gluons to be massless the gluon energies can be computed from the angels:

$$E_\ell^J = W \sin\theta_L^J/(\sin\theta_1^J + \sin\theta_2^J + \sin\theta_3^J)$$

(Note: $W = \sqrt{s}$ = total c.m. energy)

The normalized energies are defined as

$$x_\ell^J = 2\, E_\ell^J/W .$$

Due to the ordering of the $\vec{p}(C_\ell)$, $x_1^J \geq x_2^J \geq x_3^J$.

The result of the analysis is summarized in Fig. 10.6 displaying for the direct Υ decays and off resonance the distributions of thrust T, triplicity T_3, smallest and largest jet energies and smallest and largest jet angles. The distributions were determined including charged particles as well as photons detected in the shower counters (which cover 94 % of 4 π).

In Fig. 10.6 the observed (i.e. uncorrected) distributions are shown. They were compared to the predictions of the two-jet model 10.9), of the phase space model and of the three-gluon model 10.1). In the model calculations the effects of the detector acceptance and of the experimental cuts were included. The off-resonance data are well represented by the two-jet model. For the direct decays of the Υ two-jet formation as well as phase space are ruled out as the dominant processes. The data agree well with the three-gluon decay model.

The alignment of the jet axes is sensitive to the spin of the gluon. Koller and Krasemann 10.12) for direct Υ decays analyzed the distribution of the angle θ between the thrust and the beam axes. Fig. 10.7

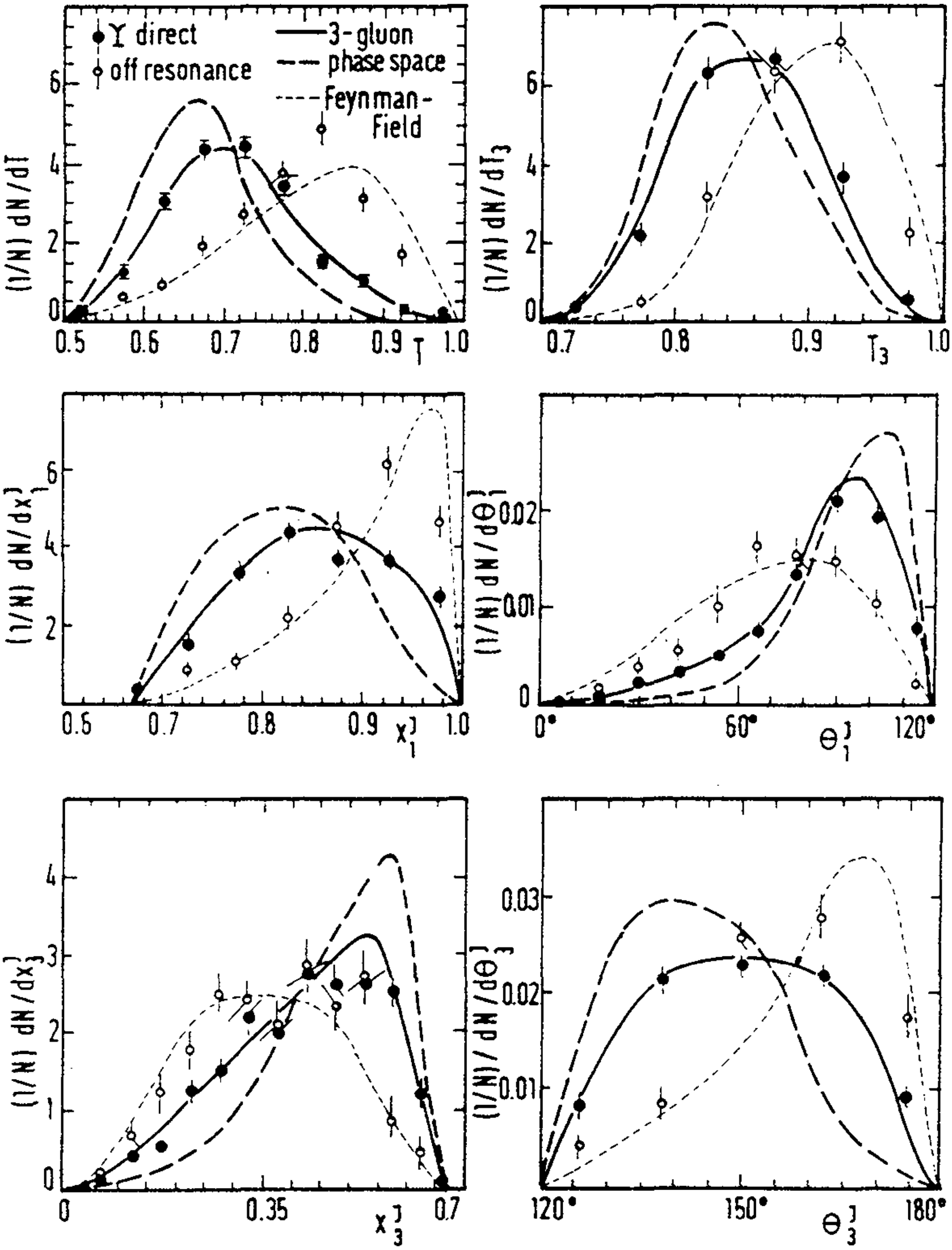

Fig. 10.6 Experimental distributions as measured by PLUTO$^{10.11)}$ of thrust T, triplicity T_3, reconstructed gluon energies x_1^J, x_3^J and reconstructed angles θ_1^J, θ_3^J between gluons compared to Monte-Carlo calculations based on various models (ref. 10.11).

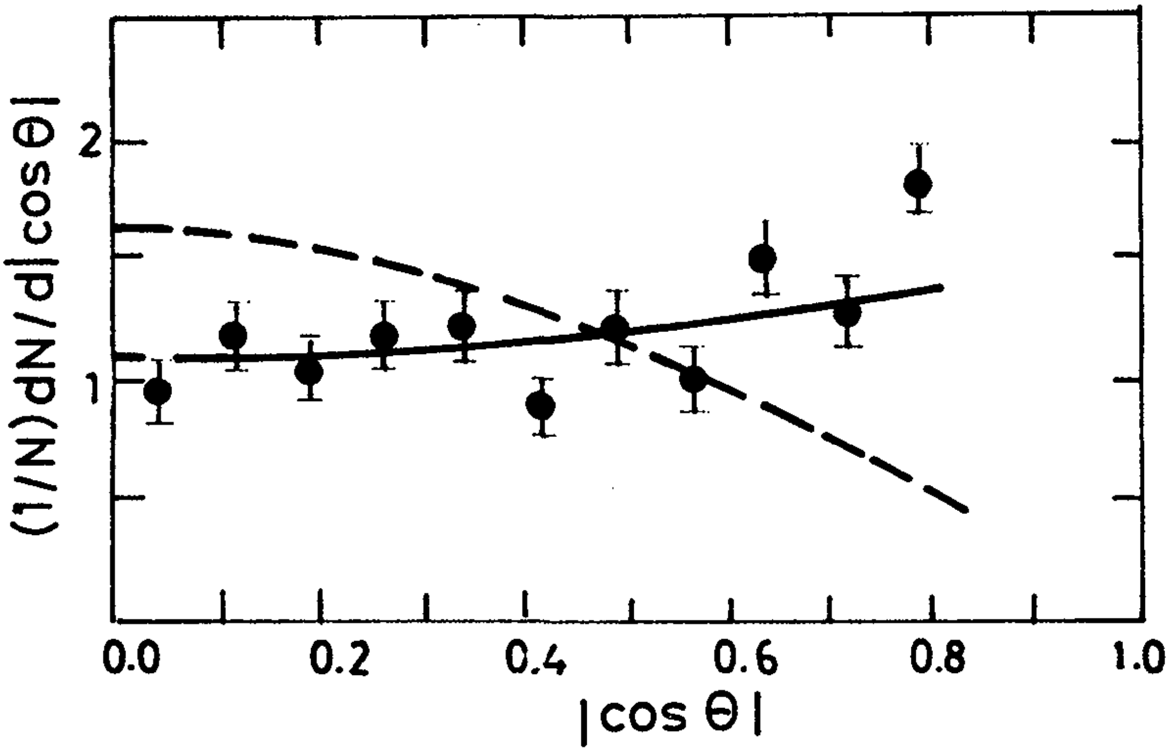

Fig. 10.7 The jet axis angular distribution as measured by PLUTO[10.12)]and the theoretical curves for scalar (dashed) and vector (solid) gluons (ref. 10.12).

shows the PLUTO data together with their predictions for scalar and vector gluons. The assumption of scalar gluons is excluded by the measurements while vector gluons match the data well. This constitutes an important verification of one of the basic assumptions of QCD, the vector nature of gluons.

The data presented in this section can be summarized as follows. The hadrons emitted in the direct decay of the Υ show a spatial structure which is different from that observed for final states off resonance: they are much less collimated. The observed features disagree with the two-jet picture but also with pure phase space. All aspects investigated so far are in accord with the assumption that the direct Υ decays proceed via a three-gluon intermediate state. This gives strong support to QCD.

11. High Energy e^+e^- Annihilation: Results from PETRA

With the commissioning of the new DESY storage ring PETRA the Q^2 range for e^+e^- physics has been extended by an order of magnitude:

	SPEAR/DORIS I	DORIS II	PETRA
Q^2_{max}	60 GeV^2	100 GeV^2	1000 GeV^2

The dominating feature of e^+e^- annihilation into hadrons at these high energies is the formation of two jets. This collimation of the final state particles in two narrow cones can now be seen directly from a visual inspection of the events. In addition to two-jet production a new process was found by the TASSO group which yields three jet events. All properties studied so far agree with the hypothesis that the three-jet events originate from hard gluon bremsstrahlung. To establish this new class of events it was essential that Q^2 values as high as 1000 GeV^2 could be reached.

11.1 The PETRA Storage Ring

PETRA (= Positron Elektron Ring Anlage) was gradually brought into operation in the second half of 1978 after a construction period of two and a half years. Fig. 11.1 shows a layout of the accelerator complex with the synchrotron (DESY) serving as injector and the small ring PIA as accumulator for positrons. Some of the PETRA parameters are listed in Table 11.1. There are four short and four long straight sections. Two of the long straight sections are used for the accelerating RF structures. The other six straight sections are available for experiments.

The number of RF cavities and therefore the maximum energy attainable was increased in steps. Until February 1979 four RF cavities were used providing a maximum total energy of W = 22 GeV. Physics data were taken at 13 and 17 GeV. In March 1979, the number of cavities was increased to 32 raising the maximum energy to 32 GeV. Physics was carried out at energies between 12 and 31.6 GeV. At the end of 1979, the number of cavities will be doubled allowing PETRA to reach energies as high as W = 38 GeV.

The maximum luminosity obtained at 30 GeV was $\sim 5 \times 10^{30} \mathrm{cm}^{-2} \mathrm{s}^{-1}$ with two positron and two electron bunches and ~12 mA current per beam. This luminosity value should be compared with the design value of $2.2 \cdot 10^{31} \mathrm{cm}^{-2} \mathrm{s}^{-1}$ for two bunches per beam and 15 m interaction region length. On the average, an integrated luminosity of 100 nb^{-1} was obtained per day at 30 GeV yielding roughly 25 hadronic annihilation events per day. Polarized beams were observed by the JADE group at W = 30 GeV with a degree of polarization of 85 ± 15 %.

Table 11.1
PETRA parameters

Maximum beam energy	19 GeV
Circumference	2.3 km
Magnetic bending radius	192 m
Number of interaction regions	6
Length of the short interaction region	15 m
RF frequency	500 MHz
Number of klystrons	8
Power per klystron	0.5 MW
Max. number of cavities	64

11.2 Experimental setups at PETRA

At present five experiments are installed or are being set up in the four short sections:

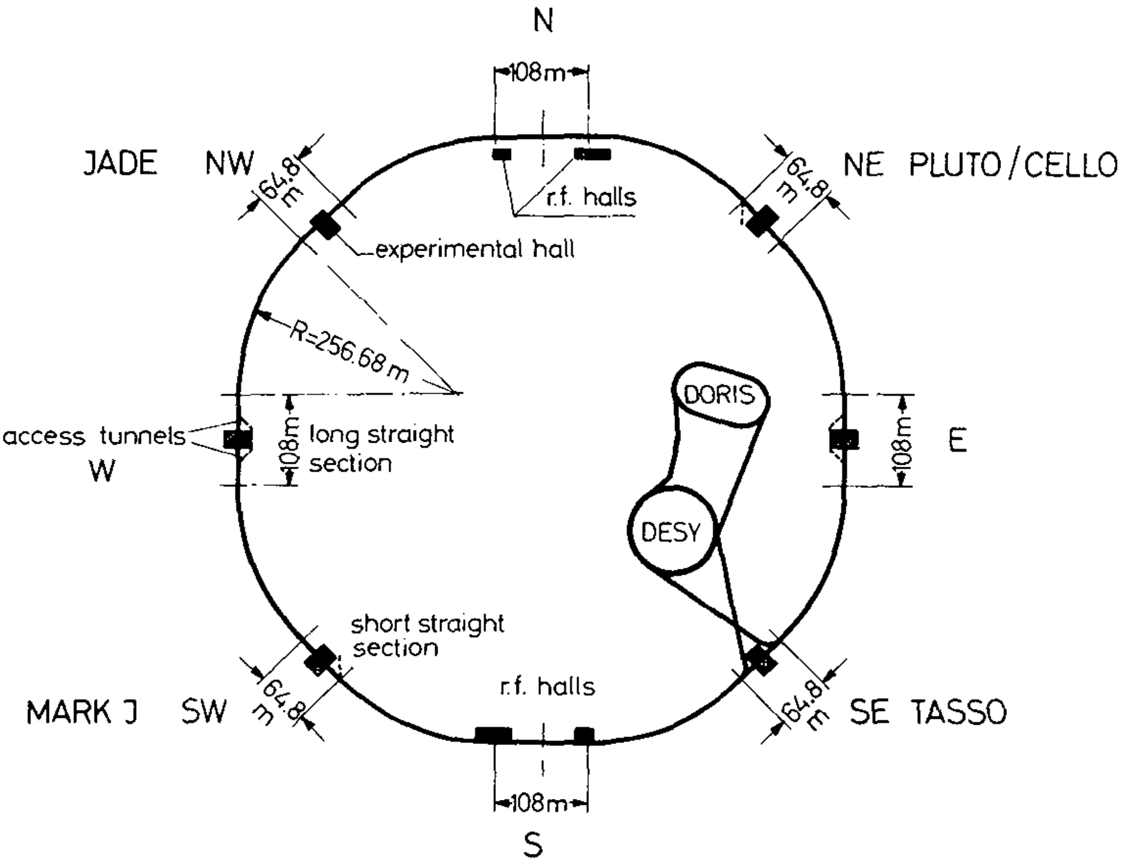

Fig. 11.1 Layout of the DESY accelerators

North - East:	PLUTO	(Aachen - Bergen - DESY - Hamburg - Maryland - Siegen - Wuppertal)
	CELLO	(DESY - Karlsruhe - München - Orsay - Saclay - Paris)
North - West:	JADE	(DESY - Hamburg - Heidelberg - Manchester - Lancaster - Rutherford - Tokyo)
South - West:	MARK J	(Aachen - DESY - MIT - Amsterdam - Peking)
South - East:	TASSO	(Aachen - Bonn - DESY - Hamburg - London - Oxford - Rutherford - Weizmann - Wisconsin)

Four of these experiments have taken data, JADE, MARK J, PLUTO and TASSO. Their setups will be described briefly.

JADE

Fig. 11.2 shows a sectional view of the JADE detector in a vertical plane containing the beam axis. A normally conducting aluminium coil of 7 cm thickness and 2 m diameter produces a uniform solenoidal field of maximum strength 0.5 Tesla over a length of 3.5 m. Inside the coil the passage of charged particles is recorded by a beam pipe hodoscope (24 counters) and a time of flight hodoscope (42 counters).

The trajectories of the charged particles are measured by a cylindrical drift chamber, called the "Jet chamber". 48 points are measured along each track in the polar angular range $|\cos\Theta| < 0.83$ and at least 8 points on a track are obtained over a solid angle of 97% of the full sphere. At each point, three coordinates, r, ϕ and z are given by the wire position, the drift time and the charge division measurements. dE/dx information, which is used for particle identification, is also obtained. The gas mixture of Argon-Methane-Isobutane is used under 4 times atmospheric pressure.

The magnet coil is surrounded by 30 rings of lead glass shower counters (Fig. 11.3) covering the angular range $|\cos\Theta| < 0.82$. Each ring contains 84 glass wedges (Schott SF5) with inner surfaces of 85 x 102 mm^2 and depths of 300 mm (12.5 X_0). These 2520 barrel shower counters, together with the 192 shower counters mounted inside the magnet on the two end caps of the yoke, cover 90% of the full solid angle and serve to detect and measure the energies of photons and electrons. The granularity of the shower counters allows a measurement of the photon emission angles to ± 2 degrees using the known interaction point.

The flux return yoke, including the end caps, forms a rectangular box surrounding the cylindrical part of the detector. It is utilized as one of the layers of the muon filter and is followed by three further layers consisting of iron loaded concrete. The total thickness of absorber amounts to at least 780 g/cm^2 (6 absorption lengths). It is interspersed with 5 layers of drift chambers which measure the trajectories of penetrating particles with a coverage of 92% of the full solid angle.

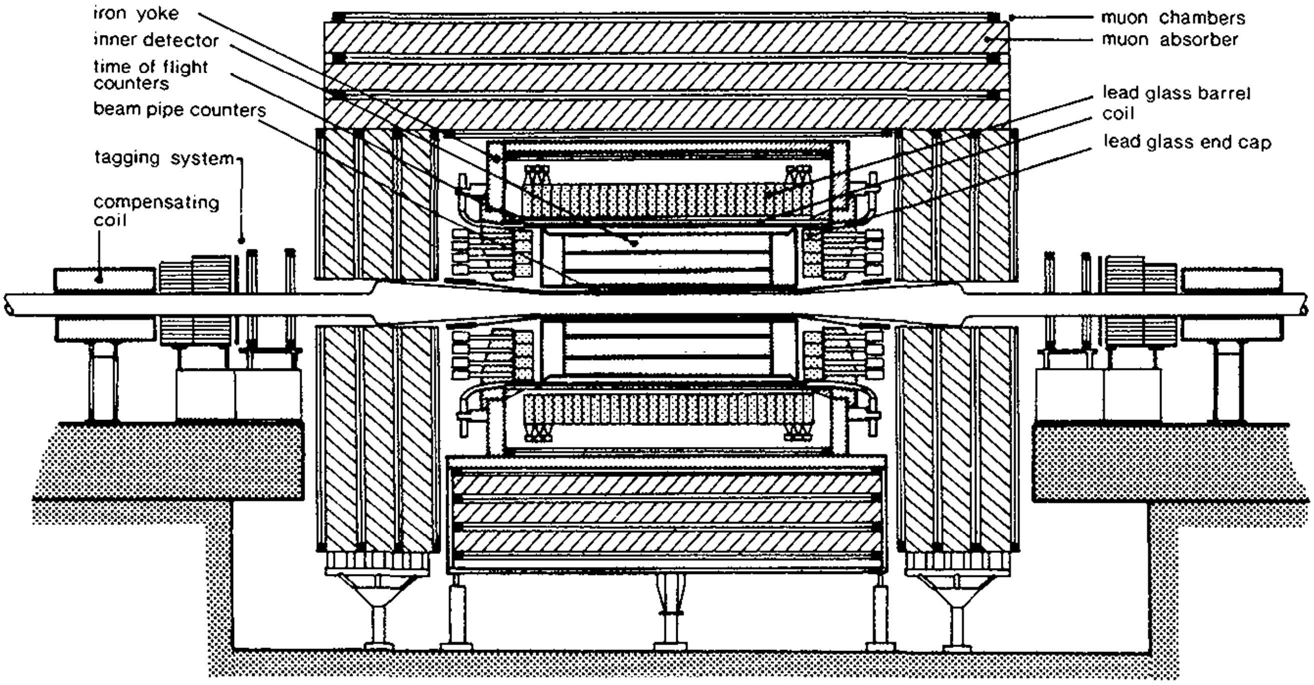

Fig. 11.2 A side view of the JADE detector.

Two small angle detectors, each consisting of an array of scintillation counters, drifts chambers and lead glass modules, record electrons and positrons close to the beam direction ($35 < \Theta < 75$ mrad). They provide an on-line measurement of the luminosity and tag the two-photon processes ($e^+e^- \rightarrow e^+e^- +$ hadrons).
In Fig. 11.3 a typical multihadron events detected by JADE is shown.

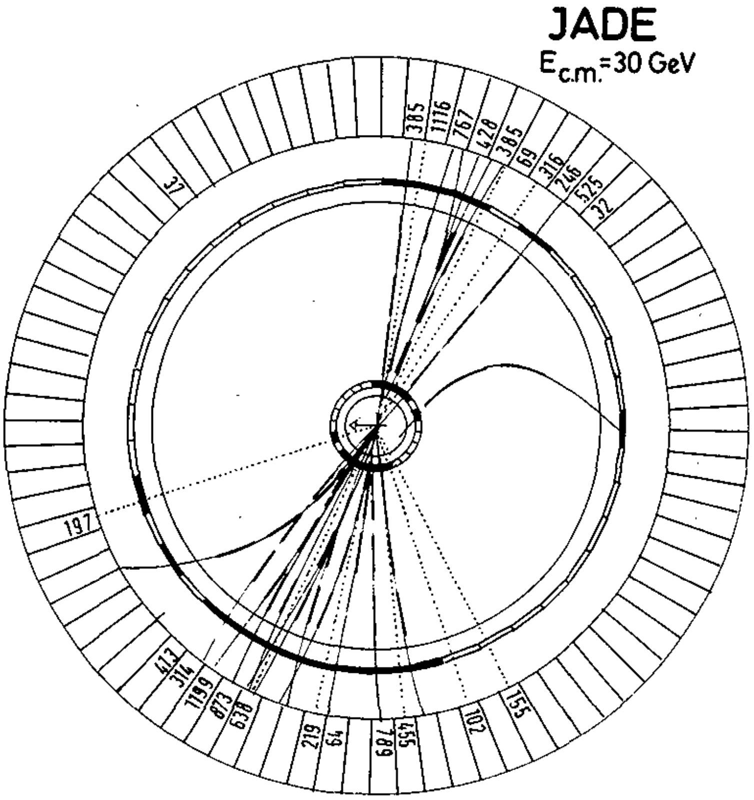

Fig. 11.3 A typical multihadron event detected in the central part of the JADE detector. Trajectories of charged and neutral particles are represented by full and dotted lines, respectively. The shower counters are also shown. The energy deposited in each row appears in MeV.

MARK J

The MARK J detector is of the calorimeter type designed to measure and distinguish hadrons, electrons, neutral particles and muons. It covers 2π in azimuth and production angles between 9° and 171°. Figs. 11.4 and 11.5 show a cross-section and a side view of the detector. Particles leaving the interaction region pass through: a ring of 32 lucite Cerenkov counters (L); a ring of 20 lead scintillator shower counters (A), 3 radiation lengths thick; a ring of 24 shower counters (B) identical to the A counters; a ring of 16 lead scintillator shower counters (C), 12 radiation lengths thick; 12 planes of drift chambers (S,T). The electromagnetic shower detector is followed by the hadron calorimeter consisting of 192 scintillation counters sandwiched between magnetized iron. The magnetic field in the iron is 1.7 T. The drift chambers P and R behind the calorimeter measure the position, angles and momenta of exciting muons.

The luminosity is determined through lead glass shower detectors positioned in the very forward direction and detecting small angle Bhasha scattering.

PLUTO

The PLUTO detector has already been in use at DORIS. For the work at PETRA the muon detection system was improved and forward spectrometers to measure photons and electrons at small angles were added. Fig. 11.6 and Fig. 11.7 show two views of the setup. A superconducting solenoid is used with length 1 m and diameter 1.4 m, providing a field of 1.65 T. The solenoid is filled with

(A) 13 cylindrical proportional chambers providing a momentum resolution of $\Delta p/p = 3\% \cdot p$ (p in GeV/c) for $p > 3$ GeV/c.

(B) Barrel and endcap shows counter equipped with proportional tubes for position measurement. The energy resolution for electrons and photons with energy $E > 1$ GeV is $\sigma_E/E \sim 35\%/\sqrt{E}$ (E in GeV) in the barrel counters and $\sim 19\%/\sqrt{E}$ in the endcap counters. The geometrical acceptance of (A) and (B) is 87% and 94% of 4π, respectively.

(C) The central detector is surrounded by an iron plate (total thickness 1m) interspersed with proportional and drift chambers for muon identification.

(D) Each of the two forward spectrometers consist of a large and a small angle tagging system, LAT and SAT. The LAT covers polar angles between 70 and 260 mrad. The energy of electrons and photons is determined with 14.5 radiation lengths thick lead scintillator shower counters ($\sigma_E/E = 11\%/\sqrt{E}$). Proportional tube chambers determine the position of charged particles. The SAT accepts polar angles between 23 and 70 mrad. It consists of lead glass shower counters ($\sigma_E/E = 8.5\%/\sqrt{E}$) preceded by proportional chambers.

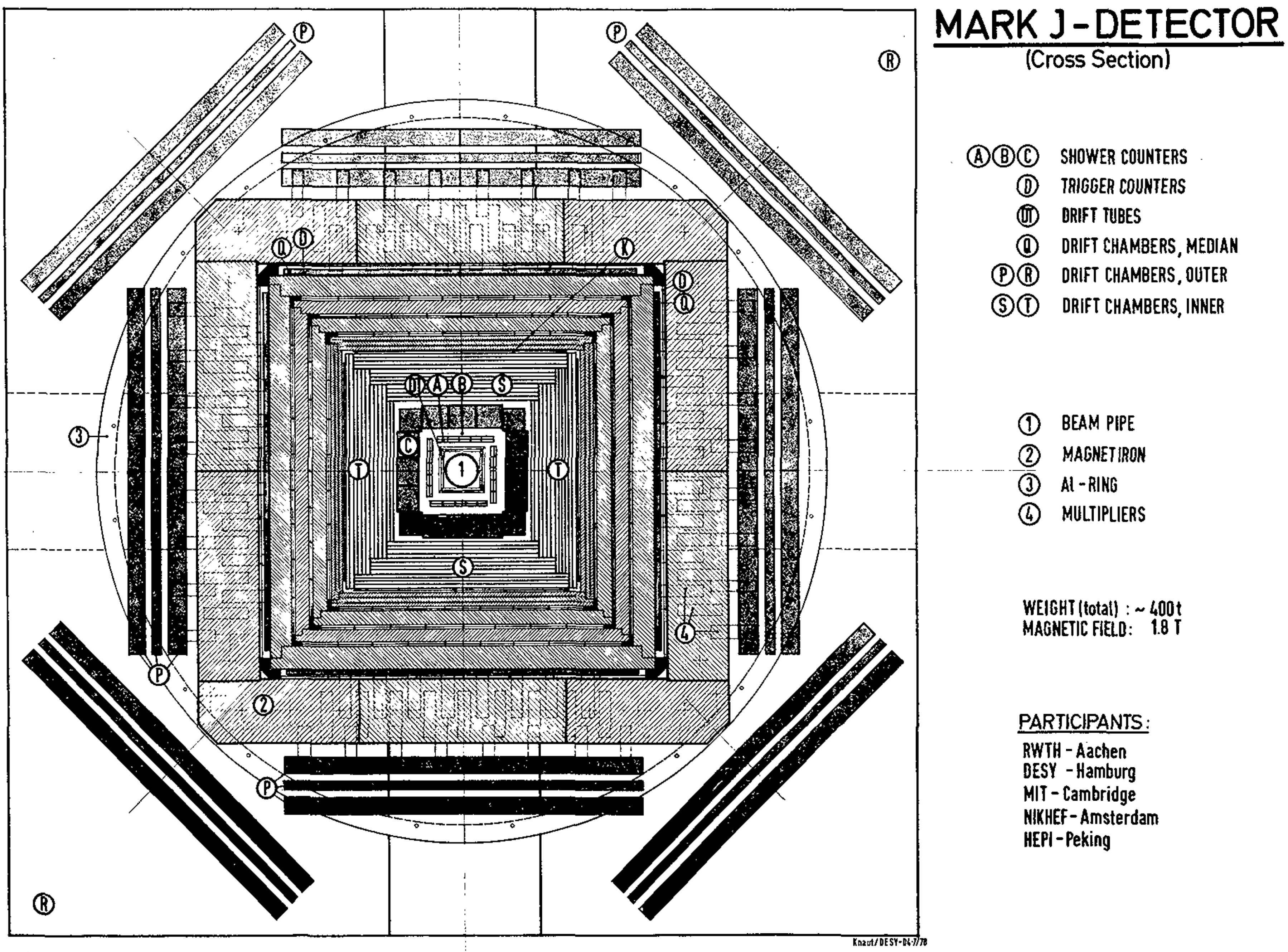

Fig. 11.4 Side view of MARK J

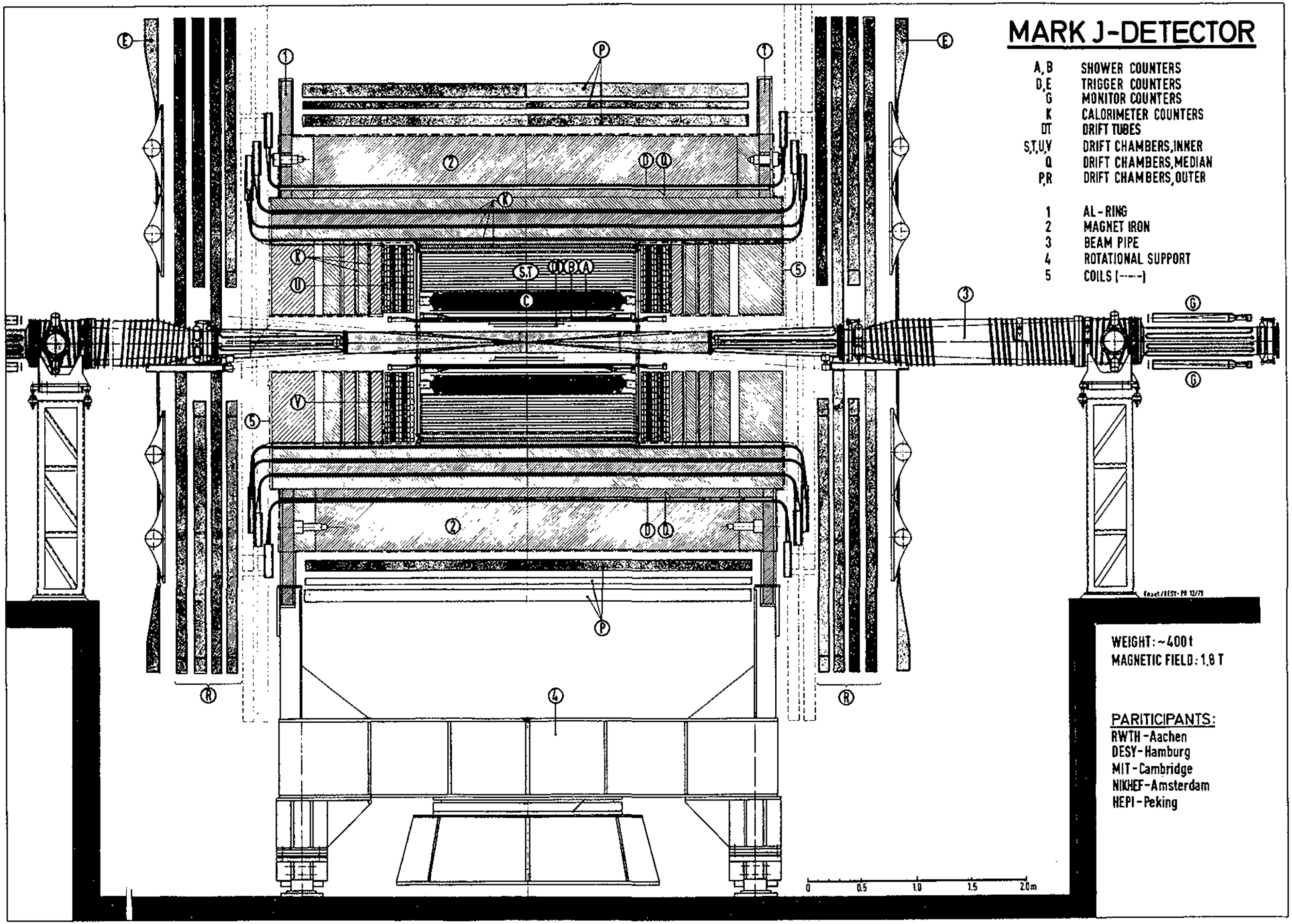

Fig. 11.5 Front view of MARK J

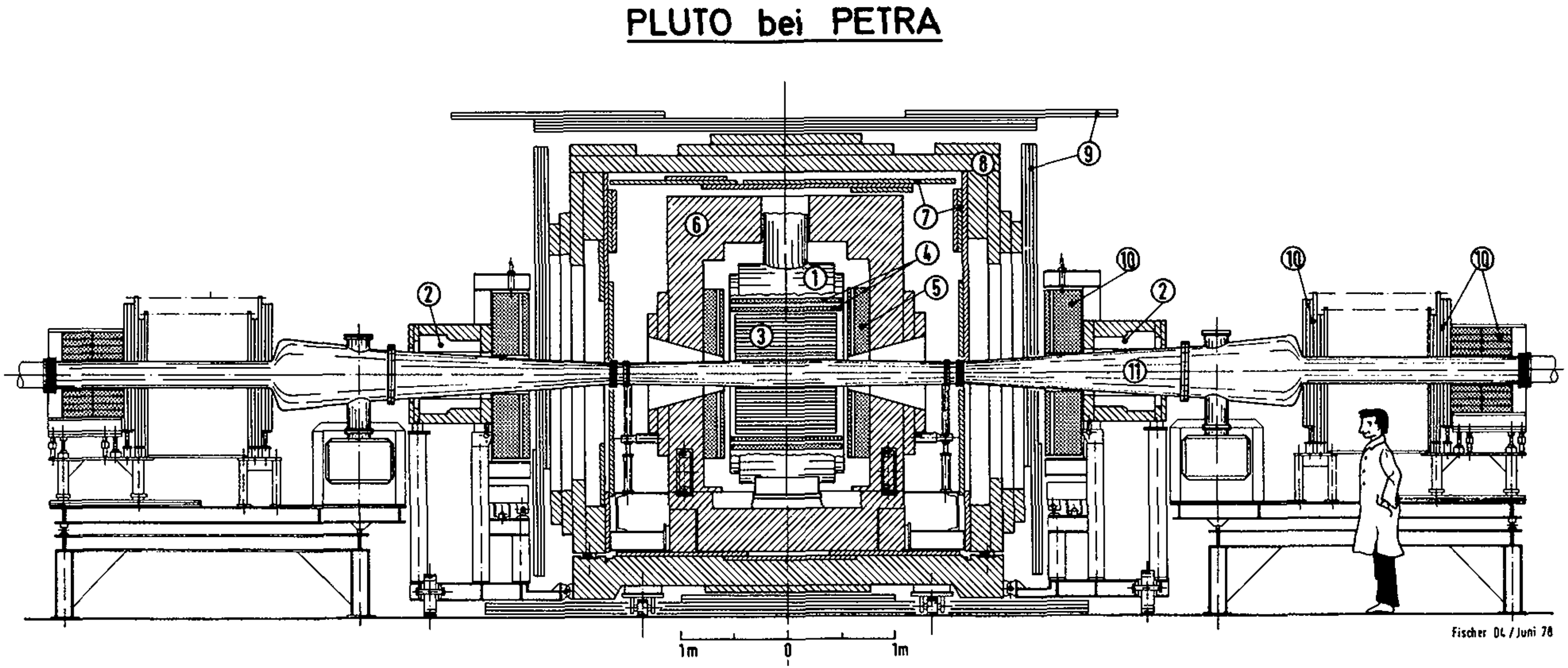

1	Superconducting coil	7	Myon-chambers
2	Compensation coils	8	Hadron-absorber
3	Cylindrical proportional chambers	9	Drift-chambers
4	Cylindrical shower-counters	10	Small-angle spectrometer
5	End-cap shower-counters	11	Vacuum-pipe
6	Iron-yoke		

Fig. 11.6 Side view of the PLUTO detector.

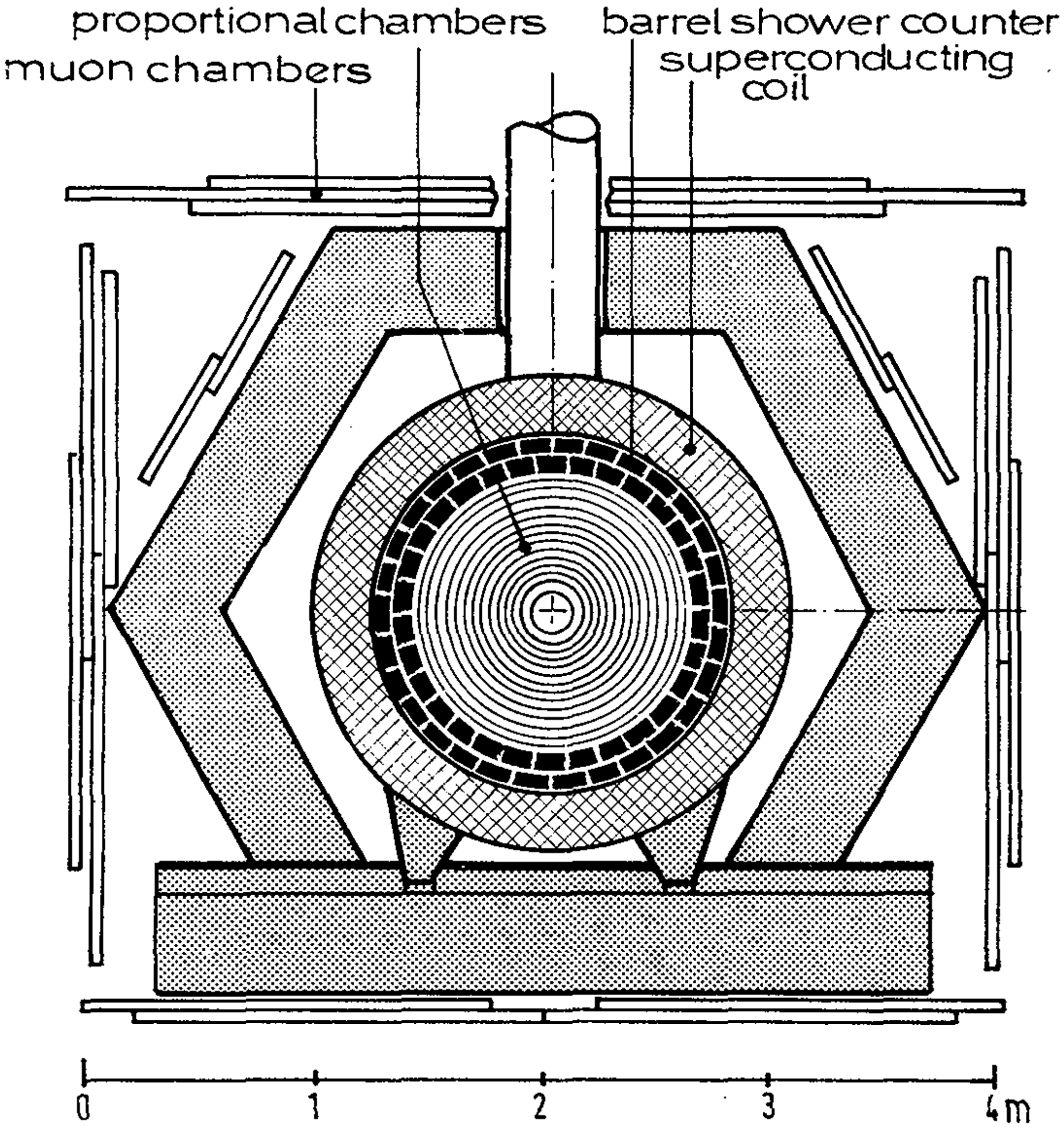

Fig. 11.7 The PLUTO detector as viewed along the beam

TASSO

Fig. 11.8 shows a cross-section of the TASSO detector. It consists of a large magnetic solenoid filled with and surrounded by tracking chambers and shower counters, plus two counter hodoscopes (= hadron arms) designed for particle identification up to the highest momenta. A luminosity monitor, which measures small angle Bhabha scattering, consists of eight counter telescopes mounted symmetrically with respect to the beamline and interaction point (Fig. 11.9).

The solenoid is 440 cm in length, 135 cm in radius and produces a field of 0.5 Tesla parallel to the beam axis. Emerging from the interaction point a particle traverses the beam pipe and one of 4 scintillation counters, which form a cylinder around the beam pipe, before entering a low mass cylinderical proportional chamber, a drift chamber and a set of 48 time-of-flight counters. The proportional chamber has four gaps each containing anode wires parallel to the beam axis and two layers of cathode strips with a pitch angle of 36.5°. The drift chamber contains 15 layers, 9 with sense wires parallel to the axis and 6 with sense wires oriented at approximately $\pm 4^{\circ}$ to the axis. The momentum resolution is $\sigma_p/p = 2\% \cdot p$ for $p > 1$ GeV/c.

Liquid argon (LA) shower counters will cover the solenoid at both ends and two thirds of its circumference. They are made of stacks of 2mm lead plates separated by gaps of 3mm (end cap counters) and 5 mm (barrel counters) width filled with liquid argon. The counters are highly segmented. Contrary to similar counters built elsewhere shower energies are measured in small towers which subtend only 0.8 - 1.5 mster.
The towers are directed towards the interaction point. Strip electrodes (2 cm wide) provide an accurate localisation of the shower and serve to measure dE/dx.

The hadron arms covering 90° in polar angle and 60° in azimuth consist each of

1. a planar drift chamber;
2. 16 cells of aerogel Cerenkov counters with a refractive index of 1.02. The thickness of the aerogel is 19 cm.
3. two normal pressure gas Cervenkov counters filled with Freon 14 ($n = 1.0014$) and CO_2 ($n = 1.0007$) and subdivided into 32 cells each;
4. 64 scintillation counters to measure time of flight;
5. lead scintillator shower counters using wavelength shifters for light collection;
6. an 87 cm thick iron wall used for shielding and muon filtering.

The magnet yoke as well as the iron walls of the hadron arms are covered by proportional tube chambers to detect muons.

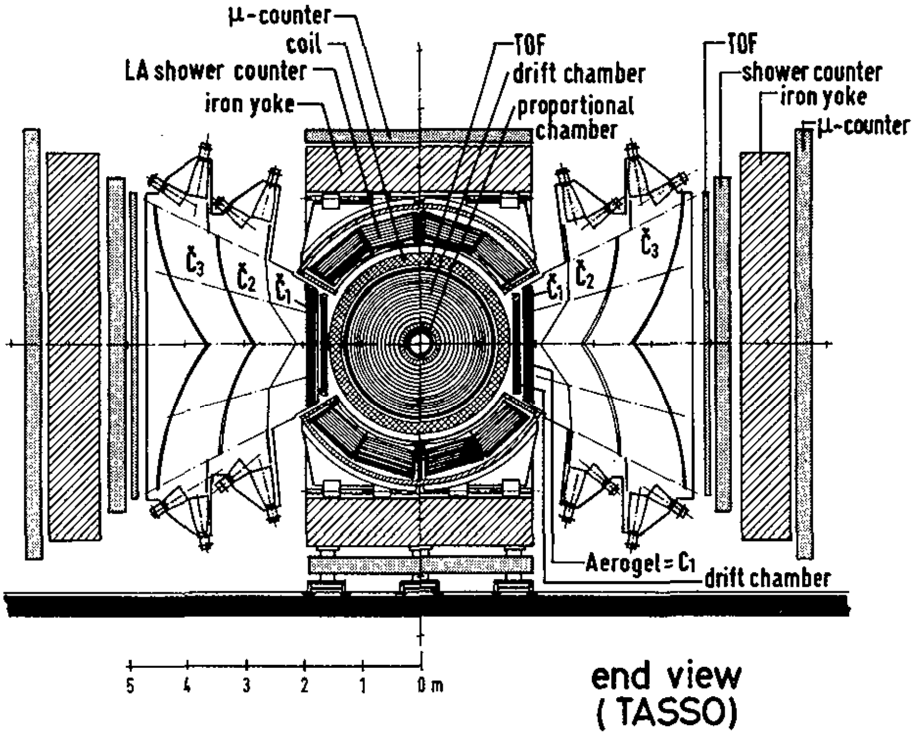

Fig. 11.8 The TASSO detector as viewed along the beam

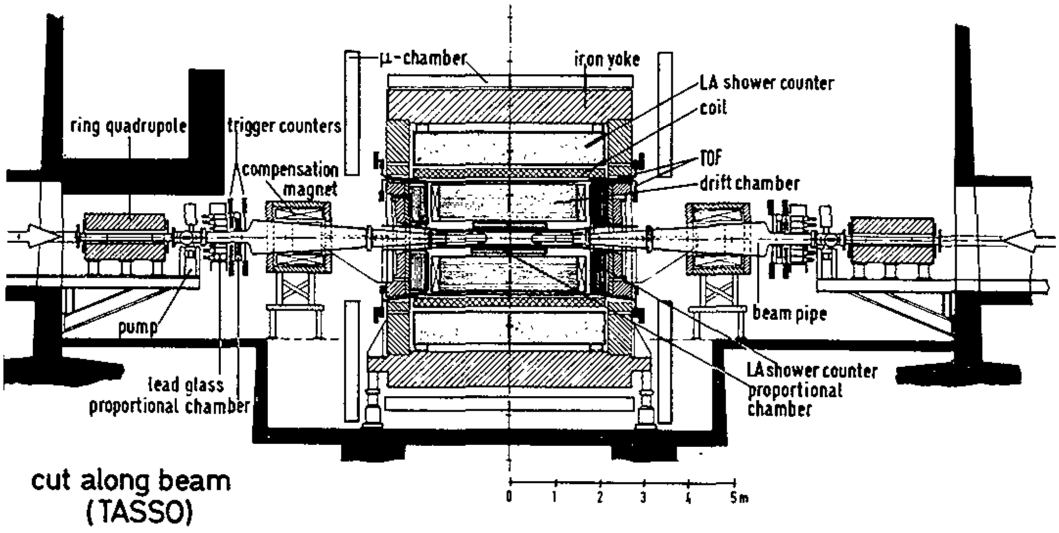

Fig. 11.9 A Side view of the TASSO detector

During the course of 1979 PETRA has been running for experiments at total energies W between 12 and 31.6 GeV. The main focus points were tests of QED (see Section 3), an extrapolation of the hadronic final states produced through one photon annihilation, the search for the top quark and a first look at two photon processes producing hadrons. The following discussion centers on hadron production through the one photon channel and on the quark search. It is based mainly on the material presented by the four experiments at the 1979 FNAL Conference (11.1. - 11.4.). Papers which were published until December 1979 are also included in this summary.

11.3 Energy Dependence of R

The one photon annihilation events have to be separated from hadronic events produced by two-photon scattering. While at low energies ($W < 5$ GeV) two photon contributions are mostly of the order of a few percent of the one photon channel, at PETRA energies the relative proportion of the two processes is reversed. A clear separation of the two processes was achieved by cutting in the visible energy for hadronic events as shown in Fig. 11.10. Note that most of the two-photon contribution is already suppressed by a multiplicity and transverse momentum cut built into the trigger.

Fig. 11.11 shows a compilation of the R values measured at PETRA between 12 and 31.6 GeV together with low energy data (11.5 - 11.9.). The PETRA points were corrected for acceptance, for contributions from beam gas and $\gamma\gamma$ scattering and $\tau\bar{\tau}$ production. Corrections for radiative effects were also applied.

Only statistical errors are shown. The systematic uncertainties are of the order of 10 to 15%.

The outstanding features of R as observed above 3 GeV are the spikes from the excitation of J/ψ, ψ' ... and of Υ, Υ'... plus the fact that in between the two families and above Υ, Υ' R is almost constant.

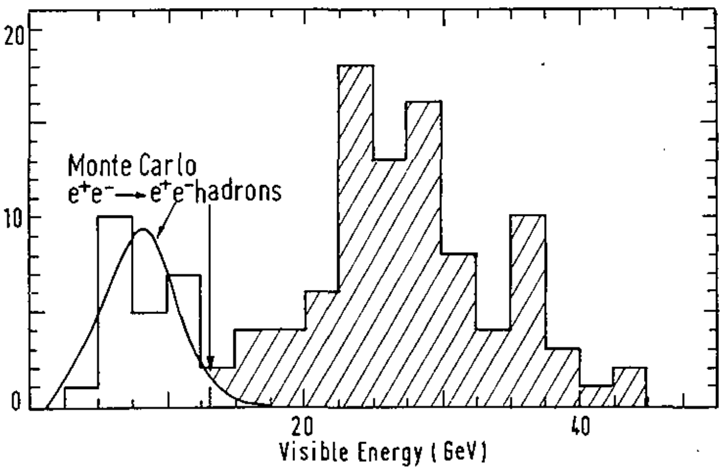

Fig. 11.10 the visible energy distribution after the momentum balance cut for hadron candidates at W = 27.7 GeV as measured by JADE (11.1). The cut $E_{vis} > E_{beam}$ is indicates by an arrow. The curve represents the expected background from the two-photon processes using a $\gamma\gamma$ total hadronic cross-section of 260 nb.

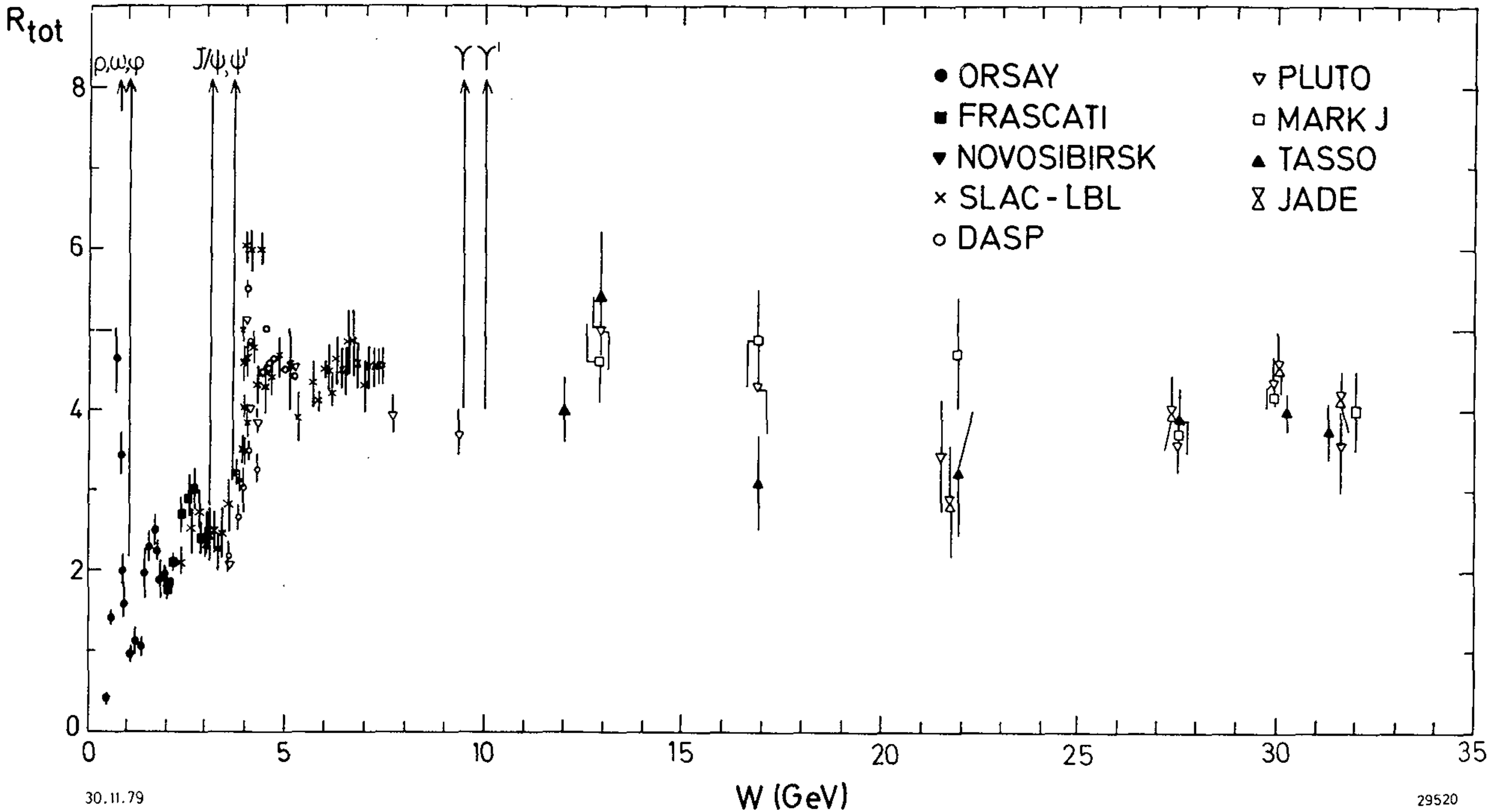

Fig. 11.11 The ratio R of the total hadronic cross section to $\sigma_{\mu\mu} = \frac{4\pi\alpha^2}{3\,s}$ as a function of the c.m. energy. Data from Refs. 11.5 - 11.9 (picture taken from Ref. 11.9).

The simple quark model is in striking agreement with the general behavior of R (see section 4):

$$R = \sum \frac{\sigma_{q\bar{q}}}{\sigma_{\mu\mu}} = 3 \sum e_q^2 \qquad q = u, d, s, c, b \tag{11.1}$$

Up to 3 GeV only u, d and s contribute and therefore R = 2 in good accord with the data between 1.5 and 3 GeV. Above charm threshold (near 4 GeV) R should rise to a level of 3.3. The data are larger mainly because of resonance effects; above 4.5 GeV the measured R values seem slowly to descend towards the quark model value. Note that the PLUTO value measured at 9.4 GeV just below the Υ is 3.7 ± 0.3 ± 0.5 (the second error being the systematic one). Beyond the Υ,Υ' family, the data seem to be again higher than the quark model value of 3.7 but tend to approach this value as the energy increases.

A possible contribution of a sixth quark will be discussed later.

As discussed before in QCD gluon emission modifies the result of the quark model, R_o:

$$R = R_o\left(1 + \frac{\alpha_s(s)}{\pi}\right) \tag{11.2}$$

At PETRA energies one expects $\alpha_s \sim 0.2$ which leads to an increase of R due to QCD corrections by approximately 10% to R = 4.1. This is well within the accuracy of the experimental points.

11.4 Gross Features of the Hadron Final States

a) *Multiplicity*

In Fig. 11.12 the average charged particle multiplicity $\langle n_{ch}\rangle$ is plotted as a function of the c.m. energy (11.10 - 11.15). The data show that above ∿ 7 GeV the multiplicity is rising (logarithmically) faster than at lower energies. The dashed and dashed-dotted curves give the energy dependence for pp collisions (11.16) and $\bar{p}p$ annihilation (11.17). The pp multiplicity is about one unit below the e^+e^- data while the $\bar{p}p$ multiplications are slightly above. All three processes have about the same energy dependence.

The simplest form of scaling of charged particle production leads to $\langle n_{ch}\rangle = a + b \ln s$. This is certainly at variance with the data if the full energy range is considered. If low and high energy data are fitted separately, TASSO (11.15) finds

$$\begin{aligned} \langle n_{ch}\rangle &= (2.67\pm0.04) + (0.48\pm0.02)\ \ln s & 1.4 < W < 7\ \text{GeV} \\ &= (-6.1\pm0.4) + (2.79\pm0.06)\ \ln s & 7.0 < W < 31.6\ \text{GeV} \end{aligned}$$

The observed rise of $\langle n_{ch}\rangle$ cannot be attributed to the production of $b\bar{b}$ final states which yield an increase of 0.2 units. In QCD an increase of $\langle n_{ch}\rangle$ over the scaling curve is predicted due to the additional fragmentation from gluons. The exact form of the resulting energy dependence is not yet clear.

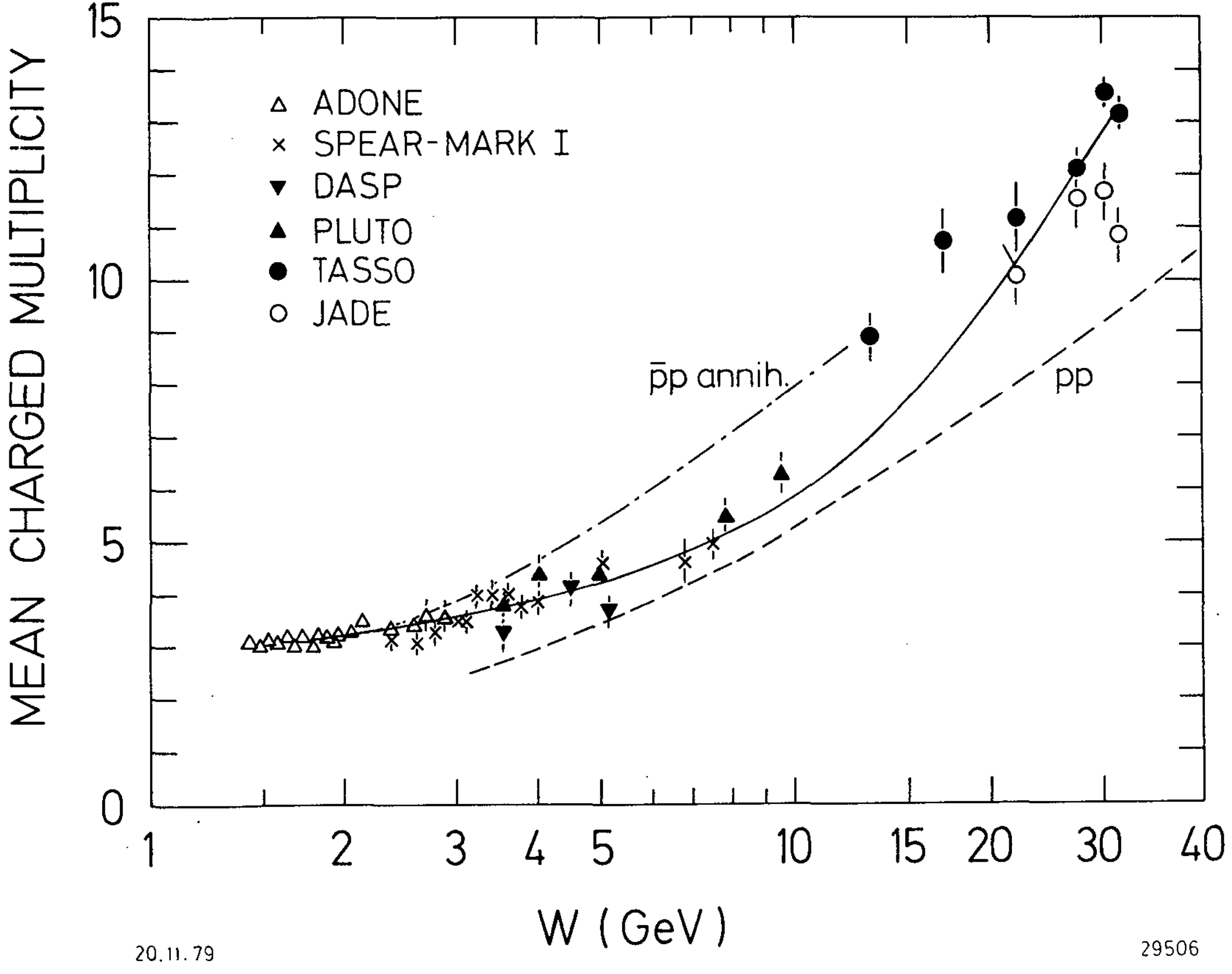

Fig. 11.12 Average charged particles multiplicity as a function of the c.m. energy[11.10–11.15]. The dashed and dashed-dotted curves show the results for pp collisions (Ref. 11.16) and $\bar{p}p$ annihilation (Ref. 11.17). The solid line is a fit to the e^+e^- data of the form

$<n_{ch}> = n_o + a \exp(b \sqrt{\ln s/\Lambda^2})$.

If the result for infinitely heavy quarks is taken for guidance, one expects[11.18] $<n_{ch}>$ to grow like

$$<n_{ch}> \; = n_o + a\exp(b\sqrt{\ln(s/\Lambda^2)})$$

The fit to the data between W = 1.4 and 31.6 GeV yields[11.15]

$$<n_{ch}> \; = (2.92 \pm 0.04) + (0.0029 \pm 0.0005) \exp((2.85 \pm 0.07)\sqrt{\ln(s/\Lambda^2)})$$

with Λ= 0.5 GeV. The fit is shown by the solid line in Fig. 11.12; it reproduces the trend of the data.

b) Inclusive particle spectra

The differential cross section for producing a particle h with momentum and energy P, E and angle Θ relative to the beam axis can be expressed in terms of two structure functions $\bar{W}_1$ and $\bar{W}_2$ which are closely related to W_1 and W_2 measured in inelastic lepton hadron scattering[11.15]

$$\frac{d^2\sigma}{dxd\Omega} = \frac{\alpha^2}{s}\beta x\,\{m\bar{W}_1 + \frac{1}{4}\beta^2\,x\,\nu\bar{W}_2\,\sin^2\theta\} \tag{11.3}$$

where m is the mass of h, β= P/E, $x = E/E_{beam} = 2E/\sqrt{s}$ and ν is the energy of the virtual photon as seen in the h rest system, $\nu = (E/m)\sqrt{s}$.

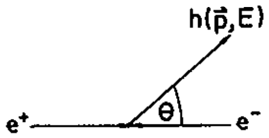

Diagram for inclusive particle production.

At particle energies large enough that particle masses can be neglected, x can be replaced by the normalized momentum $x = P/E_{beam}$ and the scaling cross section reads

$$sd\sigma/dx \approx 4\pi\alpha^2\,x\,\{m\bar{W}_1 + \frac{1}{6}\,x\,\nu\bar{W}_2\} \tag{11.4}$$

The structure functions in general depend on two variables, e.g. x and s. If scale invariance holds $\bar{W}_1$ and $\nu\bar{W}_2$ are functions of x alone and sdσ/dx is energy independent.

Scaling behaviour is e.g. expected from the hypothesis of quark fragmentation: at energies large enough that particle masses can be neglected, the number of hadrons h produced by a quark q with fractional energy x, $D_q^h(x)$, is independent of s. This leads to

$$\frac{d\sigma}{dx}(e^+e^- \rightarrow q\bar{q} \rightarrow h) = \sigma_{qq} \cdot 2D_q^h(x) = \frac{8\pi\alpha^2}{s}\,e_q^2 D_q^h(x) \tag{11.5}$$

Fig. 11.13 displays the data on $s\,d\sigma/dx$ measured by TASSO[11.15] at energies between 13 and 31.6 GeV. For $x > 0.2$ they are the same within errors and agree with those measured at low energy by DASP (11.13, 5 GeV) and SLAC - LBL (11.20, 7.4 GeV) to within 30%. At low x values the particle yield shows a dramatic rise when the c.m. energy increases from 5 to 31.6 GeV. This rise is related to the growth of the multiplicity seen above.

Gluon emission will lead to scale breaking effects: the primary momentum is now shared by quark and gluon resulting in a depletion of particles at high x and an excess of particles at low x values. The effect becomes more pronounced as the energy rises, e.g. the 30 GeV data at $x = 0.2$ are predicted to be higher by ∿10%, and at $x = 0.7$ lower by ∿20% than the 5 GeV data[11.21]. The measurements are not precise enough to test this prediction.

11.5 Jet Formation

a) Sphericity and thrust measurements

As discussed before, the quark model views e^+e^- annihilation into hadrons as a two-step process: first a pair of quarks is produced which then fragment into hadrons. If the hadron momenta transverse to the quark direction of flight are limited and the number of produced hadrons grows only logarithmically with energy, the emitted hadrons will be more and more collimated around the primary quark directions as the total energy increases and one will observe jets. Let $<n>$ be the average particle multiplicity, $<P_T>$ and $<P_\parallel> \sim <P> \sim W/<n>$ the average transverse and longitudinal hadron momenta, then the mean half angle $<\delta>$ of the jet cone can be estimated:

$$<\delta> \approx \left\langle \frac{P_T}{P_\parallel} \right\rangle \approx \frac{<P_T> \cdot <n>}{W} \sim \frac{1}{W} \tag{11.6}$$

The jet cone decreases roughly $\sim W^{-1}$. Actually, in a realistic calculation of the quark model using the fragmentation functions of Field and Feynman[10.9] one finds $<\delta> \sim W^{-1/2}$

The occurrence of jets is commonly tested in terms of sphericity S and thrust T (see Section 10)

$$S = 3/2 \;\; (\textstyle\sum P_{Ti}^2)/\sum P_i^2 \qquad\qquad T = \sum |P_{\parallel i}| / \sum P_i \tag{11.7}$$

Approximately speaking, sphericity measures the square of the jet cone half opening angle:

$$S \simeq 3/2 < \delta^2 >$$

likewise

$$T \simeq \sqrt{1 - < \delta >^2} \tag{11.8}$$

In general, not all final state particles are detected; e.g. neutrals are usually not registered. As a consequence, the reconstruction of the true jet axis is only approximate. The effects of acceptance, detection efficiency and radiative corrections have to be studied

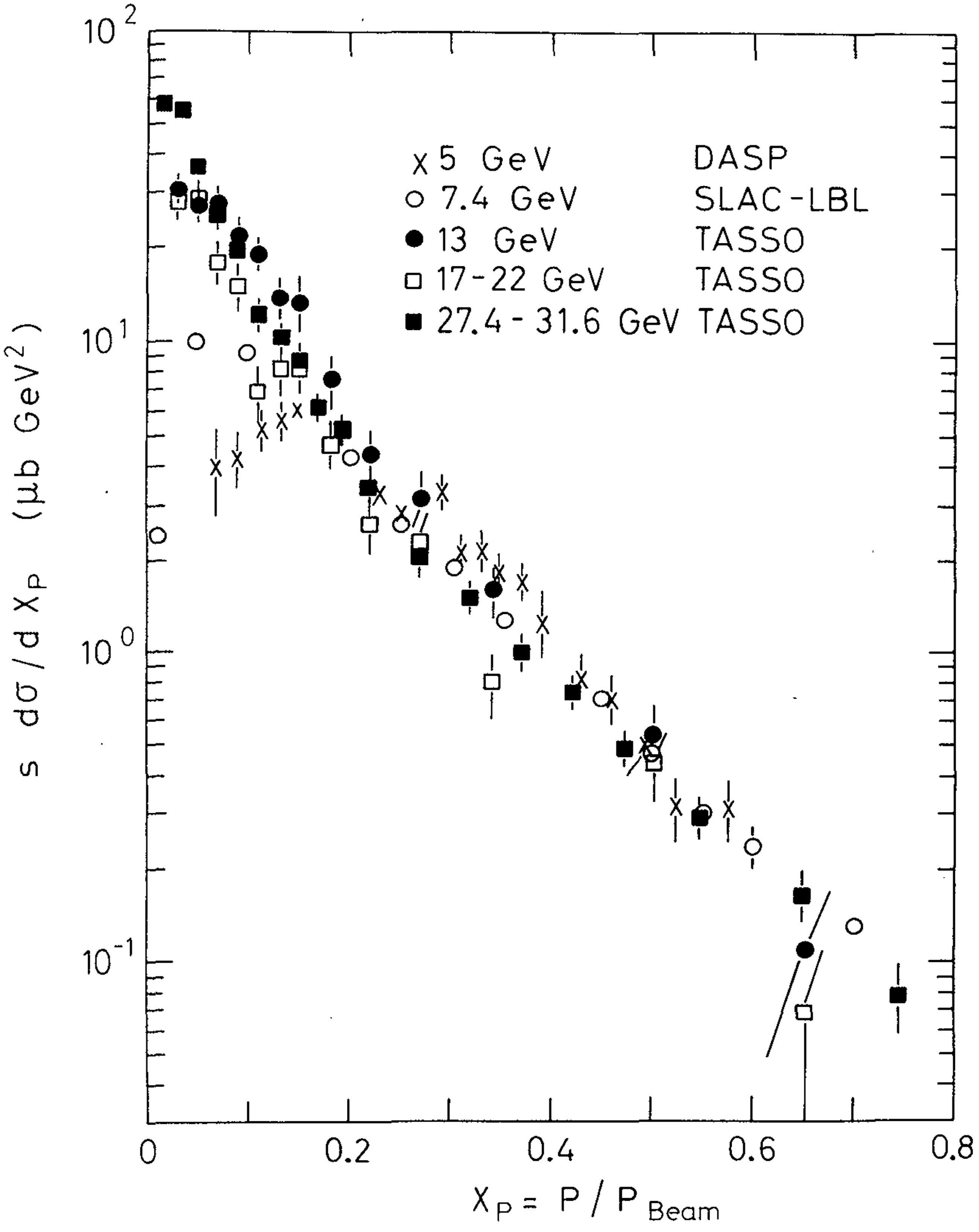

22.11.79 29509

Fig. 11.13 The scaling cross section $sd\sigma/dx$ ($x = p/E_{beam}$) for inclusive charged particle production measured at energies of 5 GeV (Ref.11.13) 7.4 GeV (11.20) and between 13 and 31.6 GeV (Ref. 11.15).

by an elaborate Monte Carlo analysis in order to separate physics effects from systematic biases. The figures shown below for S and T indicate whether observed or corrected quantities are displayed.

In Fig. 11.14a TASSO has made a comparison between the observed sphericity distributions determined from charged particles plus neutrals. The agreement between the two is good indicating that the corrections must be small if only charged particles are considered.

The energy dependence of the average sphericity and thrust is shown in Figs. 11.14b and 11.14c (11.6-11.9). The increasing collimation with rising energy is clearly borne out by the data. The average jet cone half opening angle computed from $<S>$ drops from ∿ 31° at 4 GeV to ∿ 17° at 31.6 GeV. However, the shrinkage of the jet cone is slower than expected from the quark model. The observed energy dependence of $<S>$ can be described by $<S> = 0.8\ W^{-1/2}$ (see Fig. 11.14) compared to the W^{-1} behavior expected. We will come back to this observation.

11.6 Longitudinal Momentum distributions

The production of hadrons with respect to the jet axis has been extensively studied. If the quark model is correct, these analyses permit in a clean manner the study of quark fragmentation, clean, since e.g. smearing effects due to quark Fermi motion in the nucleon are absent. The data have been analyzed in terms of the longitudinal and transverse momenta, $P_{\parallel}$ and P_T, the rapidity $y = 1/2 \ln [(E+P_{\parallel})/(E-P_{\parallel})]$ and the fractional momentum $x = P/E_{beam}$.

Fig. 11.15 shows the rapidity distributions normalized to the total cross section as measured by TASSO[11.15] between 13 and 31.6 GeV. The thrust axis was taken as the jet axis since in this way the corrections for the y-axis relative to the true axis were found to be smaller at large y than if the sphericity axis had been chosen. To compute y, the particles were assumed to be pions. Also plotted in Fig. 11.15 are data from SLAC-LBL[11.23] measured at low energies (4.8 and 7.4 GeV). They were determined with respect to the sphericity axis. One observes a plateau near $y = 0$ that broadens with increasing c.m. energy. The height of the plateau is not constant but rises with increasing energy (see insert in Fig. 11.15). In the fragmentation region (y close to $y_{max} \approx 0.5 \ln(s/m^2)$) the particle yield is a steeply descending function of y. The width of the fragmentation region is roughly one unit, which is similar to what has been observed in hadron-hadron scattering. In Fig. 11.16 the same data were plotted in terms of $y - y_{max}$ to study the energy behavior of the fragmentation region. The high energy data lie systematically below the low energy data. This is qualitatively what is to be expected from QCD effects: near $y = y_{max}$ one has $Y \approx 0.5 \ln(4P_{\parallel}^2/(P_T^2 + m^2))$. QCD predicts an increase in $< P_T>$ with energy pushing the high y particles to lower y values. Unfortunately, the intrinsic resolution of y near $y = y_{max}$ is about one unit in rapidity due to the limited accuracy (∿5°) in determining the jet direction.

The energy dependences of the plateau and fragmentation regions show that the faster than logarithmic growth of the average multiplicity at high energies is correlated with a rise of the plateau which is due to low energy particles. The same effect was observed in PP collisions[11.17].

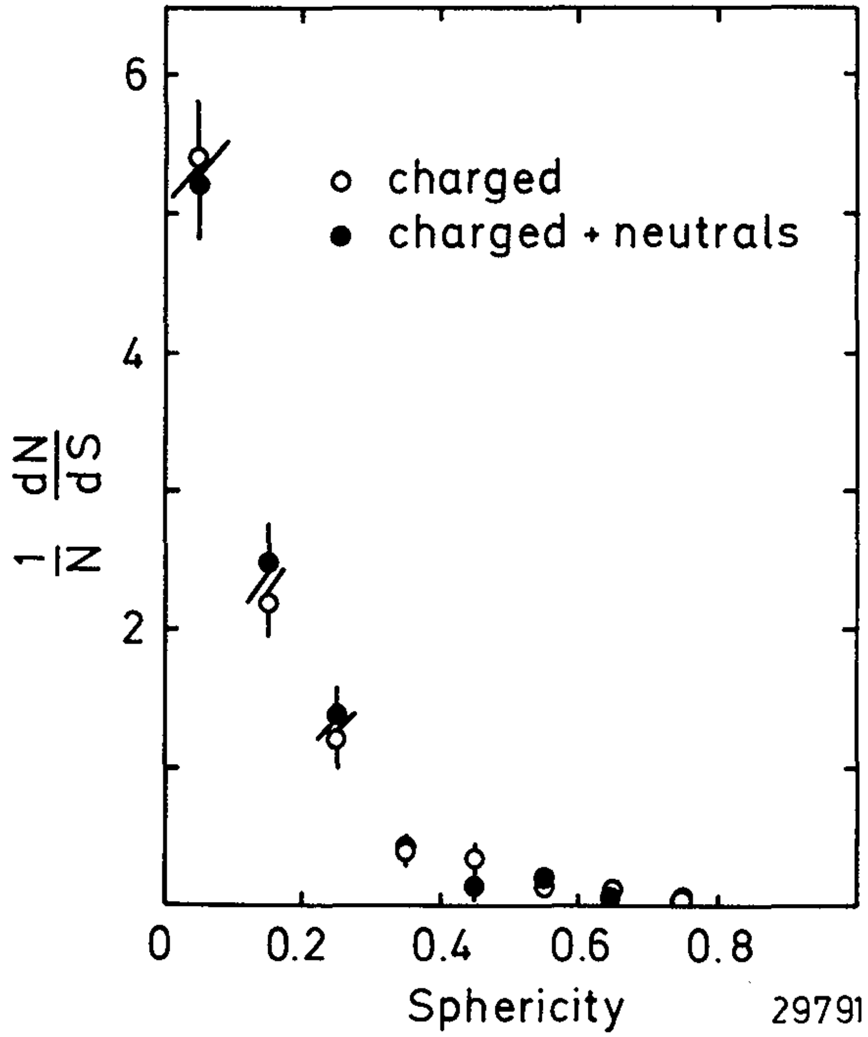

Fig. 11.14a Sphericity distributions at W = 27.4 - 31.6 GeV, measured with charged particles alone (○) and with charged and neutral particles (●) (TASSO).

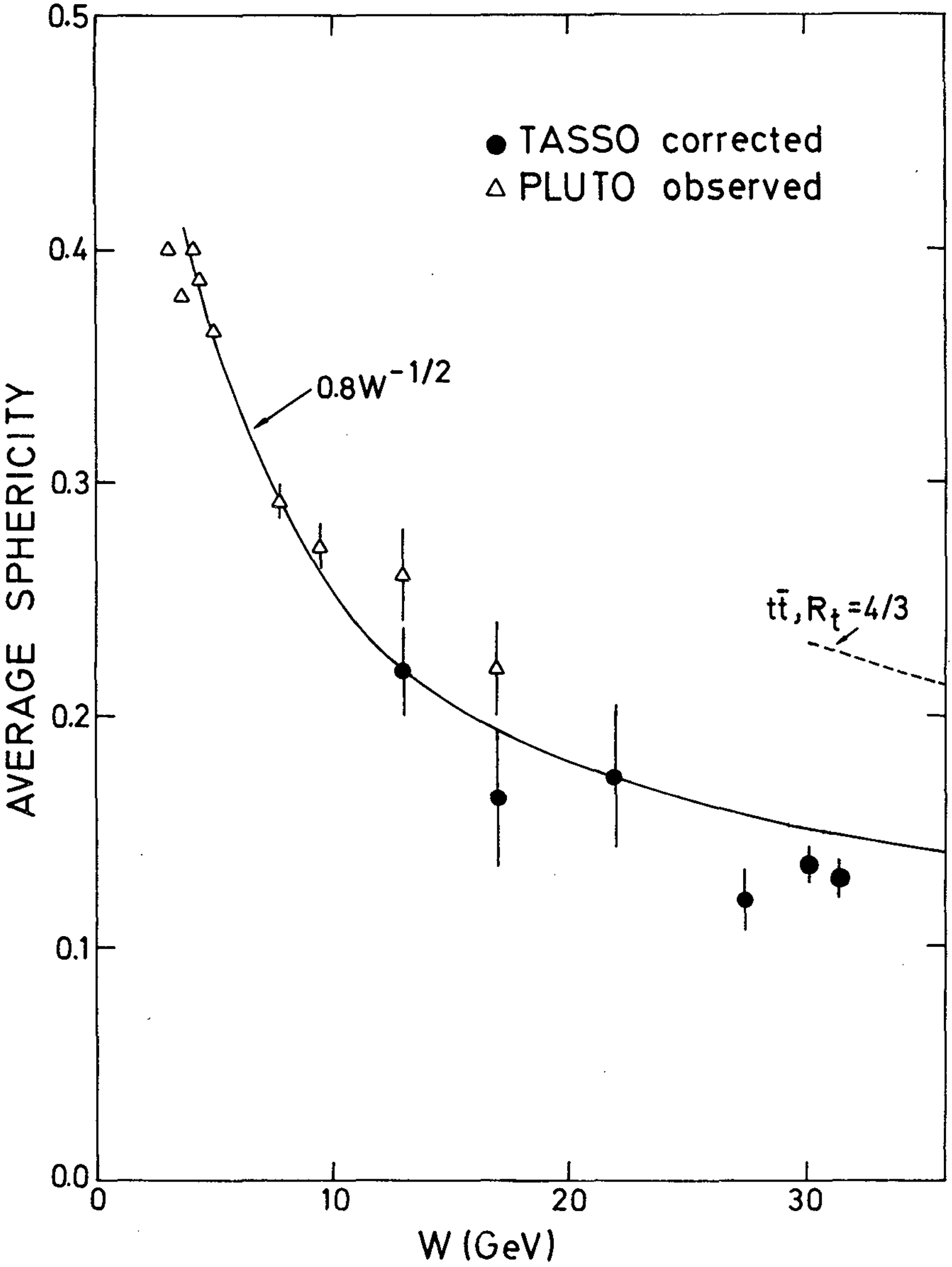

27.11.79

29518

Fig. 11.14b The average sphericity as a function of the c.m. energy as measured by PLUTO (11.12) and TASSO (11.9).

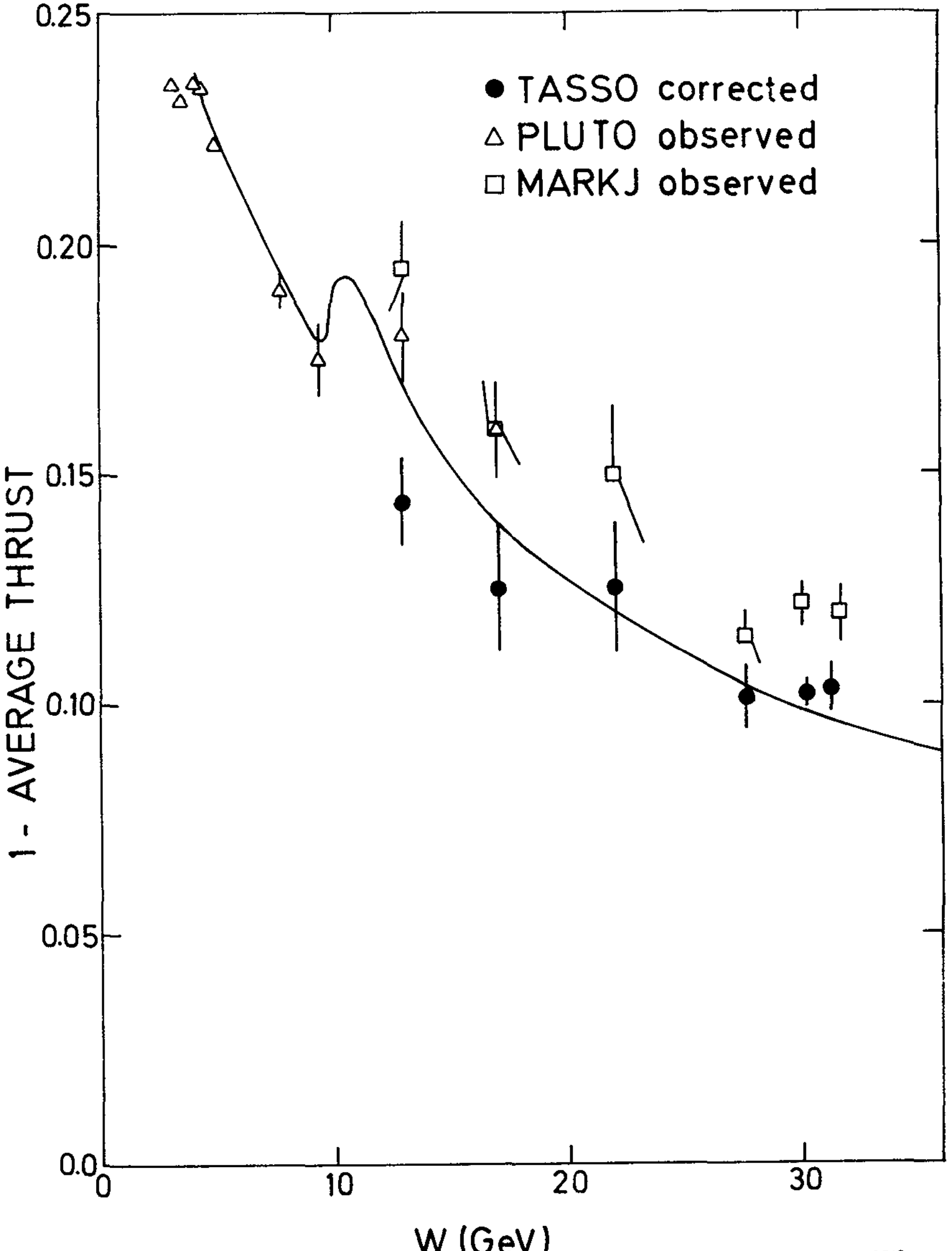

27.11.79

29519

Fig. 11.14c The average thrust <T> plotted as 1 − <T> versus the c.m. energy. Data from Refs. 11.7, 11.9 and 11.12. The solid curve represents the QCD prediction (11.22).

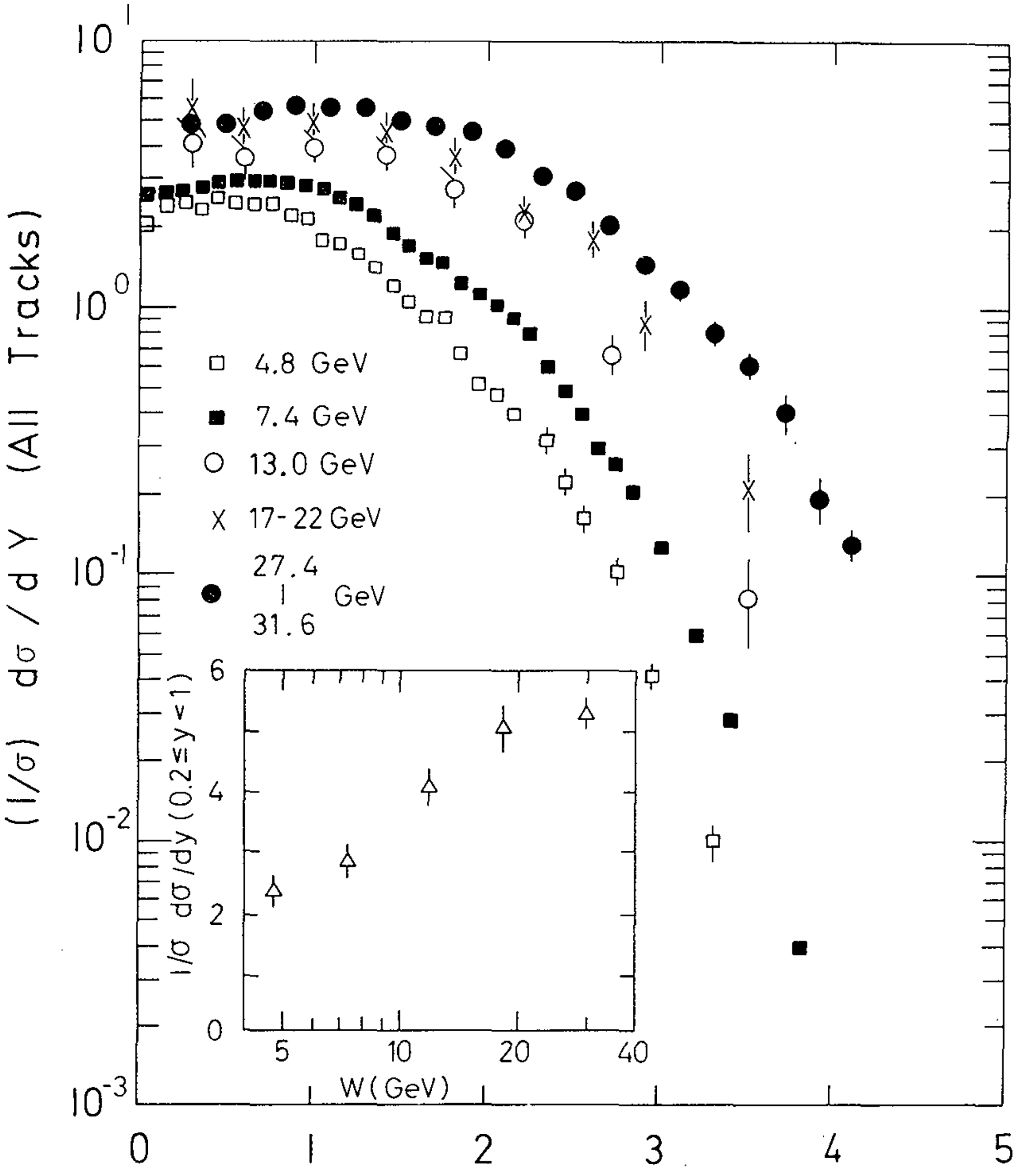

20.11.79

29507

Fig. 11.15 Rapidity distributions $1/\sigma_{tot}$ $d\sigma/dy$ for charged particles (assuming the mass to be the pion mass) measured by SLAC-LBL at 4.8 and 7.4 GeV (Ref.11.23) and by TASSO between 13 and 31.6 GeV (Ref. 11.15). SLAC-LBL used the spericity axis, TASSO the thrust axis. The insert shows $1/\sigma_{tot}$ $d\sigma/dy$ averaged over $0.2 < y < 1$ as a function of the c.m. energy.

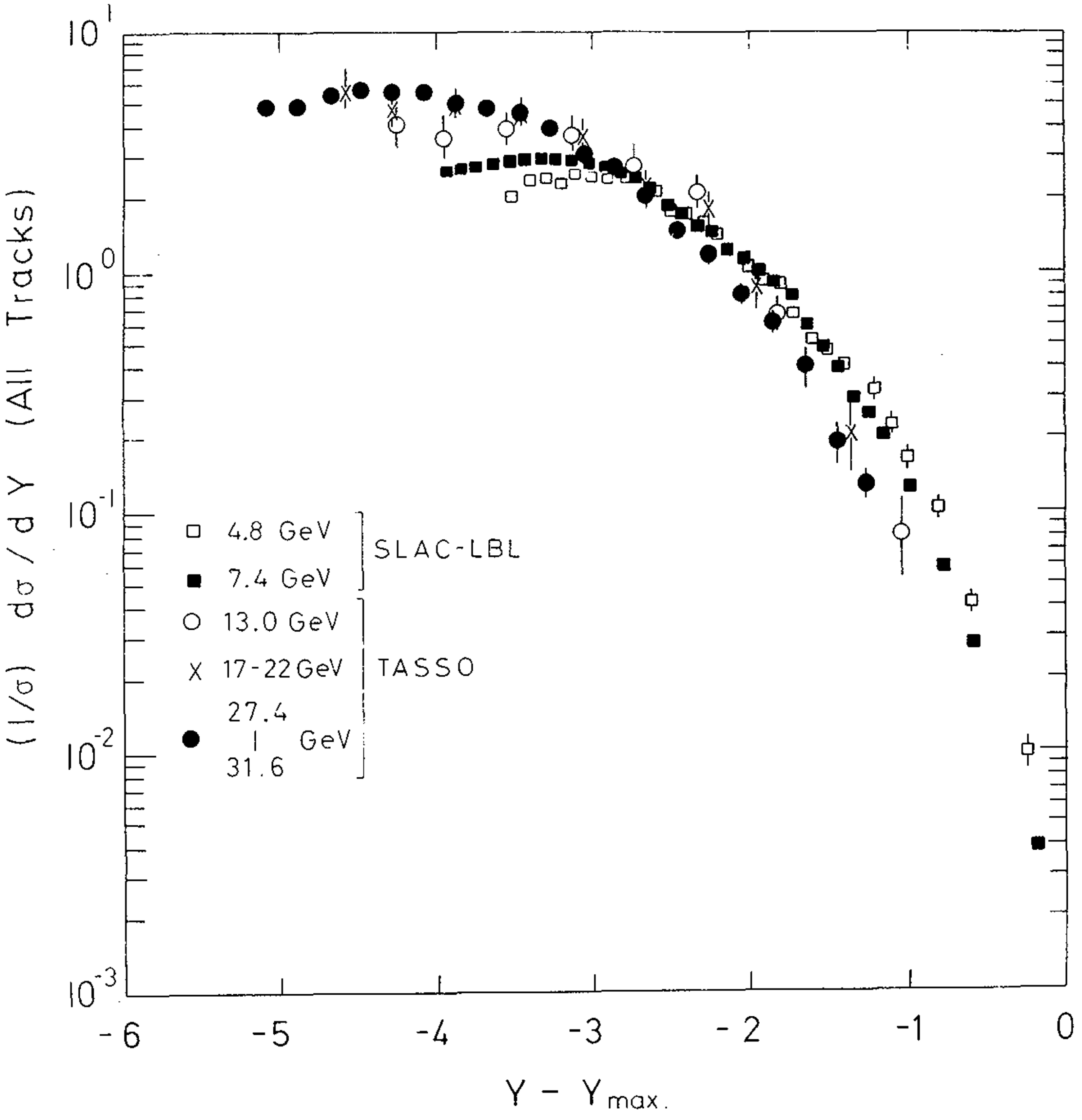

20.11.79

29508

Fig. 11.16 The same data as in Fig. 11.15 plotted as a function of $y - y_{max}$ (Refs. 11.15, 11.23).

11.7 Transverse Momentum Distributions and Jet Broadening

The transverse momentum distribution of hadrons produced in hadron scattering suggested a Gaussian p_T distribution for quark fragmentation into hadrons:

$$\frac{d\sigma}{dp_T^2} \sim e^{-\frac{p_T^2}{2\sigma q^2}} \tag{11.9}$$

The parameter σ_q e.g. for pions was found to be of the order of 300 MeV/c almost independent of the reaction energy. The analysis of e^+e^- annihilation at energies up to 7.4 GeV led to the same conclusion[11.23]. Deviations from a simple Gaussian behavior - a flattening of the p_T distribution - were observed recently in pp collisions at high p_T values (see lecture by M. Jacob).

In June of 1979 the TASSO group[11.24] when comparing e^+e^- annihilation data taken at 13, 17 GeV with data from 27 GeV noticed a large broadening of the p_T distribution with increasing energy. As was shown by the same experiment the broadening was correlated with the appearance of planar events, some of which had a definite three jet structure. The properties of these events as well as their production rate agreed well with the predictions made before for gluon bremsstrahlung by Ellis, Gaillard and Ross[11.25]. At the time of the FNAL conference more high energy data had been collected and the evidence found by TASSO[11.4] was corroborated by the other PETRA experiments[11.1-11.3].

We now discuss the experimental evidence for three jet events. Fig. 11.17 shows the normalized transverse momentum distribution $1/\sigma_{tot}\ d\sigma/dp_T^2$ evaluated with respect to the sphericity axis for 13 - 17 and 27 - 31.6 GeV [11.26] as measured by TASSO. The measurement for both energy regions are in reasonable agreement for $p_T^2 < 0.2\ (\mathrm{GeV}/c)^2$, but the high energy data are well above the low energy data for larger values of p_T^2 in contradiction to the naive parton model which assumes the quark to fragment with an energy independent transverse momentum distribution. The low energy data were fitted for $p_T^2 < 1\,(\mathrm{GeV}/c)^2$ with the jet model[10.9] including c and b quarks[11.27]. Increasing the parameter σ_q (e.q.11.9) from its original value of 0.25 GeV/c to 0.30 GeV/c gave a good fit to the 13 - 17 GeV data (see Fig. 11.17). To fit the higher energy data with the same model σ_q had to be increased to 0.45 GeV/c.

The widening of the transverse momentum distribution can have its origin in

1. the production of a new quark flavor. As will be discussed later, the data do not show any evidence for the production of a new heavy quark and we can dismiss that as a possible explanation.

2. the p_T distribution for quark fragmentation into hadrons is energy dependent: the average p_T grows as the energy increases. In this case the hadrons are still produced in two jets but the diameter of the "cigar" in terms of p_T^2 increases with energy (see sketch). Note also that both jets will grow in the same manner.

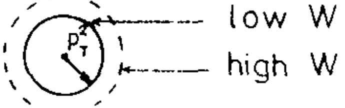

3. gluon bremsstrahlung from the outgoing quarks[11.25, 11.28 -11.33]. The radiated gluon is expected to turn into a jet of hadrons. In QCD single gluon emission is proportional to $\alpha_s(s)$, double gluon emission proportional to $\alpha_s^2(s)$, etc. At low energies

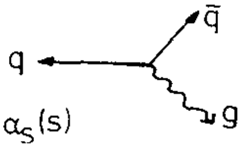

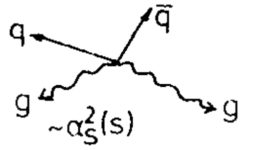

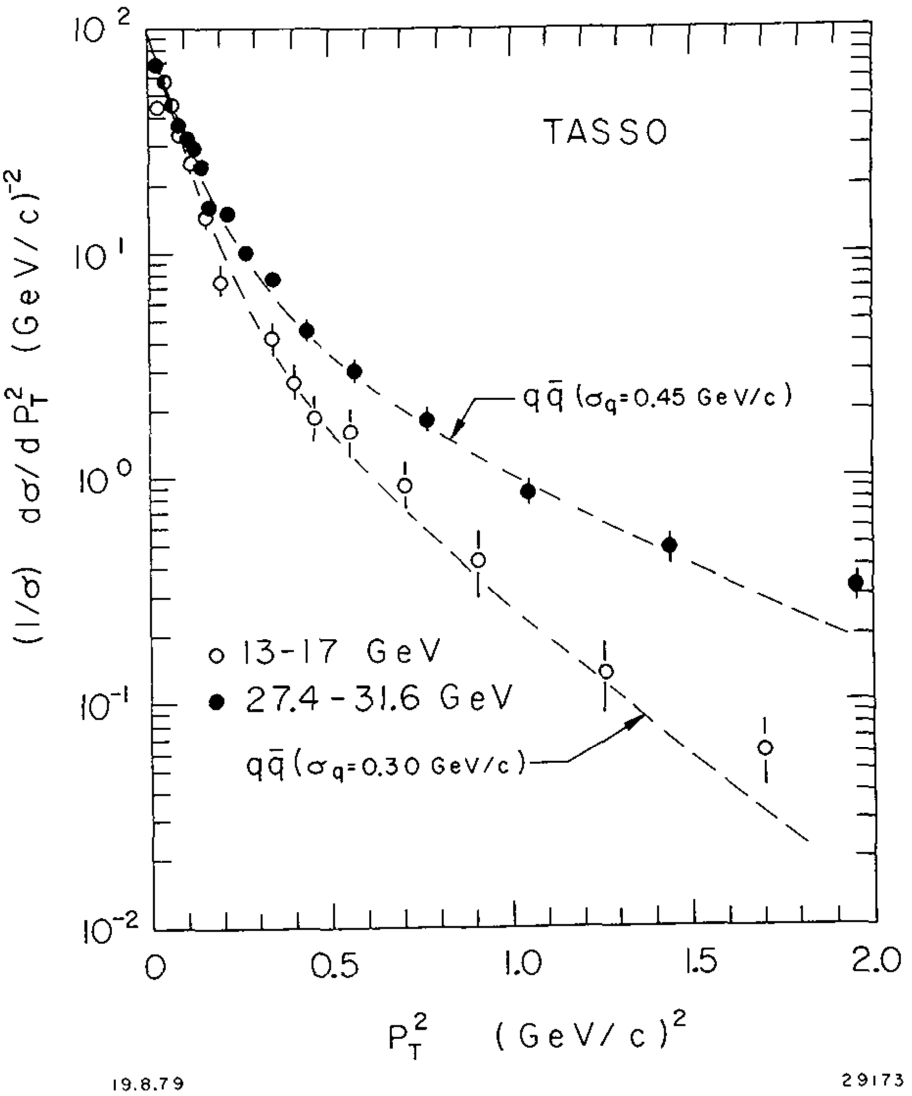

Fig. 11.17 $1/\sigma_{tot}\ d\sigma/dp_T^2$ as measured by TASSO[11.26] at 13 and 17 GeV (o) combined and for 27.4, 27.7, 30.0 and 31.6 GeV combined (●) as a function of p_T^2. The curves are fits to the data for $p_T^2 < 1$ $(\mathrm{GeV}/c)^2$ using the Field-Feynman quark parton model including u, d, s, c and b quarks with σ_q as a free parameter.

where $\alpha_s(s)$ is of order one, single as well as multigluon emission will be important. At our high energies where $s \sim 1000\ \mathrm{GeV}^2$ and $\alpha_s(s) \ll 1$ (e.g. $\alpha_s(s = 1000\ \mathrm{GeV}) = 0.2$ for $\Lambda = 0.5$ GeV) the emission of several hard gluons can be neglected. As a result there will be a tendency for only one jet to broaden. The $q\bar{q}g$ state is necessarily planar. This should reflect itself in the final hadron configuration which should retain the planarity with small transverse momenta out of the plane and large transverse momenta in the plane. The average transverse momentum of the gluon will rise linearly with energy.

Qualitatively, the broadening of $\langle p_T \rangle$ can easily be understood. Similar to the emission of photons from an electron, the gluon distribution radiated off a quark is approximately given by[10.2]

$$\frac{d\sigma(q\bar{q}g)}{dk\,d\cos\theta} \sim \frac{\alpha_s}{K(1-\cos\theta)^2}\,\sigma_{q\bar{q}}$$

or

$$\frac{d\sigma(q\bar{q}g)}{dk\,d\theta} \sim \frac{\alpha_s}{K\sin\theta}\,\sigma_{q\bar{q}}$$

where $\sigma_{q\bar{q}} = e_q^2 \cdot \sigma_{\mu\mu}$, K and θ are the gluon energy and emission angle relative to the quark direction of flight.

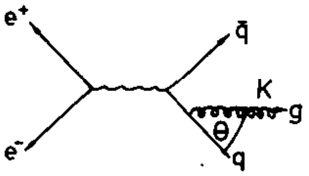

Schematic diagram for gluon emission

The average transverse momentum of the (hard) gluon jet is

$$\langle K_T\rangle \sim \frac{\alpha_s \cdot \sigma_{qq} \iint \frac{K\sin\Theta}{K\sin\Theta}\,dK\,d\Theta}{\sigma_{qq}\left(1+\frac{\alpha_s}{\pi}\right)}$$

$$\sim \alpha_s \cdot W \qquad \text{(up to log terms)}$$

The remarkable result is that contrary to many other predictions of QCD which lead to logarithmic deviations from the pure quark model and are therefore difficult to test experimentally, the transverse momentum is predicted to rise linearly with energy. If K_T is large compared to the typical transverse momentum of 0.3 GeV/c, then the event will have a three jet topology.

In Fig. 11.18 the average values of the longitudinal and transverse momentum as measured by PLUTO and TASSO are plotted as a function of c.m. energy. The average $p_{\parallel}$ grows almost linearly with W. The transverse momentum shows a small but significant rise between 13 and 31.6 GeV. The average $\langle p_T^2\rangle$ is rapidly rising above 13 GeV. At 13 GeV the measured value is in accordance with the prediction of the $q\bar{q}$ model. At higher energies it is well above this prediction. However, gluon emission[11.33] describes the data rather well.

In Figs. 11.19 and 11.20 each event was divided into two halves by a plane perpendicular to the jet axis and $\langle p_T^2\rangle$ was determined separately for the two sides[11.26]. The jet with the smaller $\langle p_T^2\rangle$ was called the narrow jet, the other one the wide jet. Then $\langle p_T^2\rangle$ was determined as a function of $z = p/p_{beam}$ and averaged over all narrow and wide jets, respectively. The result (also called the seagull plot) is shown separately for 13 - 17 and 27 - 31.6 GeV. The wide jet has larger $\langle p_T^2\rangle$ values than the narrow one. The $q\bar{q}$ model with σ_q = 0.3 GeV/c used by TASSO, 0.25 GeV/c by PLUTO, fits the low energy data which implies that here the observed narrow-wide asymmetry is due to statistical fluctuation. The model using the same value for σ_q

fails for the high energy data which would mean that there a genuine narrow/wide asymmetry exists. However, increasing σ_q to 0.45 GeV/c (a value which fitted the p_T^2 distribution of TASSO, Fig. 11.17) approximately reproduces the data. Therefore, the p_T^2 distributions as well as the seagull plot can be fitted with the $q\bar{q}$ model by increasing σ_q with energy.

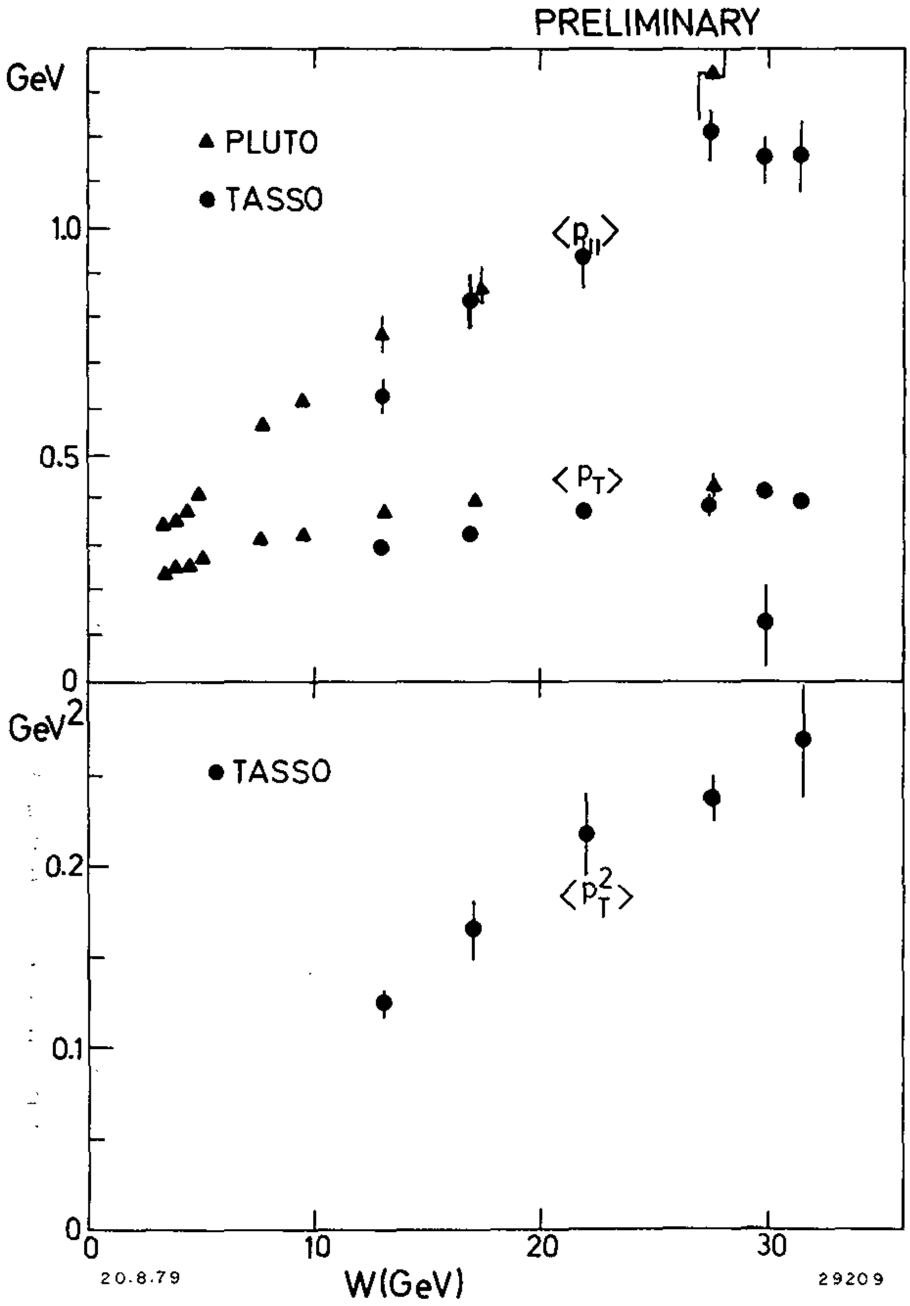

Fig. 11.18 The energy dependence of $< p_{\parallel} >$, $< p_T >$ and $< p_T^2 >$ relative to the thrust axis for charged particles[11.3]. The curves show the prediction for $q\bar{q}$ (dashed) and $q\bar{q}$ + gluon production (11.33).

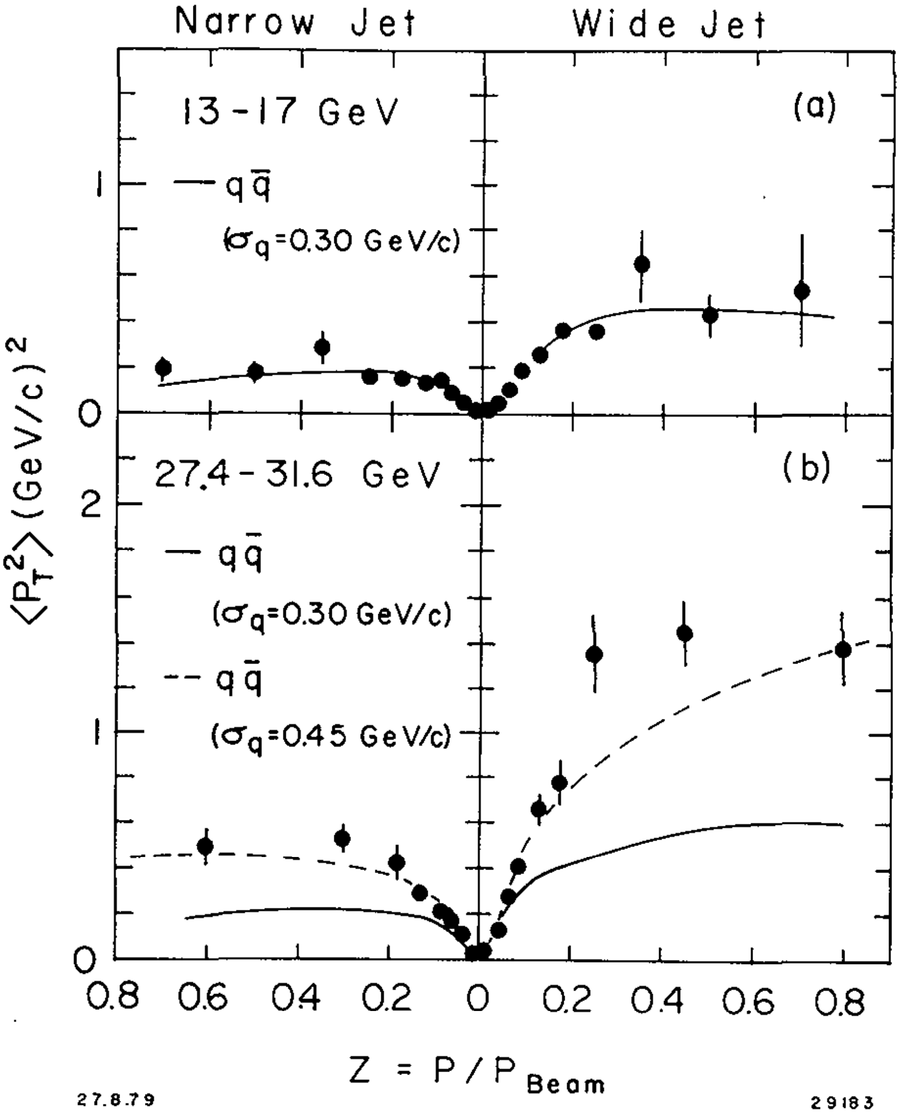

Fig. 11.19 Average p_T^2 for charged hadrons with respect to the jet axis as a function of the fractional hadron momentum $z = P/P_{beam}$ separately for the narrow and the wide jet.
(a) for 13, 17 GeV combined
(b) for 27.4 - 31.6 GeV combined.
The curves show the prediction of the $q\bar{q}$ model with σ_q= 0.3 GeV/c (solid) and 0.45 GeV/c (dashed). The model includes u, d, s, c, b quarks. (TASSO 11.26).

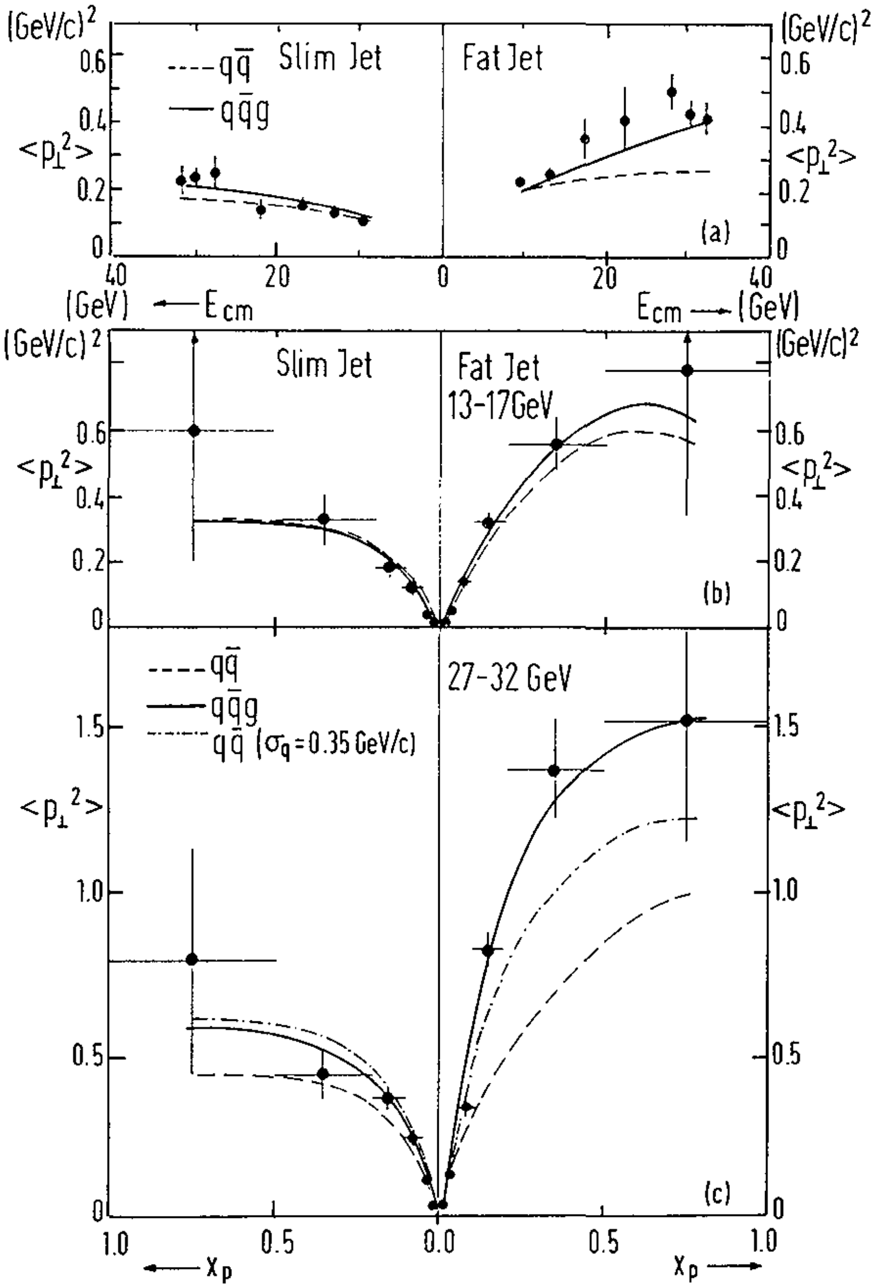

Fig. 11.20 Average observed p_T^2 of charged particles in the slim and fat jets, respectively, as function of the cm energy (a). Sea-gull plots: $<p_T^2>$ of charged particles as function of x_p - for slim and fat jets in two separate energy ranges (b and c). The solid and dashed lines are $q\bar{q}g$ and $q\bar{q}$ predictions, respectively. (PLUTO 11.34).

11.8 Planar Events and Three-Jet Structure

The event shapes were studied by TASSO, PLUTO and JADE using the momentum tensor ellipsoid[11.35] and by MARK J determining the oblateness.

Momentum tensor ellipsoid

For each event one constructs the second rank tensor from the hadron momenta

$$M_{\alpha\beta} = \sum_{j=1}^{N} p_{j\alpha}\, p_{j\beta} \qquad (\alpha,\beta = x, y, z)$$

summing over all N observed charged particles. Let $\hat{n}_1$, $\hat{n}_2$ and $\hat{n}_3$ be the unit eigenvectors of this tensor associated with the eigenvalues Λ_1, Λ_2 and Λ_3 which are ordered such that $\Lambda_1 < \Lambda_2 < \Lambda_3$. Note that

$$\Lambda_i = \Sigma(\vec{p}_j \hat{n}_i)^2$$

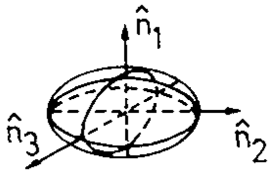

The principal axis is the $\hat{n}_3$ direction, the event plane is the $\hat{n}_2$, $\hat{n}_3$ plane and $\hat{n}_1$ defines the direction in which the sum of the square of the momentum components is minimized.

Define the normalized eigenvalues

$$Q_i = \frac{\Lambda_i}{\Sigma p_j^2} = \frac{\Sigma(\vec{p}_j \cdot \hat{n}_i)^2}{\Sigma p_j^2}$$

The Q_i satisfy the relation

$$Q_1 + Q_2 + Q_3 = 1$$

The events will be expressed in terms of the two variables aplanarity A and sphericity S

$$A = \frac{3}{2} Q_1$$

$$S = \frac{3}{2}(Q_1 + Q_2) = \frac{3}{2}(1 - Q_3)$$

Since $0 < Q_1 < Q_2 < Q_3 < 1$ all events lie inside a triangle. Collinear events are found at $S \approx 0$, noncollinear coplanar at $S \neq 0$, $A \approx 0$ and spherical events have both S and A large.

Planar events

In Figs. 11.21 - 11.23 the distributions of

$$\langle p_T^2 \rangle_{out} = \frac{1}{N} \sum_{j=1}^{N} (\vec{p}_j \cdot \hat{n}_1)^2$$

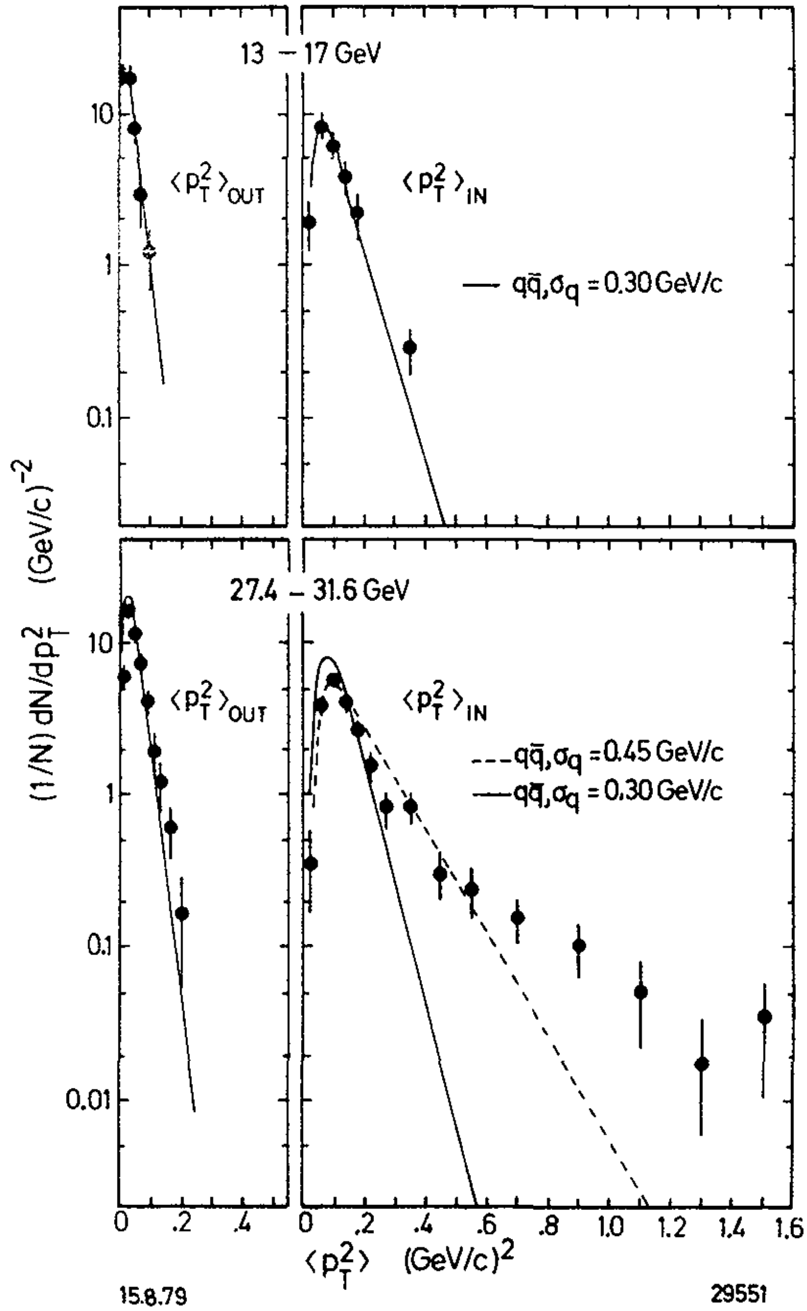

Fig. 11.21 The mean transverse momentum squared normal to the event plane $<p_T^2>_{out}$ and in the event plane $<p_T^2>_{in}$ per event as measured by TASSO (Ref.11.26) at 13, 17 GeV and 27.4 - 31.6 GeV. The predictions from the quark model are shown assuming σ_q = 0.30 GeV/c (solid curves) and σ_q = 0.45 GeV/c (dotted curve). The model includes u,d,s,c and b quarks.

(= square of the momentum component normal to the event plane given by $\hat{n}_2$ and $\hat{n}_3$) are compared with that of

$$\langle p_{T\,in}^2 \rangle = \frac{1}{N} \sum_{j=1}^{N} (\vec{P}_j \cdot \hat{n}_2)^2$$

(= square of the momentum component in the event plane perpendicular to the jet axis). The data from TASSO[11.26], PLUTO[11.34] and JADE[11.36] show little increase in $\langle p_{T\,out}^2 \rangle$ from low to high energy data. The distribution of $\langle p_{T\,in}^2 \rangle$, however, becomes much wider at high energies; in particular there is a long tail of events with high $\langle p_{T\,in}^2 \rangle$. The predictions of the $q\bar{q}$ model are also shown. Hadrons resulting from pure $q\bar{q}$ jets will on the average be distributed uniformly around the jet axis. However, some asymmetry between $\langle p_{T\,out}^2 \rangle$ and $\langle p_{T\,in}^2 \rangle$ is caused by statistical fluctuations. Fair agreement with the $q\bar{q}$ model is found at the low energy point. Thus the asymmetry observed at this energy can be explained by statistical fluctuations alone.

At high energy, one finds fair agreement for $\langle p_{T\,out}^2 \rangle$ with the $q\bar{q}$ model with $\sigma_q \sim 0.3$ GeV/c, however, the long tail of the $\langle p_{T\,in}^2 \rangle$ distribution is not reproduced by the model. This discrepancy cannot be removed by increasing σ_q. The result with $\sigma_q = 0.45$ GeV/c is also plotted in Fig. 11.21. The agreement is poor. One therefore must conclude that the data include a number of planar events that are not reproduced by the $q\bar{q}$ model independent of the assumption on the average p_T in that model.

The same conclusion was reached by the MARK J[11.37] group which studied the energy distribution ("energy flow") in the events. The coordinate system used is defined by the <u>thrust axis</u> ($\hat{e}_1$ = jet axis),

$$\text{Thrust} = \max. \frac{\sum_i |\vec{p}_i\ \hat{e}_1|}{\sum_i |p_i|}$$

where $\vec{p}_i$ is the energy flow detected by a counter; the <u>major axis</u> ($\hat{e}_2$) which is perpendicular to $\hat{e}_1$ and which is the direction along which the projected energy flow in that plane is maximized:

$$\text{Major} = \max. \frac{\sum_i |\vec{p}_i\ \hat{e}_2|}{\sum_i |p_i|} ;$$

the <u>minor axis</u> which is orthogonal to $\hat{e}_1$ and $\hat{e}_2$.

The difference Major - Minor is a measure for the planarity of an event and is called oblateness,

$$O = \text{Major} - \text{Minor}$$

The distribution of the oblateness is plotted in Fig. 11.24 together with predictions of the $q\bar{q}$ and $q\bar{q}g$ models. The 17 GeV data are reproduced by both models. At the higher energies (27.4 - 31.6 GeV) an excess of events with large oblateness, i.e. planar events, is observed. This conclusion is reached independently of the value of σ_q used for the quark model.

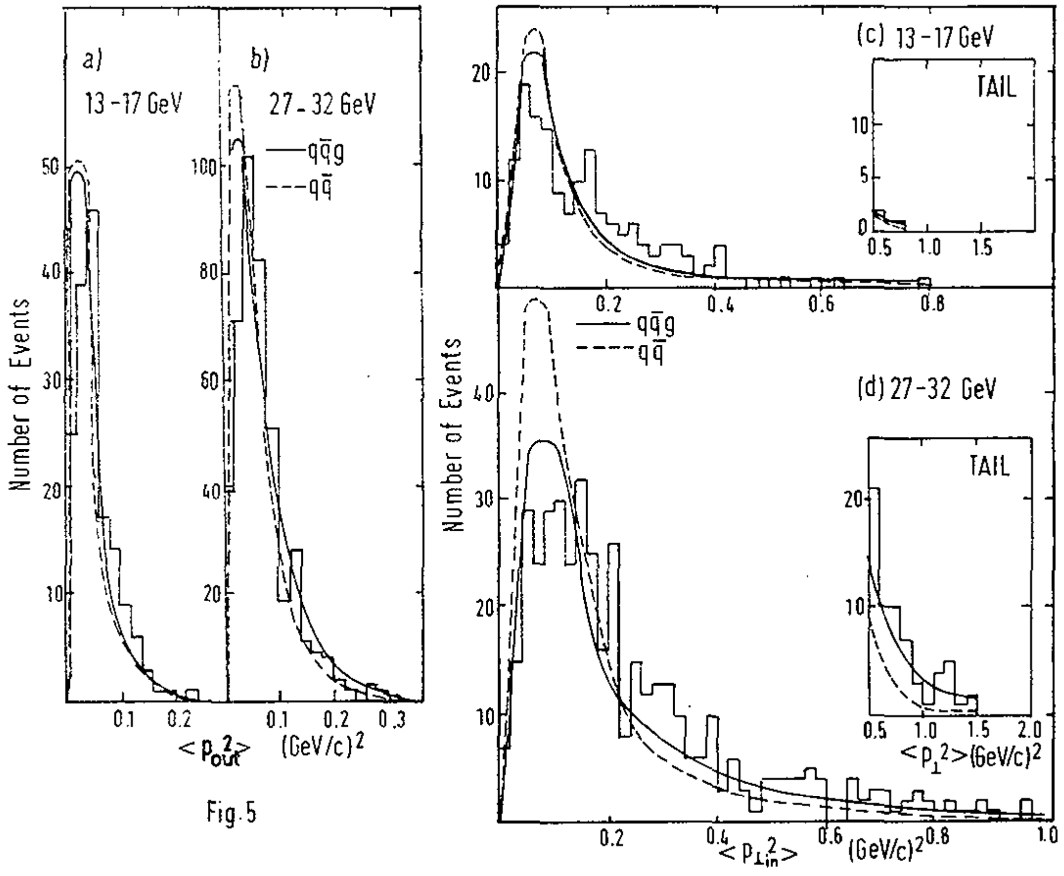

Fig. 11.22 Distributions of $<p^2_{Tout}>$ and $<p^2_{Tin}>$ for the lower and higher energy regions. Solid and dashed lines are $q\bar{q}g$ and $q\bar{q}$ predictions, respectively. (PLUTO 11.34)

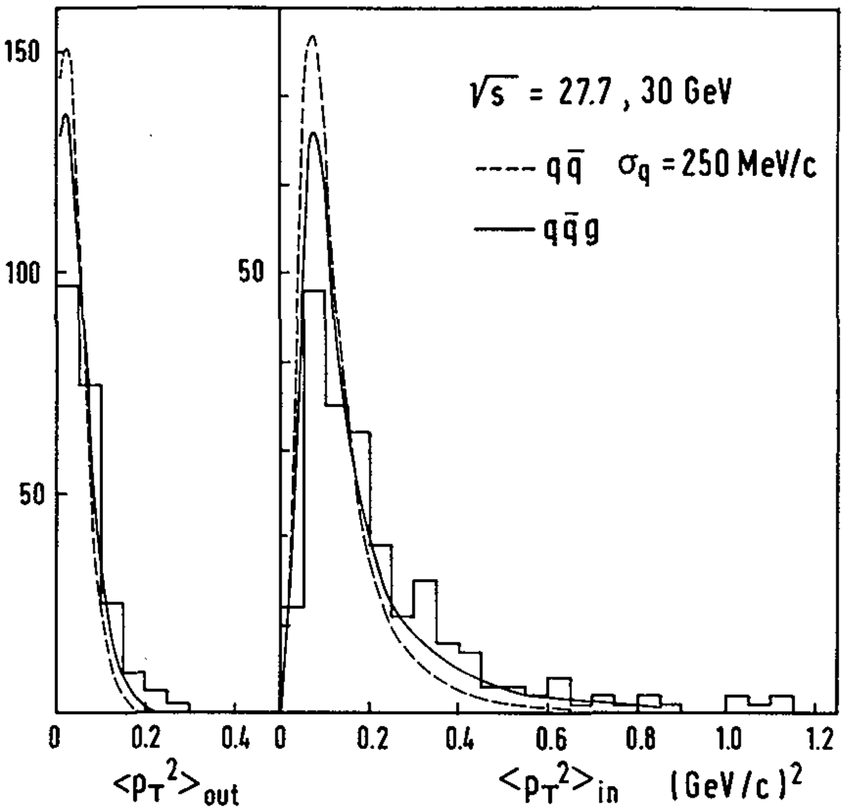

Fig. 11.23 Distributions of mean transverse momentum squared per event for charged particles, normal to ($\langle p_T^2 \rangle_{out}$) and in ($\langle p_T^2 \rangle_{in}$) the event plane. (JADE, Ref.11.1).

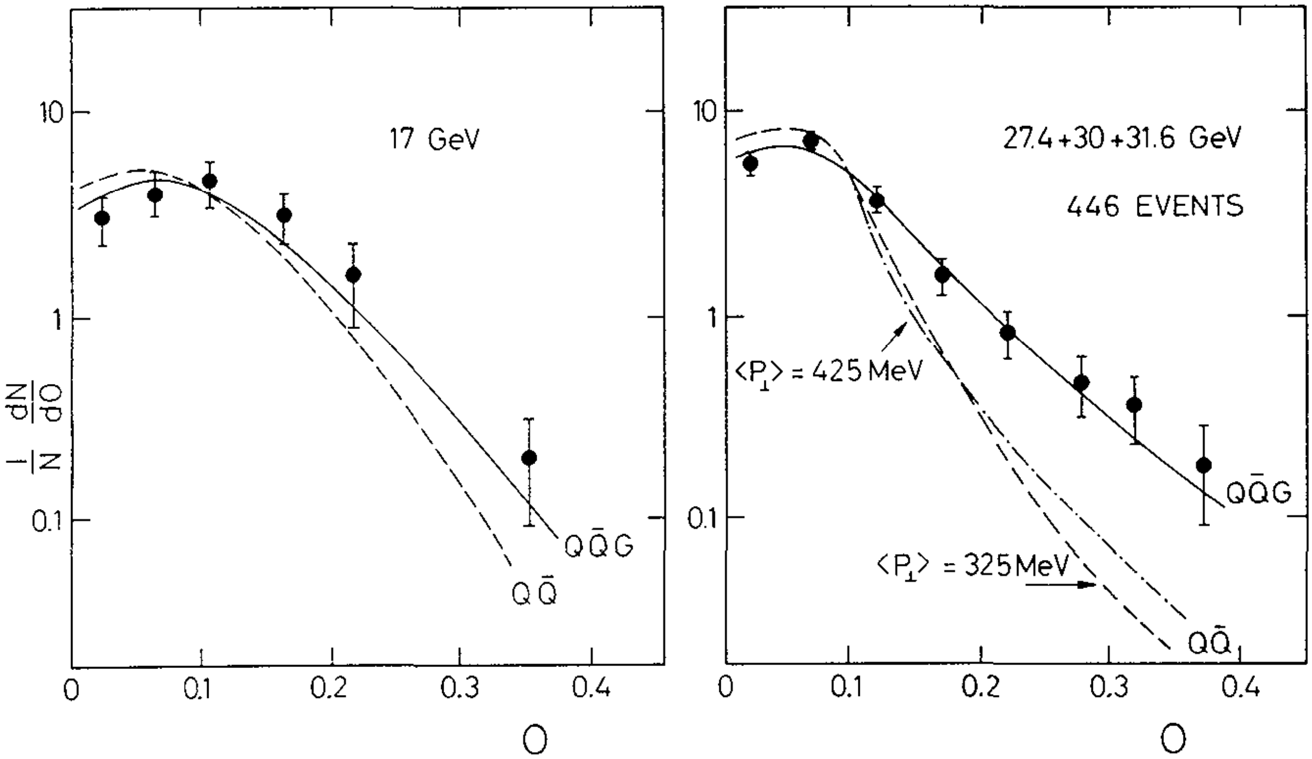

Fig. 11.24 The Oblateness distribution, O = Major-Minor, at 17 and 27.4-31.6 GeV (MARK J, Ref. 11.37).

Three jet structure

The data presented in the preceding paragraph demonstrated the existence of planar events. In order to check whether the particle momenta are distributed uniformly in the plane (disc like) or collimated into three jets the TASSO group adopted the procedure by Wu and Zobernig[11.35]. Each events is analysed as a three jet event. The particles are grouped into three classes C_1, C_2 and C_3 and for each class the sphericity is determined:

$$S_n = 3/2 \sum_{j\in C_n} \frac{q_{T_j}^2}{p_j^2}$$

The q_{T_j} are transverse momentum components in the event plane (defined by $\hat{n}_2$, $\hat{n}_3$) relative to the jet axis which is chosen such as to minimize S_n. By considering all possible combinations one finds that grouping for which

$$S_1 + S_2 + S_3 = \text{minimum}.$$

Fig. 11.25 shows the first data of TASSO at W = 27.4 GeV presented by Söding at the Geneva Conference (Ref. 11.24): on top the $<p_{T\ out}^2>$ and $<p_{T\ in}^2>$ distributions, the latter with an excess of large $<p_{T\ in}^2>$ events extending beyond 1 GeV^2. For the bottom figure the events were treated as three-jet events. Plotted is the average of the transverse momentum per jet measured relative to the three jet axes. The average value is around 0.1 GeV^2, the largest value 0.55 GeV^2. The shape of the distribution agrees with that predicted for $q\bar{q}$ jets (two jets) with σ_q = 0.3 GeV/c (see curve). Thus, for the large $<p_{T\ in}^2>$ events (when analysed as two jet events) the particle momenta are collimated along three jet axes.

The following figures show results for c.m. energies between 27.4 and 31.6 GeV obtained with the larger data sample available for the FNAL meeting. In Fig. 11.26a the Dalitz plot distribution of the angles Θ_1, Θ_2 and Θ_3 between the jets is shown; the ordering is such that $\Theta_1 \leq \Theta_2 \leq \Theta_3$. Two-jet events cluster near $\Theta_1 = 0$ and along $\Theta_3 \approx 180^o$. In order to suppress these, events with $\Theta_1 > 40^o$ were selected. Approximately 15 % of all events satisfied this requirement. Let $<p_T^2>$ be the average of the transverse momentum squared per jet (treating the events as three-jet events). Fig. 11.26b shows the $<p_T^2>$ distribution; the average $<p_T^2>$ value is 0.27 GeV/c. This demonstrates again the strong collimation of the particle momenta around three axes.
At lower energy (13, 17 GeV) the data had been found to be in good agreement with the $q\bar{q}$ model. In Fig. 11.26c the $<p_T^2>$ distribution is shown for all events at 13, 17 GeV treating them as two-jet events. The distribution is almost identical to the one in Fig. 11.26b. In other words the high energy events analysed as three-jet events and the lower energy events analysed as two-jet events exhibit nearly the same p_T^2 distributions.

Comparison with gluon bremsstrahlung

As we have seen above the jet broadening and the existence of planar events which in fact are three-jet events was demonstrated in a model independent way. The observation of three-jet events at high energies lends strong support to QCD. In this section we discuss briefly the quantitative comparison between theory and data.

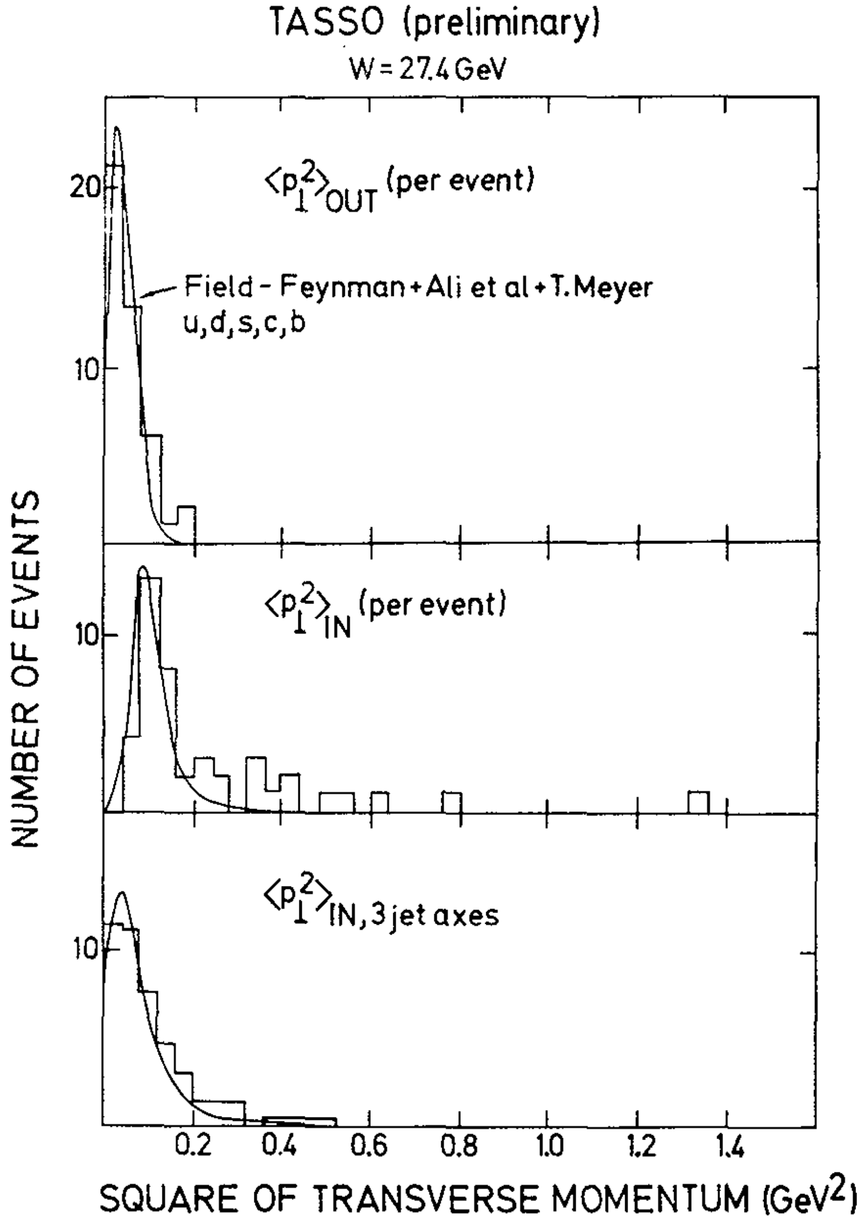

Fig. 11.25 Distribution of the average squared transverse momentum component out of the event plane (top), and in the event plane (center), for events at W = 27.4 GeV (averaging over charged hadrons only). The curves are for $q\bar{q}$ jets without gluon bremsstrahlung. Comparison of these distributions gives evidence that broadening (compared to $q\bar{q}$ jets) occurs in one plane. The bottom figure shows $\langle p_\perp^2\rangle$ per jet when 3 jet axes are fitted, again compared with the q jet model. (TASSO, Ref. 11.24)

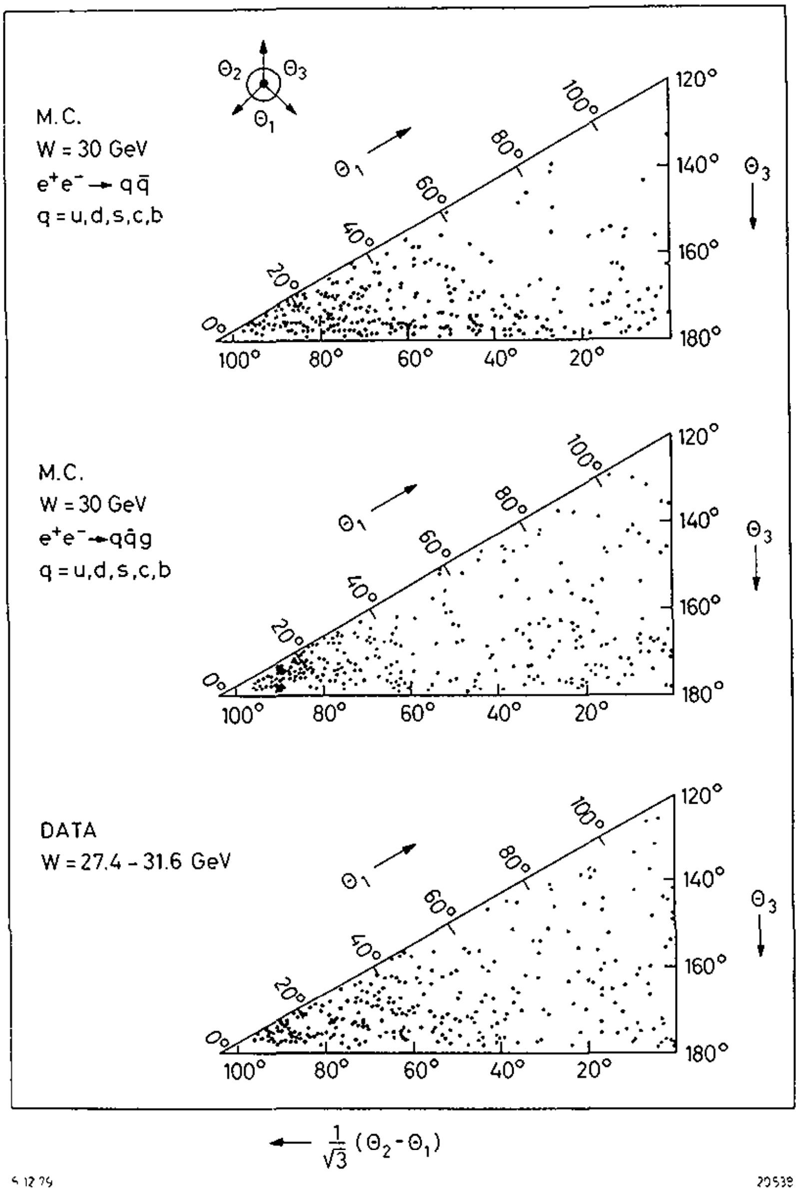

Fig. 11.26a Events analysed as three-jet events. Shown are the Dalitz plot distributions for the angles $\Theta_1, \Theta_2, \Theta_3$ between the jet axes for Monte Carlo events produced according to the $q\bar{q}$ model (a), the $q\bar{q}g$ model (b) and for the measured data (c). Θ_1 is defined as the angle opposite the jet with the largest total momentum, Θ_3 is opposite the jet with the smallest total momentum. (TASSO)

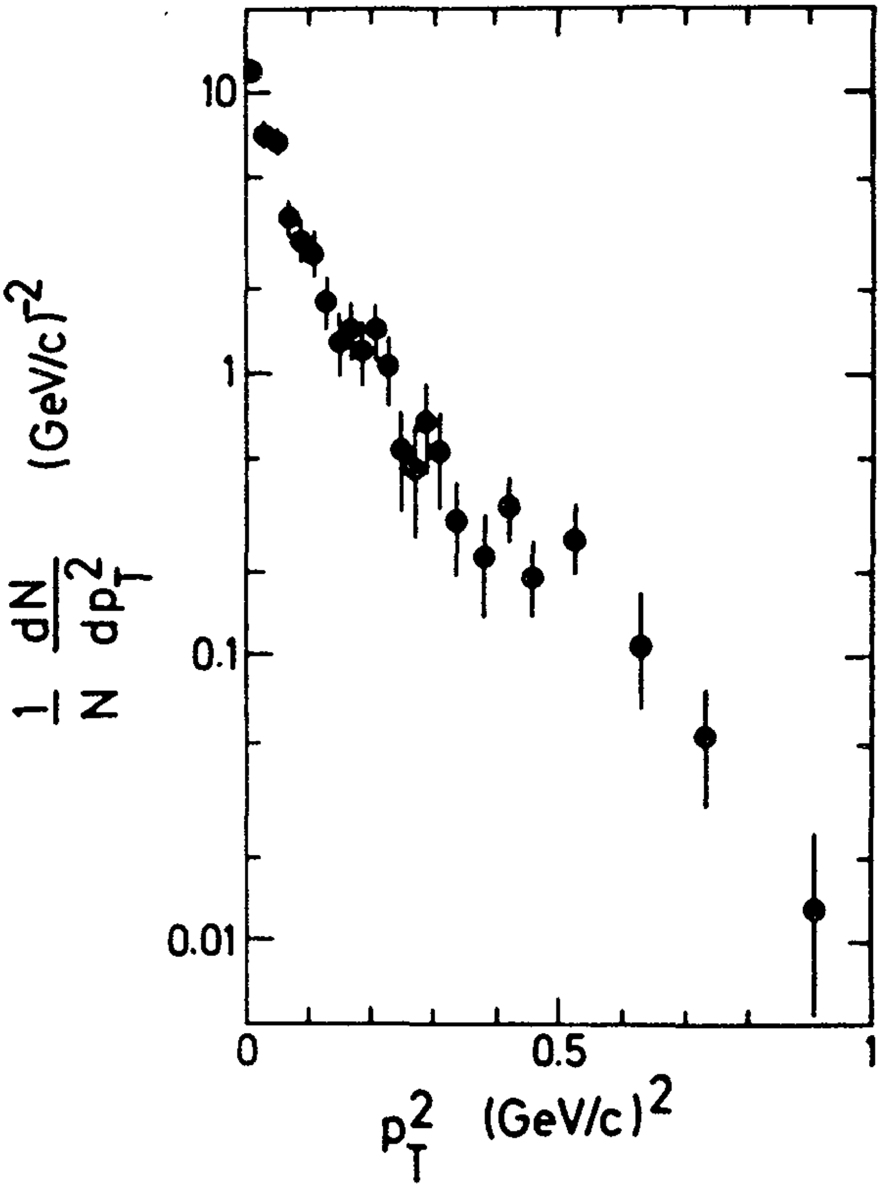

Fig. 11.26b The distribution of the square of the transverse momentum relative to the jet axis at 27.4 - 31.6 GeV for three jet candidates selected by the requirement $\Theta_1 > 40^o$ and analysed as three-jet events. (TASSO)

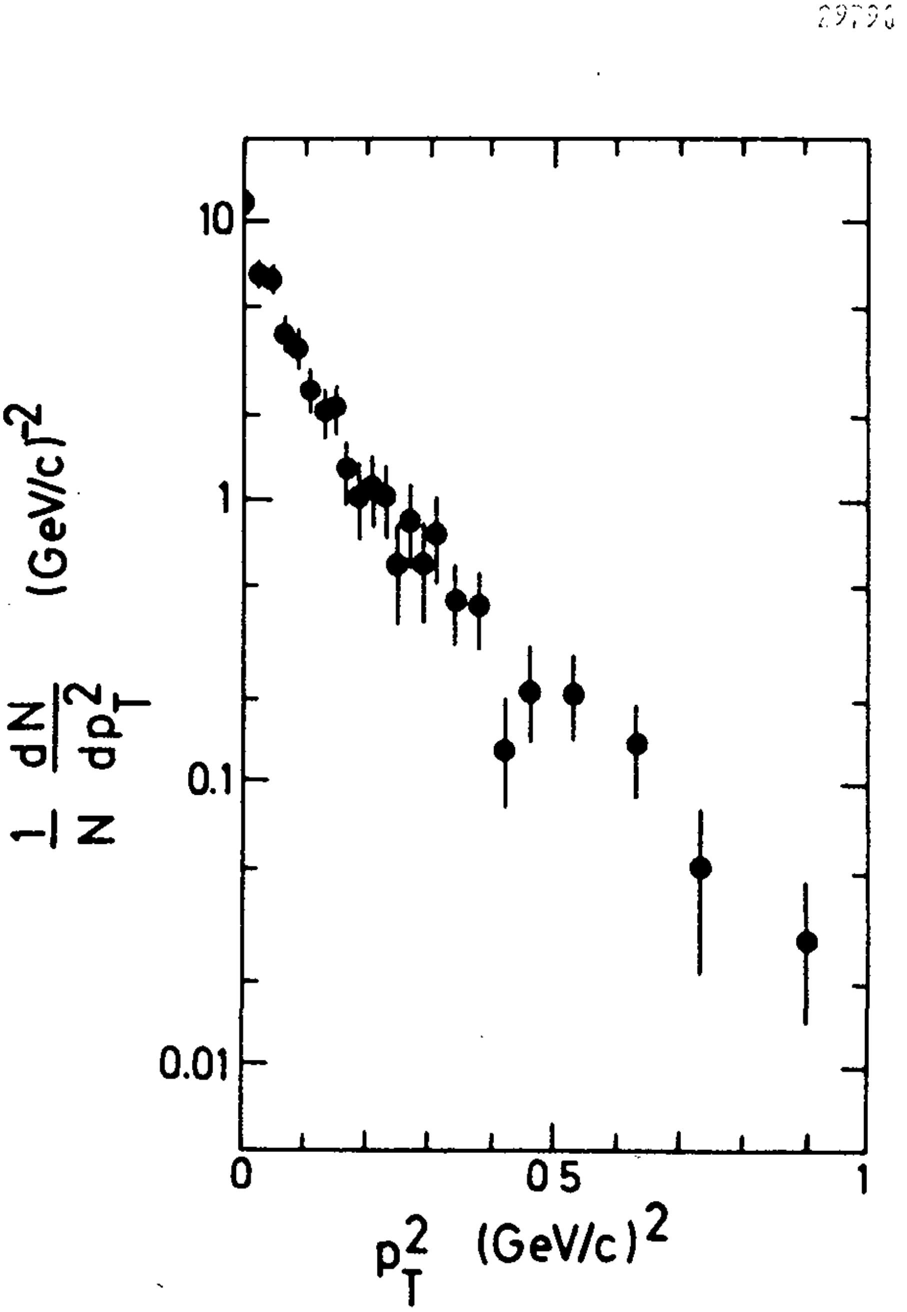

Fig. 11.26c The distribution of the square of the transverse momentum relative to the jet axis at 13 GeV for all events analysed as two-jet events. (TASSO)

Fig. 11.27 shows from TASSO[11.26] the distribution of aplanarity versus sphericity S for low and high energies. Collinear two-jet events are seen to dominate at all energies. To exclude collinear events $S > 0.25$ was required. The remaining events were classified as planar (nonplanar) demanding $A < 0.04$ ($A > 0.04$). Table 11.2 lists the number of events observed together with the predictions of the $q\bar{q}$ model for $\sigma_q = 0.30$ and 0.45 GeV/c, and for $q\bar{q}$ production with gluon bremsstrahlung ($q\bar{q}g$) taking Λ to be 0.5 GeV. The gluon fragmentation function - which is unknown - was assumed to be the same as for quarks (with $\sigma_q = 0.30$ GeV/c). The number of planar events agrees well with the $q\bar{q}g$ prediction.

Table 11.2: Comparison of the observed number of noncollinear events with the qq and $q\bar{q}g$ predictions for 27.4 - 31.6 GeV (11.26). (TASSO)

	observed	σ_q=0.30 GeV/c	σ_q=0.45 GeV/c	$q\bar{q}g$[11.33]
noncollinear planar events $S>0.25$, $A<0.04$	18	4.5	4.5	~17
noncollinear nonplanar events $S>0.25$, $A>0.04$	38	32	38	~35

A similar comparison was performed by JADE[11.1, 11.36] which is shown in Fig. 11.28 and Table 11.3.

Table 11.3: Observed and expected numbers of events at 27.4 - 31.6 GeV inside the cut (11.1) $(Q_3 - Q_2)/\sqrt{3} < 0.35$ and $Q_1 < 0.07$ (JADE).

observed	expected	
	$q\bar{q}$ model σ_q = 250 MeV/c	$q\bar{q}g$ model
23 events	6 events	22 events

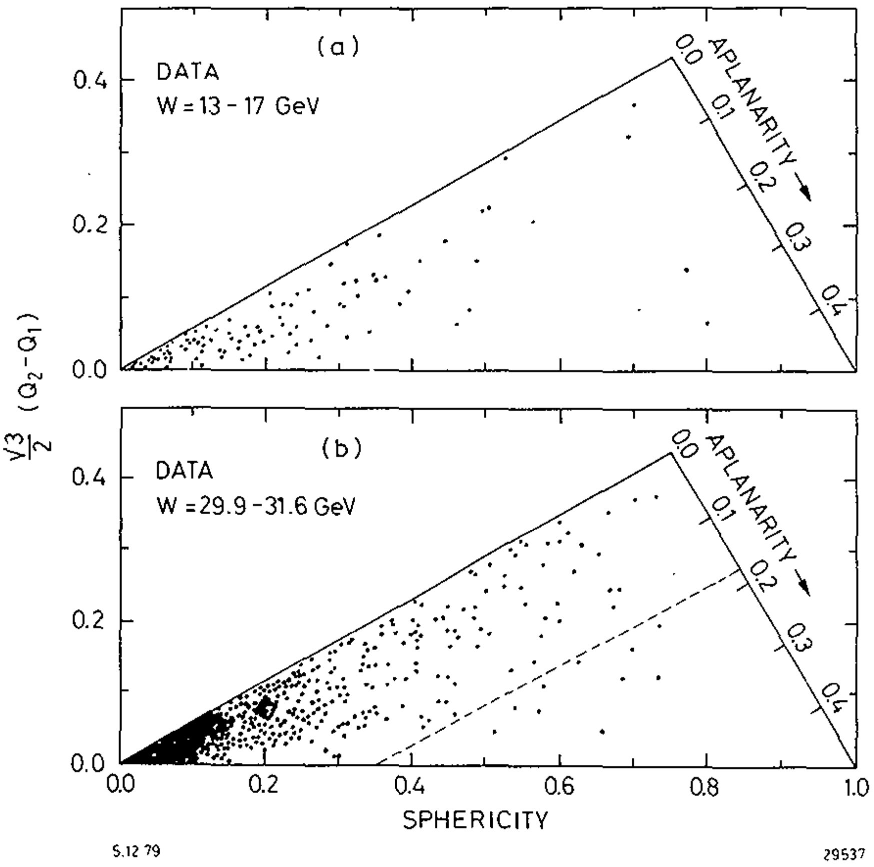

Fig. 11.27 Distribution of the events as a function of aplanarity A = 3/2 Q_1 = 3/2 $\langle p_{T\ out}^2 \rangle / \langle p^2 \rangle$ and sphericity S = 3/2 $(Q_1 + Q_2)$ = 3/2 $\langle p_T^2 \rangle / \langle p^2 \rangle$ at 13 - 17 GeV (a) and 29.9 - 31.6 GeV (b). (TASSO, Ref. 11.26).

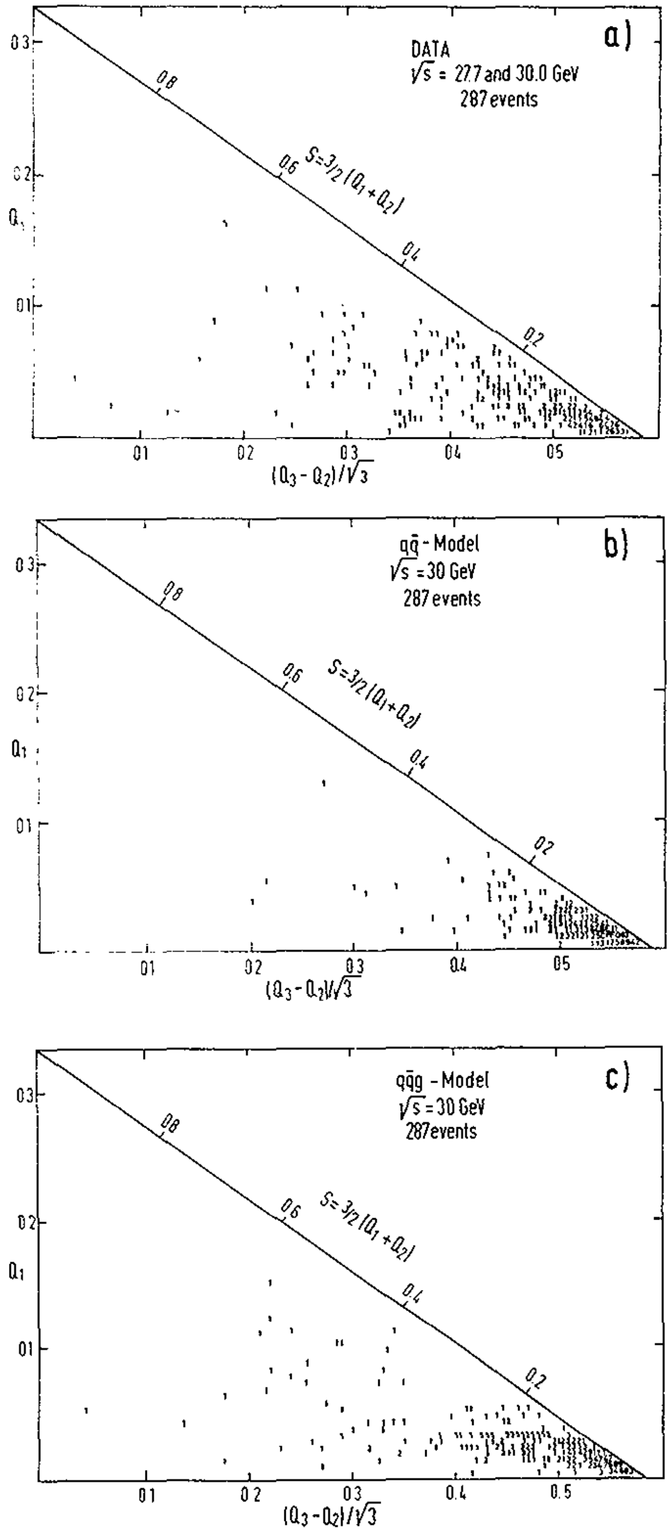

Fig. 11.28 "Event shape" Q-plot (JADE, 11.1)

a) High energy data

b) $q\bar{q}$ model prediction with σ_q = 250 MeV/c

c) $q\bar{q}g$ model prediction

The planarity ($Q_2 - Q_1$) axis is perpendicular to the sphericity axis. The dotted line indicates planarity = 0.07.

The PLUTO group 11.34) used the triplicity method (see sect. 10) to study the jet angular distribution (see Fig. 11.29). The angular Dalitz plot distribution serves as a direct test of hard gluon bremsstrahlung: It is rather insensitive to the quark and gluon fragmentation functions.

Fig. 11.29d shows a scatter diagram of triplicity T_3 thrust T. Two-jet events have T close to 1. Three jet events are characterized by T_3 close to 1. Fig. 11.29 gives the angular Dalitz plot. Three-jet events defined by $T_3 > 0.9$ and $T < 0.8$ are marked by open circles. In Table 11.4 a comparison between observed and predicted event numbers is made. The high energy data are inconsistent with the $q\bar{q}$ model, but are in good agreement with gluon bremsstrahlung.

Table 11.4: Observed and expected numbers of events obeying different selection criteria (PLUTO 11.34)

E_{cm} (GeV)	selected region	events observed	events expected (σ_q=250MeV/c)		events exp. (σ_q=300MeV/c)		events exp. (σ_q=350MeV/c)
			$q\bar{q}$	$q\bar{q}g$	$q\bar{q}$	$q\bar{q}g$	$q\bar{q}$
13-17	$T_3 > 0.9$, $T < 0.8$ (3-jet events)	24	11	15	15.5	17.5	20
	$\theta_3 < 150^o$	32	25	32	27	33	29
	$<p^2_{\perp in}> > 0.5 GeV^2/c^2$	5	5	5	7	10	9
	$S>0.25$, $Q_1<0.03$ (planar events)	7	8	8	9	9	11
27-32	$T_3 > 0.9$, $T < 0.8$ (3-jet events)	48	11	43	23.5	48.5	36
	$\theta_3 < 150^o$	52	19	51	25	50	31
	$<p^2_{\perp in}> > 0.5 GeV^2/c^2$	68	23	56	30	61	37
	$S>0.25$, $Q_1<0.03$ (planar events)	35	12	30	17	30	22

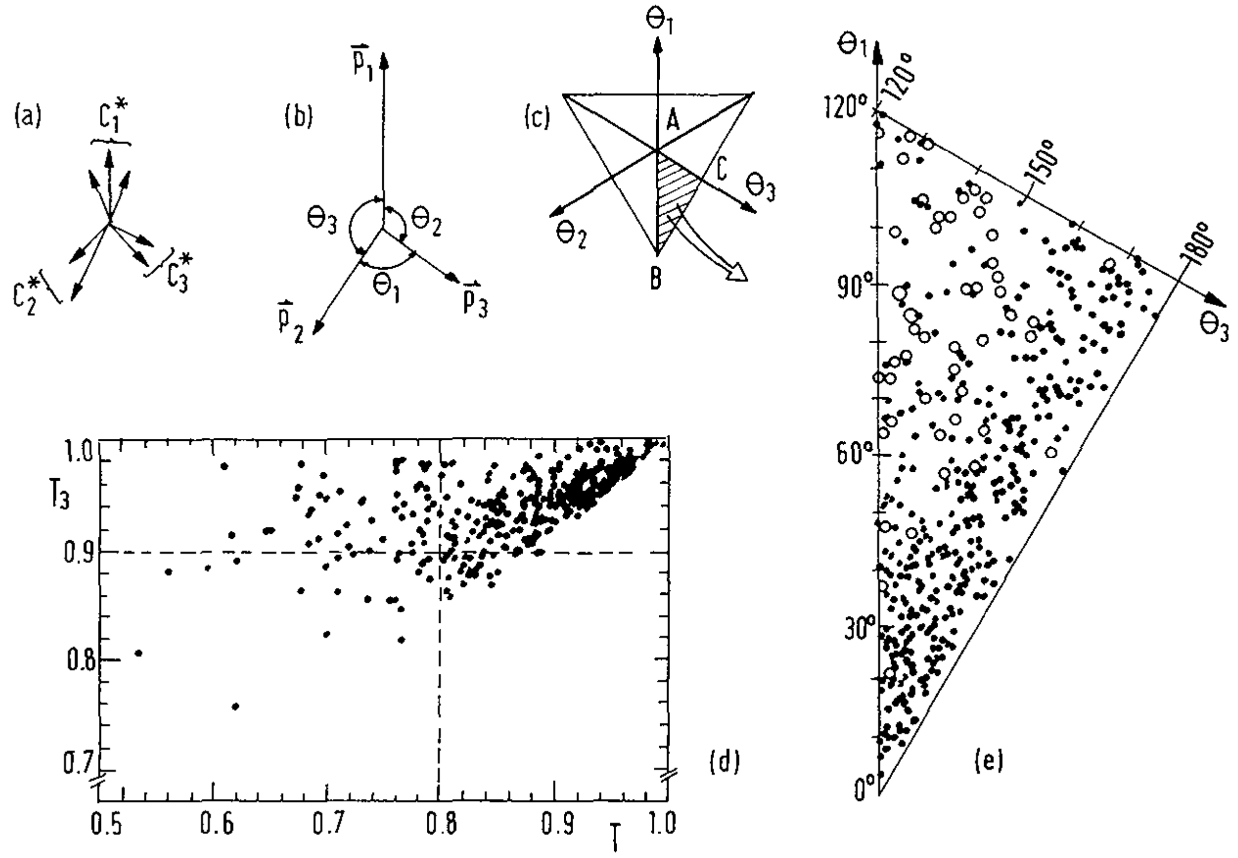

Fig. 11.29 Momentum configuration of hadrons (a) and jets (b) obtained by grouping hadrons into 3 classes according to the triplicity method. A Dalitz plot (c) can be spanned by the angles between the jets whose shaded area only is populated. Nearly symmetrical 3-jet events will be situated near point A. The data at E_{cm} = 27.6, 30 and 31.6 GeV are shown in a scatter diagram of triplicity versus thrust (d) and in the angular Dalitz plot (e). In (d) planar events will be in the upper left of the plot characterized by low thrust and high triplicity, e.g. $T < 0.8$ and $T_3 > 0.9$. Events falling in this category show up as large circles in (e). (PLUTO, Ref. 11.34).

Recently, an attempt was made to confront in a consistent way the various experimental results from PETRA with the predictions of QCD treating σ_q and $\alpha_s(s)$ (or Λ) as free parameters[11.38]. The one s.d. limits found were $0.28 \leq \sigma_q \leq 0.30$ GeV/c and $0.20 \leq \alpha_s$ ($Q^2 = 900$ GeV^2) ≤ 0.25 corresponding to $0.5 \leq \Lambda \leq 1.2$ GeV. With these parameter values an impressive fit to the data was obtained.

If gluon bremsstrahlung is the correct explanation and if the gluon materializes as a jet of hadrons with limited transverse momentum then for a small fraction of the events the three-jet structure should be directly visible. In Figs. 11.30 - 11.33 we display a two-jet and several three-jet events observed by TASSO [11.26], PLUTO[11.3] and JADE[11.1].

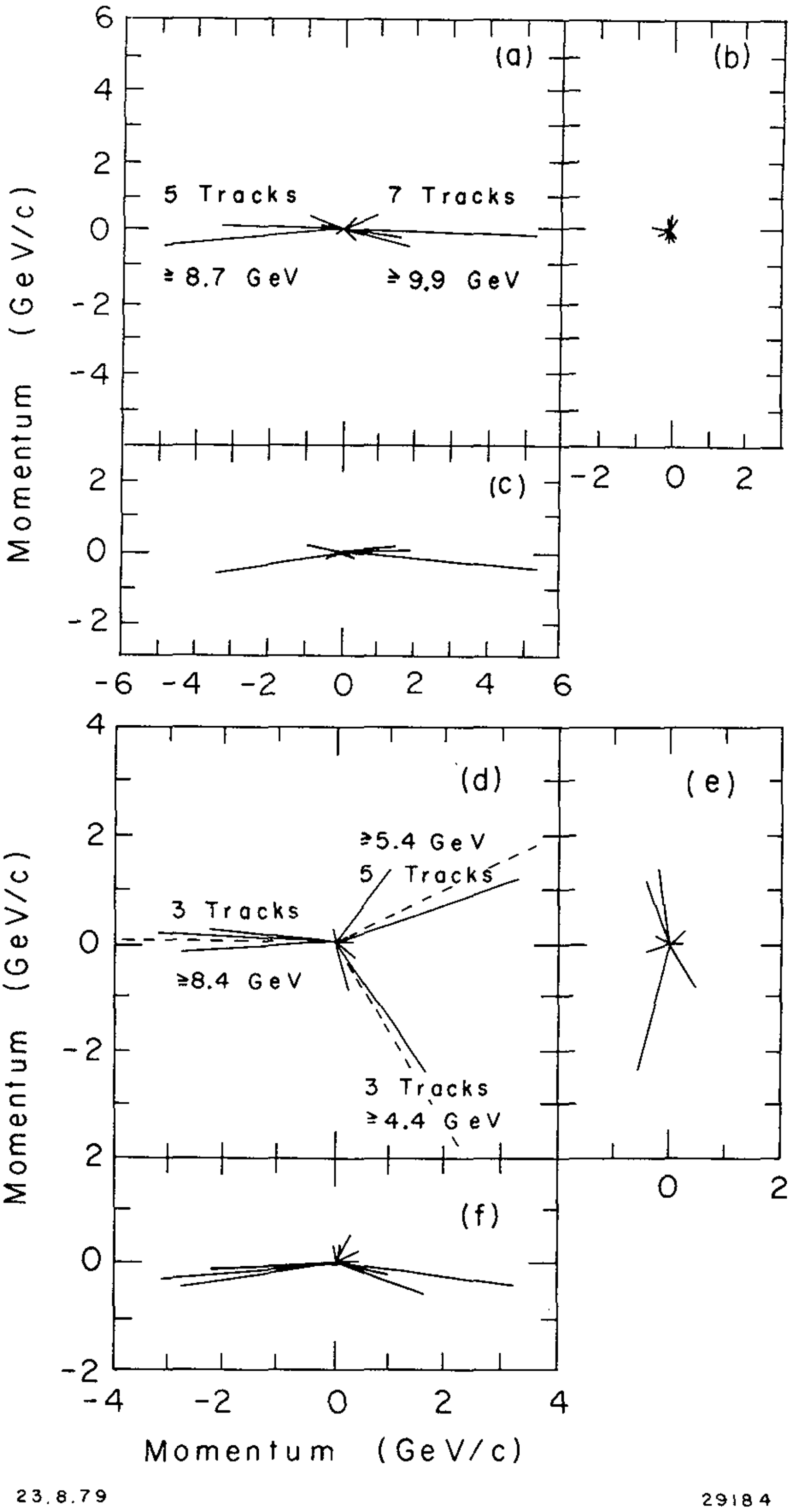

Fig. 11.30 Momentum space representation of a 2-jet event (a–c) and a 3-jet event (d–f) in each of three projections.

(a,d) = $\hat{n}_2 - \hat{n}_3$ plane

(b,e) = $\hat{n}_1 - \hat{n}_2$ plane

(c,f) = $\hat{n}_1 - \hat{n}_3$ plane.

The dotted lines show the fitted jet exes. (TASSO, Ref. 11.26).

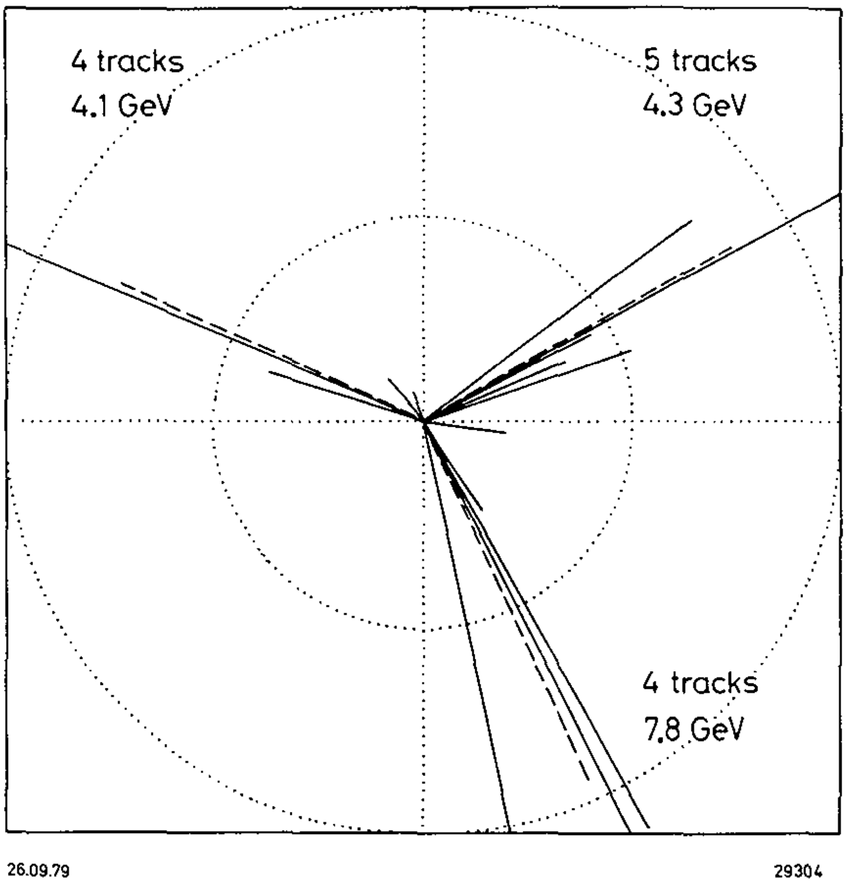

Fig. 11.30g Another 3-jet event projected into the event plane. (TASSO Ref. 11.4)

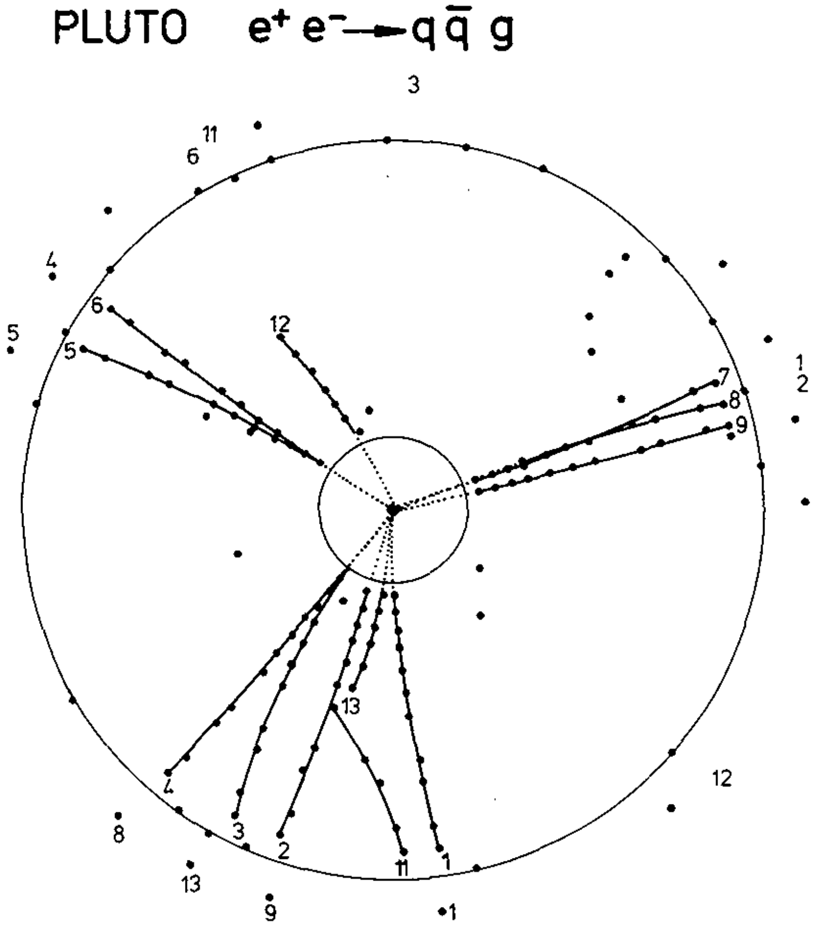

Fig. 11.31 A three jet event observed by PLUTO.

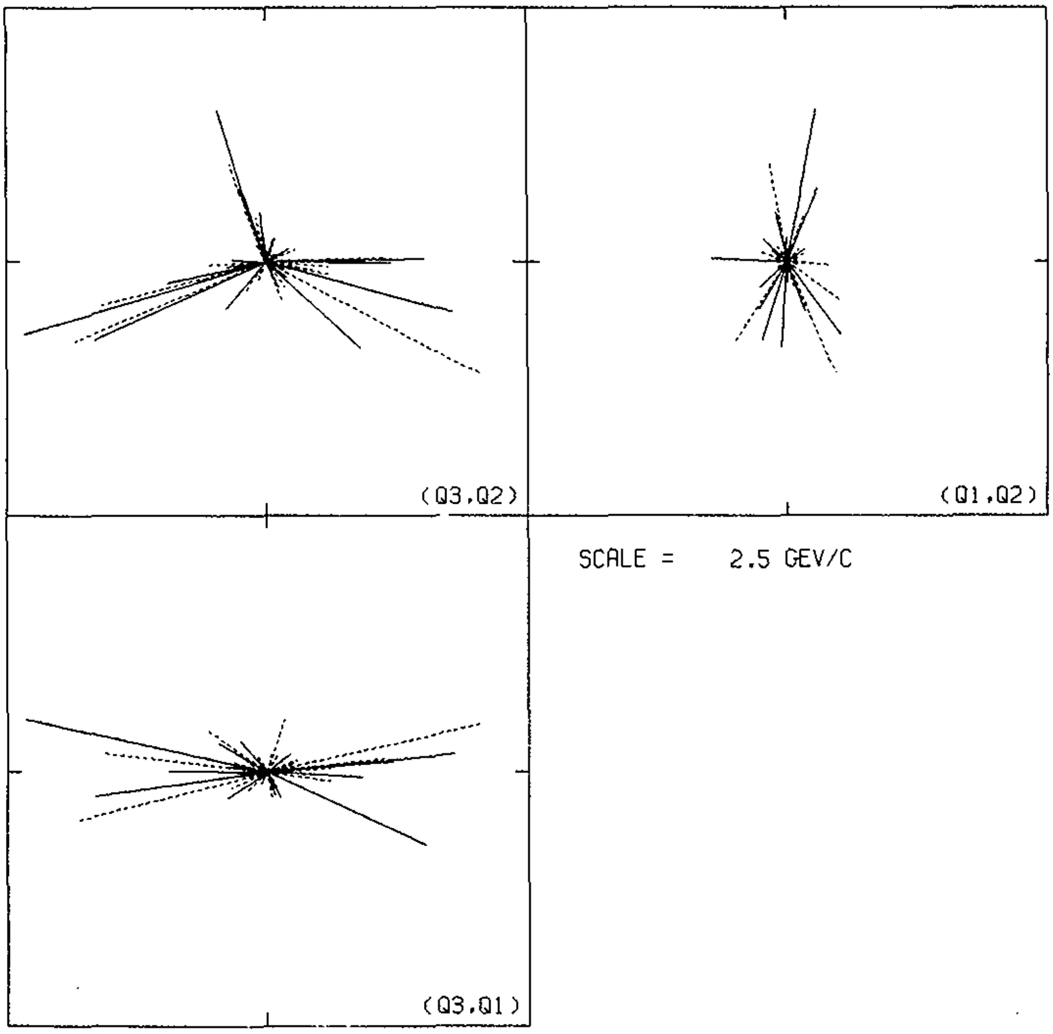

Fig. 11.32 The three projections of a three jet event. The solid lines indicate charged particle tracks, the dashed photons (JADE, Ref. 11.1).

11.9 Search for the t Quark

The observed symmetry between leptons and quarks suggests besides u, d, s, c, b the existence of a sixth quark, t. The charge of the t quark is predicted to be +2/3 if one groups the quarks in weak isospin doublets, viz.

$$\begin{pmatrix} u \\ d \end{pmatrix}, \quad \begin{pmatrix} c \\ s \end{pmatrix}, \quad \begin{pmatrix} t \\ b \end{pmatrix}$$

The theoretical predictions for the t mass populate mass values between 10 and 40 GeV[11.39]. The observed spacing between ψ, J/ψ and Υ would suggest for the $t\bar{t}$ vector ground state

$$m_{V_t} = m_{\Upsilon}^2 / m_{J/\psi} = 28 \text{ GeV}$$

which is in the reach of PETRA. The peak height of the total cross section at the position of V_t depends on the leptonic decay width Γ_{ee} and on the energy spread of the storage ring beams. The Breit-Wigner without energy spread reads

$$\sigma(e^+e^- \to V_t) = \frac{3\pi}{s} \frac{\Gamma_{ee}\,\Gamma}{(M_o - W)^2 + \Gamma^2/4}$$

The energy spread of the beams, ΔE, reduces the peak cross section - very roughly - to

$$\sigma_{peak} \approx \frac{3\pi}{s} \cdot \frac{\Gamma_{ee}}{\Delta W}$$

where $\Delta W = 2 \cdot \Delta E$. For PETRA

$$\Delta E/E = 6.5 \cdot 10^{-5}\, E, \qquad E \text{ in GeV}$$

For a mass of 28 GeV (E = 14 GeV) the energy spread is ΔE = 13 MeV. The leptonic width Γ_{ee} depends on the shape of the $t\bar{t}$ potential. Various models studied[11.40] suggest that Γ_{ee} is approximately the same as for the J/ψ, Γ_{ee} = 5 keV. This yields

$$\sigma_{peak} \text{ (28 GeV)} \approx 1.3 \text{ nb}$$

$$R_{peak} \text{ (28 GeV)} \approx 11.$$

The signal to noise ratio is 11:4 or ≈3. This may be compared with the J/ψ seen at SPEAR or DORIS where the signal to noise ratio is roughly 100.

The $c\bar{c}$ system has two bound $^3S_1$ vector states, J/ψ and ψ'; the $b\bar{b}$ system probably has three while the $t\bar{t}$ is expected[11.40] to have 6 or 7 bound states 1^3S_1 .... 6^3S_1 as sketched in Fig. 11.33. One may guess that the $t\bar{t}$ continuum is likely to begin two or three pion masses above the $T\bar{T}$ threshold (where T denotes a $t\bar{q}$ meson), i.e. $W_{continuum} = M(6^3S_1) + 2{:}3\, m_\pi = M(V_t) + 2$ GeV.

While it may require a large effort to localize the vector states, it should be straight forward to detect the $t\bar{t}$ continuum contribution provided the available energy is sufficient. The asymptotic $t\bar{t}$ contribution should be $R_t = 3 \cdot (\frac{2}{3})^2 = \frac{4}{3}$. Near threshold it is likely to be larger. Comparing with the charm contribution near 4 - 4.5 GeV, one may expect $R_t = 2$ or $R = 6$ above $t\bar{t}$ threshold. The R values measured by the PETRA experiments from 12 to 31.6 GeV (see Fig. 11.11) do not show the expected rise in R from 4 to 6.

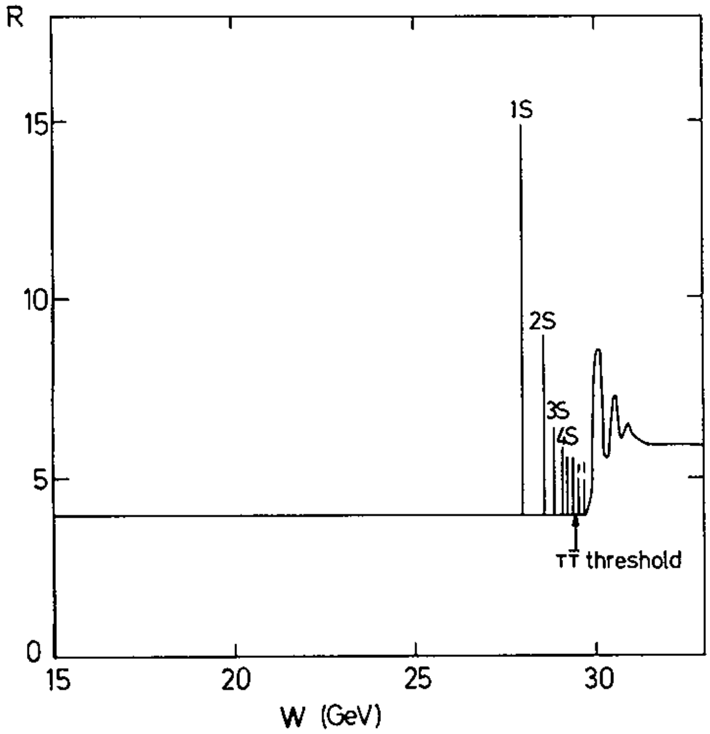

Fig. 11.33 The energy dependence of R expected near the $t\bar{t}$ threshold.

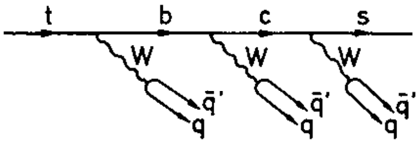

Fig. 11.34 (Hadronic) Decay scheme for t quarks.

As mentioned before the event shape is very sensitive to contributions from the continuum production of $t\bar{t}$. The $t\bar{t}$ events are expected to have a high particle multiplicity and a phase space-like configuration near threshold. According to the Kobayashi-Maskawa generalized Cabibbo matrix[11.41] the favoured decay sequence for t quarks is t → b → c → s. As a consequence $t\bar{t}$ decays may have 14 or more quarks in the final state, presumably leading to a large hadron multiplicity. At threshold the t, $\bar{t}$ quarks are at rest and will emit hadrons more or less isotropically. As the energy increases the t, $\bar{t}$ quarks receive a boost and the events start to become two-jet like. However, this happens only well above threshold. For example a t quark of 10 GeV mass reaches a velocity of $\beta = 0.7$ only at W = 28 GeV, i.e. 8 GeV above threshold. This implies that just above threshold one cannot miss the $t\bar{t}$ continuum contribution.

The final state particles from $t\bar{t}$ events near threshold will be distributed phase space like leading to an average sphericity of $\langle S_{PS} \rangle \sim 0.5$. Fig. 11.35 shows sphericity distributions measured by TASSO[11.9] for different energies between 13 and 31.2 GeV. The dashed-dotted curves indicate the expected S distributions in the presence of the $t\bar{t}$ contribution assuming $R_t = 4/3$. The data show no evidence for such a contribution. Similar conclusions were reached by the other PETRA experiments[11.2, 11.42, 11.43]. The $t\bar{t}$ contribution will also lead to an increase in $\langle S \rangle$. The size of this increase can be readily estimated. The average S for the u, d, s, c, b contribution, e.g. at 30 GeV is $\langle S_{u,d,s,c,b} \rangle = 0.15$. Averaging over the two components predicts for $\langle S \rangle$ above the $t\bar{t}$ threshold

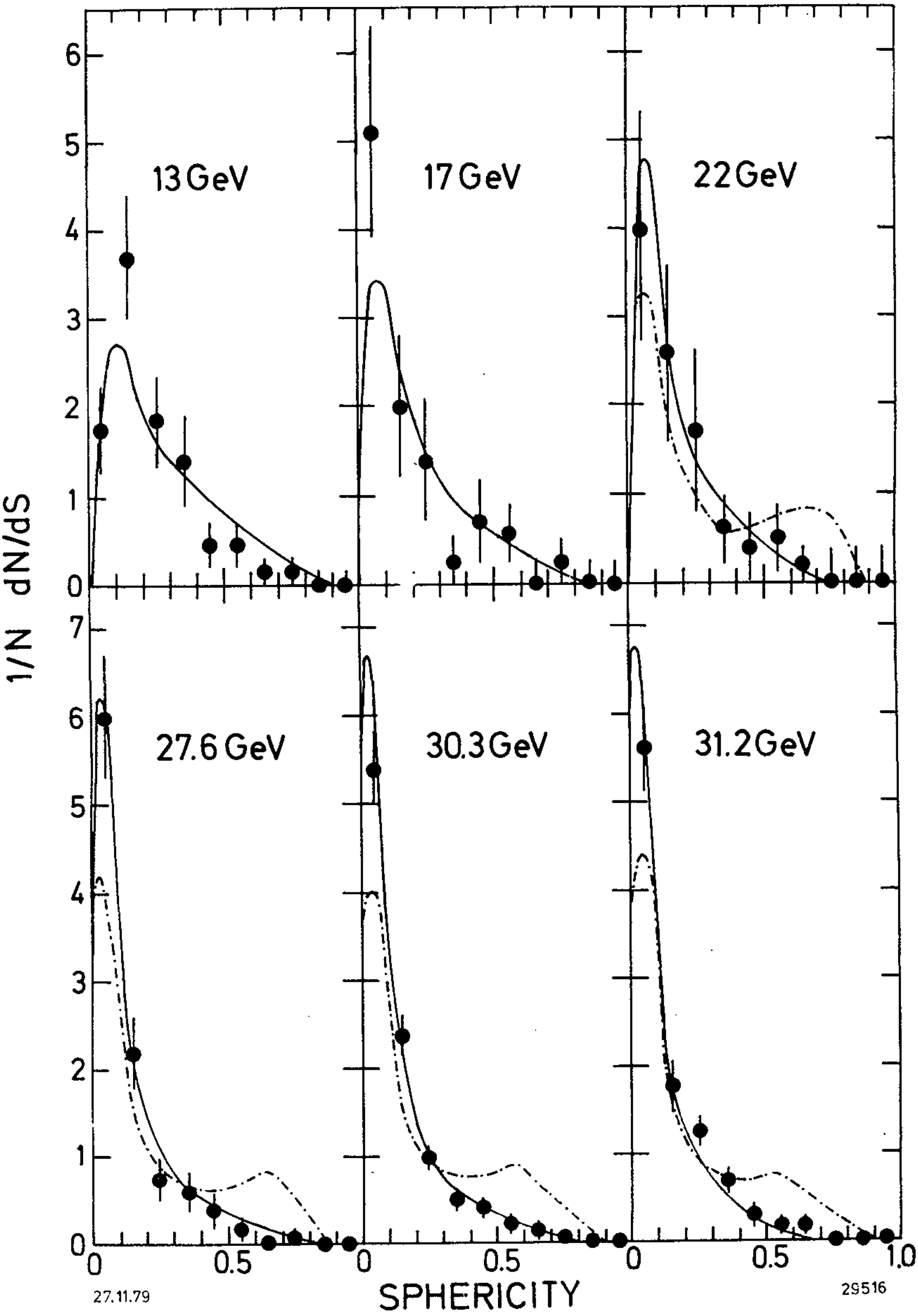

Fig. 11.35 Spericity distribution for different c.m. energies. The curves show the predictions of the quark model with u, d, s, c, b quarks plus gluon corrections (solid) plus a t quark contribution (mass = 10 GeV) (dashed-dotted). (TASSO Ref. 11.9).

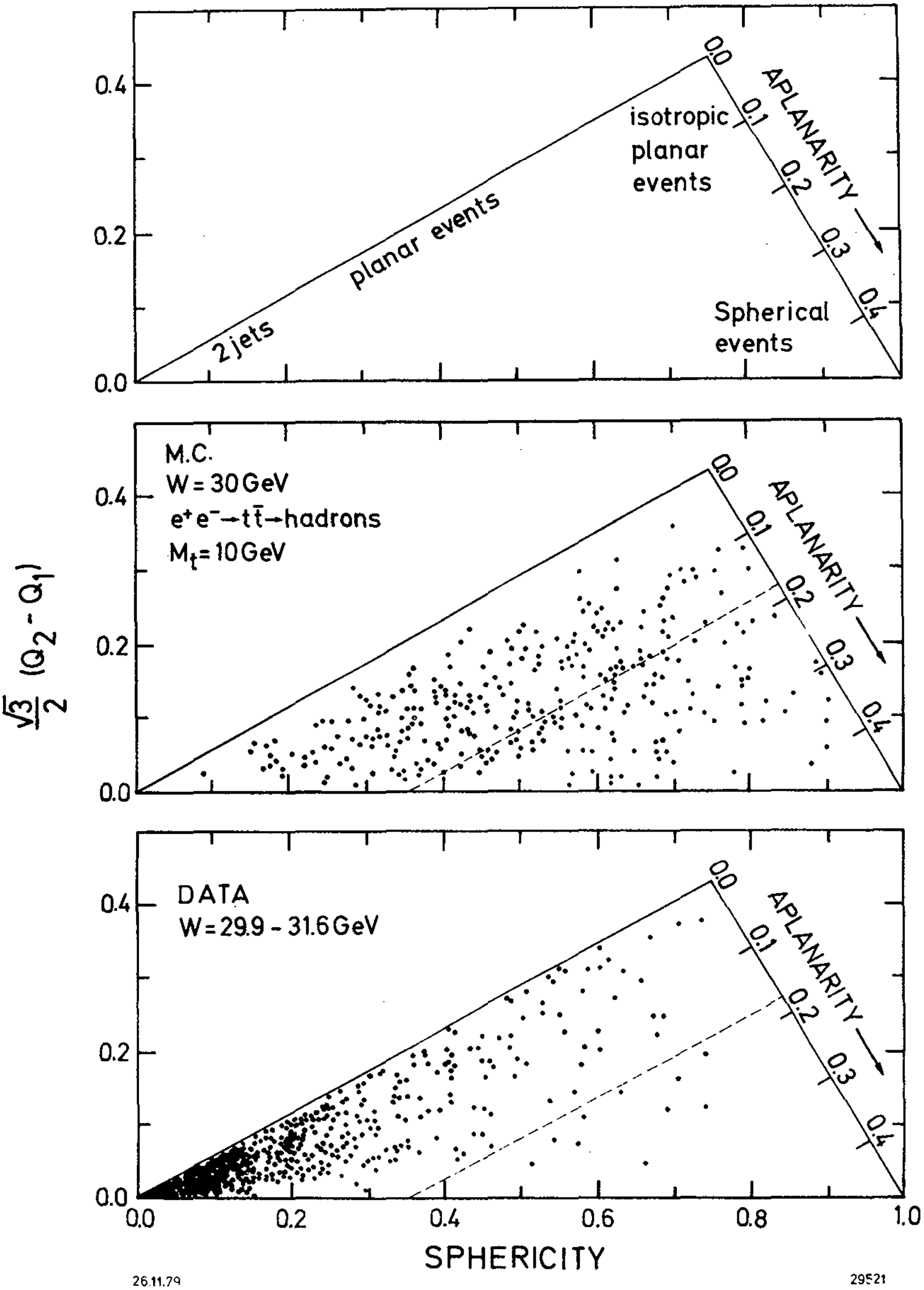

Fig. 11.36 Distribution of events as a function of coplanarity A = 3/2 Q_1 and sphericity S = 3/2 $(Q_1 + Q_2)$ as seen by TASSO (Ref. 11.9).

a) illustrating the regions for two-jet, planar and spherical events;

b) for Monte Carlo generated events from $t\bar{t}$ production, assuming a t mass of 10 MeV and W = 30 GeV;

c) for real events at c.m. energies between 29.9 and 31.6 GeV.

The dashed lines indicate the aplanarity cut at 0.18.

$$\langle S\rangle = \frac{R_t \; \langle S_{PS}\rangle + R_{u,\ldots,b}\langle S_{u,\ldots,b}\rangle}{R_t + R_{u,\ldots,b}} = 0.23$$

corresponding to an increase of ~ 0.08. If the $t\bar{t}$ contribution rises rapidly at threshold to $R_t = 4/3$ one would expect a step in $\langle S\rangle$. The data do not show such a step (see Fig. 11.14).

Sphericity measures the degree of collinearity of the final state particles. Two-jet events tend to be collinear, three-jet events from gluon bremsstrahlung tend to be planar, while phase space-like events are noncollinear and nonplanar. For this reason an inspection of the events in terms of sphericity and aplanarity provides an even more stringent test on a $t\bar{t}$ (or other heavy quark) contribution.

Fig. 11.36 shows the triangle plot distribution in terms of S and A. The sketch given in Fig. 11.36a indicates the areas for collinear ($S \approx 0$), noncollinear coplanar ($S \neq 0$, $A \approx 0$) and for spherical events (S and A large). Fig. 11.36b shows the event distribution expected from the $t\bar{t}$ contribution. It was computed for W = 30 GeV under the conservative assumption that the t mass is 10 GeV and propagating the particles from t fragmentation through the detector. The $t\bar{t}$ events populate the triangle plot rather uniformly. Fig. 11.36c shows for comparison the distribution for events observed at W = 29.9 - 31.6 GeV[11.9]. They concentrate in the collinear, planar corner; only few events are observed at large S and A.

The number of events observed at large S and A in the JADE[11.43] and TASSO[11.9] experiments are compared to the predicted ones in Tables 11.5 and 11.6 assuming a $t\bar{t}$ contribution of $R_t = 4/3$. A t quark contribution is clearly ruled out for a t mass* of 8 GeV or larger. For instance, in the TASSO experiment 10 events were found. Of these 8.2 ± 1 events are expected from u, d, s, c, b production with gluon bremsstrahlung. The remaining 1.8 events are to be compared with 45 ± 3 events expected for a $t\bar{t}$ contribution with $m_t = 8$ GeV.

The TASSO data indicate also that the continuum contribution of a heavy quark with charge 1/3 ($R_Q = 1/3$) appears unlikely. For $m_Q = 10$ GeV and assuming the Q to decay in a manner similar to the t quark, 20 events are predicted compared to 2 ± 4 events observed after subtracting the $q\bar{q}g$ contribution.

Due to the cascade decay $t \rightarrow b \rightarrow c$ the $t\bar{t}$ contribution should yield also a fair fraction of multimuon events. The PLUTO group[11.42] investigated the inclusive muon signal at 27.6 - 31.6 GeV. The observed signal is consistent with u, d, s, c and b production (see Table 11.7). A $t\bar{t}$ contribution assuming a 10% branching ratio for each of the decays $t \rightarrow b\mu\nu$, $b \rightarrow c\mu\nu$ and $c \rightarrow s\mu\nu$ is ruled out on the 5 - 6 s.d. level.

---

* The mass m_t of the t quark is defined such that the threshold for the $t\bar{t}$ continuum is at $2m_t$.

Table 11.6: Search for a heavy quark Q contribution, assuming the Q to decay as the hypothetical t quark. Comparison of the number of events observed for aplanarity $A > 0.18$ with the prediction of the quark-model for u, d, s, c, b production plus gluon correction and for $Q\bar{Q}$ production alone. The $Q\bar{Q}$ estimate assumed a Q mass of 8 GeV or 10 GeV and a contribution to R of $R_Q = 3\, e_Q^2$ where e_Q is the charge of the quark (from TASSO, Ref. 11.9).

W (GeV)	Number of events					
	observed	predicted: u,d,s,c,b + gluon	m_Q=10GeV		m_Q=8 GeV	
			$Q\bar{Q}, e_Q=2/3$	$Q\bar{Q}, e_Q=1/3$	$Q\bar{Q}, e_Q=2/3$	$Q\bar{Q}, e_Q=1/3$
29.9-31.6	10	8.2 ± 1.0	80 ± 8	20 ± 2	45 ± 3	11 ± 1
30.9-31.6	2	2.6 ± 0.4	25 ± 2.5	6 ± 0.6	14 ± 1	3.5 ± 0.2

Table 11.7: Comarison of the inclusive muon signal with expectations from u, d, s, c, b and u, d, s, c, b, t quarks (PLUTO, Ref. 11.42).

E_{cm} (GeV)	# events with a muon ($p > 2$ GeV/c)	computed back-ground	corrected signal	expected	
				udscb	udscbt
27.6	7	2.9 ± 0.8	4.1 ± 2.7	4.7	14.6
30.0	8	4.1 ± 1.2	3.9 ± 3.1	5.1	15.9
31.6	2	1.7 ± 0.5	0.3 ± 1.5	1.7	5.3
total	17	8.7 ± 2.6	8.3 ± 4.9	11.5	35.8

Since quarkonia models predict the first $t\bar{t}$ vector bound state, V_t, to lie approximately 2 GeV below the threshold for the $t\bar{t}$ continuum[11.40] (see Fig. 11.33), an energy scan sensitive to narrow states up to the highest energy will extend the mass range searched for $t\bar{t}$ states by ∿ 2 GeV. Such an energy scan was performed at PETRA between 29.9o and 31.46 GeV in steps of 20 MeV. Results from this were published by TASSO[11.45]. Fig. 11.37 shows R measured as a function of the c.m. energy. No statistically significant structure is observed. The upper limit on the energy integrated cross section contribution of a narrow state ($\Gamma < 20$ MeV) is

$$\int \sigma_V \, dW = \frac{6\pi^2}{M^2} B_h \Gamma_{ee} < 40 \text{ nb MeV}$$

or $\Gamma_{ee} \cdot B_h < 1.6$ keV with 90% C.L. B_h is the branching ratio for hadronic decays. The upper limit on $\Gamma_{ee} \cdot B_h$ is considerably lower compared to what is expected for V_t, $\Gamma_{ee} > 5$ KeV and $B_h \sim 0.7$.

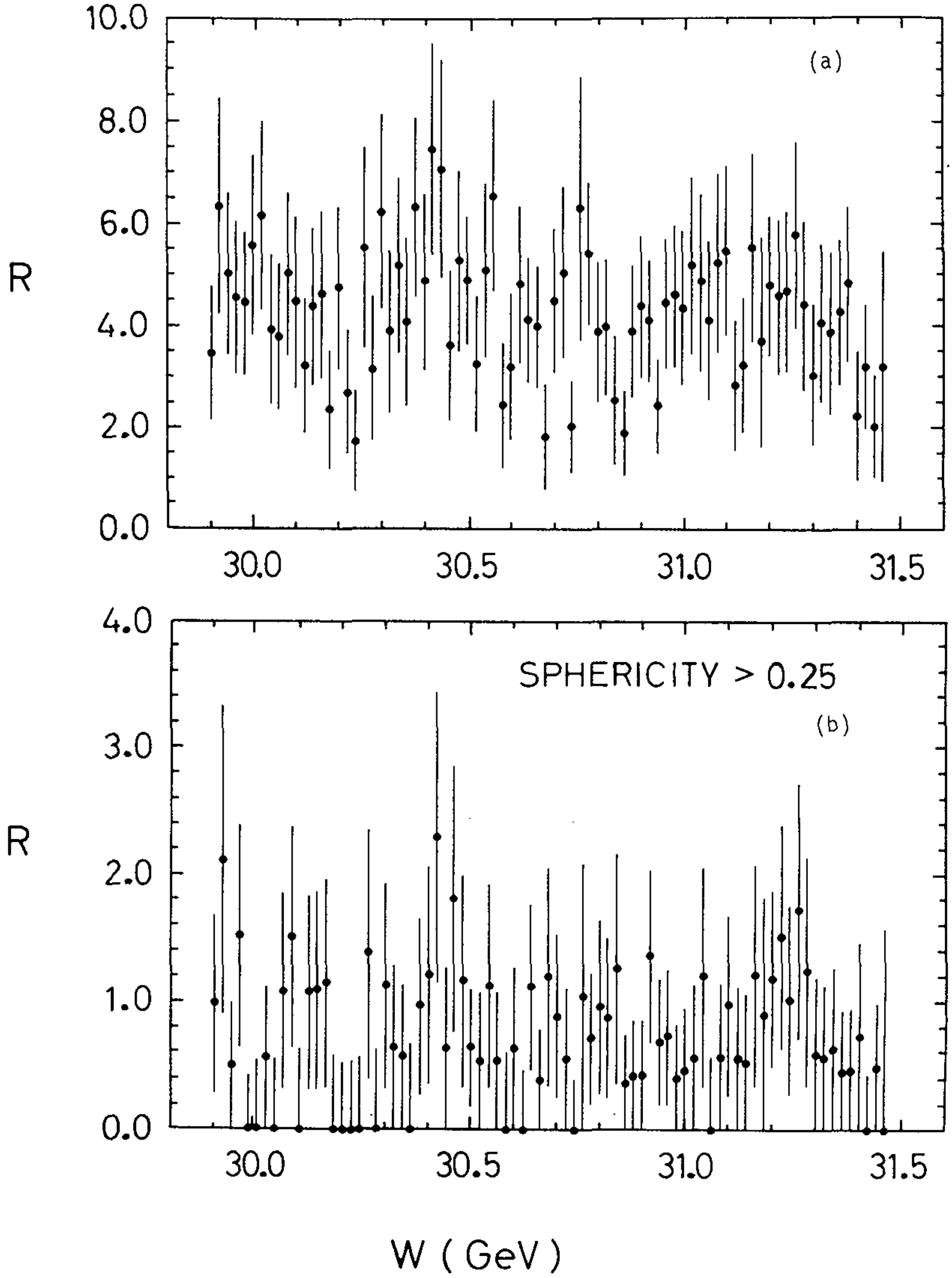

Fig. 11.37 The ratio R of the cross section σ_T for $e^+e^- \to$ hadrons to the τ pair cross section as a function of the c.m. energy W. (TASSO, Ref. 11.45).
a) for all events, b) for events with a sphericity S > 0.25.

11.11 Conclusions

1. The ratio R of the total cross section for e^+e^- annihilation into hadrons to the μ pair cross section is constant within errors between c.m. energies of 17 and 31.6 GeV and has a value close to 4.

2. No evidence has been found for the t quark. A possible $t\bar{t}$ continuum with size R_t=4/3 can be excluded for c.m. energies between 16 and 31 GeV.

3. The multiplicity for charged particles above 10 GeV is found to rise faster than at lower energies.

4. The cross section quantity s $d\sigma/dx$ scales for $x > 0.2$ and $W \geq 5$ GeV to within ±30 %.

5. The shape and magnitude of the total cross section, the observed scaling of s $d\sigma/dx$, the occurence of jets and their gross features are in astonishing agreement with the quark hypothesis.

However:

6. The transverse momentum distribution of headrons relative to the jet axis broadens with increasing energy: $\langle p_T^2 \rangle$ rises rapidly. Hence in the $q\bar{q}$ model the fragmentation function is not energy dependent.

7. The increase of $\langle p_T^2 \rangle$ occurs primarily in only one of the two jets. The distribution of the transverse momentum perpendicular to the "event plane" does not show a pronounced energy dependence while a strong broadening takes place in the event plane at the highest values of $s(= Q^2) \approx 1000$ GeV^2.

8. Planar events were first observed by TASSO and later by all four PETRA-experiments at a rate which is well above the rate computed for statistical fluctuations of the $q\bar{q}$ jets.

9. The planar events when analysed as three-jet events yield an average transverse momentum of 0.3 GeV/c relative to the jet axis which shows that the emitted particles are collimated around three axes.

10. The planar events establish in a model independent way that a small fraction of the e^+e^- annihilation events proceeds via the emission of three constituents, each of which materializes as a jet of hadrons in the final state.

    The data are most naturally explained by hard noncollinear gluon bremsstrahlung, $e^+e^- \rightarrow q\bar{q}g$.

Acknowledgements

Dr. K. Szegö, the scientific director of the school has provided a very enjoyable and stimulating atmosphere. I have profitted a great deal from my fellow lectures, and I am particular grateful to Dr. Maurice Jacob for his encouragement. Special thanks are due to Mrs. Hell for her patience and untiring efforts with the manuscript.

References

The following shorthand notations shall be used: 1971 Cornell Conference for the Proceedings of the 1971 Symposium on Electron and Photon Interactions at High Energies, Cornell, ed. by N. Mistry.

1975 Stanford Conference for the Proceedings of the 1975 Symposium on Lepton and Photon Interactions at High Energies, ed. by W.T. Kirk.

1976 Tbilisi Conference for the XVIIIth International Conference on High Energy Physics, Tbilisi, USSR (1976).

1977 Hamburg Conference for the Proceedings of the 1977 International Symposium on Lepton and Photon Interactions at High Energies, Hamburg, edited by F. Gutbrod.

1978 Tokyo Conference for the XIXth International Conference on High Energy Physics, Tokyo, 1978.

1979 EPS Conference for the International Conference on High Energy Physics, Geneva, 27 June-4 July 1979.

1979 FNAL Conference for the IXth International Symposium on Lepton and Photon Interactions at High Energies, Batavia, Illinois, August 1979.

1.1 B.H. Wiik, Proceedings of the 1978 CERN School of Physics,
E. Lohrmann, DESY Int. Report F79-1 (1979),
G. Flügge, DESY Int. Report PLUTO 80-1 (1980).

1.2 G. Feldman and M.L. Perl, Physics Reports 33 (1977) 285,
Björn H. Wiik and Günter Wolf, Electron Positron Interactions, Springer Tracts in Modern Physics, Volume 86 (1979).

1.3 see e.g. rapporteur talks given at the 1979 EPS Conference and at the 1979 FNAL Conference.

2.1 M. Sands in Physics with intersecting storage rings,
B. Touschek, editor (Academic Press, New Yori, 1971) p. 257,
H. Wiedemann, DESY Internal Report 1974.

3.1 V.E. Balakin et al., Phys.Lett. 34B (1971) 663.

3.2 C. Bacci et al., Frascati report LNF 73/50 (1973)

3.3 see e.g. R. Gatto, Proc. Int. Symp. Electron and Photon Interactions at High Energies, Hamburg 1965, Vol. I, p. 106.

3.4 H. Salecker, Z.Phys. 160, (1960) 385 and
K. Ringhofer and H. Salecker, contrib. to the 1975 Stanford Conference.

3.5 N.M. Kroll, Nuovo Cimento 45A (1966) 65.

3.6 see R. Hofstadter, rapporteur talk, 1975 Stanford Conference, p. 869,
R.F. Schwitters, rapporteur talk, 1976 Tbilisi Conference, B34.

3.7 JADE Collaboration, S. Orito, invited talk, 1979 FNAL Conference, DESY Report 79/77 (1979).

3.8 MARK J Collaboration, D.P. Barber et al., Phys. Rev. Lett. 43 (1979) 1915

3.9 PLUTO Collaboration, G. Flügge, rapporteur talk, 1979 EPS Conf., Geneva, DESY report 79/37 (1979),
PLUTO Collaboration, Ch. Berger, invited talk, 1979 FNAL Conf., PITHA 79/29 (1979).

4.1 F.E. Low, Phys. Rev. 120, (1960) 582,
F. Calogero and C. Zemach, Phys. Rev. 120 (1960) 1860.

4.2 A. Jaccarini, N. Arteago-Romero, J. Parisi and P. Kessler, Compt.Rend. 269B (1969) 153, 1129; Nuovo Cimento 4 (1970) 933;
N. Arteago-Romero, A. Jaccarini, P. Kessler and J. Parisi, Phys. Rev. D3 (1971) 1569;
S.J. Brodsky, T. Kinoshita and H. Terazawa, Phys.Rev.Lett. 25 (1970) 972.

4.3 S. Orito et al., Phys.Lett. 48B (1974) 380.

4.4 R. Feynman, Photon-Hadron Interactions, W.A. Benjamin (New York) 1972.

5.1 A. Quenzer, thesis, ORSAY report LAL 1294 (1977);
A. Cordier et al., Phys.Lett. 81B (1979) 389;
J. Perez-Y-Jorba, rapporteur talk, 1978 Tokyo Conference, p. 277.

5.2 V.A. Sidorov, rapporteur talk, 1976 Tbilisi Conference, N46.

5.3 G.P. Murtas, 1978 Toyko Conference, rapporteur talk, p. 269.

5.4 R.F. Schwitters, rapporteur talk, 1976 Tbilisi Conference, B34.

5.5 J.C. Bizot, data presented at the 1979 EPS Conference in Geneva, p. 362;
J. Augustin, rapporteur talk, ibid. p. 282.

5.6 G.J. Gounaris and J.J. Sakurai, Phys.Rev.Lett. 21 (1968) 244.

5.7 C.J. Bebek et al., Phys.Rev. D13 (1976) 25.

5.8 P. Brauel et al., DESY Report 79/59 (1979).

5.9 F.M. Renard, Nucl.Phys. B82 (1974) 1 and ref. cited.

5.10 J. Buon, private communication.

5.11 M. Castellane et al., data cited by V. Silvestrini, Proc. XVI Int. Conf. on High Energy Physics, 1972, Vol. 4, p.1.

5.12 B. Delcourt, rapporteur talk, 1979 FNAL Conference.

5.13 G. Bassompierre et al., Phys.Lett. 68B (1977) 477.

5.14 J.G. Körner and M. Kuroda, Phys.Rev.D16 (1977) 2165.

5.15 F.M. Renard, Nucl.Phys. B82 (1974) 1.

6.1 H.B. Thacker and J.J. Sakurai, Phys.Lett. 36B (1971) 103;
Y.S. Tsai, Phys.Rev. D4 (1971) 2821;
J.D. Bjorken and C.H. Llewellyn-Smith, Phys.Rev. D7 (1973) 887;
K. Fujikawa and N. Kawamoto, Phys.Rev. D14 (1976) 59;
Y.I. Azimov, L.L. Frankfurt and V.A. Khoze, Zh Eksperim I Teor. FIZ.30 (1977) 63.

6.2 N. Kawamoto and A.I. Sanda, Phys.Lett. 76B (1978) 446;
F.J. Gilman and D.H. Miller, Phys.Rev. D17 (1978) 1846;
Y.S. Tsai, private communication.

6.3 C.H. Llewellyn-Smith, Proc. Royal Soc. A355 (1977) 585.

6.4 M. Bernadini et al., Nuovo Cim. 17 (1973) 383.

6.5 S. Orito et al., Phys.Lett. 48B (1974) 165.

6.6 M.L. Perl et al., Phys.Rev.Lett. 35 (1975) 1489;
M.L. Perl et al., Phys.Lett. 63B (1976) 366.

6.7 PLUTO Collaboration, J. Burmester et al., Phys.Lett. 68B (1977) 301.

6.8 PLUTO Collaboration, J. Burmester et al., Phys.Lett. 68B (1977) 297.

6.9 M.L. Perl, Proceedings of the XII Rencontre de Moriond, Flaine, Vol. 1, 75, 1977 and
1977 Hamburg Conference, p. 145;
G. Flügge, Zeitschrift für Physik C, 1 (1979) 121.

6.10 DASP - Collaboration, R. Brandelik et al., Phys.Lett. 73B (1978) 109.

6.11 DASP - Collaboration, private communication.

6.12 M.L. Perl et al., Phys.Lett.70B (1977) 487;
M.L. Perl et al., Phys.Lett. 63B (1976) 466;
G.J. Feldman et al., Phys.Rev.Lett. 38 (1977) 117;
F.B. Heile et al., Nucl.Phys. B138 (1978) 187.

6.13 Contribution to the Hamburg Conference, see H. Sadrozinski, rapporteur talk, 1977 Hamburg Conference, p. 47.

6.14 M. Cavalli-Sforza et al., Phys.Rev.Lett. 36 (1976) 558.

6.15 A. Barbaro-Galtieri et al., Phys.Rev.Lett. 39 (1977) 1058.

6.16 DASP Collaboration, S. Yamada, 1977 Hamburg Conference, p. 69.

6.17 J.G. Smith et al., Phys.Rev. D18 (1979) 1

6.18 W. Bartel et al., Phys.Lett. 77B (1978) 331

6.19 W. Bacino et al., Phys.Rev.Lett. 41 (1978) 13 and
J. Kirz, data reported at the 1978 Tokyo Conference.

6.20 W. Alles, Ch. Boyer and A.J. Buras, CERN-TH-220 (1977)

6.21 Y.S. Tsai, private communication.

6.22 J. Kirkby, rapporteur talk, 1979 FNAL Conference, SLAC-PUB-2419 (1979).

6.23 G.J. Feldman, International Conference on Neutrino Physics, Purdue University 1978, also SLAC-PUB-2138.

6.24 G.S. Abrams et al., Phys.Rev.Lett. 43 (1979) 1555.

6.25 PLUTO Collaboration, G. Alexander et al., Ohys.Lett. 73B (1978) 99 and W. Wagner et al., Z.Physik C 3 (1980) 193.

6.26 PLUTO Collaboration, G. Alexander et al., Phys.Lett. 81B (1979) 84

6.27 W. Bacino et al., SLAC-PUB-2249 (1979)

6.28 T. Kinoshita and A. Sirlin, Phys.Rev. 108 (1957) 844.

6.29 R.B. Palmer, results presented at the 13th Rencontre de Moriond (1978), Vol. II, Gauge Theories and Leptons, edited by J.Tran Thanh Van, o. 361.

6.30 G.J. Feldman et al., Phys.Rev.Lett. 38 (1977) 117.

6.31 M.L. Perl, rapporteur talk, 1977 Hamburg Conference, p. 145.

6.32 PLUTO Collaboration, G. Alexander et al., Phys.Lett. 78B (1978) 162.

6.33 G. Feldman, rapporteur talk, 1978 Tokyo Conference.

7.1 J.J. Aubert et al., Phys.Rev.Lett. 33, (1974) 1404.

7.2 J.-E. Augustin et al., Phys.Rev.Lett. 33 (1974) 1406.

7.3 G.S. Abrams et al., Phys.Rev.Lett. 33 (1974) 1453.

7.4 B. Knapp et al., Phys.Rev.Lett. 34 (1975) 1040.

7.5 S.L. Glashow, J. Iliopoulos and L. Maiani, Phys.Rev. D2 (1970) 1285.

7.6 An up to date description of the theoretical framework used to describe the new particles with a complete set of references can be found in K. Gottfried, invited paper at the 1977 Hamburg Conference, p. 667; see also :
J.D. Jackson, Proc. of the 1977 European Conference on Particle Physics, Budapest, p. 603;
V.A. Novikov, L.B. Okun, M.A. Shifman, A.I. Vainsthein, M.B. Voloshin and V.I. Zakharov, Physics Reports 41 (1978) 1;
M. Krammer and H. Krasemann, Lecture given at the Advanced Summer Institute, Karlsruhe (1978); DESY report 78/66 (1978), and Acta Physica Austriaca, suppl. 21 (1979) 259.

7.7 T. Appelquist et al., Phys.Rev.Lett. 34 (1975) 43;
C.G. Callan et al., Phys.Rev.Lett. 34 (1975) 52.

7.8 E. Eichten et al., Phys.Rev.Lett. 34 (1975) 369;
E. Eichten et al., Phys.Rev.Lett. 36 (1976) 500.

7.9 DASP Collaboration, W. Braunschweig et al., Phys.Lett. 57B (1975) 407, and Z. Physik C 1 (1979) 233; see also E. Gadermann, thesis, Hamburg University, 1978.

7.10 P.A. Rapidis et al., Phys.Rev.Lett. 39 (1977) 526.

7.11 W. Bacino et al., Phys.Rev.Lett. 40 (1978) 671.

7.12 R. Barbieri et al., Nucl.Phys. 105 (1976) 125,
Celmaster SLAC-PUB-2151 (1978)

7.13 J. Siegrist et al., Phys.Rev.Lett. 36 (1976) 700.

7.14 PLUTO Collaboration, J. Burmester et al., Phys.Lett. 66B (1977) 395;
G. Knies, rapporteur talk, 1977 Hamburg Conference, p. 93.

7.15 DASP Collaboration, R. Brandelik et al., Phys.Lett. 76B (1978) 361,
A. Petersen, thesis, University of Hamburg, 1978.

7.16 J.-E. Augustin et al., Phys.Rev.Lett. 33 (1974) 1406;
G.S. Abrams et al., Phys.Rev.Lett. 33 (1974) 1453;
A.M. Boyarski et al., Phys.Rev.Lett. 34 (1975) 764.

7.17 K. Gottfried, rapporteur talk, 1977 Hamburg Conference, p. 667;
M. Caichian and R. Kögerler, Phys.Lett. 80B (1978) 105;
A multichannel analysis of the 4 GeV region has been presented by D. Horn and D.E. Novoseller, preprint, 1978.

7.18 R. Barbieri, R. Gatto and R. Kögerler, Phys.Lett. 60B (1976) 183.

7.19 Crystal Ball Collaboration, data presented by E. Bloom at the 1979 FNAL Conference, SLAC-PUB-2425 (1979) and R. Partridge et al., SLAC-PUB.2430 (1979).

7.20 W.D. Apel et al., Phys.Lett. 72B (1978) 500.

7.21 DESY-Heidelberg-Collaboration, see J. Olsson, rapporteur talk, 1977 Hamburg Conference, p. 117;
W. Bartel et al., Phys.Lett. 79B (1978) 492.

7.22 C.J. Biddick et al., Phys.Rev. 38 (1977) 1324; see also
H.F.W. Sadrozinski, rapporteur talk, 1977 Hamburg Conference, p. 47.

7.23 J.S. Whitaker et al., Phys.Rev.Lett. 37 (1976) 1596;
G.H. Trilling in Proceedings of the SLAC Summer Institute on Particle Physics, 1976 SLAC report 198.

7.24 J.S. Whitaker et al., Phys.Rev.Lett. 37 (1976) 1596.

7.25 F.M. Pierre, LBL report LBL-5324 (1976);
G.H. Trilling, Proceedings of the SLAC-Summer Institute on Particle Physics, 1976, SLAC-report 198, p. 437.

7.26 R. Barbieri, R. Gatto and E. Remiddi, Phys.Lett. 61B (1976) 465.

7.27 DASP Collaboration, W. Braunschweig et al., Phys.Lett. 67B (1977) 243 and 249;
S. Yamada, rapporteur talk, 1977 Hamburg Conference, p. 69.

7.28 F.A. Berends and R. Gastman, Nucl.Phys. B61 (1973) 414.

8.1 M.K. Gaillard, B.W. Lee and J.L. Rosner, Rev.Mod.Phys. 47 (1975) 277.

8.2 J. Ellis, M.K. Gaillard and D.V. Nanopoulos, Nucl.Phys. B100 (1975) 313; see also M.K. Gaillard, rapporteur talk, 1979 FNAL Conference FERMILAB Conf. 79/87 - THY (1979) and references given there.

8.3 V. Lüth, invited talk, 1979 FNAL Conference, SLAC-PUB-2405 (1979);
G.S. Abrams et al., Phys.Rev.Lett. 43 (1979) 481;
G.S. Abrams et al., Phys.Rev.Lett. 44 (1980) 10.

8.4 J. Kirkby, invited talk, 1979 FNAL Conference, SLAC-PUB-2419 (1979);
W. Bacino et al., Phys.Rev.Lett. 43 (1979) 1073.

8.5 DASP Collaboration, R. Brandelik et al., Phys.Lett. 70B (1977) 132 and 80B (1979) 412.

8.6 DASP Collaboration, W. Braunschweig et al., Phys.Lett. 63B (1976) 471; DASP Collaboration, R. Brandelik et al., Phys.Lett. 70B (1977) 125 and 70B (1977) 387.

8.7 M. Katuya, Phys.Rev. D18 ((1978) 3510. Y. Hara, Progr.Theor.Phys. (1979); M. Katuya and Y. Koide, Phys.Rev. D19 (1979) 2631.

8.8 J.M. Feller et al., Phys.Rev.Lett. 40 (1978) 274 and
A. Barbaro-Galtieri, rapporteur talk, 1977 Hamburg Conference, p.21.

8.9 see e.g. M.K. Gaillard, ref. 8.2; H. Fritzsch and P. Minkowski, University of Bern, preprint 1979.

8.10 D. Lüke, invited talk given at the 1977 Meeting of the Division of Particles and Fields of the A.P.S., Argonne, Illinois, Oct. 1977. SLAC-PUB-2086 (February 1978) and A. Barbaro-Galtieri, Lectures presented at the XVI International School of Subnuclear Physics, Erice, 1978, LBL report-8537 (1978).

8.11 F. Richard, invited talk at the 1979 FNAL Conference, Orsay Report LAL 79/35 (1979).

8.12 E.G. Cazzoli et al., Phys.Rev.Lett. 34 (1975) 1125.

8.13 B. Knapp et al., Phys.Rev.Lett. 37 (1976) 882.

8.14 For a review of charmed baryon data see F. Muller, Cargèse Lectures 1979, CERN Report EP-148 (1979).

9.1 S.W. Herb et al., Phys.Rev.Lett. 39 (1977) 252;
W.R. Innes et al., Phys.Rev.Lett. 39 (1977) 1240;
L.M. Lederman, rapporteur talk, 1978 Tokyo Conference.

9.2 PLUTO Collaboration, Ch. Berger et al., Phys.Lett. 76B (1978) 243.

9.3 C.W. Darden et al., Phys.Lett. 76B (1978) 246.

9.4 J.K. Bienlein et al., Phys.Lett. 78B (1978) 360.

9.5 PLUTO Collaboration, Ch. Berger et al., DESY report 79/19 (1979).

9.6 C.W. Darden et al., Phys.Lett. 78B (1978) 364;
C.W. Darden et al., Phys.Lett. 80B (1979) 419.

9.7 G. Heinzelmann, data presented at the 1978 Tokyo Conference.

9.8 G. Flügge, rapporteur talk, 1978 Tokyo Conference;
H. Spitzer, talk given at the 1978 Kyoto Conference;
H. Meyer, rapporteur talk, 1979 FNAL Conference, DESY report 79/81 (1979).

9.9 J.L. Rosner, C. Quigg, and H.B. Thacker, Phys.Lett. 74B (1978) 350;
see also C. Quigg, rapporteur talk, 1979 FNAL Conference, report Fermilab-Conf. 79/74-THY (1979)

10.1 K. Koller and T.F. Walsh, Phys.Lett. B72 (1977) 227;
B73 (1978) 504 and Nucl.Phys. B140 (1978) 449;
T.A. De Grand et al., Phys.Rev. D16 (1977) 3251;
S.J. Brodsky et al., Phys.Lett. B73 (1978) 203.

10.2 see e.g. H. Fritzsch, Schladming Lectures 1978, Acta Physica Austriaca, Suppl. XIX, p. 249 and H. Fritzsch and K.H. Streng, Phys.Lett. B74 (1978) 90.

10.3 K. Hagiwara, Nucl.Phys. B137 (1978) 164;
A. de Rujula et al., Nucl.Phys.B138 (1978) 387.

10.4 D.J. Bjorken and S.J. Brodsky, Phys.Rev. D1 (1970) 1416.

10.5 S. Brandt et al., Phys.Lett. 12 (1964) 57;
E. Fahri, Phys.Rev.Lett. 39 (1977) 1587.

10.6 PLUTO Collaboration, Ch. Berger et al., Phys.Lett. B78 (1978) 176.

10.7 PLUTO Collaboration, Ch. Berger et al., DESY report 78/71, and Phys.Lett. 82B (1979) 449.

10.8 R.F. Schwitters, rapporteur talk, 1975 Stanford Conference, p.5;
R.F. Schwitters et al., Phys.Rev.Lett. 35 (1975) 1320;
G. Hanson et al., Phys.Rev.Lett. 35 (1975) 1609.

10.9 R.D. Field and R.P. Feynman, Nucl.Phys. B136 (1978) 1.

10.10 S. Brandt and H.D. Dahmen, Z. Physik C 1 (1979) 61.

10.11. PLUTO group, data presented by S. Brandt at the 1979 EPS Conference, DESY Report 79/42 (1979).

10.12 K. Koller and H. Krasemann, Phys.Lett. 88B (1979) 119.

11.1 JADE Collaboration, S. Orito, Invited talk 1979 FNAL Conference, DESY Report 79/77 (1979).

11.2 MARK J Collaboration, H. Newman, invited talk 1979 FNAL Conference.

11.3 PLUTO Collaboration, Ch. Berger, invited talk 1979 FNAL Conference, TH Aachen Report PITHA 79/29 (1979).

11.4 TASSO Collaboration, G. Wolf, invited talk 1979 FNAL Conference, DESY Report 79/57 (1979).

11.5 A. Quenzer, thesis, Orsay raport LAL 1294 (1977);
A. Cordier et al., Phys.Lett. 81B (1979) 389;
A.V. Sidorov, rapporteur talk, 1976 Tbilisi Conference, for the XVIIIth International Conference on Lepton and Photon Interactions at High Energies, Hamburg, ed. by F. Gutbrod, N 46;
G.P. Murtas, Rapporteur talk, 1978 Tokyo Conference for the XIXth International Conference on High Energy Physics, Tokyo, B2;
J. Perez-Y-Jorba, rapporteur talk, 1978 Tokyo Conference;
R.F. Schwitters, rapporteur talk, 1976 Tbilisi Conference, B 34;
PLUTO Collaboration, J. Burmester et al., Phys.Lett. 66B (1977) 395;
DASP Collaboration, R. Brandelik et al., Phys.Lett. 76B (1978) 361.

11.6 PLUTO Collaboration, Ch. Berger et al., Phys.Lett. 81B (1979) 410.

11.7 MARK J Collaboration, D.P. Barber et al., MIT Report 107 (1979).

11.8 JADE Collaboration, W. Bartel et al., DESY Report 79/64 (1979).

11.9 TASSO Collaboration, R. Brandelik et al., DESY Report 79/74 (1979) and Z. Physik C, to be published.

11.10 C. Bacci et al., Phys.Lett. 86B (1979) 234.

11.11 SLAC-LBL Collaboration, G.G. Hanson, 13th Rencontre de Moriond (1978), ed. by J. Tran Thanh Van, Vol. III.

11.12 PLUTO Collaboration, Ch. Berger et al., Phys.Lett. 81B (1979) 410, 78B (1978) 176, and V. Blobel, private communication.

11.13 DASP Collaboration, R. Brandelik et al., Nucl.Phys. B148 (1979) 189.

11.14 JADE Collaboration, W. Bartel et al., Phys. Lett. 88B (1979) 171

11.15 TASSO Collaboration, R. Brandelik et al., Phys.Lett. 89B (1980) 418.

11.16 W. Thomé et al., Nucl. Phys. B129 (1977) 365; see also the review by E. Albini, P. Capiluppi, G. Giacomelli, and A.M. Rossi, Nuovo Cimento 32A (1976) 101.

11.17 Data given by R. Stenbacka et al., Nuovo Cimento 51A (1979) 63; see also S. Barshay, A. Fridman and P. Juillot, Phys.Rev. D15 (1977) 2702.

11.18 J. Ellis (private communication), motivated by W. Furmanski, R. Petronzio and S. Pokorski, Nucl.Phys. B155 (1979) 253.

11.19 see e.g. S.D. Drell, D. Levy and T.M. Yan, Phys.Rev. 187(1969) 2159; D1 (1970) 1035, 1617, 2402.

11.20 G.J. Feldman and M.L. Perl, Physics Reports 33 (1977) 285.

11.21 R. Baier, J. Engels and B. Peterson, University of Bielefeld report BI-TP 79/10 (1979);
W.R. Frazer and J.F. Gunion, Phys.Rev. D20 (1979) 147.

11.22 A. de Rujula, J. Ellis, E.G. Flotatos and M.K. Gaillard, Nucl.Phys. B138 (1978) 387. Compared to the original version the nonperturbative part was readjusted; J. Ellis, private communication.

11.23 G.G. Hanson, results presented at the 13th Rencontre de Moriond (1978), Vol. II, Gauge Theories and Leptons, edited by J. Tran Thanh Van and SLAC-PUB-2118.

11.24 B.H. Wiik, Proceedings of the International Neutrino Conference, Bergen, Norway, 18-22 June 1979.
R. Cashmore, Proceedings of the EPS International Conference on High Energy Physics, Geneva, Switzerland, 27 June - 4 July 1979 and DESY-Report 79/50 (1979),
P. Söding, ibid.
G. Wolf, ibid. and DESY-Report 79/14 (1979).

11.25 J. Ellis, M.K. Gaillard and G.G. Ross, Nucl.Phys. B111 (1976) 253 erratum B130 (1977) 516.

11.26 TASSO Collaboration, R. Brandelik et al., Phys.Lett. 86B (1979) 243.

11.27 The branching ratios for B decay were taken from A. Ali, J.G. Körner, J. Willrodt, and G. Kramer, Z. Physik C 2 (1979) 233.

11.28 J. Kogut and L. Susskind, Phys.Rev. D9 (1974) 697, 3391;
A.M. Polyakov, Proc. 1975 Int. Symp. on Lepton and Photon Interactions at High Energies, Stanford, ed. by W. T. Kirk, p. 855.

11.29 A. de Rujula, J. Ellis, E.G. Floratos and M.K. Gaillard, Nucl. Phys. B139 (1978) 387.

11.30 T.A. de Grand, Y.J. Ng and S.-H.H. Tye, Phys.Rev. D16 (1977) 3251.

11.31 G. Sterman and S. Weinberg, Phys.Rev.Lett. 39 (1977) 1436.

11.32 G. Kramer and G. Schierholz, DESY-Report 78/62 (1978);
G. Kramer, G. Schierholz and J. Willrodt, Phys.Lett. 79B (1978) 249.

11.33 P. Hoyer, P. Osland, H.G. Sander, T.F. Walsh and P.M. Zerwas, DESY-Report 78/21 (1978).

11.34 PLUTO Collaboration, Ch. Berger et al., Phys.Lett. 86B (1979) 418;
DESY Report 79/57.

11.35 J.D. Bjorken and S.J. Brodsky, Phys.Rev. D1 (1970) 1416;
S.L. Wu and G. Zobernig, Z. Physik C 2 (1979) 107.

11.36 JADE Collaboration, W. Bartel et al., DESY Report 79/80 (1979)

11.37 MARK J Collaboration, D.P. Barber et al., Phys.Rev.Lett. 43 (1979) 830.

11.38 A. Ali, E. Pietarinen, G. Kramer and J. Willrodt, DESY-Report 79/86 (1979).

11.39 see e.g. C.J. Aubrecht II and D.M. Scott, COO-1545 - 247;
G. Preparata, CERN TH 2599 (1978);
M.A. Combrugghe, Phys.Lett. 80B (1979) 365;
H. Georgi and D.V. Nanopoulos, HUTH-78/A039 (1978);
H. Harari, H. Haut and J. Weyers, Phys.Lett. 78B (1978) 459;
J.D. Bjorken, SLAC-PUB-2195 (1978);
T.F. Walsh, DESY-Report DESY 78/68 (1978);
T. Kitazoe and K. Tanaka, Phys.Rev. D18 (1978) 3476;
S. Pakvasa and H. Sugawara, Phys.Lett. 82B (1979) 105.

11.40 C. Quigg and J.C. Rosner, Phys.Lett. 72B (1978) 462;
G. Bhanot and S. Rudaz, Phys.Lett. 78B (1978) 119;
H. Krasemann and S. Ono, Nucl.Phys. B154 (1979) 283;

11.41 M. Kobayashi and M. Maskawa, Prog.Theor.Phys. 49 (1973) 652.

11.42 PLUTO Collaboration, Ch. Berger et al., Phys.Lett. 86B (1979) 413.

11.43 JADE Collaboration, W. Bartel et al., Phys.Lett. 89B (1979) 136.

11.44 A. Ali, J.G. Körner, G. Kramer, and J. Willrodt, Z. Physik C1b (1979) 203

11.45 TASSO Collaboration, R. Brandelik et al., Phys.Lett. 88B (1979) 199.